

**DISSERTAÇÃO DE MESTRADO EM ENGENHARIA DE SISTEMAS
ELETRÔNICOS E DE AUTOMAÇÃO**

**QUANTITATIVE ANALYSIS OF THE AUTONOMIC NERVOUS
SYSTEM: TOOLBOX DEVELOPMENT AND APPLICATION**

Luisa Santiago Contreiras Brito da Silva

DEPARTAMENTO DE ENGENHARIA ELÉTRICA

UNIVERSIDADE DE BRASÍLIA

FACULDADE DE TECNOLOGIA

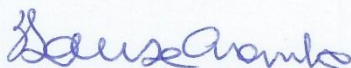
**UNIVERSIDADE DE BRASÍLIA
FACULDADE DE TECNOLOGIA
DEPARTAMENTO DE ENGENHARIA ELÉTRICA**

**QUANTITATIVE ANALYSIS OF THE AUTONOMIC NERVOUS
SYSTEM: TOOLBOX DEVELOPMENT AND APPLICATION**

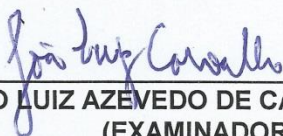
LUIZA SANTIAGO CONTREIRAS BRITO DA SILVA

DISSERTAÇÃO DE MESTRADO SUBMETIDA AO DEPARTAMENTO DE ENGENHARIA ELÉTRICA DA FACULDADE DE TECNOLOGIA DA UNIVERSIDADE DE BRASÍLIA, COMO PARTE DOS REQUISITOS NECESSÁRIOS PARA A OBTENÇÃO DO GRAU DE MESTRE.

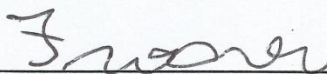
APROVADA POR:



FLÁVIA MARIA GUERRA DE SOUSA ARANHA OLIVEIRA, Dra., ENE/UNB
(ORIENTADORA)



JOÃO LUIZ AZEVEDO DE CARVALHO, Dr., ENE/UNB
(EXAMINADOR INTERNO)



FABIANO ARAUJO SOARES, Dr., FGA/UNB
(EXAMINADOR EXTERNO)

Brasília, 27 de novembro de 2017.

FICHA CATALOGRÁFICA

SILVA, LUISA SANTIAGO CONTREIRAS BRITO DA

Quantitative Analysis of the Autonomic Nervous System: Toolbox Development and Application [Distrito Federal] 2017.

xxix, 139p., 210 x 297 mm (ENE/FT/UnB, Mestre, Engenharia Elétrica, 2017).

Dissertação de Mestrado – Universidade de Brasília. Faculdade de Tecnologia.

Departamento de Engenharia Elétrica

1.CRSIDLab

2.Autonomic Nervous System

3.Cardiorespiratory System

4.System identification

I. ENE/FT/UnB

II. Título (série)

REFERÊNCIA BIBLIOGRÁFICA

SILVA, L. S. C. B. (2017). Quantitative Analysis of the Autonomic Nervous System: Toolbox Development and Application. Dissertação de Mestrado em Engenharia de Sistemas Eletrônicos e de Automação, Publicação PPGEA.DM – 680/2017. Departamento de Engenharia Elétrica, Universidade de Brasília, Brasília, DF, 139p.

CESSÃO DE DIREITOS


AUTOR: Luisa Santiago Contreiras Brito da Silva.

TÍTULO: Quantitative Analysis of the Autonomic Nervous System: Toolbox Development and Application.

GRAU: Mestre

ANO: 2017

É concedida à Universidade de Brasília permissão para reproduzir cópias desta dissertação de mestrado e para emprestar ou vender tais cópias somente para propósitos acadêmicos e científicos. O autor reserva outros direitos de publicação e nenhuma parte dessa dissertação de mestrado pode ser reproduzida sem autorização por escrito do autor.



Luisa Santiago Contreiras Brito da Silva
Departamento de Engenharia Elétrica (ENE) - FT
Universidade de Brasília (UnB)
Campus Darcy Ribeiro
CEP 70.919-970 Brasília - DF - Brasil

ACKNOWLEDGMENTS

Initially I would like to thank my advisor Flavia for her guidance and assistance since we first started working together in an undergraduate research project. I had never considered pursuing a graduate degree when I came to you looking to know more about biomedical engineering, but discovering this amazing universe and having such a great experience under your guidance encouraged me to continue my studies.

I would like to thank my family, especially my mother, father and sister: Christiane, Fernando and Beatriz. Thank you for your support on this new path, for your patience and for understanding my absence at times. Thank you for having my back at all times.

I thank my boyfriend, Pedro, for sharing this experience with me. Thank you for listening, even when you didn't fully understand what I was talking about, but always doing your best to put in a constructive word. Thanks for constantly refreshing my energy.

I would like to thank my friends and colleagues, Ana, Êmille and Victor, for their companionship, shared frustrations, and for providing much needed entertainment through stressful times. I would also like to give special thanks to Victor's mother, Tânia, and Êmille's sister, Jamille, for providing assistance that was essential for the successful completion of this work.

I also thank my friends from school who went on to pursue their own graduate degrees, Gustavo, Ian, and Luis Guilherme, for our academic rants, their words of encouragement, all the knowledge exchange and for the moments of fun and leisure.

Finally, I thank Fundação de Apoio à Pesquisa do DF (FAP/DF) for their financial support granted through a scholarship (Edital 06/2015).

Luisa Santiago

RESUMO

O sistema nervoso autônomo (SNA) controla as funções involuntárias do corpo e seu desequilíbrio é associado a um risco aumentado de mortalidade cardíaca. A análise da variabilidade da frequência cardíaca (VFC) é comumente utilizada como um método não-invasivo de avaliar a modulação do SNA. Medidas tradicionais de VFC se baseiam em análises das oscilações da frequência cardíaca (ou o seu recíproco, o intervalo entre ondas R consecutivas no eletrocardiograma – IRR) a cada batimento, já que o ritmo da frequência cardíaca (FC) é uma consequência das atividades simpática e parassimpática no nó sinoatrial do coração. Entretanto, essas oscilações da FC também são influenciadas por mecanismos que afetam a VFC, como o baroreflexo e a arritmia sinusal respiratória (ASR). Portanto, neste trabalho, uma análise multivariável do sistema cardiorrespiratório é usada.

Este estudo consiste em duas partes: o desenvolvimento do laboratório de identificação do sistema cardiorrespiratório (CRSIDLab), uma interface gráfica para Matlab que fornece indicadores quantitativos da atividade do SNA a partir da análise de um modelo multivariável do sistema cardiorrespiratório, seguido por sua aplicação em dados obtidos de sujeitos nas posturas supino e de pé, ilustrando sua capacidade. O eletrocardiograma (ECG), pressão arterial (PA) contínua e fluxo de ar de 23 sujeitos foram registrados nas posturas supino e de pé por 10 min e pré-processados no CRSIDLab.

Neste trabalho as análises clássicas de VFC e variabilidade da PA (VPA) foram feitas através da análise da densidade espectral de potência (DEP) do IRR e da PA sistólica (PAS), respectivamente. O CRSIDLab implementa três métodos de análise espectral: a transformada de Fourier, o método de Welch e o modelo autorregressivo (AR). Todos os métodos foram utilizados para calcular a potência das bandas de baixa frequência (BF: 0.04-0.15 Hz) e alta frequência (AF: 0.15-0.4 Hz), como a área sob a curva da DEP. Para a VFC, a razão BF/AF também foi calculada. Estimativas tradicionais de sensibilidade do baroreflexo (SBR) foram calculadas a partir da relação entre VFC a VPA.

Funções de transferência espectrais foram estimadas entre a PAS e o IRR, caracterizando o baroreflexo, e entre o volume pulmonar instantâneo (VPI, derivado do registro de fluxo de ar) e o IRR, caracterizando a ASR, ou os efeitos da respiração na FC, para determinação dos ganhos em BF e AF. A SBR foi estimada a partir dos ganhos da função de transferência entre a PAS e o IRR.

A dinâmica entre a PA e a FC é de malha fechada, na qual a PA influencia a FC através do baroreflexo e a FC influencia a PA através da dinâmica circulatória. A respiração exerce uma influência direta sobre a FC que é mediada pelo SNA, chamada de acoplamento cardiorrespiratório (ACR), e também um efeito mecânico indireto mediado pelo baroreflexo. Enquanto análises espectrais univariáveis e bivariáveis podem ser usadas para avaliar esses mecanismos, são técnicas de malha aberta que são incapazes de diferenciar efeitos de retroalimentação dos efeitos de alimentação direta e também de separar o ACR das influências indiretas da respiração na FC.

Para lidar com essas limitações, uma abordagem de identificação de sistemas foi aplicada. O CRSIDLab implementa três modelos: o modelo AR com entradas exógenas (ARX), o modelo de funções de base de Laguerre (FBL) e o modelo de funções de base de Meixner (FBM). As respostas ao impulso, que caracterizam a dinâmica entre cada par de variáveis, são calculadas a partir do modelo estimado. Esses modelos são capazes de isolar o ACR ao considerar ambos VPI e PAS como entradas e conseguem abrir a malha do baroreflexo computacionalmente pela imposição de atrasos entre a PAS e o IRR, caracterizando a resposta ao impulso do baroreflexo arterial (BRA). A partir dessas análises, não só o ganho em cada banda de frequência é fornecido através da transformada de Fourier da resposta ao impulso, mas também informações temporais como o atraso entre duas variáveis.

Os resultados mostram que ficar de pé é acompanhado por uma supressão vagal e tom vascular simpático aumentado. Análises de correlação mostraram que as estimativas de ASR e SBR baseadas em análises espectrais não apresentam a mesma informação que as estimativas baseadas no modelo de ACR e BRA. As diferenças encontradas sugerem que as análises baseadas em modelo são efetivas em representar o ACR como uma medida dos efeitos diretos da respiração na FC e o BRA como expressão do baroreflexo independente da dinâmica circulatória.

Assim, o CRSIDLab é uma ferramenta poderosa para a determinação não-invasiva de diferentes indicadores quantitativos do SNA. Os resultados mostram que os indicadores estimados refletem a fisiologia subjacente, pois ficar de pé é um estímulo simpático que deveria levar a supressão vagal, conforme observado. Os resultados obtidos também mostram que a abordagem de modelagem de sistemas multivariáveis pode fornecer importantes informações adicionais àquelas encontradas pelas abordagens espectrais mais tradicionais, podendo levar a indicadores quantitativos mais específicos do SNA.

ABSTRACT

The autonomic nervous system (ANS) controls the involuntary functions of the body and its imbalance has been linked to increased risk of cardiac mortality. Heart rate variability (HRV) analysis is usually employed as a non-invasive method for assessing ANS modulation. Traditional measures of HRV are based on the analysis of the beat-to-beat oscillations in heart rate (or its reciprocal, the interval between consecutive R waves on the electrocardiogram - RRI), since heart rate (HR) rhythm is a consequence of sympathetic and parasympathetic activity on the sinoatrial node of the heart. However, these oscillations in beat-to-beat HR are also influenced by mechanisms, such as baroreflex and respiratory sinus arrhythmia (RSA), that affect HRV. Therefore, in this work, a multivariate analysis of the cardiorespiratory system is used.

This study consists of two parts: the development of the cardiorespiratory system identification lab (CRSIDLab), a Matlab graphical user interface that provides quantitative indicators of ANS activity from a multivariate system model analysis of cardiorespiratory data, followed by its application on data obtained from subjects in supine and standing postures, illustrating its capabilities. Electrocardiogram (ECG), continuous blood pressure (BP) and airflow were recorded from 23 subjects in supine and standing postures for 10 min and preprocessed on CRSIDLab.

In this work the classical HRV and BP variability (BPV) analyses were performed through power spectral density (PSD) analysis of the RRI and the systolic BP (SBP), respectively. CRSIDLab implements three methods for spectral analysis: the Fourier transform, Welch method and AR model. All methods were used to calculate the power of the low frequency (LF: 0.04-0.15 Hz) and high frequency (HF: 0.15-0.4 Hz) bands, as the areas under the PSD curve. For the HRV, the LF/HF ratio was also calculated. Traditional baroreflex sensitivity (BRS) estimates were calculated from the relation between HRV and BPV in the LF and HF regions.

Spectral transfer functions were estimated between SBP and RRI, characterizing baroreflex, and between instantaneous lung volume (ILV, derived from the airflow record) and RRI, characterizing RSA, or the effects of respiration on HR, for the determination of the LF and HF gains. BRS was estimated from the gains of the transfer function between SBP and RRI.

The dynamics between BP and HR are closed-loop, where BP influences HR through baroreflex and HR influences BP through circulatory dynamics. Respiration has a direct influence on HR that is mediated through the ANS, called the respiratory-cardiac coupling (RCC), and also a mechanical indirect effect mediated through baroreflex. While univariate and bivariate spectral analyses can be used to assess these effects, they are open-loop techniques that are unable to differentiate feedforward from feedback effects and also to separate RCC from the indirect effects of respiration on HR.

To address these limitations a system model identification approach was applied. CRSIDLab implements three types of models: the autoregressive with exogenous inputs (ARX) model, the Laguerre basis function (LBF) model, and the Meixner basis function (MBF) model. The impulse responses, which characterize the dynamics between each pair of variables, are calculated from the estimated model. These multivariate models are able to isolate RCC by considering both SBP and ILV as system inputs and are able to computationally open the baroreflex loop through the imposition of time delays between SBP and RRI, characterizing the arterial baroreflex (ABR) impulse response. From this analysis not only the gain for each frequency band is provided from the Fourier transform of the impulse response, but also temporal information such as delays between variables.

The results show that standing is accompanied by significant vagal withdrawal and increased sympathetic vascular tone. Correlation analyses showed that the spectral-based RSA and BRS estimates do not present the same information as the model-based RCC and ABR estimates. The differences found suggest the model-based analyses are effective in representing RCC as a measure of the direct effects of respiration on HR and ABR as an expression of baroreflex that is independent from circulatory dynamics.

Thus, CRSIDLab is a powerful tool for the non-invasive determination of different quantitative indicators of the ANS. The results show that all estimated indicators reflect the underlying physiology, in the sense that standing is a sympathetic stimulus that should lead to vagal withdrawal, as observed. The results obtained also show that the multivariate system modeling approach can provide important additional information to those found by the more traditional spectral analyses approaches, which could potentially lead to more specific quantitative indicators of the ANS.

SUMMARY

1. INTRODUCTION	1
2. PHYSIOLOGICAL CONCEPTS	6
2.1. AUTONOMIC NERVOUS SYSTEM	6
2.2. ARTERIAL BAROREFLEX	8
2.3. RESPIRATORY SINUS ARRHYTHMIA	8
2.4. CARDIORESPIRATORY SYSTEM	9
2.4.1. The Cardiac Cycle	10
2.4.1.1. Electrocardiogram.....	12
2.4.1.2. Ectopic Heart Beats	12
2.4.2. Arterial Blood Pressure	13
2.4.3. Ectopic Beats and Blood Pressure	15
2.4.4. Airflow	15
2.4.5. The Cardiorespiratory System Model	16
2.5. HEART RATE VARIABILITY	18
2.6. BLOOD PRESSURE VARIABILITY	19
3. CRSIDLAB	20
3.1. PATIENT DATA OBJECT AND CREATING A PATIENT FILE	22
3.2. PRE-PROCESSING	23
3.2.1. Filter ECG/BP data	23
3.2.2. Extract variables from ECG/BP	27
3.2.2.1. RRI extraction.....	28
3.2.2.2. SBP extraction	31
3.2.2.3. DBP extraction.....	32
3.2.3. Pre-process respiration data	35

3.2.4. Align and resample data set.....	36
3.2.4.1. Ectopic beats and corresponding BP variables	37
3.2.4.2. Data borders	38
3.2.4.3. Resampling algorithms	40
3.3. ANALYSIS.....	44
3.3.1. Power Spectral Density	44
3.3.1.1. Windowing.....	45
3.3.1.2. Fourier Transform.....	47
3.3.1.3. Welch method	48
3.3.1.4. AR model.....	49
3.3.1.5. Quantitative indicators	51
3.3.2. System Identification.....	52
3.3.2.1. Create a new system	52
3.3.2.2. Autoregressive model with exogenous inputs	54
3.3.2.3. Orthogonal basis function models	55
3.3.2.4. Model estimation: least-squares minimization	60
3.3.2.5. Model optimization.....	61
3.3.2.6. Impulse response and quantitative indicators	63
4. METHODOLOGY.....	65
4.1. EXPERIMENTAL PROTOCOL	65
4.2. CARDIORESPIRATORY VARIABLES ANALYZED.....	66
4.3. METHODS EMPLOYED FROM CRSIDLAB	66
4.3.1. Pre-processing.....	66
4.3.2. PSD analysis	68
4.3.3. System identification	69
4.3.3.1. ARX models	70

4.3.3.2.	LBF and MBF models	72
4.4.	TRANSER FUNCTION ESTIMATION	75
4.5.	BAROREFLEX SENSITIVITY INDEXES.....	77
4.6.	STATISTICAL ANALYSIS.....	78
5.	RESULTS.....	79
5.1.	HRV AND BPV	79
5.2.	RCC AND RSA.....	82
5.2.1.	Frequency domain transfer function	82
5.2.2.	Impulse response	83
5.3.	ABR AND BRS.....	86
5.3.1.	Power spectral density	87
5.3.2.	Frequency domain transfer function	89
5.3.3.	Impulse response	91
5.4.	CORRELATION ANALYSES	93
5.4.1.	HRV and RSA/RCC	93
5.4.1.1.	HF supine	93
5.4.1.2.	HF standing.....	94
5.4.1.3.	LF supine	96
5.4.1.4.	LF standing	97
5.4.1.5.	LF and HF correlations	98
5.4.2.	HRV and BRS/ABR	100
5.4.2.1.	HF supine	101
5.4.2.2.	HF standing.....	102
5.4.2.3.	LF supine	104
5.4.2.4.	LF standing	106
5.4.2.5.	LF and HF correlations	110

6. DISCUSSION.....	115
7. CONCLUSION AND RECOMMENDATIONS.....	121
REFERENCES	124
APPENDICES	133
A. PATIENT DATA OBJECT DESCRIPTION.....	134

LIST OF FIGURES

Figure 2.1 – The ANS sympathetic and vagal branches, its innervations and effects on the different organs (Biological Science, 2002 [50]).	7
Figure 2.2 - Heart’s basic anatomy and circulatory circuits (Marieb & Hoehn, 2013 [15]).	11
Figure 2.3 – Conduction system of the heart (Guyton & Hall, 2006 [56]).	11
Figure 2.4 – Electrocardiogram and the cardiac cycle (OpenStax College, 2013 [58]).	12
Figure 2.5 – Example of a presentation of an ectopic beat (EB) followed by a compensatory pause (CP) on an ECG record (blue), highlighting RRI durations (red).	13
Figure 2.6 – Pressure variation through blood vessels (Guyton & Hall, 2006 [59]).	14
Figure 2.7 – Continuous BP in relation to the ECG and cardiac cycle events (adapted from Guyton & Hall, 2006 [49]).	14
Figure 2.8 – Examples of how ectopic beats can affect blood pressure by lowering the amplitude of the correlated cycle (a) or suppressing it completely (b). The dashed red lines indicate the R-peaks position, delimiting the cardiac cycles.	15
Figure 2.9 – Lung volumes and capacities (Guyton & Hall, 2006 [64]).	16
Figure 2.10 – Cardiorespiratory system model (Jo <i>et al.</i> , 2003 [66]). The dynamics in the dashed line box are the focus of this study.	17
Figure 3.1 – Overview of the pre-processing and analysis steps. Pre-processing: raw ECG and BP can be filtered separately, then processed either simultaneously or individually for RRI, SBP and/or DBP extraction; airflow is transformed to ILV and ILV can be filtered; any combination of available variables can be aligned and resampled (A&R) either individually or as a data set. Analysis: the PSD of any resampled variable is estimated using the Fourier transform, the Welch method and/or an AR model; system identification is performed with a combination of up to three A&R variables and the impulse response is estimated from an AR/ARX, LBF or MBF model.	21
Figure 3.2 – Window that manages variables to create a new patient file. Variables uploaded to Matlab’s workspace are listed as options for the main variable and associated time vector, sampling frequency and start time. The sampling frequency and start time can alternatively be typed in. Variable type and specification can be selected from a list of options. Clicking the “View data” button opens a window to display the indicated variable	

for visual inspection. Clicking the “Refresh variables from WS” updates the options listed for variables selection to include any new variables that were uploaded to Matlab’s workspace.	22
Figure 3.3 – 60 Hz notch filter squared magnitude for 1% width tolerance (blue) and 20% tolerance (green), representing the magnitude effects after reverse and forward filtering, with phaseless response.	24
Figure 3.4 – Example of ECG record contaminated with 60 Hz powerline noise (a) and after applying a notch filter of 1% width tolerance (b).	25
Figure 3.5 – Example of ECG record contaminated with EMG noise (a) and after applying a 35 Hz low-pass filter (b).	25
Figure 3.6 – Raw ECG record (a) and after filtering for baseline wander with a 0.01 Hz high-pass filter (b).	26
Figure 3.7 – Example of BP record contaminated with high-frequency noise (a) and after applying a 35 Hz low-pass filter (b).	27
Figure 3.8 – Relation between the R wave on the ECG and SBP and DBP values (Rompleman & Ten Voorde, 1995 [80]).	28
Figure 3.9 – ECG record (blue) and the signal obtained after QRS enhancing for R peak identification (green). The varying threshold is applied to the signal with enhanced QRS to detect the R wave.	29
Figure 3.10 – Example of RRI extraction (red) from the ECG record (blue) in a situation where the “Fast algorithm” fails to detect two R peaks correctly (a) while the “Slow algorithm” is able to identify the location properly (b), both highlighted by the black circles.	30
Figure 3.11 – ECG record (a) with extracted RRI (red dots) along with the corresponding BP record (b) and SBP (red dots) extracted using method 1. The highlighted BP cycle in (b) shows an example where method 1 failed to identify the SBP due to an ectopic beat that resulted in a very low BP compared with neighboring values.	31
Figure 3.12 – ECG record (a) with extracted RRI (red dots) and the corresponding BP record (b) and SBP (red dots) extracted using method 2. The BP data is segmented from the previously extracted RRI, as indicated by the dashed red lines, to find the local maximums, or SBP. The highlighted SBP is a wrongful detection due to an ectopic beat that both altered the timing used for BP segmentation and significantly lowered the SBP of the following cycle.	32

Figure 3.13 – ECG record (a) with extracted RRI (red dots) along with the corresponding BP record (b) and DBP (red asterisks) extracted using method 1. The highlighted BP cycle in (b) shows an example where method 1 failed to identify the SBP due to an ectopic beat that resulted in a very low BP compared with neighboring values. 33

Figure 3.14 – BP record with the previously extracted SBP (red dots), which are used in method 2 to segment the BP data, as indicated by the red dashed lines, and find local minimums (red asterisks). The highlighted DBP is a misdetection due to a low dirotic notch combined with a rising low frequency trend. 34

Figure 3.15 – ECG record (a) with extracted RRI (red dots) along with the corresponding BP record (b), SBP (red dots) and DBP (red asterisks) extracted using method 3. The search region for each DBP, delimited by the previously extracted RRI and SBP, is shown in yellow (b). The highlighted BP cycle in (b) shows an example where method 3 wrongfully detects the DBP due to noise in the search region. 34

Figure 3.16 – Integrated airflow presenting a drift after integration (a) and the results after applying the detrending methods (b): linear detrend (blue), polynomial detrend of order 3 (green) and high-pass filter with cut-off frequency of 0.01 Hz (red). 35

Figure 3.17 – The raw airflow (a), given in L/s, is integrated (b) to present volume information in L. The trend resulting from the transformation is removed, in this case using a 0.01 Hz high-pass filter, resulting in the instantaneous lung volume (c). 36

Figure 3.18 – Examples of the effect of ectopic beat related variables on RRI (a,c,e) and corresponding SBP (b,d,f) and the effects of the available correction methods. The yellow background highlights the first ectopic beat and related SBP, while the orange background highlights the second ectopic beat and related SBP. Ectopic beats as they present on RRI and SBP records (a,b), after removal (c,d) and after interpolation (e,f). 38

Figure 3.19 – Example of border gaps at the beginning of time aligned RRI, SBP and ILV records. The gaps in RRI and SBP are filled (red) using constant padding (a) and symmetric extension (b), while the grey line delimits the latest starting signal, RRI, which could be used as reference to truncate all records. 39

Figure 3.20 – ECG record (a) and the traditional tachometer generated from it (b), which is obtained by applying a zero-order hold to the RRI. 41

Figure 3.21 – Illustration of the algorithm proposed by Berger *et al.* [86] where evenly sampled HR (b) is derived from an ECG record (a) based on the tachometer (c). The number of beats in a window of length $a = 2/f_r$ is counted and then multiplied by $f_r/2$.

For t_1 the number of beats is given by a/I_2 and for t_2 by $(b/I_3 + c/I_4)$ (adapted from Berger <i>et al.</i> , 1986 [86]).	42
Figure 3.22 – ECG record (a) with the corresponding tachometer (blue) and resampled RRI (green) for $f_r = 4$ using the adapted Berger algorithm. The red dashed lines indicate the R-peaks position.	43
Figure 3.23 – Example of the adapted Berger algorithm used to resample SBP and DBP (red) extracted from the BP record (blue) and the equivalent adapted tachometers (green).	44
Figure 3.24 – Time function and frequency response of the available windows: (a) rectangular, (b) Bartlett, (c) Hanning, (d) Hamming and (e) Blackman.	46
Figure 3.25 – Example of HRV estimates as the PSD of and RRI using the Fourier transform with 2048 points using a Hanning window (blue), the Welch method with 256 samples per segment and 50% overlap using a Hanning window (green) and an AR model of order 20 (black). The red lines delimit the frequency bands of interest: very low frequency (VLF: 0-0.04 Hz), low frequency (LF: 0.04-0.15 Hz) and high frequency (HF: 0.15-0.4 Hz).	51
Figure 3.26 – Block diagram of a two-input ARX model.	54
Figure 3.27 – Block diagram of a two-input FIR model.	56
Figure 3.28 – Block diagram of the linear Orthogonal Basis Functions model.	56
Figure 3.29 – Laguerre basis functions of order k ranging from 0 to 4 for $p = 0.6$ (a) and $p = 0.8$ (b). A pole value closer to 1 yields a longer settling time for the basis function set.	58
Figure 3.30 – Meixner basis functions for $p = 0.8$ with orders k ranging from 0 to 4 for generalization order $n = 1$ (a) and $n = 5$ (b). Higher generalization orders cause the basis function set to have a slower initial onset.	58
Figure 3.31 – Quantitative indicators extracted from the impulse response (a) and from the Fourier transform of the impulse response, or transfer function (b). From the impulse response (a), the impulse response magnitude (IRM), response latency (D) and time-to-peak duration (T _{peak}) are calculated. From the transfer function (b), the dynamic gain (DG) is calculated (Jo, 2002 [14]).	64
Figure 4.1 – AR model order effects on NRMSE between measured and predicted outputs for RRI (a) and SBP (b) records expressed as mean NRMSE \pm standard deviation for both supine (blue) and standing (red) postures.	69

Figure 4.2 – Effects of the percentage of data used for model estimation in the NRMSE between measured and predicted outputs expressed as mean NRMSE \pm standard deviation for subjects in supine (blue) and standing (red) postures using an ARX model with the ILV and SBP as inputs and the RRI as output. 70

Figure 4.3 – (a) Model order effects on NRMSE between measured and predicted outputs for an AR model for RRI; (b) a model with ILV input and RRI output without an AR component; and (c) a model with SBP input and RRI output without an AR component, obtained in both supine (blue) and standing (red) postures. The mean NRMSE for each group at each order is presented with the error bars indicating the standard deviation. 72

Figure 4.4 – Effects of the system memory length in the NRMSE between measured and predicted outputs expressed as mean NRMSE \pm standard deviation for subjects in supine (blue) and standing (red) postures using a LBF model with ILV and SBP as inputs and the RRI as output. 73

Figure 4.5 – ARX model impulse responses h_{RCC} and h_{ABR} for subjects in supine (a) and standing (b) postures presented as mean value (blue) \pm standard deviation (red). 74

Figure 4.6 – Pole selection of $p = 0.82$ for the first 12 Laguerre basis functions, ranging from orders 0 to 11, with a system memory of 140, so that the last basis function approaches zero close to the memory length. 74

Figure 4.7 – Pole selection of $p = 0.76$ for the first 12 Meixner basis functions, ranging from orders 0 to 11, with a system memory of 140 and a generalization order of 5, so that the last basis function approaches zero close to the memory length. 74

Figure 5.1 – High frequency heart rate variability, HRV_{HF} (0.15-0.4 Hz), for supine and standing postures calculated as the power spectral density (PSD) of the R-R interval (RRI) using the Fourier transform, the Welch method, and the AR model. The decrease in HRV_{HF} in standing is an indicator of tonal vagal withdrawal. 80

Figure 5.2 – Heart rate variability LF/HF ratio, $HRV_{LF/HF}$, for supine and standing postures calculated as the power spectral density (PSD) of the R-R interval (RRI) using the Fourier transform, the Welch method, and the AR model. The increase in $HRV_{LF/HF}$ in standing indicates a shift towards dominant sympathetic activity in sympathovagal balance. 80

Figure 5.3 – Low frequency blood pressure variability, BPV_{LF} (0.04-0.15 Hz), for supine and standing postures calculated as the power spectral density (PSD) of systolic blood

pressure (SBP) using the Fourier transform, the Welch method, and the AR model. The increase in BPV_{LF} upon standing indicates increased sympathetic vasomotor tone. 81

Figure 5.4 – High frequency blood pressure variability, BPV_{HF} (0.15-0.4 Hz), for supine and standing postures calculated as the power spectral density (PSD) of systolic blood pressure (SBP) using the Fourier transform, the Welch method, and the AR model. The meaning of the increase in BPV_{HF} upon standing is not a consensus among researchers. . 81

Figure 5.5 – Low frequency respiratory sinus arrhythmia, RSA_{LF} (0.04-0.15 Hz), quantifying the direct and indirect effects of respiration on heart rate, for supine and standing postures calculated from the transfer function estimated the Fourier transform, and Welch method. The interpretation of the decrease verified in RSA_{LF} in standing posture reflex combined vagal and sympathetic activity changes. 82

Figure 5.6 – High frequency respiratory sinus arrhythmia, RSA_{HF} (0.15-0.4 Hz), quantifying the direct and indirect effects of respiration on heart rate, for supine and standing postures obtained from the transfer function estimated using the Fourier transform, and Welch method. The decrease in RSA_{HF} in standing indicates tonal vagal withdrawal. 83

Figure 5.7 – Respiratory-cardiac coupling impulse response magnitude, RCC_{IRM} , as an overall measure of gain quantifying the direct effects of respiration on heart rate, for supine and standing postures, obtained from the impulse response estimated using the ARX, LBF, and MBF models. The decreased RCC_{IRM} found in standing posture indicates vagal withdrawal. 84

Figure 5.8 – Respiratory-cardiac coupling total dynamic gain, RCC_{TOT} (0.04-0.4 Hz), as an overall measure quantifying the direct effects of respiration on heart rate, for supine and standing postures, obtained from the impulse response estimated using the ARX, LBF and, MBF models. The decrease in RCC_{TOT} upon standing indicates vagal withdrawal. 85

Figure 5.9 – Respiratory-cardiac coupling low frequency dynamic gain, RCC_{LF} (0.04-0.15 Hz), quantifying the direct effects of respiration on heart rate, for supine and standing postures obtained from the impulse response estimated using the ARX, LBF, and MBF models. The meaning of the decrease in RCC_{LF} upon standing results from the interaction of sympathetic and vagal activity shifts. 85

Figure 5.10 – Respiratory-cardiac coupling high frequency dynamic gain, RCC_{HF} (0.15-0.4 Hz), quantifying the direct effects of respiration on hear rate, for supine and standing

postures obtained from the impulse response estimated using the ARX, LBF, and MBF models. The decrease in RCC_{HF} upon standing is an indicator of vagal withdrawal. 86

Figure 5.11 – Low frequency baroreflex sensitivity, α_{LF} (0.04-0.15 Hz), calculated as the square root of the HRV/BPV ratio, obtained from power spectral density (PSD) analysis using the Fourier transform, the Welch method, and the AR model, for subjects in supine and standing postures. The decrease in α_{LF} in standing reflects both vagal and sympathetic activities..... 87

Figure 5.12 – High frequency baroreflex sensitivity, α_{HF} (0.15-0.4 Hz), calculated as the square root of the HRV/BPV ratio, obtained from power spectral density (PSD) analysis using the Fourier transform, the Welch method, and the AR model, for subjects in supine and standing postures. The decrease in α_{HF} in standing is related to decreased vagal activity. 88

Figure 5.13 – Overall baroreflex sensitivity, α , calculated as the mean value between low frequency (0.04-0.15 Hz) and high frequency (0.15-0.4 Hz) sensitivities, α_{LF} and α_{HF} for subjects in supine and standing postures. α_{LF} and α_{HF} were calculated as the square root of the HRV/BPV ratio in each frequency band, obtained from power spectral density (PSD) analysis using the Fourier transform, the Welch method, and the AR model. The diminished reflex vagal activity in standing is indicated by the decrease in α 88

Figure 5.14 – Low frequency baroreflex sensitivity, BRS_{LF} (0.04-0.15 Hz), calculated from the transfer functions estimated using the Fourier transform, and the Welch method, for subjects in supine and standing postures. The reduction in BRS_{LF} in standing results from shifts in both vagal and sympathetic activities. 89

Figure 5.15 – High frequency baroreflex sensitivity, BRS_{HF} (0.15-0.4 Hz), calculated from the transfer functions estimated using the Fourier transform, and the Welch method, for subjects in supine and standing postures. The decrease in BRS_{HF} in standing relates to vagal activity withdrawal..... 90

Figure 5.16 – Overall baroreflex sensitivity, BRS_{α} , calculated as the mean value between low frequency (0.04-0.15 Hz) and high frequency (0.15-0.4 Hz) sensitivities, BRS_{LF} and BRS_{HF} , for subjects in supine and standing postures. BRS_{LF} and BRS_{HF} were calculated in each frequency band from the transfer functions estimated using the Fourier transform, and the Welch method. BRS_{α} is proportional to reflex vagal activity. 90

Figure 5.17 – Arterial baroreflex impulse response magnitude, ABR_{IRM} , as a measure of overall gain calculated from the impulse responses estimated through the ARX, LBF, and MBF models, for subjects in supine and standing postures. 91

Figure 5.18 – Arterial baroreflex total dynamic gain, ABR_{TOT} (0.04-0.4 Hz), as an overall measure of gain calculated from the impulse responses estimated through the ARX, LBF, and MBF models, for subjects in supine and standing postures..... 92

Figure 5.19 – Arterial baroreflex low frequency dynamic gain, ABR_{LF} (0.04-0.15 Hz), calculated from the impulse responses estimated through the ARX, LBF, and MBF models, for subjects in supine and standing postures. 92

Figure 5.20 – Arterial baroreflex high frequency dynamic gain, ABR_{HF} (0.15-0.4 Hz), calculated from the impulse responses estimated through the ARX, LBF, and MBF models, for subjects in supine and standing postures. 93

Figure 5.21 – Correlations between HRV_{HF} obtained from the Fourier transform method and RSA_{HF} , which quantifies direct and indirect effects of respiration on HRV and is derived from the Fourier transform transfer function (a,c); and between HRV_{HF} obtained from the Fourier transform method and RCC_{HF} , which accounts only for the direct influence of respiration on HRV, referred to as respiratory-cardiac coupling (RCC), derived from the Meixner basis function (MBF) impulse response (b,d). Comparing the correlations in supine (a,b) and standing (c,d) postures, it is shown that while the correlation between HRV_{HF} and RSA_{HF} is stronger in standing posture, the opposite is true between HRV_{HF} and RCC_{HF} 96

Figure 5.22 – Correlations for supine posture between HRV obtained from the AR model and respiratory sinus arrhythmia (RSA), which quantifies direct and indirect effects of respiration on HRV, derived from the Fourier transform transfer function (a,d); between HRV obtained from the Welch method and respiratory-cardiac coupling (RCC), which accounts only for the direct influence of respiration on HRV, from the MBF impulse response (b,e); and between HRV obtained from the Welch method and the impulse response magnitude (IRM) , as a measure of overall gain, from the ARX impulse response (c,f). The correlations are stronger in HF (a,b,c) compared to LF (d,e,f) for all combinations..... 99

Figure 5.23 – Correlations for standing posture between HRV obtained from the AR model and respiratory sinus arrhythmia (RSA), which quantifies direct and indirect effects of respiration on HRV, derived from the Fourier transform transfer function (a,d); between

HRV obtained from the Welch method and respiratory-cardiac coupling (RCC), which accounts only for the direct influence of respiration on HRV, from the MBF impulse response (b,e); and between HRV obtained from the Welch method and the impulse response magnitude (IRM), as a measure of overall gain, from the ARX impulse response (c,f). The correlations are stronger in HF (a,b,c) compared to LF (d,e,f) for all combinations..... 100

Figure 5.24 – Correlations between HRV_{HF} and spectral baroreflex sensitivity (BRS) indicators, all obtained from the Fourier transform: α_{HF} , which quantifies BRS from the square root of the ratio between HRV and BPV powers, obtained from PSD analysis (a,c); and BRS_{HF} , calculated from the transfer function analysis (b,d). The correlations are stronger in standing posture for spectral indicators (c,d) than supine (a,b)..... 103

Figure 5.25 – Correlations between HRV_{HF} obtained from the Fourier transform and arterial baroreflex (ABR) ARX impulse response indicators: ABR_{HF} (c,g); and ABR_{IRM} , which is a measure of overall gain (d,h). The correlations are stronger in supine posture (a,b), rather than standing (e,f). 104

Figure 5.26 – Correlations between HRV_{LF} estimated through the Welch method and α_{LF} , which quantifies baroreflex sensitivity (BRS) from the square root of the ratio between HRV and BPV powers, obtained from PSD analysis using the AR model (a,c); and between HRV_{LF} estimated using the AR model and BRS_{LF} , calculated from the Welch method transfer function analysis (b,c). The correlations are stronger in standing (c,d) rather than supine (a,b) posture. 108

Figure 5.27 – Correlations between HRV_{LF} obtained from the Fourier transform and arterial baroreflex (ABR) impulse response indicators: ABR_{LF} , obtained from the Meixner basis function (MBF) impulse response (a,c); and ABR_{IRM} , which is a measure of overall gain, obtained from the Laguerre basis function (LBF) impulse response (b,d). The correlations are stronger in standing (c,d) rather than supine (a,b) posture. 109

Figure 5.28 – Correlations between the arterial baroreflex (ABR) Meixner basis function (MBF) impulse response ABR_{LF} and spectral baroreflex sensitivity (BRS) indicators: α_{LF} , which quantifies BRS from the square root of the ratio between HRV and BPV powers, obtained from PSD analysis using the Welch method (a,c); and BRS_{LF} , calculated from the Fourier transfer function analysis (b,d). The correlations are stronger in standing (c,d) rather than supine (a,b) posture. 110

Figure 5.29 – Correlations for supine posture between HRV obtained from the Welch method (a,c) and Fourier transform (b,d), and spectral baroreflex sensitivity (BRS) indicators: α_{HF}/α_{LF} , which quantifies BRS from the square root of the ratio between HRV and BPV powers, obtained from PSD analysis using the AR model (a,c); and BRS_{HF}/BRS_{LF} , calculated from the Fourier transfer function analysis (b,d). The correlations are stronger in HF (a,b) rather than LF (c,d). 111

Figure 5.30 – Correlations for standing posture between HRV obtained from the Welch method (a,c) and the Fourier transform (b,d), and spectral baroreflex sensitivity (BRS) gain indicators: α_{HF}/α_{LF} , which quantifies BRS from the square root of the ratio between HRV and BPV powers, obtained from PSD analysis using the AR model (a,c); and BRS_{HF}/BRS_{LF} , calculated from the Fourier transfer function analysis (b,d). The correlations are stronger in HF (a,b) rather than LF (c,d), but the difference is small..... 112

Figure 5.31 – Correlations for supine posture between HRV obtained from the AR model (a,c) and Fourier transform (b,d), and arterial baroreflex (ABR) impulse response gain indicators obtained from the ARX impulse response (a,b), and ABR_{IRM} , as a measure of overall gain, from the Meixner basis function (MBF) impulse response (c,d). The correlations are stronger in HF (a,b) rather than LF (c,d). 113

Figure 5.32 – Correlations for standing posture between HRV obtained from the AR model (a,c) and Fourier transform (b,d), and arterial baroreflex (ABR) impulse response gain indicators obtained from the ARX impulse response (a,b), and from the Laguerre basis function (LBF) impulse response (c,d). The correlations are slightly stronger in HF for the ARX impulse response indicators (a), but are much stronger in LF for LBF impulse response indicators (d)..... 114

LIST OF TABLES

Table 3.1 – Quantitative indicators extracted from the PSDs of an RRI series, presented in Figure 3.25. The absolute (ms^2), relative (%) and normalized areas of the very low frequency (VLF: 0-0.04 Hz), low frequency (LF: 0.04-0.15 Hz) and high frequency (HF: 0.15-0.4 Hz) as well as the total area (0-0.4 Hz) are provided along with the LF/HF ratio for the PSDs calculated from the Fourier transform (FFT), the Welch method and AR model.	52
Table 5.1 – Respiratory-cardiac coupling (RCC) impulse response latency for subjects in supine and standing positions obtained from ARX, LBF and MBF models presented as mean value \pm standard deviation. There is no significant difference between postures, but the selection of negative delays implies a non-causal relationship.	84
Table 5.2 – Pearson’s correlation coefficients and level of significance between HRV_{HF} , and both HF indicators of respiratory sinus arrhythmia (RSA) obtained from subjects in supine posture: RSA_{HF} , which quantifies direct and indirect effects of respiration on HRV and is derived from transfer function analysis, and RCC_{HF} , the respiratory-cardiac coupling (RCC), which accounts only for the direct influence of respiration on HRV and is derived from impulse response analysis.	94
Table 5.3 – Pearson’s correlation coefficients and level of significance between HRV_{HF} and the impulse response magnitude (IRM), as a measure of overall gain of the respiratory-cardiac coupling (RCC), quantifying the direct effects of respiration on HRV through impulse response analysis, from subjects in supine posture.	94
Table 5.4 – Pearson’s correlation coefficients and level of significance between HRV_{HF} and both HF indicators of respiratory sinus arrhythmia (RSA) obtained from subjects in standing posture: RSA_{HF} , which quantifies direct and indirect effects of respiration on HRV and is derived from transfer function analysis, and RCC_{HF} , the respiratory-cardiac coupling (RCC), which accounts only for the direct influence of respiration on HRV and is derived from impulse response analysis.	95
Table 5.5 – Pearson’s correlation coefficients and level of significance between HRV_{HF} and the impulse response magnitude (IRM), as a measure of overall gain, of the respiratory-cardiac coupling (RCC), quantifying the direct effects of respiration on HRV through impulse response analysis, from subjects in standing posture.	95

Table 5.6 – Pearson’s correlation coefficients and level of significance between HRV_{LF} , and both LF indicators of respiratory sinus arrhythmia (RSA) obtained from subjects in supine posture: RSA_{LF} , which quantifies direct and indirect effects of respiration on HRV and is derived from transfer function analysis, and RCC_{LF} , the respiratory-cardiac coupling (RCC), which accounts only for the direct influence of respiration on HRV and is derived from impulse response analysis..... 97

Table 5.7 – Pearson’s correlation coefficients and level of significance between HRV_{LF} and the impulse response magnitude (IRM), as a measure of overall gain, of the respiratory-cardiac coupling (RCC), quantifying the direct effects of respiration on HRV through impulse response analysis, from subjects in supine posture..... 97

Table 5.8 – Pearson’s correlation coefficients and level of significance between HRV_{LF} , and both LF indicators of respiratory sinus arrhythmia (RSA) obtained from subjects in standing posture: RSA_{LF} , which quantifies direct and indirect effects of respiration on HRV and is derived from transfer function analysis, and RCC_{LF} , the respiratory-cardiac coupling (RCC), which accounts only for the direct influence of respiration on HRV and is derived from impulse response analysis..... 98

Table 5.9 – Pearson’s correlation coefficients and level of significance between HRV_{LF} and the impulse response magnitude (IRM), as a measure of overall gain, of the respiratory-cardiac coupling (RCC), quantifying the direct effects of respiration on HRV through impulse response analysis, from subjects in standing posture..... 98

Table 5.10 – Pearson’s correlation coefficients and level of significance between indicators of HRV_{HF} , and both baroreflex sensitivity (BRS) indicators, in supine posture: α_{HF} , calculated as the square root of the ratio between HRV and BPV powers, derived from PSD analyses; and BRS_{HF} , derived from the transfer function analysis. 101

Table 5.11 – Pearson’s correlation coefficients and level of significance between HRV_{HF} and both indicators derived from the arterial baroreflex (ABR) impulse response, obtained in supine posture: ABR_{HF} , and ABR_{IRM} , the impulse response magnitude (IRM) as a measure of overall gain..... 101

Table 5.12 – Pearson’s correlation coefficients and level of significance between indicators of HRV_{HF} , and both baroreflex sensitivity (BRS) indicators, in standing posture: α_{HF} , calculated as the square root of the ratio between HRV and BPV powers, derived from PSD analyses; and BRS_{HF} , derived from the transfer function analysis. 102

Table 5.13 – Pearson’s correlation coefficients and level of significance between HRV_{HF} and both indicators derived from the arterial baroreflex (ABR) impulse response, obtained in standing posture: ABR_{HF} , and ABR_{IRM} , the impulse response magnitude (IRM) as a measure of overall gain.....	102
Table 5.14 – Pearson’s correlation coefficients and level of significance between indicators of HRV_{LF} , and both baroreflex sensitivity (BRS) indicators, in supine posture: α_{LF} , calculated as the square root of the ratio between HRV and BPV powers, derived from PSD analyses; and BRS_{LF} , derived from the transfer function analysis.....	104
Table 5.15 – Pearson’s correlation coefficients and level of significance between HRV_{LF} and both indicators derived from the arterial baroreflex (ABR) impulse response, obtained in supine posture: ABR_{LF} and ABR_{IRM} , the impulse response magnitude (IRM) as a measure of overall gain.	105
Table 5.16 – Pearson’s correlation coefficients and level of significance between the impulse response indicator of arterial baroreflex (ABR) ABR_{LF} , and the baroreflex sensitivity (BRS) indicators obtained from spectral methods in supine posture: α_{LF} , calculated as the square root of the ratio between HRV and BPV, and BRS_{LF} , obtained from the transfer function analysis.	105
Table 5.17 – Pearson’s correlation coefficients and level of significance between indicators of HRV_{LF} , and both baroreflex sensitivity (BRS) indicators, in standing posture: α_{LF} , calculated as the square root of the ratio between HRV and BPV powers, derived from PSD analyses; and BRS_{LF} , derived from the transfer function analysis.....	106
Table 5.18 – Pearson’s correlation coefficients and level of significance between HRV_{LF} and both indicators derived from the arterial baroreflex (ABR) impulse response, obtained in standing posture: ABR_{LF} , and ABR_{IRM} , the impulse response magnitude (IRM) as a measure of overall gain.....	106
Table 5.19 – Pearson’s correlation coefficients and level of significance between the impulse response indicator of arterial baroreflex (ABR) ABR_{LF} , and the baroreflex sensitivity (BRS) indicators obtained from spectral methods in standing posture: α_{LF} , calculated as the square root of the ratio between HRV and BPV, and BRS_{LF} , obtained from the transfer function analysis.	107
Table A.1 – <i>patientData</i> object description	134
Table A.2 – <i>dataUnit</i> object description	135

Table A.3 – <i>ilvUnit</i> object description.....	135
Table A.4 – <i>varUnit</i> object description	136
Table A.5 – <i>patientSys</i> object description	136
Table A.6 – <i>sysModel</i> object description	136
Table A.7 – <i>imResp</i> object description.....	137
Table A.8 – <i>specs</i> property fields according to the type of data in a <i>dataUnit</i> object.....	138

LIST OF SYMBOLS

Latin Symbols

f	Discrete frequency	[Hz]
h	Impulse response	
j	Imaginary unit	
P	Periodogram	
r_{xx}	Autocorrelation function	
r_{xy}	Cross-correlation function	
S_{uu}	Power spectral density	
S_{uy}	Cross-power spectral density	
u	System input	
y	System output	
V	Cost function	

Greek Symbols

α	Baroreflex sensitivity index	[ms/mmHg]
θ	Vector of model parameters	
σ^2	Variance	
Φ	Regression matrix	

Superscript

$\hat{}$	Estimated value	
$\bar{}$	Average value	
T	Transposed	

Acronyms

ABR	Arterial baroreflex	
ADC	Analogue to digital converter	
AIC	Akaike's information criterion	
ANOVA	Analysis of variance	
ANS	Autonomic nervous system	
AR	Autoregressive	
ARX	Autoregressive with exogenous inputs	
AV	Atrioventricular	
BMI	Body mass index	[kg/m ²]
BP	Blood pressure	[mmHg]
BRS	Baroreflex sensitivity	[ms/mmHg]
BPV	Blood pressure variability	
CID	Circulatory dynamics	
CPSD	Cross power spectral density	
CRSIDLab	Cardiorespiratory system identification lab	
DBP	Diastolic blood pressure	[mmHg]
DG	Dynamic gain	
ECG	Electrocardiogram	
EMG	Electromyography	
FFT	Fast Fourier transform	
FIR	Finite impulse response	
GUI	Graphical user interface	
HF	High frequency band (0.15-0.4 Hz)	[Hz]
HR	Heart rate	[bpm]
HRV	Heart rate variability	

ILV	Instantaneous lung volume	[L]
IRM	Impulse response magnitude	
LBF	Laguerre basis function	
LF	Low frequency band (0.04-0.15 Hz)	[Hz]
MAP	Mean arterial pressure	[mmHg]
MBF	Meixner basis function	
MSE	Mean squared error	
MDL	Minimum description length	
NRMSE	Normalized root mean squared error	
OBF	Orthogonal basis function	
PP	Pulse pressure	[mmHg]
PSD	Power spectral density	
RCC	Respiratory-cardiac coupling	
RRI	R-R interval	[ms]
RSA	Respiratory sinus arrhythmia	
SA	Sinoatrial	
SBP	Systolic blood pressure	[mmHg]
VLf	Very low frequency band (0-0.04 Hz)	[Hz]
WSS	Wide sense stationary	

1. INTRODUCTION

The autonomic nervous system (ANS) regulates involuntary activities of the human body. The sympathetic and vagal branches act continuously, normally with opposing effects, to maintain a state of homeostasis. In the cardiorespiratory system, vagal withdrawal and sympathetic activation is associated to higher heart rate (HR), blood pressure (BP) and breathing rate, while vagal activation and sympathetic withdrawal lower those measures [1, 2].

Heart rate variability (HRV) analysis has been extensively used to study the ANS, predicting autonomic neuropathy in diabetics and mortality after cardiac infarction [3, 4]. HRV studies the beat-to-beat variation of HR or its reciprocal R-R interval (RRI), given in milliseconds, around a mean value [3, 5]. It can be quantified through statistical, geometrical, and non-linear methods, and through power spectral density (PSD) analysis in the frequency domain [3, 4, 5].

There are three main frequency bands defined for short-term HRV analysis, the very low frequency (VLF: 0-0.04 Hz), low frequency (LF: 0.04-0.15 Hz) and high frequency (HF: 0.15-0.4 Hz), as defined by a task force of the European Society of Cardiology and the North American Society of Pacing and Electrophysiology assembled to develop standards of measurement, physiological interpretation, and clinical use of HRV [4]. While VLF interpretation is unclear for short-term records [4], HF is widely accepted as an indicator of vagal activity [3, 4, 6, 7] and LF has been suggested to reflect sympathetic activity, both sympathetic and vagal activities, or baroreflex activity in different studies [3, 4, 6, 8, 9].

There are reflex and control mechanisms, modulated by the ANS, which result in HRV. The two main mechanisms responsible for HRV are the arterial baroreflex (ABR), which modulates HR through the ANS according to inputs from arterial stretch sensors called baroreceptors in order to maintain BP homeostasis [10, 11], and respiratory sinus arrhythmia (RSA), in which HR increases with inspiration and decreases with expiration, due to mechanical and control level coupling [12, 13, 14]. Respiratory activity provokes intrathoracic pressure changes, which influence venous return to the heart, affecting BP [11, 15]. This mechanical effect indirectly affects HR through the baroreflex. The respiratory-cardiac coupling (RCC) represents the direct effects of respiration on HR, modulated by the ANS, excluding these indirect mechanical effects [16]. RSA has been

shown to relate mainly to vagal activity and to be reflected in HF HRV in different studies both in frequency and time domains [12, 13].

Baroreflex sensitivity (BRS) can be assessed through different methods, in time and frequency domains, expressing how BP fluctuations affect HR [17]. However, since HR also affects BP through the mechanically and sympathetically mediated circulatory dynamics (CID), techniques that do not introduce sufficient delay between BP and HR cannot accurately represent ABR, but include the CID effects. This is true for the frequency domain analyses, which do not differentiate between feedforward and feedback mechanisms due to a lack of time-domain information, and also for traditional time domain techniques, such as the sequence method, which do not introduce sufficient delay. At the same time, if respiration is not considered as part of the system, BRS will also reflect the indirect effects of respiration that affect HR through BP [14, 18]. These confounding factors make the interpretation of results less direct.

Therefore, a multivariate system model identification approach might be able to provide more comprehensive information on these mechanisms, as opposed to the univariate HRV analyses that take only variations in the output variable into account [14, 19, 20]. Models that allow the incorporation of delays between input and output enable the restraining of causal relationships that exist on closed-loop systems, uncoupling the different mechanisms that regulate the cardiorespiratory system and computationally opening the loop [16, 21]. For its ability to disentangle the influences of the cardiorespiratory variables on one another, including the closed-loop baroreflex dynamics and the direct and indirect influences of respiration on HR, this modeling approach has been employed by several studies [22, 23, 24, 25, 26].

There are several non-commercial programs available for HRV analysis. ECGLab [27], KARDIA [28], ARTiiFact [29] and Kubios HRV [30] are all examples of Matlab-based software, while RHRV [31] and gHRV [32] are options developed for other platforms, using R-programming language and Python, respectively. These programs sometimes provide electrocardiogram (ECG) pre-processing tools, such as filtering and QRS extraction, and perform different forms of HRV analysis. POLYAN [33] accepts as input not only the ECG, but also arterial BP and airflow, providing pairwise evaluation of the variables in frequency domain, which has the limitations previously discussed. HeartScope [34] employs a multivariate model to provide BRS estimates from the slope of the system's

response to a unitary ramp, besides providing frequency domain analyses between pairs of variables. This BRS estimate accounts for the effects of respiration and can effectively separate the CID effects from the BRS index, but does not provide information such as the dynamics delay. It also does not provide model-based assessment of the respiration effects on HR.

In this work we present the cardiorespiratory system identification lab (CRSIDLab), a Matlab-based toolbox for multivariate cardiorespiratory system analysis. CRSIDLab is built as a graphical user interface (GUI), providing visual verification of the processing steps. It first started being developed as an undergraduate thesis and continued through the present study, with the addition of methods and models and a reformulation of the interface to help guide the user through the various processing and analysis stages. The software accepts ECG, continuous BP, and airflow or lung volume data as inputs and provides tools to condition the data, extract RRI from the ECG, systolic and diastolic BP (SBP and DBP, respectively) from the continuous BP, and transform airflow to instantaneous lung volume (ILV). Single variable PSD analyses are available, which can be estimated through the Fourier transform, the Welch method, or the autoregressive (AR) model. Time domain system identification can be performed for systems composed of up to three of the available variables in any combination. The AR model is available for univariate systems, while for multivariate systems the AR model with exogenous inputs (ARX), the Laguerre basis function (LBF) model, and the Meixner basis function (MBF) model are available. Once the model is estimated, the impulse response between each input and output variable is calculated and quantitative indicators are extracted, both directly from the impulse response, and from the transfer function estimated as the Fourier transform of the impulse response.

The goal in developing this toolbox is to provide a rather complete non-commercial toolbox for researchers of both engineering and medical backgrounds to investigate the control and reflex mechanisms present in the cardiorespiratory system through a multivariate time modeling approach. The specific goal is to properly characterize RCC, as a measure of HRV that is independent of the direct effects of respiration, and ABR, as a measure of HRV that is independent of BP, since these have been shown to be among the most relevant dynamics that influence HRV and, for that reason, have been the aim of many studies.

To demonstrate the utility of the proposed toolbox in characterizing those dynamics, the toolbox is used to investigate the effects of posture on ANS indicators generated through CRSIDLab. The data used for the study consists of ECG, continuous BP and airflow records of 23 male subjects taken for 10 min in supine posture and 10 min in standing posture.

The effects of posture and orthostatic stress on ANS indicators has been widely studied using different approaches [24, 35, 36, 37, 38, 39, 40] and, from the underlying physiology, a shift towards sympathetic dominance is expected in standing when compared to supine. Thus, our hypothesis is that the indicators related to vagal activity, such as RSA, RCC, HF HRV and HF BRS and ABR will be lower in standing when compared to supine [41, 42], while LF BPV and the HRV LF/HF ratio should be greater, as they are proportional to sympathetic activity. Some differences are expected between spectral measures of BRS and RSA when compared to the impulse response measures of ABR and RCC, due to the discussed limitations of spectral methods.

The dominant causality between BP and HR shifts from CID to baroreflex upon standing. While the spectral BRS estimates cannot differentiate feedforward and feedback effects, as they are open-loop analysis methods, incorporating CID to its measure, impulse response analysis can [43, 44, 45, 46]. The modeling approach also allows the direct and indirect effects of respiration on HR, the latter mediated through ABR, to be separated, providing indicators of RCC, while spectral transfer function analysis will include both. The direct link between respiration and HR decreases in standing, while the indirect link increases [47, 48], which could lead to conflicting results.

This work is divided in seven chapters, including this introduction. Chapter 2 discusses the physiological concepts that are relevant to the study, including the reflex and control mechanisms involved, how the variables relate to those mechanisms and finally presents the cardiorespiratory model upon which this research is based. Chapter 3 describes CRSIDLab, the Matlab toolbox developed as part of this study and used to process the data. Chapter 4 presents the methodology applied in this study, specifying the methods and parameters used in CRSIDLab, as well as the additional transfer function estimation process and the statistical tests performed. Chapter 5 presents the results obtained from processing the data using CRSIDLab, detailing the effects of a sympathetic stimulus on ANS indicators obtained from various methods by comparing supine and standing posture

data, while also applying correlation analyses to compare indexes calculated from the univariate and multivariate analyses as well as frequency and time-domain analyses. Chapter 6 details the discussion of those results. Finally, Chapter 7 presents the conclusion and future work recommendations.

2. PHYSIOLOGICAL CONCEPTS

This section presents an overview of the physiological concepts that are necessary to understand the context of this study, its relevance and findings.

2.1. AUTONOMIC NERVOUS SYSTEM

The ANS modulates involuntary activities, such as the digestive system activity, involuntary breathing, HR and BP. The ANS is divided in two branches, the sympathetic and the parasympathetic or vagal nervous systems, which usually act in opposition to one another [1, 2]. In this study, the known effects of the ANS modulation of the cardiorespiratory system are used to evaluate its health.

The sympathetic nervous system induces what is called the “fight or flight” response, increasing heart and respiration rates, BP and muscle contraction force, while inhibiting digestion and dilating pupils. The vagal nervous system, on the other hand, induces the “rest and digest” response, decreasing heart and respiration rates, BP and muscle contraction force, stimulating digestion and constricting pupils. These effects and more are described in Figure 2.1. Together these branches work to keep the human body in homeostasis, a state of physiological balance.

Sympathetic stimulation of the heart increases both HR and the heart’s contraction force, which leads to increased BP. Vagal nerve fibers are mostly present on the atria, and so its effects on diminishing the heart’s contraction force are limited, producing little effect on BP [1, 15, 49]. Vagal stimulation of the heart decreases HR and may even stop heart activity for a short period of time. On baseline conditions, there is a dominating vagal activity modulating the heart, keeping its rate about 25 bpm lower than it would be if regulated only by the sinoatrial (SA) node, the heart’s pacemaker [15, 49].

The ANS modulates BP through its modulation of the heart, but also through the modulation of blood vessels. Sympathetic stimulation induces the constriction of most blood vessels, while vagal stimulation has little effect, causing only the peripheral blood vessels to dilate. Therefore, BP control is mainly modulated by the sympathetic nervous system and the vascular system is said to have a sympathetic tone [1, 2].

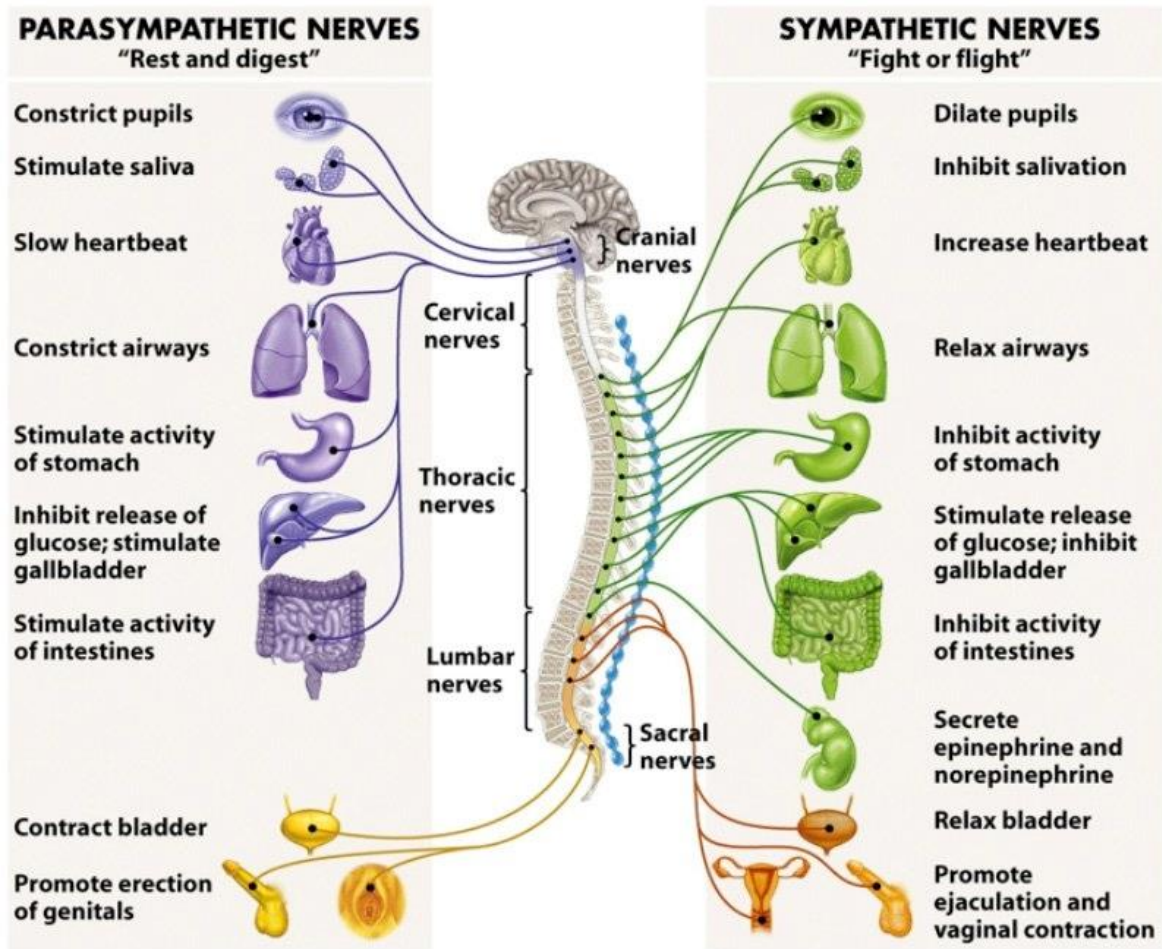


Figure 2.1 – The ANS sympathetic and vagal branches, its innervations and effects on the different organs (Biological Science, 2002 [50]).

The autonomic modulation of respiration acts mainly by dilating or constricting the bronchioles, stimulating or inhibiting gas exchange, respectively. Bronchi dilation is a result of sympathetic stimulation, while bronchi constriction results from vagal stimulation [1, 2].

Homeostatic imbalance of the ANS may lead to several physiological conditions, such as hypertension or Raynaud's disease, which is characterized by intermittent reduced blood flow to toes and fingers and can lead to gangrene [2]. Cardiovascular mortality has been linked to ANS imbalance, associating increased sympathetic activity, with or without reduced vagal activity, to lethal arrhythmias and sudden cardiac death [51, 52].

2.2. ARTERIAL BAROREFLEX

ABR is the best known mechanism for BP homeostasis control and it is mediated by the ANS. Sensors that are stimulated when the walls of arteries are stretched, called baroreceptors, are present mainly in large arteries of the neck, thorax, the carotid sinuses and the aortic arch. These sensors send signals to the central nervous system indicating a rise in BP, causing the ANS to respond by slowing the HR through vagal stimulation of the heart, bringing the BP back to its normal levels. At the same time the vasoconstrictor center is inhibited. If the baroreceptors send no signals, this inhibiting stimulus is removed and sympathetic stimulation of the heart is triggered, causing HR to increase and vasodilation to occur, elevating the BP [10, 11].

The ABR is a mechanism that acts rapidly and is the major controller of BP on short term. An impaired baroreflex may cause orthostatic hypotension, which is characterized as dizziness or fainting from standing up fast, or hypertension, among other effects [10, 14].

The BRS is a measure of baroreflex efficiency that focuses on its ability to regulate HR from BP fluctuations, and is usually given in ms/mmHg. Here the HR is not represented in the usual frequency unit (bpm), but in the reciprocal time unit, representing its period [17]. This representation of HR is further described in section 2.4.1.1.

Higher BRS indicates a greater ability to respond and adapt to changes in BP, while lower BRS indicates lower ability to adapt, which may lead to a higher risk of strokes, myocardial infarction and heart failure [14].

2.3. RESPIRATORY SINUS ARRHYTHMIA

RSA is the coupling of respiration effects to HR, which occurs both from a mechanical coupling of the cardiac and respiratory systems and from the coupling of the respiratory control center and the ANS.

The intrathoracic pressure variation that happens during respiration affects the baroreceptors, the lung stretch sensors and the venous return to the heart. Inspiration decreases intrathoracic pressure, which the baroreceptors interpret as a BP drop, causing HR to increase via baroreflex. At the same time, the lung stretch sensors are stimulated, inhibiting cardiac vagal activity, leading to an increase in HR as well. Finally, the

increased venous return triggers the Bainbridge reflex, in which HR increases along with heart contraction force in response to the accumulation of blood in the atria. During expiration, intrathoracic pressure increases, causing opposing effects [12, 14].

Previous studies have found RSA to be a non-causal phenomenon, where the changes in HR due to respiration occur slightly before inspiration or expiration takes place [14, 19, 24, 53]. While respiration is mainly controlled by the brainstem, it is generally acknowledged that RSA modulates heart activity through cardiac vagal discharge of the ANS [12, 13]. This suggests a neural coupling that may explain the apparent non-causal relation, where the ANS would respond to the intent of the respiration control center, rather than to inspiration or expiration itself [14, 53].

The function of RSA is still unknown. One study proposes the theory that it promotes a more efficient gas exchange, providing greater blood flow while there is more gas available [13]. A later study suggested that RSA actually allows the heart to function with less strain instead of promoting a more efficient gas exchange [54].

2.4. CARDIORESPIRATORY SYSTEM

The cardiorespiratory system is a combination of two other systems: the cardiovascular and the respiratory systems. Together they work to maintain homeostasis of blood gas on the body.

The cardiovascular system is formed by the heart and the blood vessels, composing a delivery system that transports oxygen and nutrients to the body's tissues and cells and carries away any waste to be properly filtered and disposed of. It also transports immune cells such as lymphocytes and antibodies [11]. Though the heart is the main responsible for blood circulation, acting as a pump, the blood vessels are also active in the process, being able to constrict or dilate and even create new paths [11, 15].

The main function of the respiratory system is to promote gas exchange, supplying the body with the oxygen needed for metabolic reactions and disposing of carbon dioxide that is produced by them. This gas concentration control works to maintain the pH of the body, which is essential for normal cell metabolism.

These two systems are closely related at a functional level, once the cardiovascular system is responsible for the transportation of the gases exchanged in the lungs throughout the

body and the intrathoracic pressure variations generated during breathing act as a pump promoting the return of venous blood to the heart [11, 15]. These systems are also coupled through RSA, which affects both HR and BP, as described in section 2.3, which means respiration acts as an input to the autonomic control system modulating cardiovascular activity [24]. Hence, studying the cardiorespiratory system as a single system allows the observation of the influence that these variables have on one another [14, 19, 20]. The following sections describe the variables that are used in this study to model and assess the cardiorespiratory system.

2.4.1. The Cardiac Cycle

A brief description of the heart's anatomical structure, especially regarding its conduction system, is necessary to describe the cardiac cycle and its ECG representation.

Figure 2.2 illustrates the heart's main structures as well as the pulmonary and systemic circulation circuits. The heart has four chambers, two atria and two ventricles. Blood enters the heart from the systemic circulation through the right atrium and from the pulmonary circulation to the left atrium. The right ventricle pumps blood to the pulmonary circulation, while the left ventricle pumps blood to the systemic circulation [15, 49].

To keep blood flow through the body, synchronized contractions are coordinated through the heart's conduction system, illustrated by Figure 2.3. The SA or sinus node is the heart's pacemaker. It can generate action potentials spontaneously and the ANS modulates its activity. The action potential travels through the internodal pathways and arrives at the atrioventricular (AV) node, which delays the signal propagation, allowing the atria to evacuate all the blood before ventricular contraction. Then the signal moves on to through the AV bundle to the right and left bundle branches finally arriving to the Purkinje fibers, the final points of the conduction system, which infiltrate the ventricles to induce a strong contraction [15, 55].

This electrical activity triggers the events that compose the cardiac cycle. Before the beginning of the cycle, the heart is in diastole, a state of relaxation. Firing of the SA node starts atrial depolarization, leading to atrial systole, a state of contraction, sending the blood from the atria to the ventricles. After the delay induced by the AV node, the atria repolarize and ventricular depolarization starts, leading to the ventricular systole, pumping

the blood to the respective circulation circuits. Finally, the ventricles depolarize, bringing the whole heart to a state of diastole, ending the cycle [15, 55].

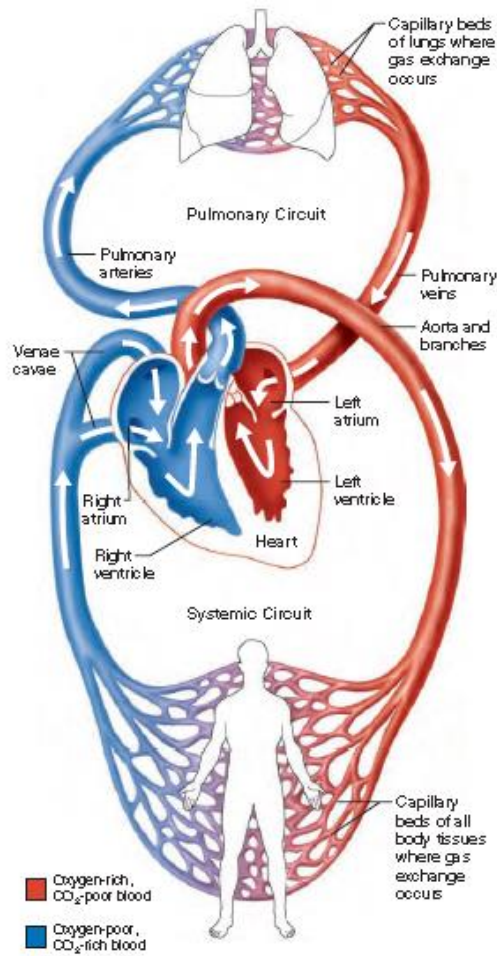


Figure 2.2 - Heart's basic anatomy and circulatory circuits (Marieb & Hoehn, 2013 [15]).

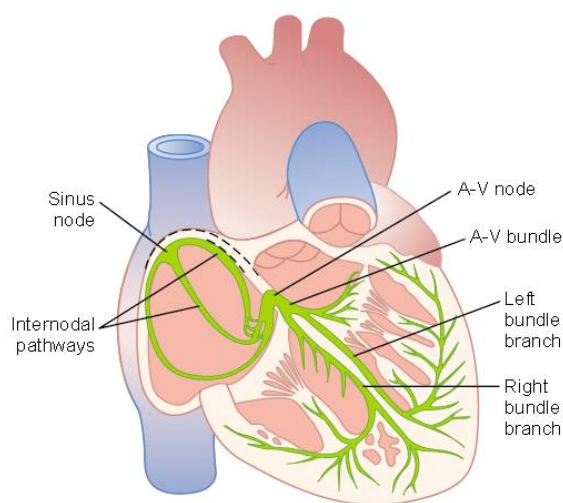


Figure 2.3 – Conduction system of the heart (Guyton & Hall, 2006 [55]).

2.4.1.1. Electrocardiogram

The ECG is a record of the heart's electrical activity, which propagates through the body and reaches the skin surface. Several electrodes are positioned strategically on the body to register this activity. Depending on the position of the electrodes, different derivations of the ECG are obtained, providing different information on the heart's anatomy, health and functioning.

For this study, it is important to understand how the ECG reflects the cardiac cycle and HR information is extracted from it, as shown in Figure 2.4. The P wave is the firing of the SA node, indicating the beginning of atrial depolarization. The P-Q interval represents the delay induced by the AV node. The QRS complex represents the beginning of ventricular depolarization. Atrial repolarization occurs at the same time, but the magnitude of the QRS complex hides it from the ECG. The S-T segment is a period of complete ventricular depolarization. The T wave indicates ventricular repolarization, ending the cycle [15, 56].

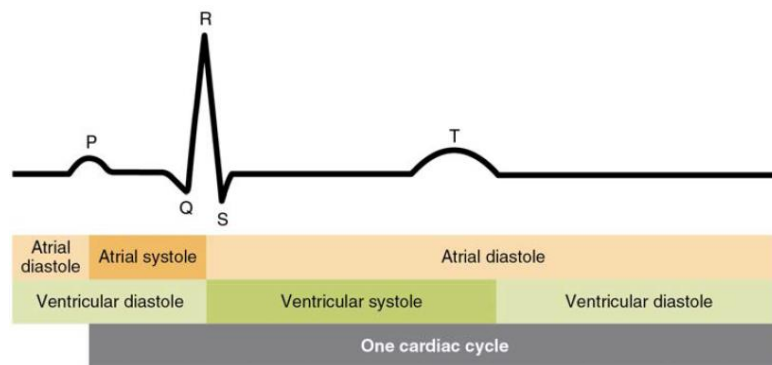


Figure 2.4 – Electrocardiogram and the cardiac cycle (OpenStax College, 2013 [57]).

Theoretically HR should be measured by the distance from consecutive P waves, but it is usually obtained from the distance between R waves, since its magnitude makes it a good candidate for automatic extraction [5]. The RRI characterizes the cardiac period, given in milliseconds (ms), which is inversely proportional to the HR and is the information that is actually used in the study.

2.4.1.2. Ectopic Heart Beats

The SA node, the AV node and the Purkinje fibers are formed by cells that have what is called an intrinsic rhythmical excitation. This means that these fibers can generate action potentials even if an external stimulus is absent. The SA node's intrinsic firing rate is around 75 times per minute, while the AV node's is around 50 times per minute and the

Purkinje fibers' is around 30 times per minute. As the SA node has the fastest rhythm, it usually triggers the firing of these other cells before their intrinsic rhythms reaches a threshold and these cells fire on their own. Under specific conditions, such as signal blocks, these other cells may come to fire spontaneously [15, 55]. It is also possible for muscle cells to become pacemakers, forming an ectopic focus to take over the pacemaker function. Though this effect may come from health conditions, it also occurs due to substances such as caffeine and nicotine [15].

These premature beats generated by the firing of cells that are not the SA node are called ectopic beats or extrasystoles. Though the presentation of an ectopic beat on an ECG may vary according to its origin, they are usually characterized by a premature beat followed by a compensatory pause, as the regular rhythm is reestablished. An example of an ectopic beat followed by a compensatory pause can be seen in Figure 2.5.

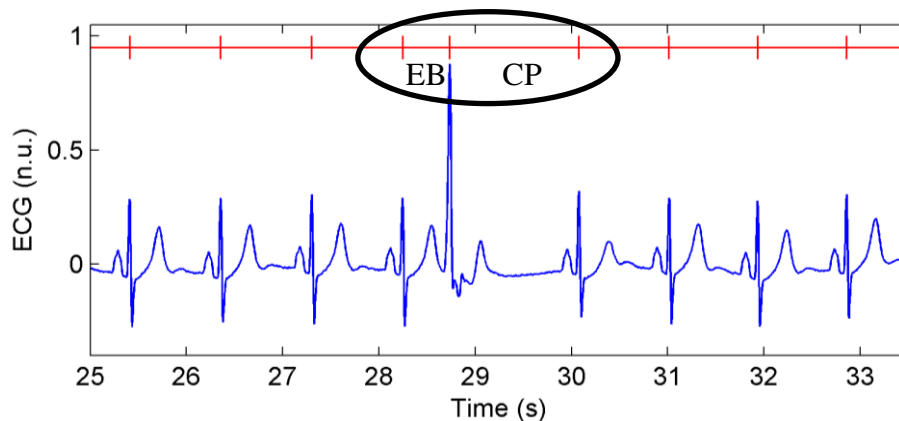


Figure 2.5 – Example of a presentation of an ectopic beat (EB) followed by a compensatory pause (CP) on an ECG record (blue), highlighting RRI durations (red).

2.4.2. Arterial Blood Pressure

Arterial blood pressure varies according to the cardiac cycle, but also varies throughout the body, with its average value decreasing as the vessels grow thinner, as show in Figure 2.6. The average BP in the pulmonary circulatory circuit is significantly lower than that in the systemic circulation circuit, which can be explained by the difference in the size of these circuits. The systemic circulation requires more pressure to travel through the whole body, requiring greater force from the ventricular contraction [11, 58].

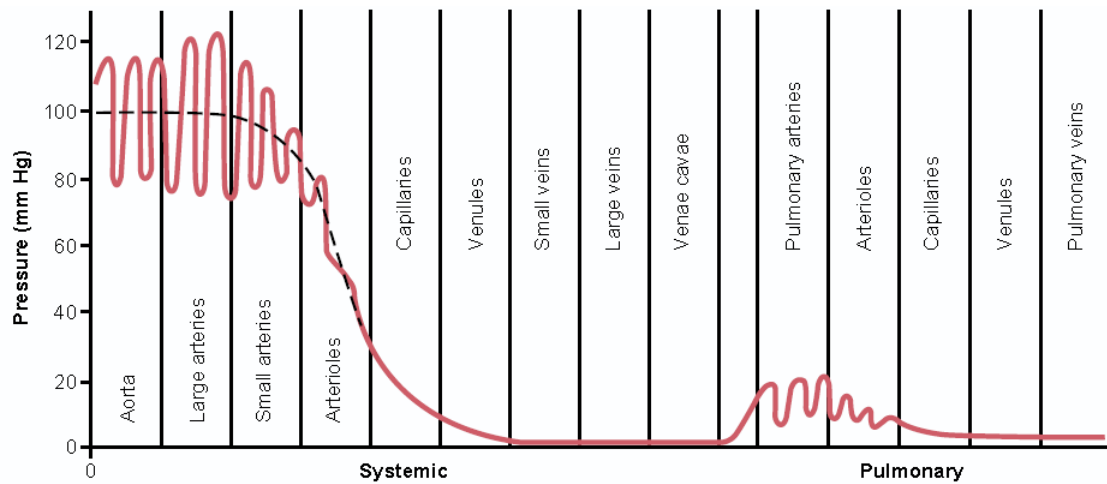


Figure 2.6 – Pressure variation through blood vessels (Guyton & Hall, 2006 [58]).

Figure 2.7 shows how the aortic BP varies within a cardiac cycle according to its events and its relation to the ECG. Right after the QRS complex, begins a period of isovolumetric contraction of the ventricles, where the ventricles have started to contract, but the pressure is not enough to push the blood through the valves that regulate the flow through the pulmonary artery and the aorta. During this period, arterial BP drops to its minimum value, which is the DBP. Once the valves open the ejection period starts, pumping all the blood to the arteries. The maximum pressure that occurs during this phase is the SBP. Though the ventricles are never completely empty, when there's not enough blood to generate pressure these valves close once again, causing the dicrotic notch [11, 15, 59].

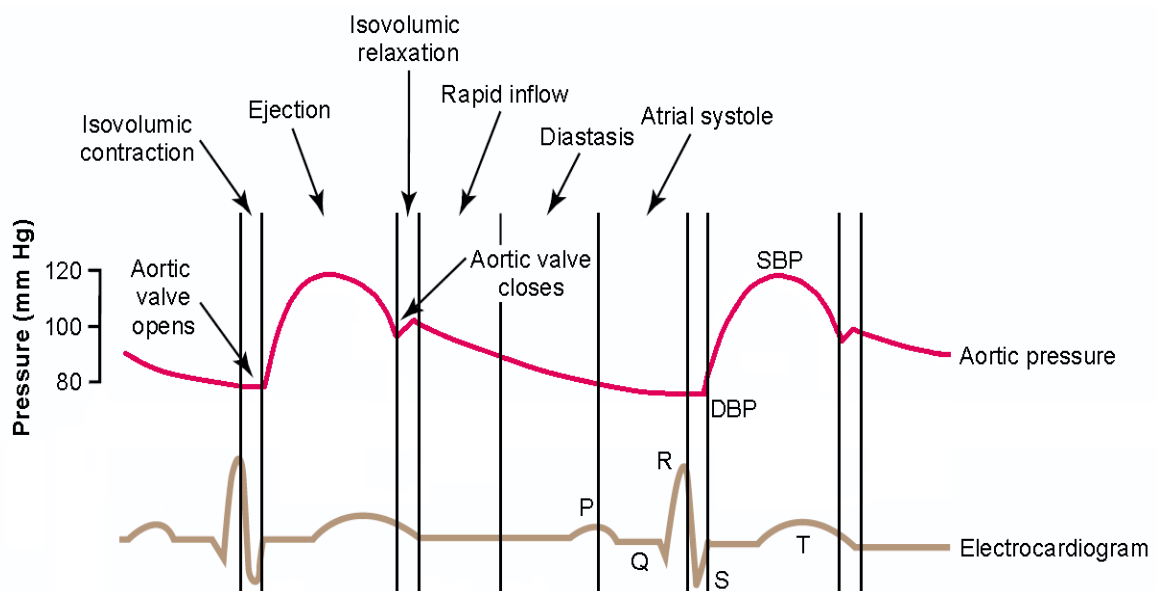


Figure 2.7 – Continuous BP in relation to the ECG and cardiac cycle events (adapted from Guyton & Hall, 2006 [49]).

2.4.3. Ectopic Beats and Blood Pressure

Ectopic beats many times present with no apparent effect on the continuous BP records other than a timing alteration. However, in some cases an ectopic beat may occur so prematurely that the heart does not have enough time to fill properly, causing the following BP cycle to present lower amplitude than the neighboring ones or even to be completely suppressed. Figure 2.8 shows an example of each of these effects. It is important to notice that when the BP cycle has lower amplitude, as in Figure 2.8 (a), the SBP presents lower than expected while the DBP is actually higher.

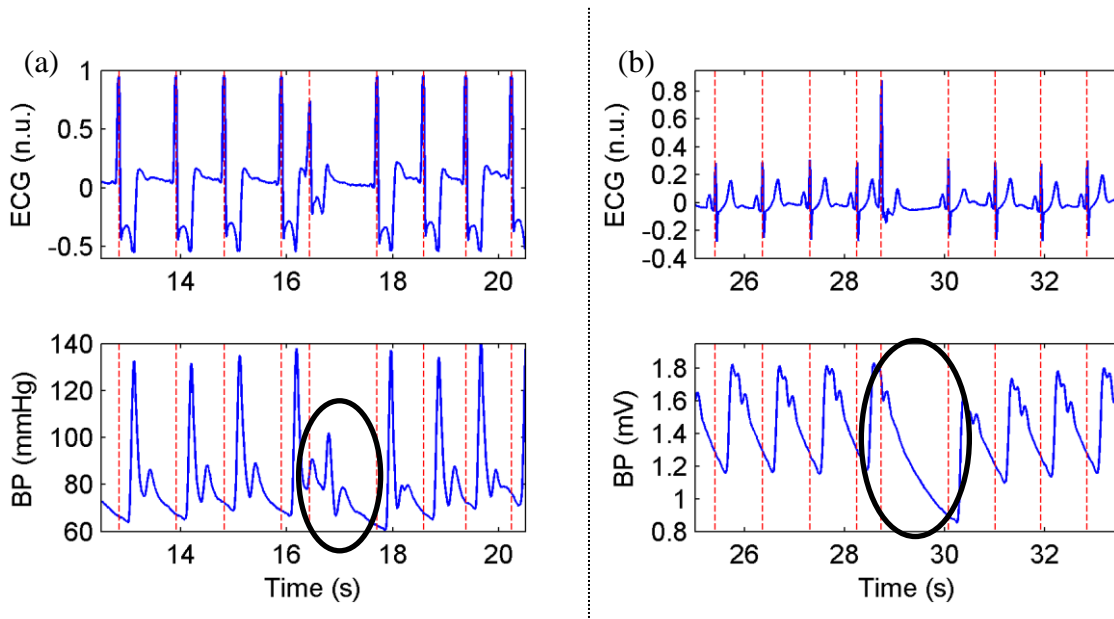


Figure 2.8 – Examples of how ectopic beats can affect blood pressure by lowering the amplitude of the correlated cycle (a) or suppressing it completely (b). The dashed red lines indicate the R-peaks position, delimiting the cardiac cycles.

2.4.4. Airflow

The ILV is a good representation of the respiratory cycle to identify the RSA phenomenon, once it is directly related to the inspiratory and expiratory activity and has a well-documented physiological meaning.

It is possible to measure ILV directly using methods such as volume based spirometers, but many times the information is provided in the form of airflow, given in liters per second (L/s), as is the case in this study. ILV can be obtained from airflow data through numerical integration [60, 61]. This process is further described in section 3.2.3.

Figure 2.9 shows lung volume under different breathing conditions as well as pulmonary capacities, which are combinations of lung volumes that have specific physiological interpretations. The tidal volume is the volume variation during normal breathing, which is usually of 0.5 L for adult males. The inspiratory reserve volume is the volume of a deep breath using full force, which exceeds the tidal volume. The expiratory reserve volume is the volume of forceful expiration beyond the regular tidal volume. Finally, the residual volume is the volume that remains after forceful expiration and keeps the lungs from collapsing [62, 63].

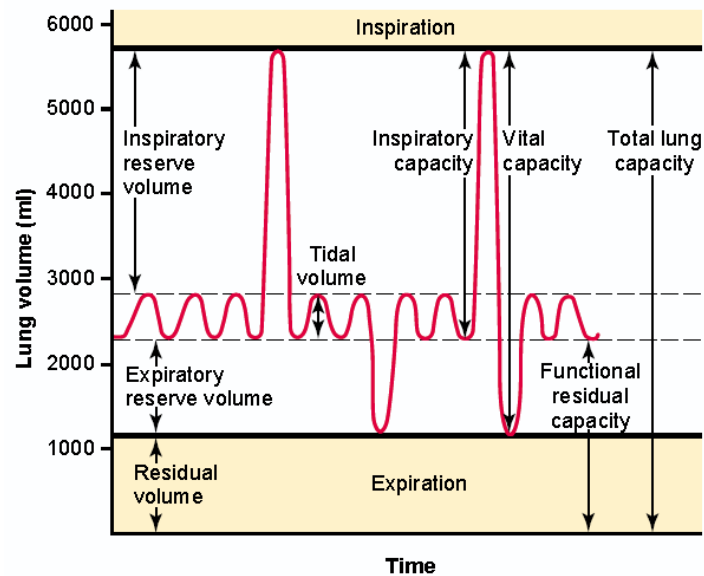


Figure 2.9 – Lung volumes and capacities (Guyton & Hall, 2006 [63]).

In this study the focus is in the volume variation, not the absolute volume itself. Therefore the residual volume is not considered and what is mainly displayed is the tidal volume variation under normal breathing conditions, though in some records it is possible to observe events of deep breathing or forceful expiration.

2.4.5. The Cardiorespiratory System Model

The cardiorespiratory system and the physiological interactions that have been described so far can be represented by the closed-loop model proposed by Belozeroff *et al.* [64]. The representation of this model by Jo *et al.* [65] is shown in Figure 2.10, highlighting the part of the model that is the object of this study. Respiration modulates RRI through autonomic coupling of respiratory and cardiac control, while the mechanical coupling resulting from

the intrathoracic pressure changes affects BP through venous return. BP affects the RRI through baroreflex dynamics, but the RRI affects BP as well.

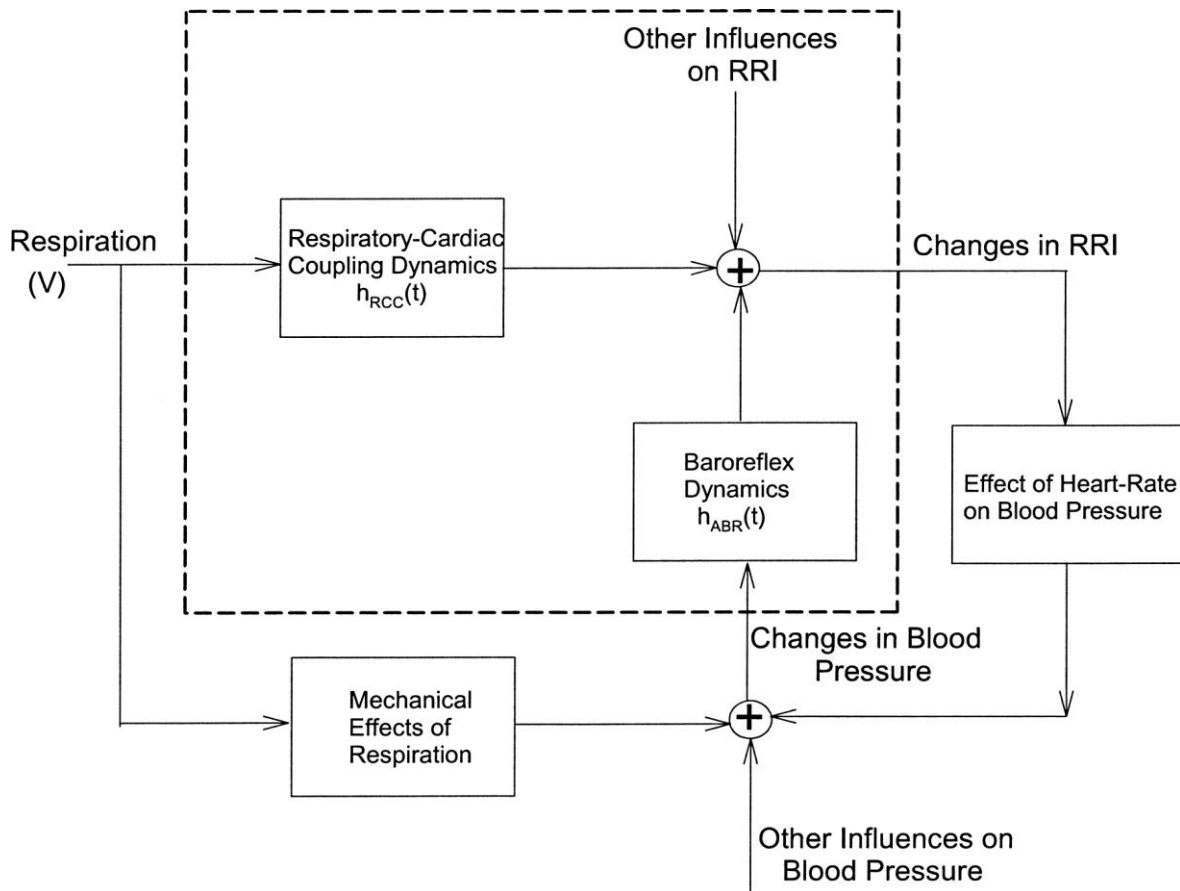


Figure 2.10 – Cardiorespiratory system model (Jo *et al.*, 2003 [65]). The dynamics in the dashed line box are the focus of this study.

Each of the dynamics of this complex closed-loop system, represented by the blocks in Figure 2.10, may be studied individually by taking different combinations of variables as input and output. They can be studied individually or as part of the broader context. Considering this, the software developed as a part of this study, CRSIDLab, allows the user to choose any variable as system output and to indicate up to two other variables as inputs, providing maximum flexibility.

In this study, the focus is on the part of the system within the dashed box in Figure 2.10, where ILV and SBP are taken as inputs and the RRI is the system output. For that purpose two subsystems are identified to generate the impulse response, which completely describes the dynamics of these systems [66]. The impulse response that represents the RCC dynamics is given by h_{RCC} , while the impulse response representing the ABR dynamics is given by h_{ABR} . In order to identify the subsystems, a few model options

implemented in CRSIDLab are used, as described in section 3.3.2. From the impulse responses, quantitative indicators are used to reach conclusions regarding the ANS.

2.5. HEART RATE VARIABILITY

HRV is the variation of the intervals between heart beats that can be observed on a beat-to-beat basis around a mean value and result from various physiological mechanisms [5]. Though factors such as spontaneous firing of the heart's pacemaker cells, circadian rhythms and body temperature play a role in this beat-to-beat variation, the most relevant of those mechanisms are modulated by the ANS, making HRV a good measure of sympathovagal balance [3, 5].

HRV analysis starts from extracting the RRI from the ECG, as this is a measure of the beat-to-beat intervals. There are many methods described in the literature to quantify HRV in both time and frequency domains, including non-linear methods. In time domain the methods can be classified as statistical or geometrical methods, while the frequency domain methods are based on the analysis of the PSD of the RRI series [3, 4, 5]. This study focuses on frequency domain methods of estimating PSD, described in section 3.3.1, since its results are easier to interpret and frequency domain methods are better for assessing short term data [4].

PSD analysis of short term RRI records, ranging from 2 to 5 min, focuses on three frequency bands: the VLF (0-0.04 Hz), the LF (0.04-0.15 Hz) and the HF (0.15-0.4 Hz) [4]. In this study records were taken over a 10 min period and the first 5 min were used for HRV analysis.

Each of these frequency bands provides different information of the ANS activity. It is widely recognized that the HF band is a measure of efferent vagal activity and is related to RSA [3, 4, 6, 7]. However, the interpretation of the LF band is controversial, with some claiming that it is a measure of sympathetic activity, some claiming it reflects both sympathetic and vagal activity [3, 4, 6]. The LF band has also been associated with baroreflex activity [3, 67]. The VLF does not have an established physiological interpretation and its analysis should be avoided when using short term recordings [4]. Though the interpretation of the LF band is not a consensus, the LF/HF ratio has been shown to be a good measure of sympathovagal balance [4, 7].

2.6. BLOOD PRESSURE VARIABILITY

As HR, BP also fluctuates around a mean value on a beat-to-beat basis. These fluctuations, which can be observed on SBP, DBP, pulse pressure (PP) or mean arterial pressure (MAP) extracted from BP records, is called blood pressure variability (BPV).

Respiration is one of the main influences of BPV and shows on the HF band, as it does on HRV. The HF band has also been related to changes in HR due to vagal activity [7]. The LF band is mainly influenced by what is called the 10-second-rhythm and is considered a measure of sympathetic vasomotor tone [67, 68, 69]. Though there are theories as to the mechanisms measured in the VLF band [70, 71], it is still not going to be addressed due to the short term nature of the data. In this study SBP is used as the variable representing BP information and so systolic BPV is evaluated.

An increased BPV associated with hypertension has been studied in connection to cardiac events such as strokes and coronary events [72]. Increased BPV has also been linked to increased sympathetic drive and reduced sensitivity of arterial and cardiopulmonary reflexes [70, 73].

3. CRSIDLAB

Part of this study consisted on the development of a Matlab-based toolbox named CRSIDLab (Cardiorespiratory System Identification Lab). Its development started as an undergraduate study and continued in the present study to include more methods. This chapter presents CRSIDLab and all methods implemented, some of which were later used to perform the ANS study, as specified in Chapter 4.

CRSIDLab allows processing of ECG, continuous arterial BP, airflow, and lung volume registers and performs univariate PSD analysis as well as system model identification using up to three variables extracted from the data. ECG processing is based on ECGLab's implementation, a Matlab-based toolbox for HRV evaluation also developed at the University of Brasília [27]. The GUI is built as a single unit with multiple nested tabs, which helps the user follow the processing flow.

CRSIDLab is meant to be a tool for quantitative ANS evaluation for academic purposes, to be used by researchers of both medical and engineering backgrounds. A major concern during development was flexibility for the user, once the cardiorespiratory system has complex interactions that can be studied from different perspectives, using different combinations of variables.

The main page on CRSIDLab is divided in three parts: the first allows creating a new patient file, which is detailed in section 3.1, or opening an existing one; the second allows viewing and editing the patient record, with proper identification, contact information, clinical and family history, information on the physical exam and protocols involved in the study, as well as any relevant comments; the last is a panel with an overview of the available data in the patient file that is currently opened.

Figure 3.1 is a flowchart of the pre-processing and analysis flows. The user can choose to supply the continuous records of ECG and BP data for pre-processing or can enter the variables of HR, RRI, SBP or DBP for aligning and resampling, as described in section 3.2.4, before analysis. Airflow or ILV can be supplied as respiration data. Univariate PSD analyses and univariate and multivariate system identification analyses are available, from models that can be specified by the user. The quantitative indicators are exported to text files that are formatted to be easily imported to statistical analysis software.

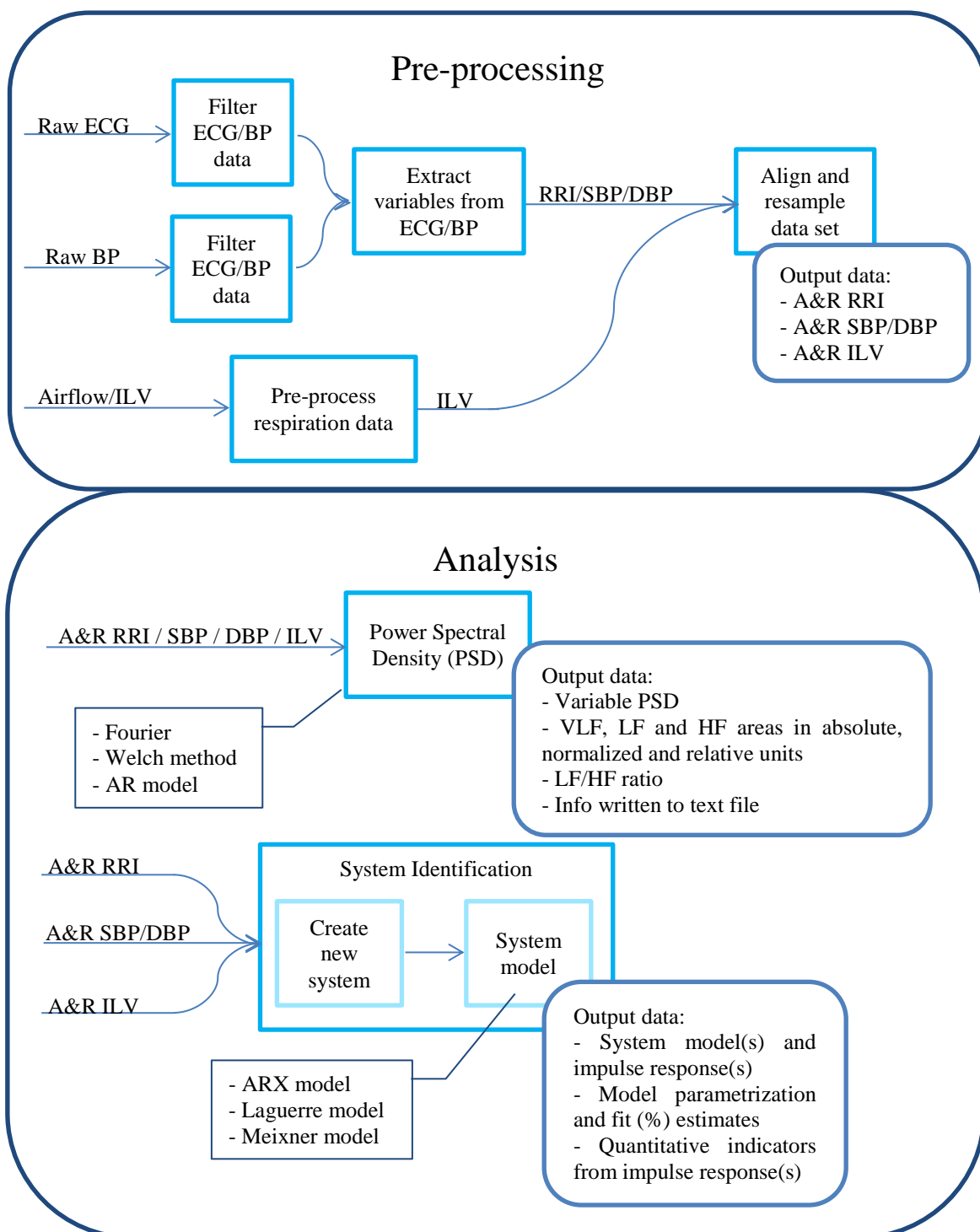


Figure 3.1 – Overview of the pre-processing and analysis steps. Pre-processing: raw ECG and BP can be filtered separately, then processed either simultaneously or individually for RRI, SBP and/or DBP extraction; airflow is transformed to ILV and ILV can be filtered; any combination of available variables can be aligned and resampled (A&R) either individually or as a data set. Analysis: the PSD of any resampled variable is estimated using the Fourier transform, the Welch method and/or an AR model; system identification is performed with a combination of up to three A&R variables and the impulse response is estimated from an AR/ARX, LBF or MBF model.

3.1. PATIENT DATA OBJECT AND CREATING A PATIENT FILE

A data object was created to store and manage all data that can be generated through the process, allowing all information to be kept in a single file. This object, named *patientData* has a rather complex structure, detailed in Appendix A, due to the amount of data that can be produced and the intended flexibility for the user.

A new patient file can be created through code, by creating a *patientData* object and adding the desired variables to the corresponding object properties, which is not recommended, as any mistakes may prevent the toolbox from working as expected. Alternatively, it can be created through the interface, which has a dedicated window, shown in Figure 3.2, to help build a new patient file, requiring the user to upload the desired variables to Matlab’s workspace and inform the type of data from a list of options and create the file. The user can also indicate a filename and destination folder for this new patient file directly in the main page.

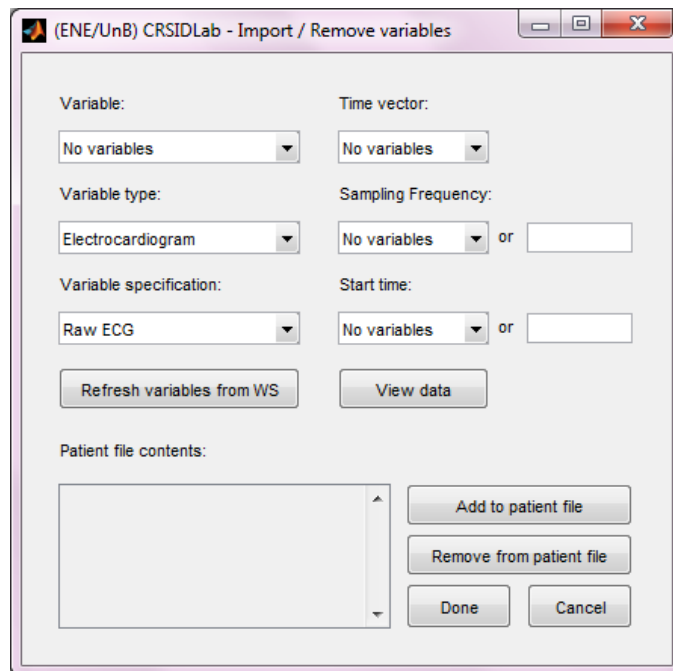


Figure 3.2 – Window that manages variables to create a new patient file. Variables uploaded to Matlab’s workspace are listed as options for the main variable and associated time vector, sampling frequency and start time. The sampling frequency and start time can alternatively be typed in. Variable type and specification can be selected from a list of options. Clicking the “View data” button opens a window to display the indicated variable for visual inspection. Clicking the “Refresh variables from WS” updates the options listed for variables selection to include any new variables that were uploaded to Matlab’s workspace.

The variables that can be imported to the patient file through the interface are raw and/or filtered ECG, RRI, raw and/or filtered continuous BP, SBP, DBP, raw and/or integrated airflow and/or ILV (detrended integrated airflow).

While the time information associated with each variable is an optional input, it is recommended that both a time vector and sampling frequency are supplied. This is because it is not unusual for the time vector not to correspond to a precise sampling frequency due to numerical representation of values, for instance. As some algorithms require the sampling frequency as input, such as digital filter implementations or the Fourier transform, and some take into account the supplied time vector, such as aligning and resampling the data set, the best results are obtained by providing both.

If the time vector is not supplied, one is created from the sampling frequency and the start time informed. If the start time is not informed, it is considered to be zero. If neither time vector nor sampling frequency is supplied, the sampling frequency is considered one. If a time vector is supplied, but not the sampling frequency, the sampling frequency is estimated from the given time vector as the rounded inverse of the average sampling interval.

3.2. PRE-PROCESSING

This section presents all methods regarding the pre-processing of ECG, continuous BP and airflow data, the extraction of variables (RRI from ECG, SBP and/or DBP from continuous BP and ILV from airflow data) and the aligning and resampling of the final dataset, which is necessary for the available analyses methods, as better explained in section 3.2.4.

3.2.1. Filter ECG/BP data

ECG and continuous BP data records are vulnerable to noise and, though many acquisition systems today perform some sort of pre-filtering, additional filtering may be necessary. CRSIDLab provides options for filtering the main sources of ECG and BP noise, but it is important to make sure protocols are in place during signal acquisition. Electrode contact, transducer displacement and patient motion artifacts may cause the signal to be completely lost for segments of time, which cannot be reversed.

Three noise sources are addressed for ECG filtering. Powerline interference occurs due to the transformation of alternate to continuous current and causes interference at powerline frequency and its harmonics. Electromyography (EMG) noise comes from muscle electrical activity that has a frequency band that overlaps with the ECG and is inevitably recorded. Finally, the baseline wander results from the relative movement of the electrodes in relation to the position of the heart, which is usually due to breathing, but may occur from other body movements [74, 75].

CRSIDLab has maintained the filtering options from ECGLab [27] for the ECG: a 60 Hz notch filter of adjustable width tolerance from 1 to 20% to remove powerline interference; a low-pass filter with cut-off frequency from 20 to 60 Hz to remove EMG noise; and a high-pass filter with cut-off frequency from 0.001 to 1 Hz to remove baseline wander.

The high and low-pass filters are 2nd order Butterworth filters. The notch filter is constructed by allocating zeros on the unit circle at 60 Hz and any harmonics within the frequency range and poles at the same frequencies close to the zeros. The poles are added to minimize the low-pass effect of the all-zeros filter. The tolerance value that can be adjusted by the user controls the distance between the poles and zeros. For all filters, forward and reverse filtering is applied so that there is no phase distortion. Figure 3.3 shows the squared magnitude of the notch filter for 1 (blue) and 20% (green) tolerance, representing the filter magnitude effects after reverse and forward filtering.

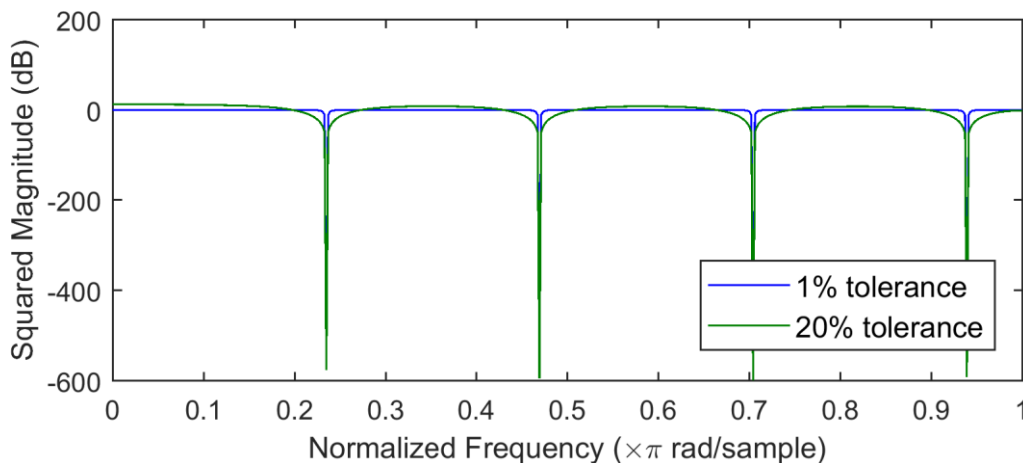


Figure 3.3 – 60 Hz notch filter squared magnitude for 1% width tolerance (blue) and 20% tolerance (green), representing the magnitude effects after reverse and forward filtering, with phaseless response.

An additional feature allows flipping the ECG vertically, so that it can be positioned correctly if the electrodes were inverted during acquisition. This is necessary for accurate RRI extraction, as explained in section 3.2.2.1.

Figure 3.4 (a) and (b) show an example of ECG contaminated with powerline interference and the effects of applying a 1% width tolerance 60 Hz notch filter, respectively. Figure 3.5 (a) shows an example of ECG contaminated with EMG noise and Figure 3.5 (b), the same signal after applying a 35 Hz low-pass filter. Finally, Figure 3.6 (a) and (b) present a wider window of the ECG record so that baseline wander can be visualized alongside the effects of applying a 0.01 Hz high-pass filter.

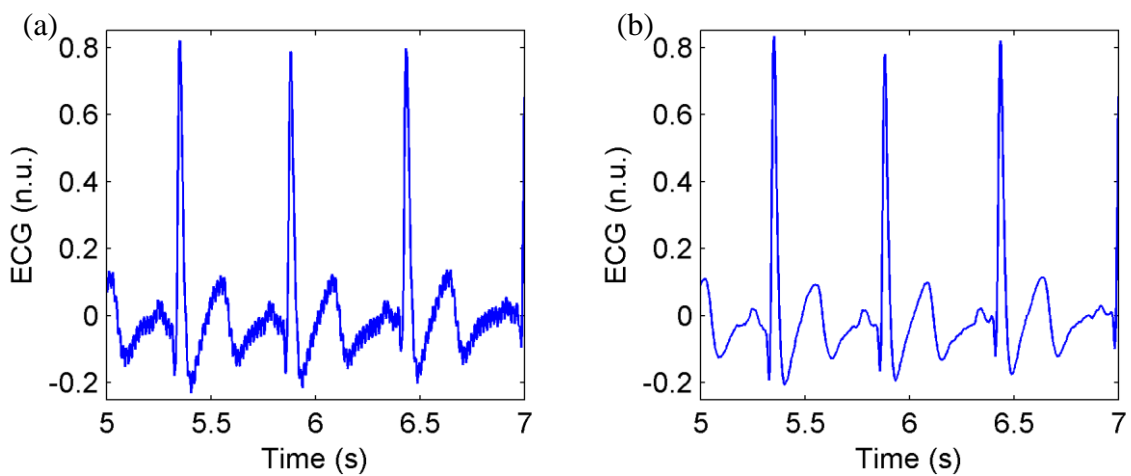


Figure 3.4 – Example of ECG record contaminated with 60 Hz powerline noise (a) and after applying a notch filter of 1% width tolerance (b).

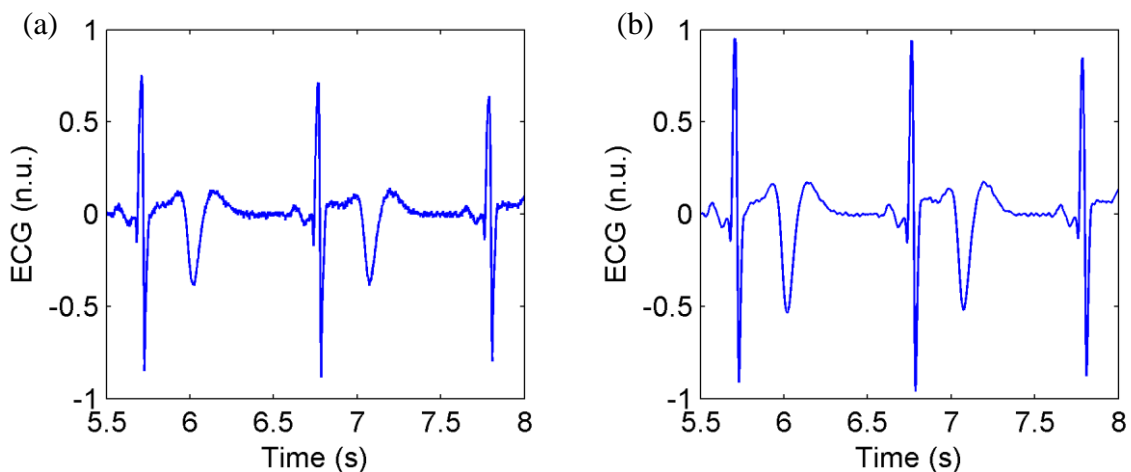


Figure 3.5 – Example of ECG record contaminated with EMG noise (a) and after applying a 35 Hz low-pass filter (b).

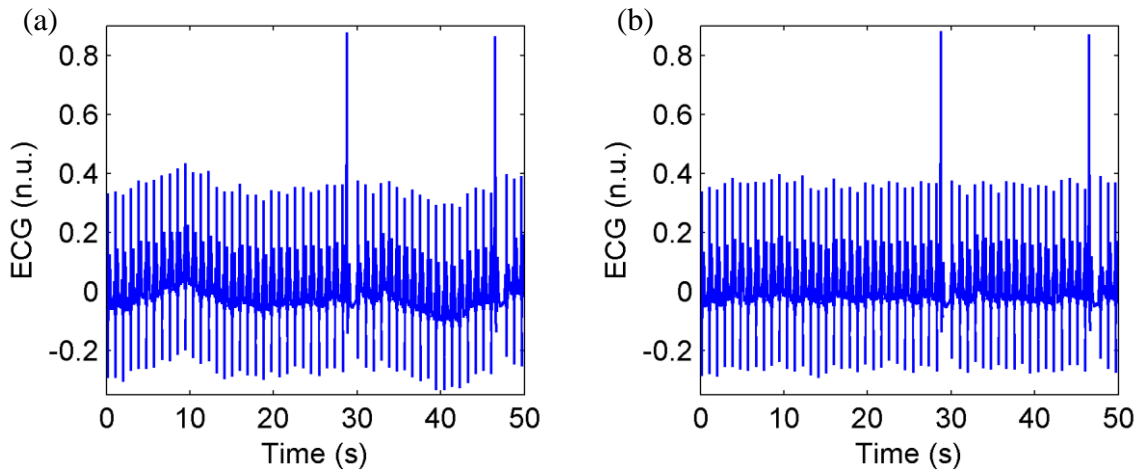


Figure 3.6 – Raw ECG record (a) and after filtering for baseline wander with a 0.01 Hz high-pass filter (b).

There are different ways of measuring continuous BP and so the noise present in records may have different sources. Powerline interference can affect BP transducers that use intra-arterial catheters and carry conductive fluids through ground loops formed by patient contact with other devices [76]. High frequency noise can usually be observed in continuous BP records. The fundamental frequency of the BP is given by the HR and not more than ten harmonics are necessary to satisfactorily represent continuous BP [77, 78]. This means that applying a 20 Hz low-pass filter to a continuous BP record would allow a good enough representation of BP for HR up to 120 bpm ($20 \times 60/10$), while a 60 Hz low-pass filter can handle HR up to 360 bpm. Therefore, the low-pass filter used for EMG removal can be applied to the BP records to remove high-frequency noise without compromising the relevant information.

An example of BP contaminated with powerline interference could not be found on the available database. Figure 3.7 (a) shows BP contaminated with high-frequency noise and Figure 3.7 (b) shows the same signal after applying a 35 Hz low-pass filter.

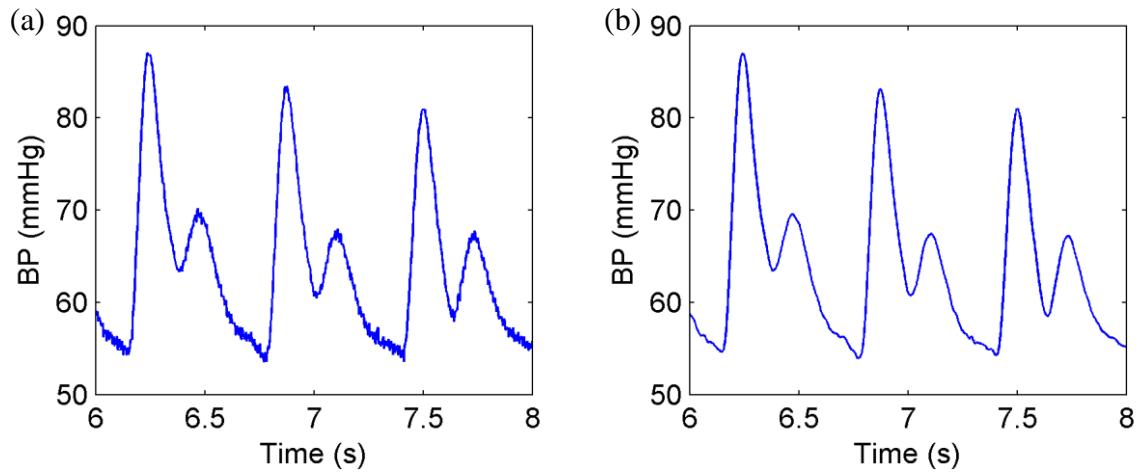


Figure 3.7 – Example of BP record contaminated with high-frequency noise (a) and after applying a 35 Hz low-pass filter (b).

3.2.2. Extract variables from ECG/BP

Variables that can be extracted from the ECG and continuous BP records can be used to characterize the cardiorespiratory system, as discussed in section 2.4. This can be done for each record individually or both simultaneously, in which case algorithms that take advantage of the combination of the data can be employed. There are several algorithms available for RRI extraction from the ECG and for SBP and DBP extraction from the continuous BP record. Each algorithm is described in the following sections.

Besides automatic variable extraction options, it is possible to make manual corrections. The extracted variables are shown on the plots so that the user may perform visual inspection. RRI and SBP show as red dots on the ECG and continuous BP records, respectively, while the DBP shows as red asterisk. Clicking on a mark will erase it, while clicking on an unmarked spot creates a new mark.

This need to differentiate SBP from DBP on manual corrections led to the introduction of the SBP/DBP threshold, which is a value that can be modified by the user and determines which part of the continuous BP plot is interpreted as SBP and which part is interpreted as DBP for the functions that depend on clicks on the screen. This value can be changed at any time, allowing the user to adapt it as needed, which is especially useful when correcting variables that result from ectopic beats and have values that differ too much from its neighbors. This threshold can be shown on the plot as a horizontal line so that the user has visual confirmation and knows when to adjust it.

Another feature in this tab is the manual indication of ectopic beats and corresponding BP variables. There is a menu where the user can indicate the variables that they wish to edit, allowing RRI, SBP and DBP to be marked as extrasystoles simultaneously. Though there are different ways to correlate these variables, for this purpose the one proposed by Rompleman and Ten Voorde [79] is used, as shown in Figure 3.8, where a heartbeat is considered to influence the following BP cycle. Later on, these marked values can be treated by interpolation or be removed if desired. If an ectopic beat occurs along with a compensatory pause, both should be marked for correction, the short and the long beats.

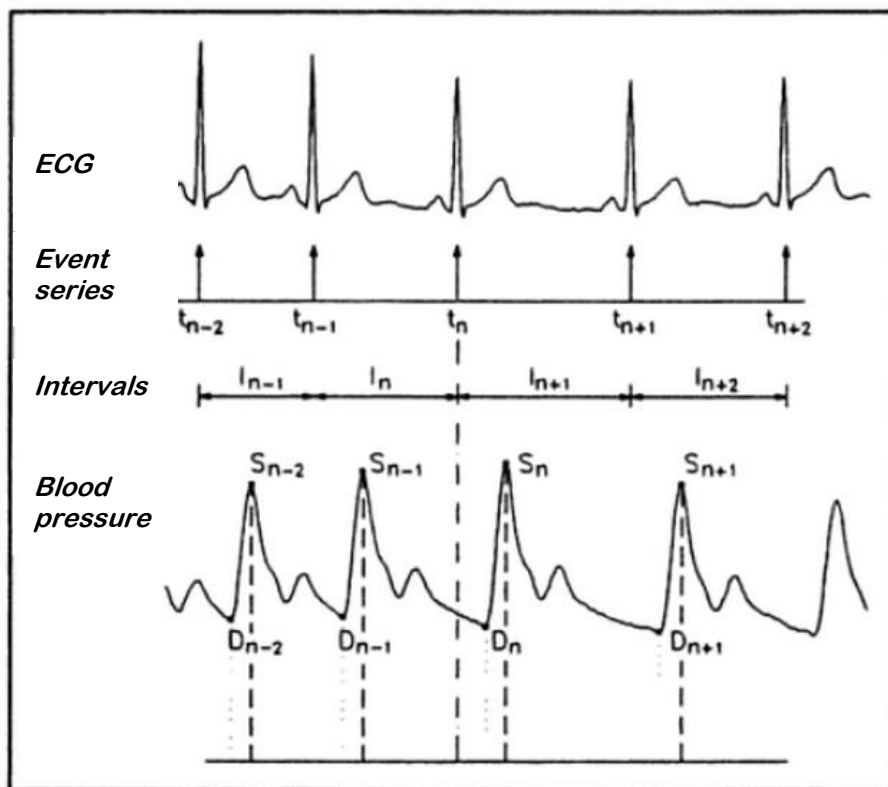


Figure 3.8 – Relation between the R wave on the ECG and SBP and DBP values (Rompleman & Ten Voorde, 1995 [79]).

3.2.2.1. RRI extraction

The RRI extraction algorithms are as implemented on ECGLab [27], with a single modification. ECGLab's algorithms used the module of the ECG to determine the R peak position for each beat, which sometimes led to S peak detection, when it presented greater than the R peak, or alternating detection of R and S peaks on the same record when their magnitudes were similar. These effects may occur depending on the ECG derivation that is being processed or due to physiological or anatomic variations on the subject being

recorded. In this implementation, only positive peaks can be found as R peaks. With the option to flip the data vertically in the filtering stage, the user should make sure the ECG is not upside down, so that the R peaks are found correctly.

There are two algorithms that differ slightly, named the “Fast” and the “Slow” algorithms. The initial steps are common to both algorithms and include low-pass filtering at 17 Hz, which maximizes signal-to-noise-ratio (SNR) [75], and calculating the derivative of this filtered signal, enhancing the QRS complex that naturally presents a fast slope, and a subsequent low-pass filtering at 30 Hz to suppress the noise enhanced by the derivative [27]. Finally the signal is squared to enhance QRS even further and a moving average low-pass filter of 17 Hz is applied to estimate the power of the 17 Hz component of each section. The moving-average window is set at 150 ms, as it must be large enough to contain at least one QRS complex, but not so large as to contain two consecutive QRS complexes [75]. This process assures QRS detection even when the T wave shows with bigger amplitude or the R wave is diminished, since it relies on the shape of the QRS complex, as well as its magnitude. Figure 3.9 shows an example of how this new filtered signal looks (green) for a given ECG record (blue), where a delay introduced by the filters can be seen. This issue is addressed later on by each algorithm.

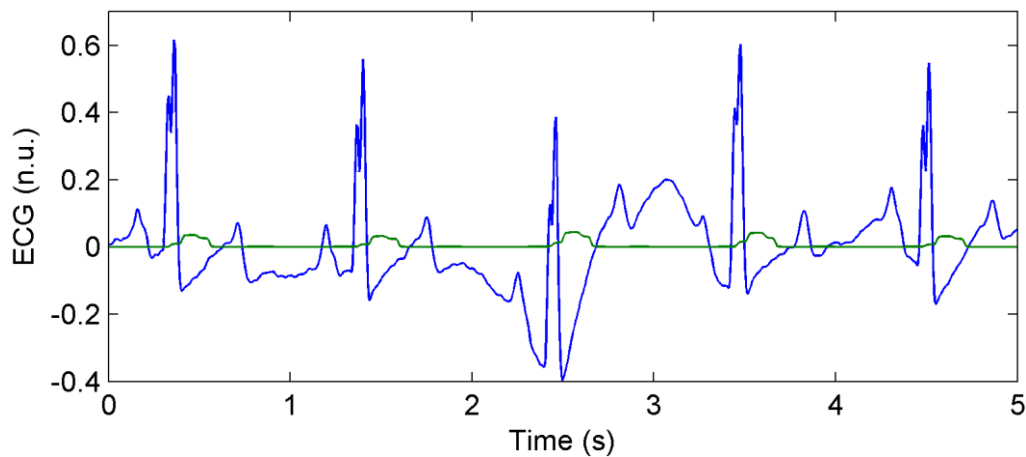


Figure 3.9 – ECG record (blue) and the signal obtained after QRS enhancing for R peak identification (green). The varying threshold is applied to the signal with enhanced QRS to detect the R wave.

The next step consists of applying a varying threshold to this filtered ECG record to find each R peak. Both algorithms initially sweep the filtered ECG record, determining a threshold equal to 0.15 times the maximum value of the next 2 s. While the “Fast

algorithm” searches for any sample above the threshold every 10 ms, jumping 350 ms when one is found, the “Slow algorithm” runs through every sample above the threshold, searching for the maximum point, jumping 200 ms when one is found. These approaches affect the processing time and precision of the algorithms.

As the filtered ECG is delayed when compared to the original ECG record, the next step is to find the actual R peaks from the reference obtained in the previous step. Here the two algorithms differ as well. While the “Fast algorithm” searches for local maximums at an interval from 30 ms prior to 40 ms after each index of the values above the varying threshold, a range of 70 ms, the “Slow algorithm” searches the 160 ms prior to each index found above its varying threshold. This range difference also accounts for the time and precision differences between the algorithms.

Finally, the RRI is obtained from the difference in the time stamps of consecutive R waves, presented in milliseconds. The occurrence of each RRI is at the second R peak, or at the end of the interval, as is recommended by the Task Force on HRV standards [4]. Figure 3.10 illustrates QRS detection using the “Fast algorithm” (a) and the “Slow algorithm” (b), with the R peaks marked as red dots on the ECG. Figure 3.10 shows an example where the lower precision of the “Fast algorithm” in exchange for faster processing time has resulted in misdetections, while the “Slow algorithm” was able to correctly identify all R peaks.

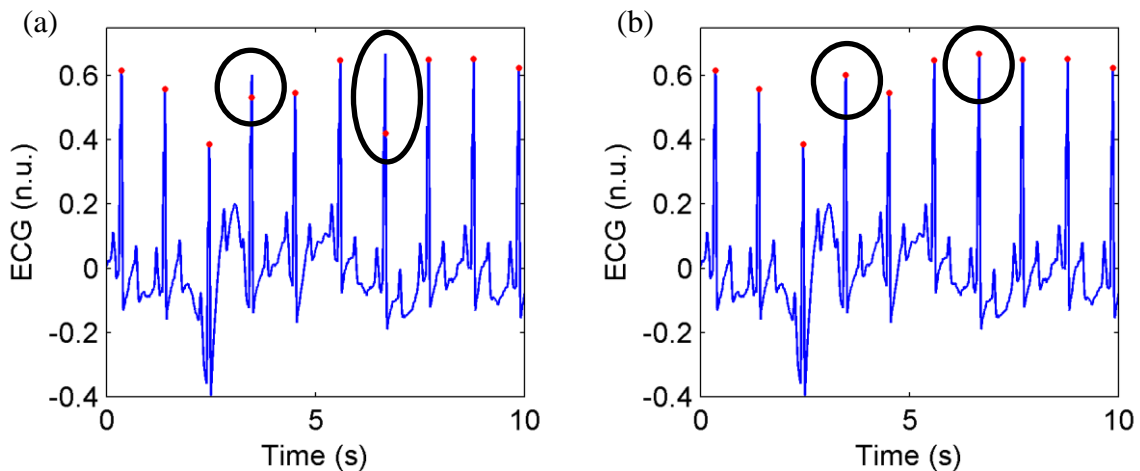


Figure 3.10 – Example of RRI extraction (red) from the ECG record (blue) in a situation where the “Fast algorithm” fails to detect two R peaks correctly (a) while the “Slow algorithm” is able to identify the location properly (b), both highlighted by the black circles.

3.2.2.2. SBP extraction

There are two methods available for SBP extraction from continuous BP records. The first identified on the interface as the “Waveform algorithm” and hereinafter referred to as method 1, was developed by Li et al. [80] and uses the first derivative of the continuous BP to locate a zero-crossing after the point of maximum inflection for each cycle, which indicates each SBP location. This algorithm is efficient in locating the region of occurrence of the SBP, but does not always select the absolute maximum value per cycle. Figure 3.11 (a) shows an ECG with the extracted RRI marked as red dots, while Figure 3.11 (b) shows the associated BP record after SBP extraction using method 1, marked as red dots. Figure 3.11 shows an ectopic beat that led to a BP was too low compared to neighboring values, leading to a misdetection, highlighted by the black circle.

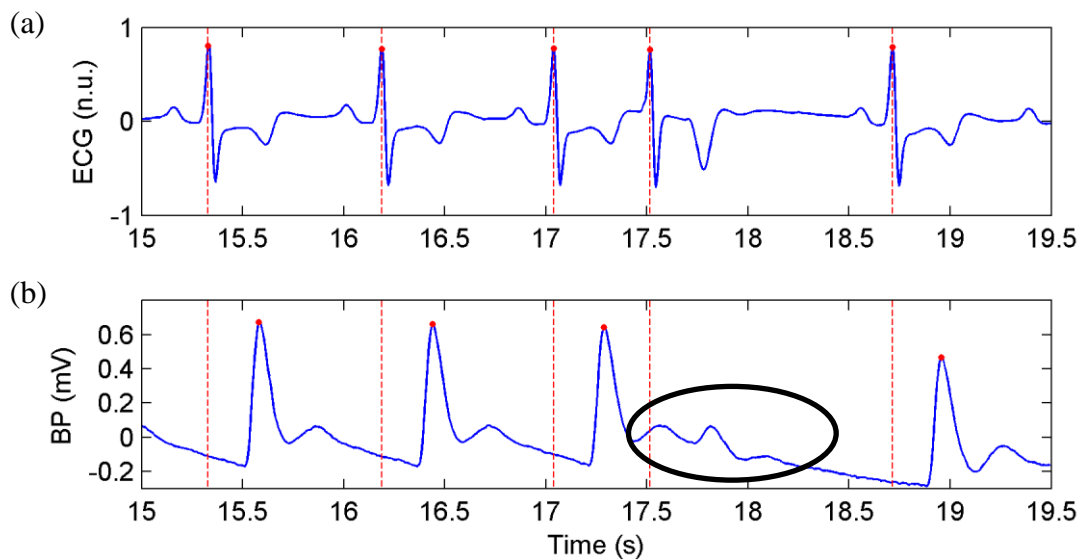


Figure 3.11 – ECG record (a) with extracted RRI (red dots) along with the corresponding BP record (b) and SBP (red dots) extracted using method 1. The highlighted BP cycle in (b) shows an example where method 1 failed to identify the SBP due to an ectopic beat that resulted in a very low BP compared with neighboring values.

Method 2, identified in the interface as “SBP from RRI”, was developed to provide a more precise SBP detection, taking advantage of the possibility of processing ECG and BP simultaneously. It requires that RRI extraction is performed first and uses the time stamps of the R peaks to segment the continuous BP data and find local maximums, corresponding to the SBP of each cycle. This algorithm is simple and very precise, failing only in very specific situations. Figure 3.12 shows the same example displayed in Figure 3.11, but now the SBP detection is performed using method 2. The black circle that highlighted a

mis-detection from method 1, now highlights a wrongful SBP detection by method 2, shown as red dots on the BP record (Figure 3.12 (b)), due to an ectopic beat that not only caused the highlighted BP to be lower, but in this case also caused part of the BP from the previous cycle to be included in the search region for local maximum.

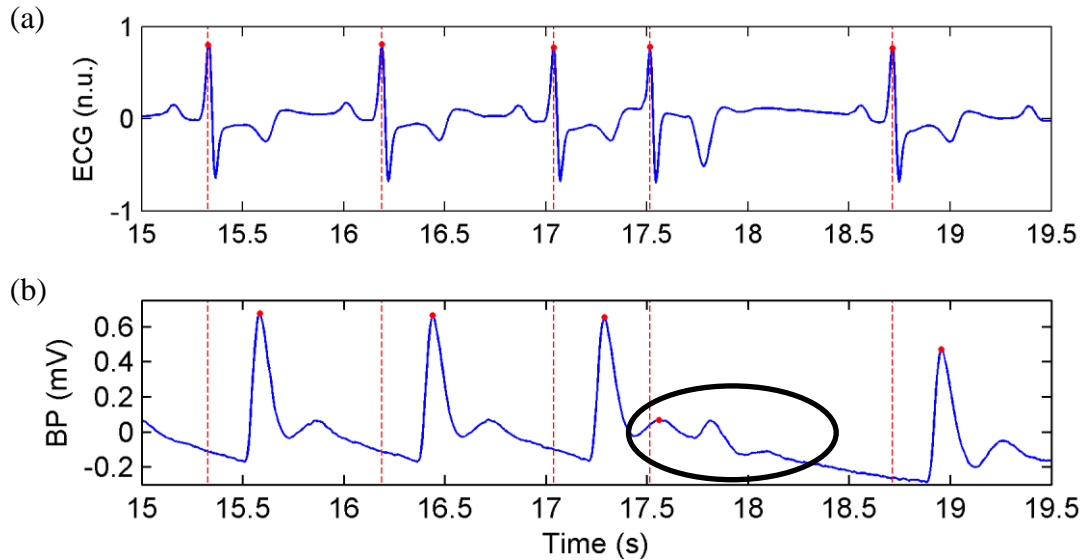


Figure 3.12 – ECG record (a) with extracted RRI (red dots) and the corresponding BP record (b) and SBP (red dots) extracted using method 2. The BP data is segmented from the previously extracted RRI, as indicated by the dashed red lines, to find the local maximums, or SBP. The highlighted SBP is a wrongful detection due to an ectopic beat that both altered the timing used for BP segmentation and significantly lowered the SBP of the following cycle.

3.2.2.3. DBP extraction

DBP extraction is more complicated than RRI or SBP extraction because the minimum BP value of a cycle does not always happen immediately before the SBP of that cycle, in which case it does not correspond to the DBP [81] and the DBP region of the continuous BP can be noisy. Thus, there are three different methods available to extract DBP that were developed to increase precision but maintain flexibility for the user.

Method 1 is the “Waveform algorithm” by Li *et al.* [80], the same used for SBP extraction. It locates a zero-crossing before the point of maximum inflection of the first derivative of the continuous BP, which indicates each DBP location. This algorithm is also efficient in locating the region of occurrence of the DBP, performing well for noisy records. Figure 3.13 displays the same example used for the SBP detection methods with the DBP extracted by method 1 marked as red asterisks (Figure 3.13 (b)). As was the case with

method 1 for SBP detection, the DBP from the highlighted BP, which results from an ectopic beat, could not be detected.

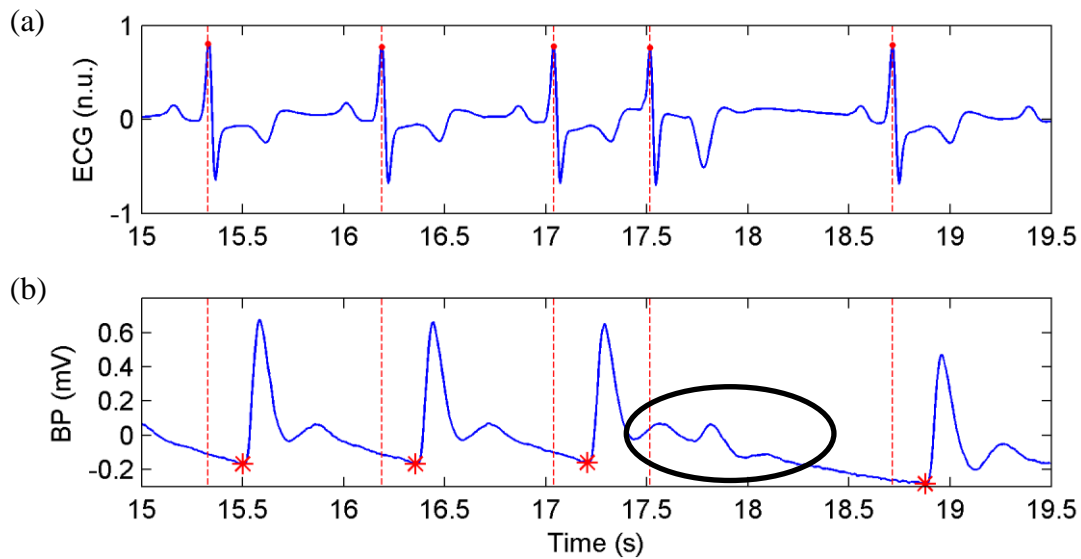


Figure 3.13 – ECG record (a) with extracted RRI (red dots) along with the corresponding BP record (b) and DBP (red asterisks) extracted using method 1. The highlighted BP cycle in (b) shows an example where method 1 failed to identify the SBP due to an ectopic beat that resulted in a very low BP compared with neighboring values.

Method 2 is an alternative for those who wish to process BP data individually, but want more precise measures. It is identified as “DBP from SBP”, requiring the previous extraction of SBP and using the time stamp of each SBP to segment the BP data and search for local minimums. Method 2 is not recommended for data that is especially noisy on the DBP region or that present a systematic issue such as a very low diastolic notch. Figure 3.14 illustrates the use of this algorithm, showing the previously extracted SBP as red dots, used to segment the BP data for the extraction of DBP, indicated through red asterisks. The highlighted DBP in Figure 3.14 is an example of misdetection caused by a low diastolic notch combined with a rising BP trend, causing the diastolic notch to be lower than the following DBP.

Method 3 is an attempt to improve the results from method 2 by narrowing the search region for the DBP. It is identified as “DBP from RRI and SBP” and requires the previous extraction of both RRI and SBP. The time stamps are used to isolate the areas between one R peak and the following SBP, which is the region where the DBP should occur. This is the most precise of the methods presented, but it is still sensitive to high frequency noise in this region. Figure 3.15 illustrates the algorithm by showing the ECG record (a) with the

previously extracted RRI marked as red dots together with the corresponding BP (b) with the previously extracted SBP marked as red dots. The yellow areas are the search areas, delimited by the dashed lines representing the RRI and SBP time stamps, where local minimums are found and marked as red asterisks. The highlighted DBP is an example of misdetection due to noise on the DBP region.

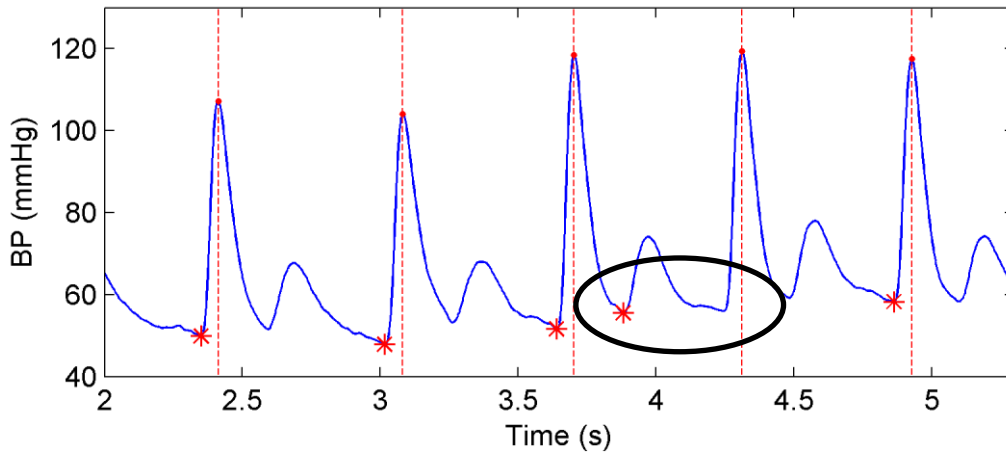


Figure 3.14 – BP record with the previously extracted SBP (red dots), which are used in method 2 to segment the BP data, as indicated by the red dashed lines, and find local minimums (red asterisks). The highlighted DBP is a misdetection due to a low diastolic notch combined with a rising low frequency trend.

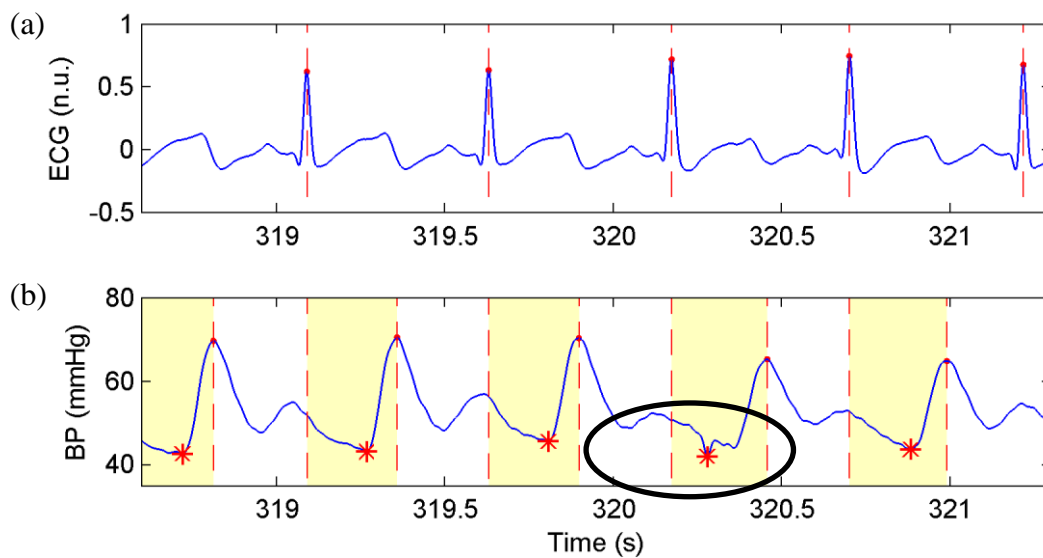


Figure 3.15 – ECG record (a) with extracted RRI (red dots) along with the corresponding BP record (b), SBP (red dots) and DBP (red asterisks) extracted using method 3. The search region for each DBP, delimited by the previously extracted RRI and SBP, is shown in yellow (b). The highlighted BP cycle in (b) shows an example where method 3 wrongfully detects the DBP due to noise in the search region.

3.2.3. Pre-process respiration data

The respiration data processing flow differs from those of ECG and continuous BP, thus it is performed separately.

If airflow data is available, given in liters per second, the first step is to convert it to lung volume information. For this purpose, numerical integration of the data is performed. The integration introduces a drift, which may be due to temperature and humidity differences in the air coming into and out of the lungs, to the fact that usually more oxygen is absorbed in the lungs than carbon dioxide is expelled, air leakages or even calibration and sensor response issues [61]. To remove this trend, linear and polynomial detrending are available, as well as a high-pass filter of low cut-off frequency, as these drifts can usually be approximated to a line or a low frequency curve [61]. Polynomial order can be set in the range of 1 to 10 and the high-pass filter cut-off frequency can be set between 0.01 and 0.15 Hz. It is possible to visually compare the effects of these methods through the GUI before selecting the one that better suits the data. Figure 3.16 (a) shows an example of integrated airflow with the resulting trend and the results from detrending the data (b) using linear detrend (blue), polynomial detrend of order 3 (green) and a high-pass filter with cut-off frequency of 0.01 Hz.

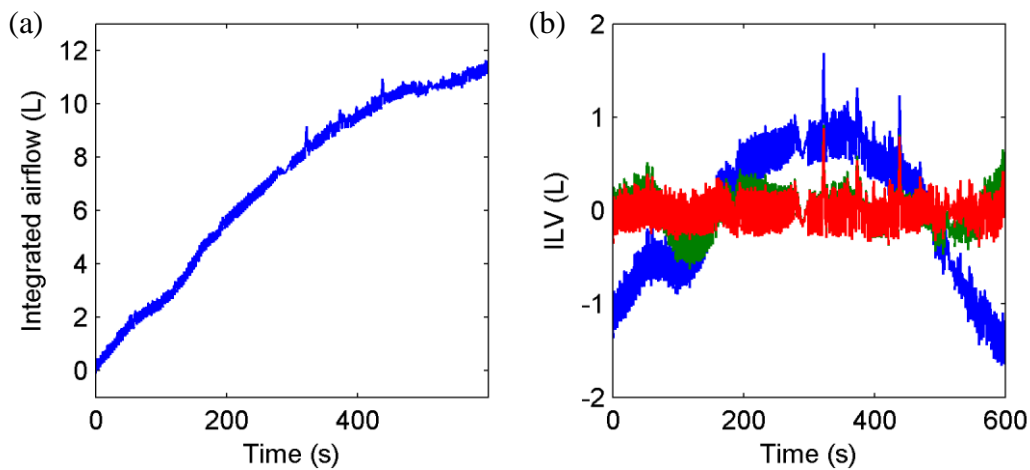


Figure 3.16 – Integrated airflow presenting a drift after integration (a) and the results after applying the detrending methods (b): linear detrend (blue), polynomial detrend of order 3 (green) and high-pass filter with cut-off frequency of 0.01 Hz (red).

Though the integration has the effect of a low-pass filter [75], some ILV data still present high-frequency noise after integration. If the data was acquired as volume directly, there may be some noise as well. Therefore, a low-pass filter with cut-off frequency ranging

from 1 to 4 Hz is provided for ILV if necessary. The effects of two different cut-off frequencies can be visually inspected through the GUI in comparison to the unfiltered signal to help set the value that is better adjusted for the data.

Figure 3.17 shows a raw airflow record (a), the integrated airflow before detrending (b) and the detrended ILV (c), as an example of transforming airflow (L/s) to ILV (L).

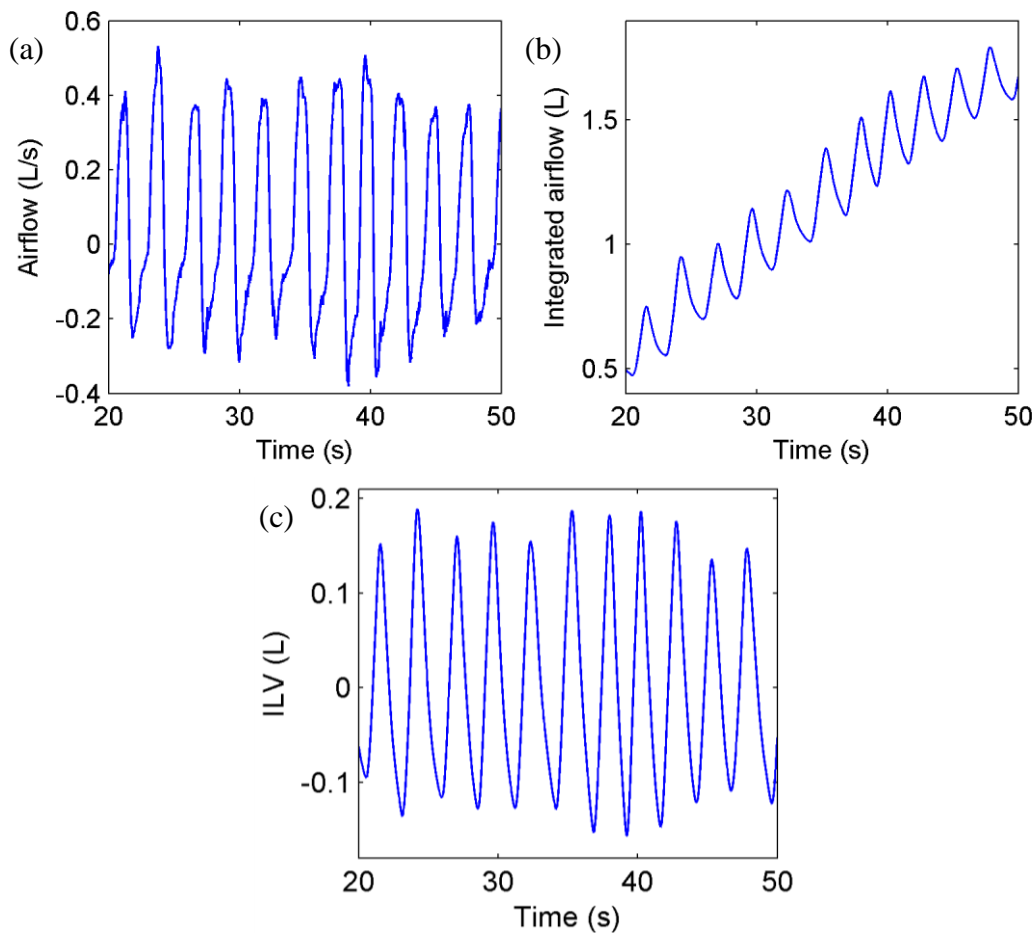


Figure 3.17 – The raw airflow (a), given in L/s, is integrated (b) to present volume information in L. The trend resulting from the transformation is removed, in this case using a 0.01 Hz high-pass filter, resulting in the instantaneous lung volume (c).

3.2.4. Align and resample data set

The RRI, SBP and DBP time series are points extracted from the ECG and continuous BP records that are unevenly sampled, as they occur on a varying beat-to-beat basis. As one RRI is only indicated at the instant of the R peak that ends the interval, the first SBP and DBP samples available always occur before the first RRI sample. The ILV record, on the other hand, is evenly sampled at a high sampling frequency, thus its first sample is available before and its last sample after any of the other data.

CRSIDLab has two analysis approaches available. The frequency domain PSD can be estimated using three different methods: the Fourier transform, the Welch method and the AR model. Both the Fourier transform and Welch methods apply the Fourier transform to the data, assuming it to be evenly sampled [5, 82, 83]. Time domain impulse response can be calculated from three different models: the AR/ARX model, the LBF model and the MBF model. These methods not only require the data to be evenly sampled, but for multivariate analysis assumes that all samples are aligned, meaning an index corresponds to the same time stamp for all data [14, 37]. The data set needs to be aligned and resampled in order to meet those requirements.

In this tab, the user can choose how to handle the ectopic beat related variables marked on the “Extract variables from ECG/BP” tab, as described in section 3.2.2, address the issues regarding the data borders that arise from the fact that the registers begin and end at different times and select one of the available methods for resampling the data. All of these features are detailed in the next sections. It is also possible to convert the RRI (ms) to HR (bpm) after resampling, which is done by adjusting the time scale and inverting the values.

3.2.4.1. Ectopic beats and corresponding BP variables

Ectopic beats do not result from the ANS modulation of HR and its effects are reflected in the BP data, both in timing and magnitude, as discussed in section 2.4.3. Though it is recommended that ectopic-free records are used, as editing may significantly alter PSD analysis [4], it is not always possible to get the necessary amount of data for a study where no ectopic beats happen.

If the user chooses to edit the ectopic beats or related BP variables, there are two options available. The first one is to remove those samples from the data, which may be the best approach if there is a large number of ectopic beats. The second one is to estimate those samples based on the neighboring ones using cubic splines interpolation, which is the usual approach [5, 82]. The time axis is also interpolated in order to fully correct the ectopic beat effects. Selecting any of these options updates the plots on the interface in real time, so that the results of applying each method can be evaluated before resampling.

Figure 3.18 shows an example of ectopic beats and corresponding SBP and the effects of applying each of the correction options. In all of the plots, the first ectopic beat and following compensatory pause are highlighted in yellow and the second in orange. Figure

3.18 (a,c,e) shows the RRI series while Figure 3.18 (b,d,f) show the corresponding SBP series. Figure 3.18 (a,b) show the RRI and SBP series without intervention. Figure 3.18 (c,d) shows the results from removing the ectopic variables. Finally, Figure 3.18 (e,f) shows the effects of applying cubic splines to estimate the variables.

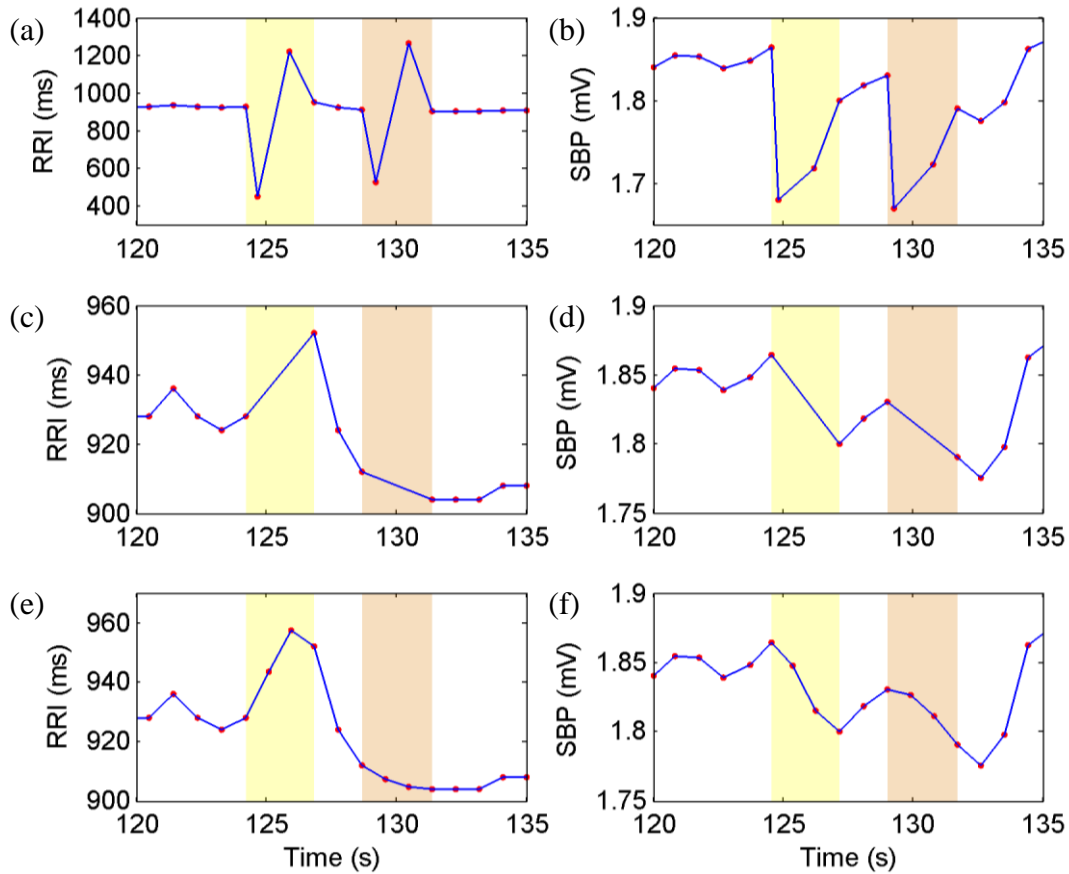


Figure 3.18 – Examples of the effect of ectopic beat related variables on RRI (a,c,e) and corresponding SBP (b,d,f) and the effects of the available correction methods. The yellow background highlights the first ectopic beat and related SBP, while the orange background highlights the second ectopic beat and related SBP. Ectopic beats as they present on RRI and SBP records (a,b), after removal (c,d) and after interpolation (e,f).

3.2.4.2. Data borders

There are two main issues regarding the data borders when aligning a data set: the fact that the records begin and end at different times and that some of the resampling algorithms cannot extrapolate the data, being unable to estimate the first and last samples.

Considering this scenario the user is given two tools. The first is to indicate the start and end points desired for the resampled data set. The start and end points can be selected as the first or last sample of one of the available variables. The end point can also be

determined by the desired number of samples. The points selected as start and end of the resampled data set are shown on the plots as vertical grey lines in real time to aid the user.

The second tool provides two methods to complete the data borders. The first option is called constant padding, where the edge sample is repeated until the necessary segment is completed. The second method is called symmetric extension, where the borders are mirrored at their limits, assuming that the variations around that edge values should be similar [84]. The border extension is also shown on the plots as a red continuance of the data for the data that have segments of missing borders in real time.

Figure 3.19 shows the first five seconds of a data set consisting of RRI, SBP and ILV with the data extensions in red, as shown on the GUI, showing RRI and SBP extension through constant padding (a) and symmetric extension (b). The grey line marks the latest starting variable, RRI, which could be used to truncate all variables.

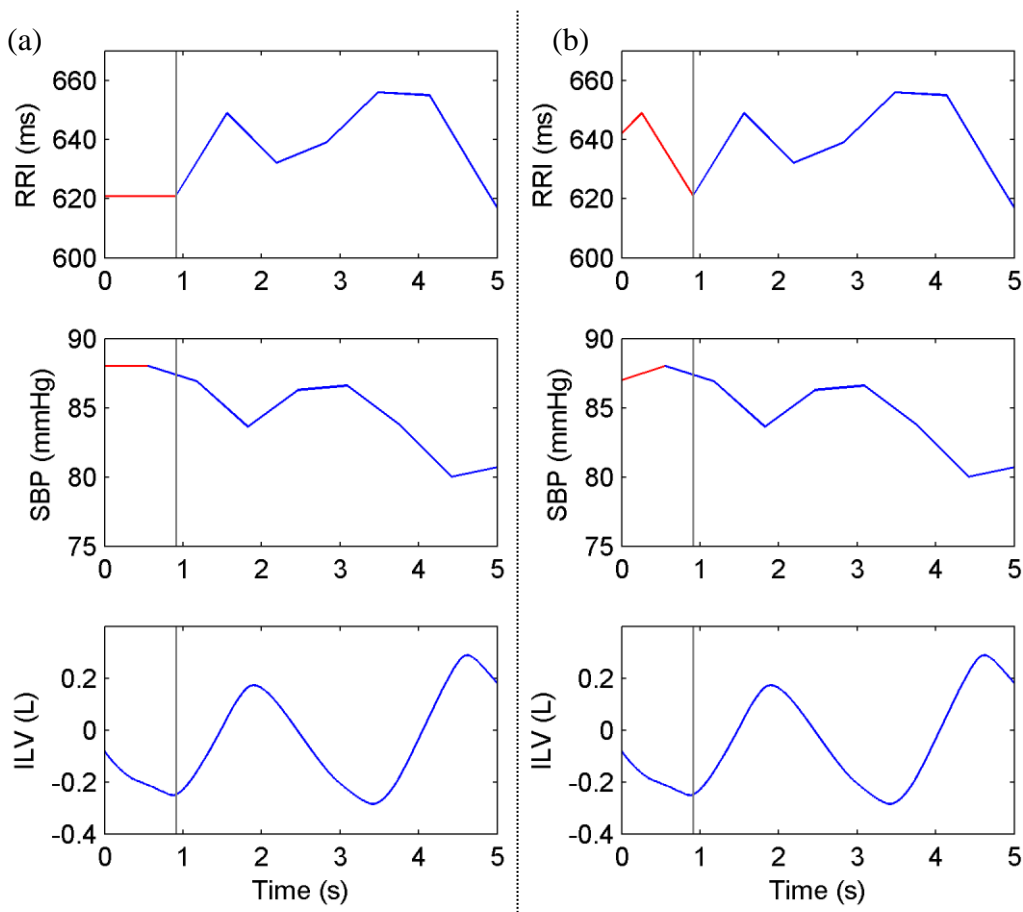


Figure 3.19 – Example of border gaps at the beginning of time aligned RRI, SBP and ILV records. The gaps in RRI and SBP are filled (red) using constant padding (a) and symmetric extension (b), while the grey line delimits the latest starting signal, RRI, which could be used as reference to truncate all records.

3.2.4.3. Resampling algorithms

Before addressing the resampling algorithms it is important to discuss the sampling frequency. The Nyquist criterion states that the sampling frequency should be at least twice the signals highest frequency for it to be well represented, therefore it is necessary to evaluate the HR of all subjects before selecting a sampling frequency. Most studies use frequencies from 2 to 4 Hz to resample the data, which assumes the highest HR to be 60 and 120 bpm respectively, but values as low as 1 Hz and as high as 10 Hz can be found in the literature [5], assuming the highest HR to range from 30 to 300 bpm. On that account, CRSIDLab allows the user to indicate a resampling frequency within this range.

The selected sampling frequency is used to create a new time vector, with time stamps that correspond to the position of the samples that must be estimated to generate the resampled data. This time vector is the same for all records being simultaneously processed, so that they also aligned in time.

Resampling the RRI time series may introduce undesirable artifacts to the analysis of the data, once the method employed makes an assumption regarding the relationship between points. Usually, this resampling is performed using linear or cubic splines interpolation [5, 82], and so both methods are available on the toolbox.

These techniques, however, have been shown to overestimate the LF components and underestimate HF components, leading to an overestimation of the LF/HF ratio. These effects are greater using linear interpolation and aggravated as the number of ectopic beats increase [82]. Berger *et al.* [85] proposed an algorithm for resampling RRI that was shown to produce a PSD estimate relatively free of artifacts when compared to other methods by using an integral pulse frequency modulation (IPFM) model. This algorithm is adapted in CRSIDLab to resample all unevenly sampled data, including SBP and DBP and is described below.

Resampling algorithm proposed by Berger et al

The traditional tachometer signal, as presented in Figure 3.20 (b) from the corresponding ECG in Figure 3.20 (a), is the equivalent of applying a zero-order hold to a sequence of inverse RRI, which can be performed in real time. This causes the step duration to be correlated to the previous RRI instead of the current one. DeBoer, Karemaker & Strackee [8] showed that this delay incurs in a biased estimate of the HR and can lead to phase shifts

in multivariate analysis. The algorithm proposed by Berger *et al.* [85] is based on a tachometer in which the inverse RRI is maintained for its own duration, avoiding these distortions [8]. This tachometer can be seen in Figure 3.21 (c), which illustrates the proposed algorithm and is further described ahead.

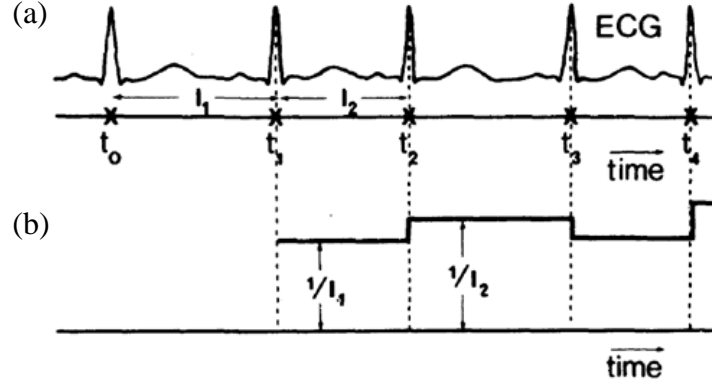


Figure 3.20 – ECG record (a) and the traditional tachometer generated from it (b), which is obtained by applying a zero-order hold to the RRI.

The discontinuities in the tachometers introduce artifacts that can be attenuated through a low-pass filter [8]. The Berger algorithm has the same result as applying the low-pass filter W , described as a function of the discrete frequency f by:

$$W(f) = \left[\frac{\sin(2\pi f / f_r)}{2\pi f / f_r} \right]^2, \quad (3.1)$$

which has an anti-aliasing effect, passing very little power over the Nyquist frequency $f_r/2$, where f_r is the chosen resampling frequency. This filtering process is equivalent to performing a convolution of the tachometer in Figure 3.21 (c) and a rectangular window of length $2/f_r$, however, the proposed algorithm avoids the convolution.

Initially, a window of length $2/f_r$ is centered at the sample that is to be estimated. The final value of the i^{th} HR sample, r_i , is given by

$$r_i = \frac{f_r}{2} \times n_i, \quad (3.2)$$

in which f_r is the selected resampling frequency and n_i is the number of RRIs inside the given window.

Figure 3.21 illustrates the algorithm highlighting the windows for estimating samples at the instants t_1 and t_2 . The window for estimating the sample at t_1 falls entirely within the

interval identified as I_2 and is of length a , where a is given in the same time unit as the RRIs. Therefore, the number of RRIs within this window is given by a/I_2 . Noting that the window length equals two sampling intervals, $2/f_r$, the final value for the sample at t_1 is then $1/I_2$, the inverse of the interval itself, by Equation (3.2). This HR signal is not scaled in beats per minute, but beats per second. The window centered at t_2 falls partly on interval I_3 and partly on the interval I_4 and so the number of RRIs is given by $b/I_3 + c/I_4$. Since both windows are the same length, $a = b + c = 2/f_r$.

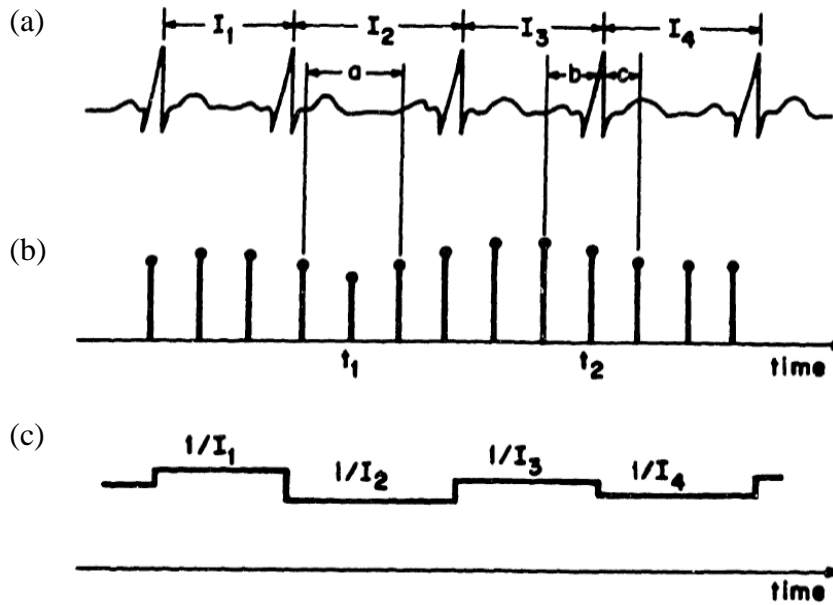


Figure 3.21 – Illustration of the algorithm proposed by Berger *et al.* [85] where evenly sampled HR (b) is derived from an ECG record (a) based on the tachometer (c). The number of beats in a window of length $a = 2/f_r$ is counted and then multiplied by $f_r/2$. For t_1 the number of beats is given by a/I_2 and for t_2 by $(b/I_3) + (c/I_4)$ (adapted from Berger *et al.*, 1986 [85]).

This algorithm was developed to generate an evenly sampled HR signal. On CRSIDLab it has been modified so that it can be used to resample RRI without necessarily converting it to HR and so the same logic can be applied to resampling SBP and DBP. The user can require the RRI to be converted to HR after resampling, which is done by taking its inverse and adjusting the time scale.

In this implementation, instead of counting the number of intervals and multiplying by half the resampling frequency, the i^{th} RRI sample r_i is given by taking the normalized lengths of the window segments that fall on different intervals and multiplying it by the corresponding intervals. Thus, in Figure 3.21 the window length is given by a and the

interval value at t_1 is $1 \times I_2$, which is the interval itself, as expected. At t_2 , however, there are two segments, b and c and so the interval value is given by $(b/a) \times I_3 + (c/a) \times I_4$, in which $(b + c)/a = 1$. This process is used for SBP and DBP as well.

Figure 3.22 shows an ECG record (a) with the R peak positions indicated by the dashed red lines and the corresponding tachometer (b, blue) and resampled RRI (b, green), as proposed by Berger *et al.* Figure 3.23 shows the continuous BP (blue) with the adapted tachometers for SBP and DBP (green) as well as the resampled SBP and DBP (red).

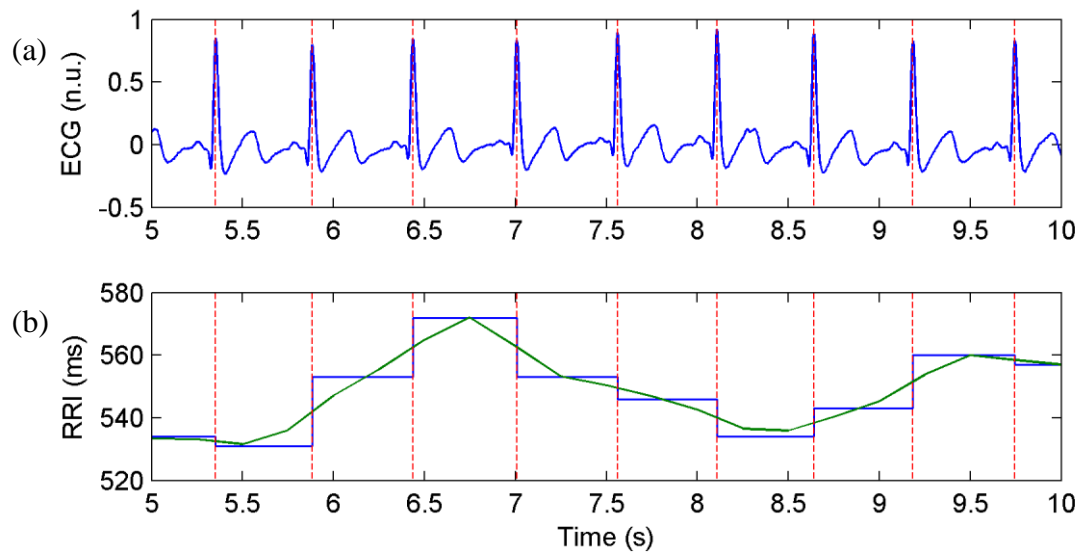


Figure 3.22 – ECG record (a) with the corresponding tachometer (blue) and resampled RRI (green) for $f_r = 4$ using the adapted Berger algorithm. The red dashed lines indicate the R-peaks position.

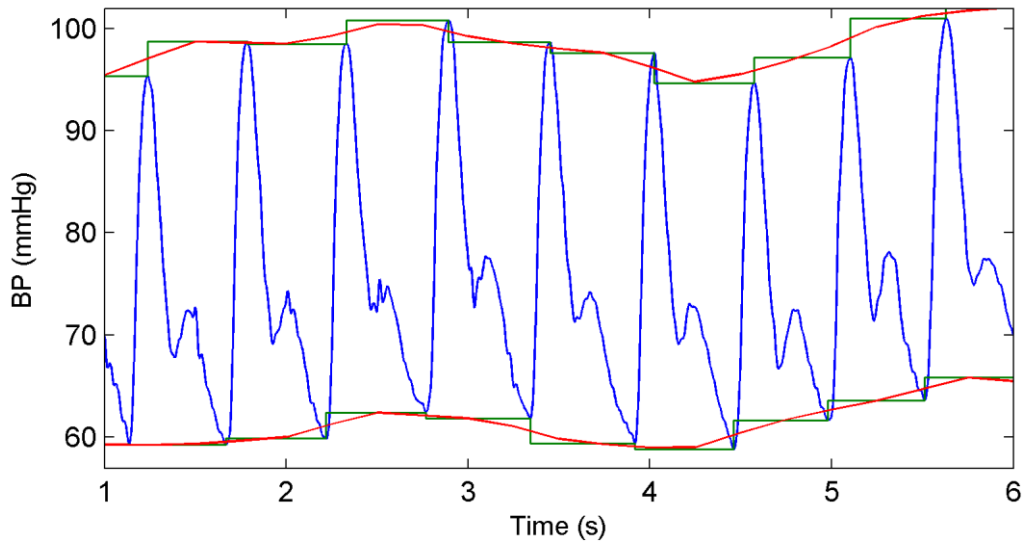


Figure 3.23 – Example of the adapted Berger algorithm used to resample SBP and DBP (red) extracted from the BP record (blue) and the equivalent adapted tachometers (green).

3.3. ANALYSIS

This section presents all methods available to perform the univariate PSD analysis as well as the univariate or multivariate system identification. To perform these analyses, the variables must be resampled and, for multivariate systems, time aligned.

3.3.1. Power Spectral Density

The PSD describes how the power of a given signal is distributed on a frequency spectrum. The PSD of the RRI provides a measure of HRV [5, 4, 14] while the PSD of variables related to BP, such as SBP and DBP, provide measures of BPV [67, 70, 86].

CRSIDLab presents three different methods for PSD estimation: the classic Fourier transform approach, the Welch method and the AR model. CRSIDLab has various window options, to address the issue of spectral leakage, further addressed in section 3.3.1.1.

The user can select any combination of PSD methods to be displayed simultaneously on the GUI, which makes it easier to select parameters for the AR model and Welch methods. Sections 3.3.1.2, 3.3.1.4 and 3.3.1.3 discuss the three methods for PSD estimation while section 3.3.1.5 presents the quantitative indicators derived from the PSD.

3.3.1.1. Windowing

The non-parametric methods are based on the Fourier transform, which assumes that the signals under analysis are infinite and periodic. However, only a finite part of a signal can be digitized and processed in a computer and this truncation introduces artifacts to the PSD estimation [5, 83, 87].

Windowing is performing the multiplication of a signal and a window in time domain, which is equivalent to convolution in the frequency domain. Truncating the signal can be interpreted as applying a rectangular window, of value 0 outside the duration of the records and value 1 for its duration, to the original infinite data. As the spectral components of the window show on the PSD of a signal, the discontinuities introduced to the data edges by such rectangular window produce spectral leakage, where the power of a given frequency leaks to the nearby frequencies [83, 87].

For a window to cause no alteration to the PSD of a signal, it would have to have a unit impulse spectrum. Windows other than the rectangular window might help attenuate the discontinuity of the edges. By comparing the frequency response of a window to a unit impulse it is possible to evaluate how it affects the PSD of that signal. The larger the mainlobe, the more neighboring frequencies are averaged together, resulting in a lower resolution PSD with less defined peaks. The sidelobes determine how much distant frequencies are merged into the PSD. Therefore, a window of narrow mainlobe and low sidelobes would be preferred [87].

CRSIDLab has five window options: rectangular, Bartlett, Hanning, Hamming and Blackman. Time and frequency representations of these windows are presented in Figure 3.24 (a) through (d), respectively.

While the rectangular window presents the narrowest mainlobe, it also has the least sidelobe attenuation. The Blackman window, on the other hand, offers the greatest sidelobe attenuation, however it also has the largest mainlobe. While choice of window is a tradeoff, it has little effect on HRV analysis [83].

On CRSIDLab a window is applied to the whole signal before performing PSD estimation using the Fourier transform method and a window is applied to each segment of the data before performing PSD estimation using the Welch method.

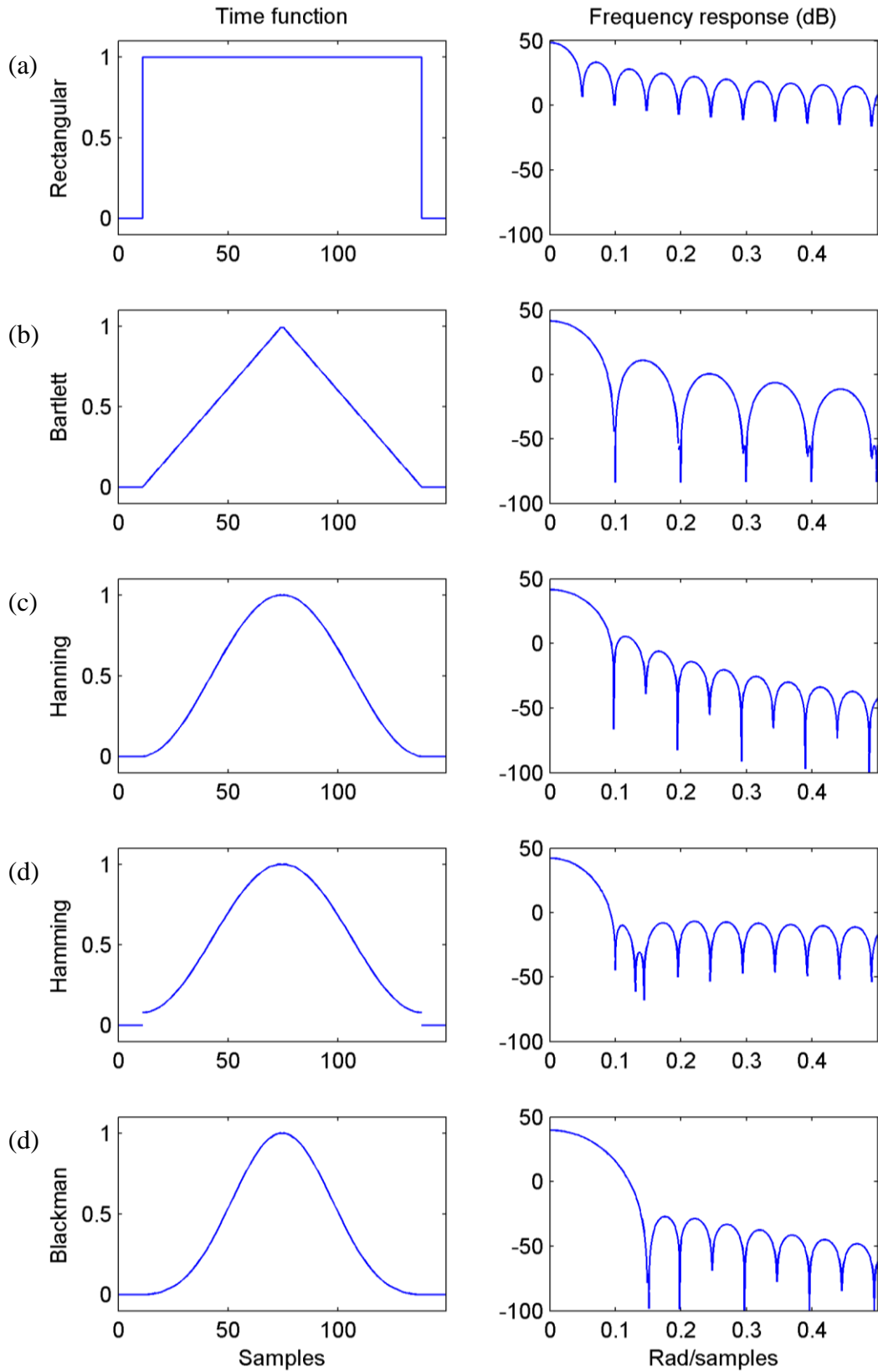


Figure 3.24 – Time function and frequency response of the available windows: (a) rectangular, (b) Bartlett, (c) Hanning, (d) Hamming and (e) Blackman.

3.3.1.2. Fourier Transform

The autocorrelation of a signal represents how the signal correlates with lagged versions of itself, providing information on the characteristics of that signal. The autocorrelation function has maximum value at 0 lags and is symmetrical in relation to 0 lags. Signals that vary rapidly and have short memory will present autocorrelation functions that approach an impulse, as is the case with white noise, while signals with longer memories will present broader autocorrelation functions [88]. The expected value of a wide sense stationary (WSS) process can be represented by its time average and so the autocorrelation function r_{xx} for a discrete WSS signal x of N samples can be expressed as a function of the discrete index k by:

$$r_{xx}(k) = \frac{1}{N} \sum_{n=1}^N x(n)x(n+k). \quad (3.3)$$

The PSD, S_{uu} , is defined as the Fourier transform of the autocorrelation function of a signal [87] and so can be estimated for discrete frequency values f through

$$\hat{P}(f) = S_{uu}(f) = \sum_{k=1}^N r_{xx}(k) e^{-\frac{j2\pi f k}{N}}, \quad f = 0, \dots, N/2, \quad (3.4)$$

where \hat{P} is the estimated PSD and j is the imaginary unit. By expanding Equation (3.4) with the autocorrelation function in Equation (3.3) and manipulating the expression, it becomes

$$\begin{aligned} \hat{P}(f) &= \frac{1}{N} \sum_{k=1}^N \sum_{n=1}^N x(n)x(n+k) e^{-\frac{j2\pi f k}{N}} \\ \hat{P}(f) &= \frac{1}{N} \sum_{k=1}^N x(n+k) e^{\frac{j2\pi f (n-k)}{N}} \sum_{n=1}^N x(n) e^{-\frac{j2\pi f n}{N}} \\ \hat{P}(f) &= \frac{1}{N} X^*(f)X(f) = \frac{1}{N} |X(f)|^2, \end{aligned} \quad (3.5)$$

where X is the Fourier transform of the signal x and X^* its complex conjugate. Equation (3.5) is usually the operation performed for PSD estimation using the fast Fourier transform (FFT) algorithm. This PSD is also called a periodogram [89].

The real spectral resolution, or the distance between each frequency point on the frequency axis of a Fourier transform PSD, Δf , is determined by the number of samples of the signal, N , and its sampling frequency, f_s , as:

$$\Delta f = \frac{f_s}{N}. \quad (3.6)$$

This resolution can be increased by calculating the FFT over a greater number of points. To be able to use more points than the signal has, zero-padding is performed, considering the data outside of the sampled window to be zero. This increase in resolution is then obtained by interpolation on the estimation process and is only apparent, as it does not add any new information, but does produce better looking spectra [87].

If the signal is windowed before applying the FFT, the resulting PSD is called a modified periodogram. In the modified periodogram, the Fourier transform of a signal windowed by a window w through time-domain convolution or frequency-domain multiplication is calculated [89]. This modified periodogram, \hat{P}_M , is expressed as

$$\hat{P}_M(f) = \frac{1}{NU} \left| \sum_{n=1}^N x(n)w(n)e^{-j2\pi fn} \right|^2, \quad f = 0, \dots, N/2. \quad (3.7)$$

The window introduces a bias to the periodogram, which is corrected by the added constant term

$$U = \frac{1}{N} \sum_{n=1}^N |w(n)|^2. \quad (3.8)$$

The frequency resolution then becomes dependent on the chosen window, with windows of larger mainlobes and reduced sidelobes leading to a smoother PSD, however of lower resolution [89].

In CRSIDLab the user can indicate the number of points for the Fourier transform. The software suggests a value that is the next power of two from the signals length, since FFT performs faster in such case [87].

3.3.1.3. Welch method

The Welch method produces a smoother PSD by taking the Fourier transform PSD of possibly overlapping segments of the signal and then averaging these PSDs at each

frequency point [90]. This spectrogram better reflects the global characteristics of that signal and has greater statistical reliability than the Fourier transform PSD [87].

To perform the Welch method, the selected window is applied to each segment before computing that segment's modified periodogram using the Fourier transform. For a signal of length N , if each segment has L samples and an offset of D samples between segments (resulting in $L - D$ overlapping samples), the number of segments, K , is given by:

$$K = \frac{N - L}{D} + 1. \quad (3.9)$$

The Welch PSD can be expressed both explicitly and in terms of the modified periodogram \hat{P}_M , described by Equation (3.7), calculated for each set of L samples with D overlapping samples [89], as:

$$\hat{P}_W(f) = \frac{1}{KLU} \sum_{i=1}^K \left| \sum_{n=1}^L x(n + iD)w(n)e^{-j2\pi fn} \right|^2 = \frac{1}{K} \sum_{i=0}^K \hat{P}_M^{(i)}(f). \quad (3.10)$$

As the Fourier transform is performed on each segment of length L the frequency resolution would then be as indicated by Equation (3.6) for $N = L$, if a rectangular window is used. Since L is necessarily smaller than N , this results in a reduced frequency resolution when compared to the Fourier transform PSD [89, 91]. However, the apparent resolution can be improved by calculating the transform of each segment using a greater number of points through zero-padding. If another window is used, then the frequency resolution depends on the window.

In CRSIDLab the user can indicate the number of samples of each segment and the number of overlapping samples, besides the number of points for the Fourier transform.

3.3.1.4. AR model

The Fourier transform does not consider the fact that the signal used to estimate the PSD usually contains noise, incorporating the noise characteristics into the PSD [91]. A parametric approach based on a model produces a smoother PSD estimate and, since the PSD is derived from the model, produces accurate estimates even when there are a small number of samples, which may be necessary to ensure stationarity [4].

The AR model is suitable for narrowband signals [91] and widely applied to HRV analysis [22, 70, 86]. It can be represented by

$$y(k) = - \sum_{n=1}^{na} a_n z^{-n} y(k) + e(k), \quad (3.11)$$

in which y is the signal as a function of the discrete index k , e represents the noise function, z^{-1} is the discrete backwards shift operator, na is the model order and a_n are the coefficients that need to be estimated to determine the model.

The AR model may also be expressed as an all-pole filter [86] with transfer function

$$H(z) = \frac{1}{1 + \sum_{n=1}^{na} a_n z^{-n}}. \quad (3.12)$$

Once the coefficients are estimated, the AR model PSD, \hat{P}_{AR} , is described as a function of the coefficients or as a function of the filter transfer function by:

$$\hat{P}_{AR}(f) = \frac{\hat{\sigma}^2}{|1 + \sum_{n=1}^{na} \hat{a}_n e^{-j2\pi f n}|^2} = \hat{\sigma}^2 \cdot |H(z)|^2, \quad (3.13)$$

in which $\hat{\sigma}^2$ is the estimated variance of the white noise input and \hat{a}_n are the estimated model coefficients [14, 89, 92].

There are several different methods that can be used to estimate the AR coefficients, such as the Yule-Walker, the covariance, the modified covariance and the Burg methods. CRSIDLab employs the Burg method that finds the coefficients by minimizing the sum of the squares of forward and backward prediction errors and ensures model stability by performing the minimization sequentially in respect to the reflection coefficients [89].

The AR PSD resolution using the Burg method does not depend on the signal length or the window employed, as is the case with the non-parametric methods, once the PSD is generated from the model and the Burg method does not require windowing, as is the case with the Yule-Walker method [89, 91]. Therefore, the resolution can be as high as desired by controlling the number of points for Fourier transform calculation [83].

In CRSIDLab, the user can indicate the order for the AR model to be estimated. To select the ideal order, it may be advisable to go to the system identification tab to estimate an AR model from a range of orders using one of the criteria available for optimization and then return to perform the PSD with the selected order.

3.3.1.5. Quantitative indicators

The quantitative indicators calculated from the PSD using any of the methods described are given as the power for three frequency ranges (VLF, LF and HF) and includes the total power, which is the sum of the three, and the LF/HF ratio. The power is calculated as the area under the PSD curve. The default values defining those frequency bands are the ones recommended by the Task Force on HRV standards of measurement, physiological interpretation, and clinical use [4] and used in many studies [26, 64, 65, 82], with VLF ranging from 0 to 0.04 Hz, LF from 0.04 to 0.15 Hz and HF from 0.15 to 0.4 Hz. These values, however, can be edited by the user, as other frequency ranges have been described and used in studies [6, 70, 93].

The areas are presented in three different units: as absolute power, given in the squared unit of the signal under analysis; relative power, given as a percentage of the total power; and normalized power of LF, LF_n , and HF, HF_n , obeying the rule $LF_n + HF_n = 100$.

These quantitative indicators are stored to the patient file but can also be exported to a text file. This text file is formatted to be imported to spreadsheets, using tab as a separator.

Figure 3.25 shows an example of HRV estimate through the PSD of a RRI record using the Fourier transform (blue), the Welch method (green) and the AR model (black). Table 3.1 shows all of the quantitative indicators generated from the estimates.

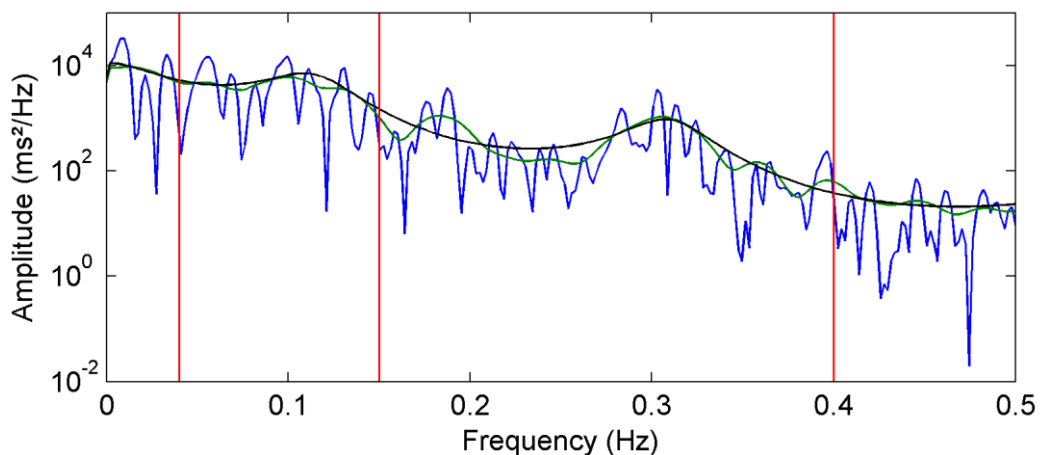


Figure 3.25 – Example of HRV estimates as the PSD of and RRI using the Fourier transform with 2048 points using a Hanning window (blue), the Welch method with 256 samples per segment and 50% overlap using a Hanning window (green) and an AR model of order 20 (black). The red lines delimit the frequency bands of interest: very low frequency (VLF: 0-0.04 Hz), low frequency (LF: 0.04-0.15 Hz) and high frequency (HF: 0.15-0.4 Hz).

Table 3.1 – Quantitative indicators extracted from the PSDs of an RRI series, presented in Figure 3.25. The absolute (ms^2), relative (%) and normalized areas of the very low frequency (VLF: 0-0.04 Hz), low frequency (LF: 0.04-0.15 Hz) and high frequency (HF: 0.15-0.4 Hz) as well as the total area (0-0.4 Hz) are provided along with the LF/HF ratio for the PSDs calculated from the Fourier transform (FFT), the Welch method and AR model.

Method	Units	Total	VLF	LF	HF	LF/HF
FFT	Absolute (ms^2)	994.4792	395.144	492.8588	106.4765	
	Relative (%)	100	39.734	49.599	10.707	4.6288
	Normalized	1	-	82.234	17.766	
Welch	Absolute (ms^2)	868.8014	304.435	461.4905	102.8759	
	Relative (%)	100	35.041	53.118	11.841	4.4859
	Normalized	1	-	81.771	18.229	
AR model	Absolute (ms^2)	962.3406	321.3646	534.2732	106.7029	
	Relative (%)	100	33.394	55.518	11.088	5.0071
	Normalized	1	-	83.353	16.647	

3.3.2. System Identification

CRSIDLab allows multiple systems to be created from the same data set, with any combination of variables, and multiple models to be estimated for each system, using different methods and parameters. Therefore, the system identification process is divided in two steps: creating a system and estimating a system model. Each step is described in the following sections.

3.3.2.1. Create a new system

The first step to creating a new system is to determine the system variables. CRSIDLab lists the available aligned and resampled variables in three different popup menus: one for the output variable, one for the first input variable and one for the second input variable, as indicated on the interface. To ensure a valid system is created, the output variable must be indicated first, followed by the first and second inputs, if desired. The following topics discuss the issues that must be observed when creating a new system.

Model validation

When estimating a model from a range of parameters, CRSIDLab uses the cross-validation approach, in which only a part of the system is used to estimate the coefficients that determine the model, hereafter referred to as estimation data. The remaining part of the data set, the validation data, is used to simulate the model and the mean squared error (MSE) between the measured and the predicted output is calculated from the validation

data set. Finally, a criterion is used to select the optimum model based on this error estimate. This process avoids over-parametrization and modeling noise [94, 95].

Thus, after selecting the variables to compose a system, the percentage of data for model estimation can be indicated. It is possible to set 100% of the data as estimation data, in which case cross-validation is not performed. It is possible to create multiple systems consisting of the same combination of variables but with different portions for the estimation and validation data sets on CRSIDLab.

Noise and Stationarity

Once the validation and estimation data sets are determined, a 0.5 Hz low-pass Kaiser filter (passband 0-0.5 Hz, stopband 0.7-1 Hz and less than 0.01 ripple in both bands) can be applied to remove high-frequency noise, considering that the cardiorespiratory dynamics of interest fall within this range [14, 19].

Slow trends should be removed from the data before system identification to avoid overestimation of LF power and ensure stationarity [95]. Though short-term records, ranging from 2 to 5 min, can be considered stationary [4], CRSIDLab does not restrict data length, allowing the analysis of longer records. Hence, a polynomial detrend can be performed before moving on to the analysis.

Cardiovascular variability is a small signal study, focusing on variations around a basal value [96] and for the model estimation to be successful, the offset component needs to either be removed from the estimation data set or expressed explicitly in the model, which is unnecessarily complicated [97]. Thus, whether polynomial detrending is applied or not, the mean is removed from the signals. Also for this reason, detrending is only performed after the validation and estimation data sets are specified, so that the sets can be detrended separately, ensuring the estimation data has zero mean.

Once a system is created, system identification using one of the available parametric models can be performed. If the system has no input variables, the only model available is the AR model. If the system has at least one input, then there are three model options: the ARX, LBF and MBF models. Each of these models is discussed in the following sections.

3.3.2.2. Autoregressive model with exogenous inputs

The ARX model can be interpreted as a simplification of the Box-Jenkins model that assumes that the input(s) and the noise present in the system are filtered by the same dynamics, which happens when noise is introduced to a closed-loop system [98]. The ARX model is sometimes called an AR with moving average (ARMA) model, considering the moving average applied to the exogenous input [24]. Many studies have employed this model, either identified as ARX or ARMA, to characterize cardiorespiratory dynamics [14, 24, 23, 64, 65, 99, 100].

Figure 3.26 shows a block diagram of a two-input ARX model, where the difference equations are represented by the polynomials A , B_1 and B_2 in the z -domain, z^{-1} is the backwards shift operator and k is the discrete time index [98]. The variables u_1 and u_2 are the inputs, while e is an error component and y is the output. For a single input ARX model the u_2 input and the corresponding block are removed, while for an AR model u_1 , u_2 and the corresponding blocks are removed.

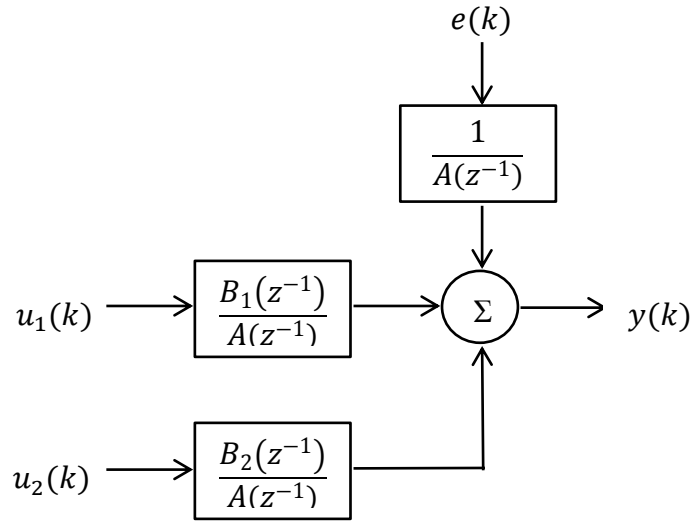


Figure 3.26 – Block diagram of a two-input ARX model.

The ARX model in Figure 3.26 can be described through

$$A(z^{-1})y(k) = B_1(z^{-1})u_1(k) + B_2(z^{-1})u_2(k) + e(k), \quad (3.14)$$

in which the polynomial $A(z^{-1})$ is given by

$$A(z^{-1}) = 1 + a_1z^{-1} + \dots + a_{na}z^{-na} \quad (3.15)$$

and the polynomials $B_1(z^{-1})$ and $B_2(z^{-1})$ are of the format

$$B(z^{-1}) = b_0 + b_1z^{-1} + \dots + b_{nb}z^{-nb}. \quad (3.16)$$

In Equations (3.15) and (3.16), na and nb are the orders of the polynomials and $a_i, i = 1, \dots, na$ and $b_j, j = 0, \dots, nb$ are the coefficients that need to be estimated. For a two-input system, different orders may be selected for each input.

In systems with exogenous inputs it is also possible to include a delay, allowing the description of causal relationships between the variables, which enables the separation of feedforward and feedback components [14, 23, 24]. This might be interpreted as a computational way of opening the loop, since all records are acquired at a closed-loop condition [21]. Each output sample can be described as a function of past output samples and delayed input samples, with nk_1 and nk_2 representing the delays from each input and nb_1 and nb_2 their respective orders, as

$$y(k) = \sum_{n=0}^{nb_1} b1_n z^{-n} u_1(k - nk_1) + \sum_{n=0}^{nb_2} b2_n z^{-n} u_2(k - nk_2) - \sum_{n=1}^{na} a_n z^{-n} y(k) + e(k). \quad (3.17)$$

3.3.2.3. Orthogonal basis function models

Another model structure that can be considered for cardiorespiratory system estimation is the finite impulse response (FIR) filter models. FIR filter models are similar to ARX models where the autoregressive polynomial $A(z^{-1}) = 1$ [98]. The FIR model structure for systems with two inputs is shown in Figure 3.27 and described mathematically by:

$$y(k) = \sum_{n=0}^{nb_1} b1_n z^{-n} u_1(k - nk_1) + \sum_{n=0}^{nb_2} b2_n z^{-n} u_2(k - nk_2) + e(k), \quad (3.18)$$

where the output signal y is described as a function of the discrete index k , e is the error component, inputs u_1 and u_2 have corresponding orders nb_1 and nb_2 and associated delays nk_1 and nk_2 with the coefficients $b1_n$ and $b2_n$ to be estimated.

The FIR model structure, illustrated in Figure 3.27, is linear in its parameters, as is the ARX model structure, which means that the coefficients can be estimated through a least-squares approach. The FIR model structure also presents independent parametrizations of the process and noise, which is not true for the ARX model since the AR term

characterizes both dynamics. This property eliminates bias introduced to the process model due to the noise component, but typically increases the order needed to characterize the system's dynamics [101].

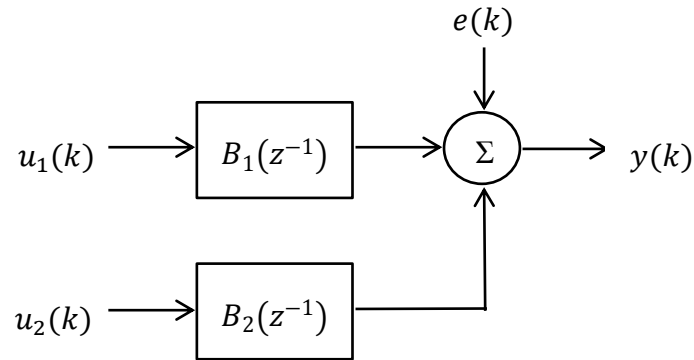


Figure 3.27 – Block diagram of a two-input FIR model.

The FIR model filter bank is typically of the form z^{-1} , which is a short memory filter, requiring high orders to describe the system's dynamics. The necessary order to describe a system can be reduced by employing a more complex filter bank, with longer memory, reducing the variance of the estimate [102, 103]. The selection of orthogonal basis functions (OBF) as filter banks provide models that are robust even to colored noise [104]. Thus the modified FIR model, or linear OBF model is shown in Figure 3.28

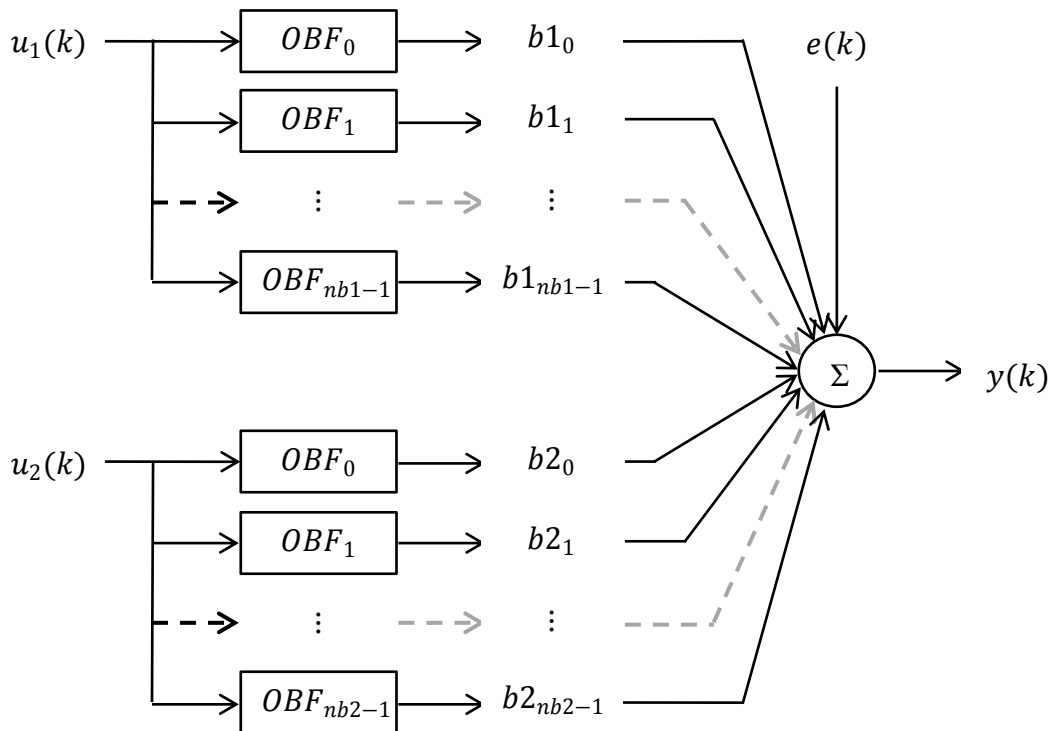


Figure 3.28 – Block diagram of the linear Orthogonal Basis Functions model.

The linear OBF model is described by:

$$\begin{aligned}
y(k) = & \sum_{i=0}^{M-1} \sum_{n=0}^{nb_1-1} b1_n OBF_n(z) * u_1(k - i - nk_1) \\
& + \sum_{i=0}^{M-1} \sum_{n=0}^{nb_2-1} b2_n OBF_n(z) * u_2(k - i - nk_2) + e(k),
\end{aligned} \tag{3.19}$$

in which M is the system memory length, describing the length of the impulse response, nb_1 and nb_2 represent the number of basis functions used to represent the data and OBF_n is the n^{th} order OBF. The choice of appropriate OBFs, with a morphology that is compatible with the underlying dynamics, requires a small number of functions to represent the system and allows accurate model estimates from a reduced number of samples [102]. There are two sets of OBFs available in CRSIDLab, the LBF and MBF, described below.

- Laguerre Basis Functions (LBF)

LBFs behave in a way that is compatible with physiological systems response, oscillating with a gradual decrease in amplitude until stabilizing at zero [102]. The discrete k^{th} order LBF is as described by:

$$L_k(z) = \frac{z\sqrt{1-p^2}}{z-p} \left(\frac{1-pz}{z-p} \right)^k, \tag{3.20}$$

in which p ($0 < p < 1$) is a pole that can be adjusted to determine longer and more oscillating the responses as it approaches the maximum limit [105]. Figure 3.29 illustrates the effects of the pole parameter by showing the first five LBFs (orders 0 to 4) for a pole of 0.6 (a) and 0.8 (b). In CRSIDLab the Laguerre functions are generated recursively from the zero order function, by multiplying the exponential term.

- Meixner Basis Functions (MBF)

LBFs start off from non-zero values, which may not be optimal for physiological systems with slower responses. The MBFs are a set of basis functions that introduce an extra parameter to the LBF set that determines how late the functions start to fluctuate, providing the desired slow initial onset. This extra parameter is called the generalization order and, when its value is set to zero, the MBF set is identical to the LBF set [19, 102]. Figure 3.30 illustrates the first 5 MBFs (orders 0 to 4) for the generalization orders of 1 (a) and 5 (b) with a fixed pole value of 0.8.

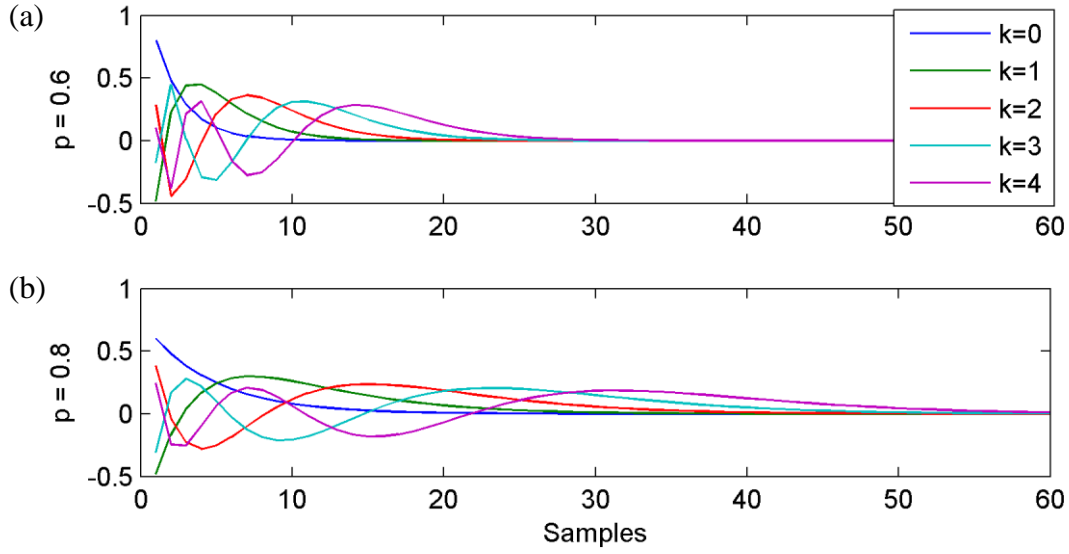


Figure 3.29 – Laguerre basis functions of order k ranging from 0 to 4 for $p = 0.6$ (a) and $p = 0.8$ (b). A pole value closer to 1 yields a longer settling time for the basis function set.

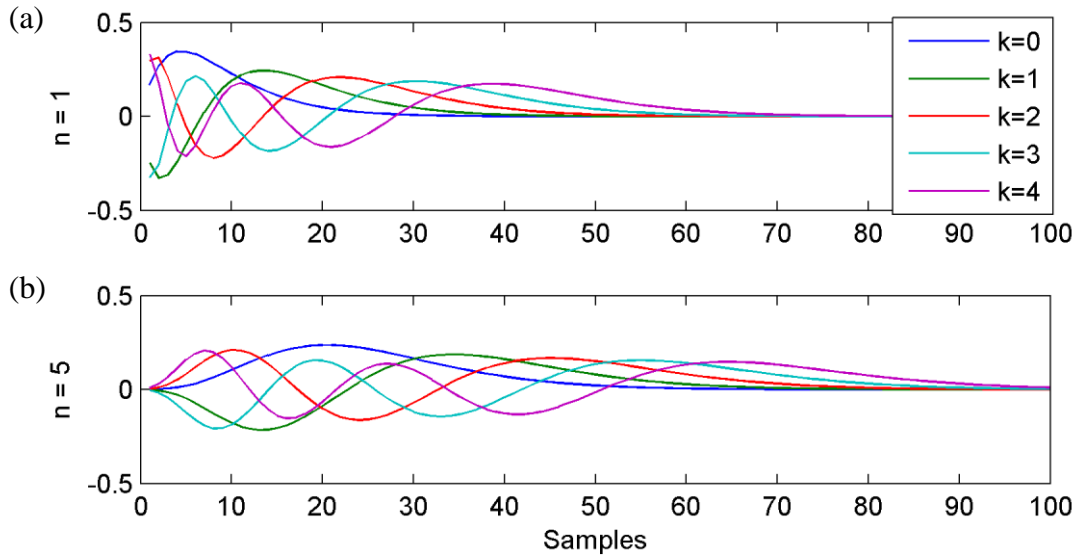


Figure 3.30 – Meixner basis functions for $p = 0.8$ with orders k ranging from 0 to 4 for generalization order $n = 1$ (a) and $n = 5$ (b). Higher generalization orders cause the basis function set to have a slower initial onset.

Though LBFs have a rational z -transform, the same cannot be said for other MBFs and so, in CRSIDLab, Meixner-like functions are implemented from an orthogonal transformation of the LBFs as proposed by Den Brinker [105]. To generate k Meixner-like functions of generalization order n , $k + n + 1$ LBFs must be multiplied by the transformation matrix

$$A^{(n)} = \{chol(U^n\{U^n\}^T)\}^{-1}U^n, \quad (3.21)$$

in which U is the square matrix of dimensions $k + n + 1$

$$U = \begin{bmatrix} 1 & p & 0 & \dots & 0 \\ 0 & 1 & p & \dots & 0 \\ 0 & 0 & 1 & \dots & 0 \\ \vdots & \vdots & \vdots & \ddots & \vdots \\ 0 & 0 & 0 & \dots & 1 \end{bmatrix}, \quad (3.22)$$

and p is the same pole used to generate the LBFs. The Cholesky factorization indicated in Equation (3.21) produces a lower triangular matrix and the final transformation matrix $A^{(n)}$ is of dimensions $k \times (k + n + 1)$.

Inputs decorrelation for OBF models

When ILV and a BP variable are inputs and RRI or HR is the output of a system, the inputs are coupled through the mechanical effects of respiration on BP, as can be seen on the cardiorespiratory system model described in section 2.4.5 and shown in Figure 2.10. In this case, a three-step procedure is used as an attempt to uncouple the effects of the interaction between the input variables and thus improve model accuracy [19].

The first step is to remove the effects of ILV on BP, which may be represented by SBP or DBP variables. An ARX model with ILV as input and BP as output is estimated, with no delay and orders that are the equivalent to the range of 1.5 to 5 seconds, adjusted according to the sampling frequency. This model is then used to estimate the BP from ILV and the resulting BP is subtracted from the measured BP, generating a BP uncorrelated with the ILV, BP_{unc} . A temporary OBF model is then estimated with the parameters chosen by the user, having ILV and BP_{unc} as inputs and RRI or HR as output.

The second step is to use the temporary model to estimate the part of the RRI or HR that is explained by BP_{unc} and remove it from the RRI or HR. This new variable is identified as RRI_{ILV} or HR_{ILV} . Then an OBF model is estimated from a system that has ILV as input and RRI_{ILV} or HR_{ILV} as output.

This model is used to estimate RRI_{ILV} or HR_{ILV} from ILV and subtract this predicted output from RRI or HR, resulting in a new variable called RRI_{BP} or HR_{BP} . Finally, an OBF model is estimated from a system that has BP as input and RRI_{BP} or HR_{BP} as output.

All the models estimated on this three-step process are estimated through a least-squares approach, further described in section 3.3.2.4, and selected from a range of parameters using some criterion chosen by the user. The final model is given by the combination of

the coefficients found from the relation between ILV and RRI_{ILV} or HR_{ILV} , characterizing RCC, and from the relation between BP as input and RRI_{BP} or HR_{BP} , characterizing ABR.

3.3.2.4. Model estimation: least-squares minimization

For output-only systems, the AR model coefficients are estimated using the Burg method, described in section 3.3.1.4, for a given model order. If a two input model is estimated, with the exception of the system with ILV and BP as inputs for the OBF case (section 3.3.2.3), a single input model is estimated from the first indicated input to the output, the influence from this input is removed from the output, and a single input model is estimated from the second indicated input to the modified output.

The ARX and OBF coefficients are estimated using least-squares minimization for a given order, in the ARX case, or number of basis functions, in the OBF case. A model can be described in the matrix form

$$y = \Phi\theta + e \quad (3.23)$$

if it is a linear function of its parameters [106, 107]. In Equation (3.23), y is the system output, Φ is the regression matrix with the samples from the inputs and output that compose the output signal, θ is a vector with the parameters to be estimated and e is the error component. Considering a single-input ARX model, Φ becomes

$$\Phi(k, :) = [-y(k-1) \quad \dots \quad -y(k-na) \quad u(k-nk) \quad \dots \quad u(k-nk-nb)], \quad (3.24)$$

where the number of columns is the number of parameters to be estimated. The corresponding θ vector is then given by

$$\theta = [a_1 \quad \dots \quad a_{na} \quad b_0 \quad \dots \quad b_{nb}]^T. \quad (3.25)$$

For OBF functions the output is not formed by samples of the inputs and output, but by a combination of filtered versions of each input, filtered using OBFs of different orders. In this case, Φ becomes the matrix

$$\Phi = [u_1^{(0)T} \quad \dots \quad u_1^{(nb1-1)T} \quad u_2^{(0)T} \quad \dots \quad u_2^{(nb2-1)T}], \quad (3.26)$$

in which each column represents a filtered input and the order of the basis function used to filter the input is indicated in parenthesis as superscripts. The number of columns still represents the number of parameters to be estimated and the corresponding θ vector is given by

$$\theta = [b1_0 \quad \dots \quad b1_{nb1-1} \quad b2_0 \quad \dots \quad b2_{nb2-1}]^T. \quad (3.27)$$

For OBF functions the values nb_1 and nb_2 represent the number of basis functions used, instead of the order as is the case with ARX, which is why the parameters indexing range from 0 to $nb_1 - 1$ or $nb_2 - 1$, representing the order of OBFs.

Least-squares minimization consists of minimizing the MSE between the measured and predicted outputs. MSE can be described as a function of the selected model, M , the parameters θ and the inputs represented by u [106] as:

$$V_N(M, \theta, u(k)) = \frac{1}{N} \sum_{k=1}^N [y(k) - \hat{y}(\theta, k)]^2, \quad (3.28)$$

where \hat{y} is the predicted output. If the model output is a linear function of its parameters, the MSE can be rewritten as:

$$\begin{aligned} V_N(\theta) &= \frac{1}{N} (y - \Phi\theta)^T (y - \Phi\theta) \\ &= \frac{1}{N} (y^T y - 2\theta^T \Phi^T y + \theta^T \Phi^T \Phi \theta). \end{aligned} \quad (3.29)$$

To minimize the MSE, it is derived in relation to θ and set equal to zero, resulting in

$$\begin{aligned} \frac{\partial V_N}{\partial \theta} &= \frac{2}{N} (\Phi^T \Phi \theta - \Phi^T y) = 0 \\ \Phi^T \Phi \theta &= \Phi^T y \\ \hat{\theta} &= (\Phi^T \Phi)^{-1} \Phi^T y, \end{aligned} \quad (3.30)$$

where $\hat{\theta}$ is the vector of estimated coefficients. This is the analytical form of finding the best estimate for the model coefficients for given orders or numbers of basis functions and delays.

3.3.2.5. Model optimization

In CRSIDLab the user can select the orders, numbers of basis functions and delays to generate a model estimate, but it is also possible to indicate a range of parameters to be tested so that the optimal model can be selected.

If that is the case, the model coefficients θ are calculated for each possible combination of parameters using the estimation data set and then the cost function, the MSE given by

Equation (3.29), is calculated for the validation data set. This is the cross-validation approach discussed in section 3.3.2.1, which results in more accurate models [94, 95].

Some criterion can then be used to select the optimal model based on the cost function. The simplest criterion is to select the model that minimizes the cost function, without taking the model complexity into account. This criterion is available in CRSIDLab and is called “Best fit”. This approach, however, may lead to overfitting, incorporating noise to the modeled output [108]. Therefore, it is interesting to use a criterion that penalizes model complexity, lowering the variance of the model estimation [109]. As several studies use either Akaike’s information criterion (AIC) [23, 21, 70, 99] or Rissanen’s minimum description length (MDL) [14, 19, 64, 100] to select the best model to characterize the cardiorespiratory system, these criteria have been included.

AIC is an estimate of the information lost by using the proposed model. The model is selected by minimizing the cost function

$$AIC = \log(V) + \frac{2d}{N}, \quad (3.31)$$

in which V is the cost function, d is the length of θ , indicating the number of estimated coefficients, and N is the number of samples used for model estimation [108].

MDL is a criterion that selects the model that minimizes the number of parameters and residual variance [14]. The model is selected by minimizing the cost function

$$MDL = V \left(1 + \frac{d \log(N)}{N} \right). \quad (3.32)$$

A measure of fit between the measured and predicted outputs is presented as a form of model validation once the model is selected and estimated. The fit is given in percentage as a function of the normalized root mean squared error (NRMSE)

$$\text{fit}(\%) = 100 \times \left(1 - \frac{\|y - \hat{y}\|}{\|y - \bar{y}\|} \right), \quad (3.33)$$

in which y is the measured output, \hat{y} is the predicted output and \bar{y} is the mean value of the measured output.

3.3.2.6. Impulse response and quantitative indicators

The impulse response, h , is a complete representation the dynamic response of a system and can be used to predict the output of a system, y , for a given input, u , through the numerical convolution

$$y(k) = \sum_{n=0}^{M-1} h(n)u(k-n), \quad (3.34)$$

in which M is the impulse response length. The Fourier transform of an impulse response is the transfer function of a system in the frequency domain [110, 111, 112]. The impulse response is obtained by simulating the model using a unit impulse as input. If the model has two inputs, two impulse responses are calculated.

The impulse response for an input-output pair using the ARX model is described by

$$h_{ARX}(k) = - \sum_{n=1}^{na} a_n h_{ARX}(k-n) + \sum_{n=0}^{nb} b_n u(k-nk-n), \quad (3.35)$$

with autoregressive order na determining the number of estimated coefficients a_n and the exogenous input order nb determining the number of estimated coefficients b_n with associated delay nk .

The impulse response of OBF models is given as the weighed sum of OBFs [14, 16, 102]

$$h_{OBF}(k) = \sum_{n=0}^{nb-1} b_n OBF_n(k), \quad (3.36)$$

in which case nb is the number of basis functions used and OBF_n is the n^{th} order OBF.

From each impulse response quantitative indicators that characterize the relationship between the variables are calculated. Figure 3.31 (a) shows the three indicators that are extracted directly from the impulse response. The impulse response magnitude (IRM) is defined as the difference between the maximum and minimum values of the impulse response. The response latency (L) is the time difference from the instant that the impulse is applied to the first response. Finally, the time-to-peak duration (T_{peak}) is the time difference from the first response to the first major peak or trough [14, 64].

The final indicator, the dynamic gain (DG), is obtained from the magnitude of the Fourier transform of the impulse response (the transfer function) as shown in Figure 3.31 (b).

The DG is calculated for a frequency band ranging from f_1 to f_2 , where $H(f)$ is the Fourier transform of the impulse response through

$$DG = \frac{1}{f_2 - f_1} \int_{f_1}^{f_2} |H(f)| df. \quad (3.37)$$

When the limit frequency values are not a part of the spectrum, cubic splines interpolation is used before calculating the integral. The DG is calculated for the LF and HF bands, 0.04-0.15 Hz and 0.15-0.4 Hz respectively, as well as the total value for the range 0.04-0.4 Hz [14, 64].

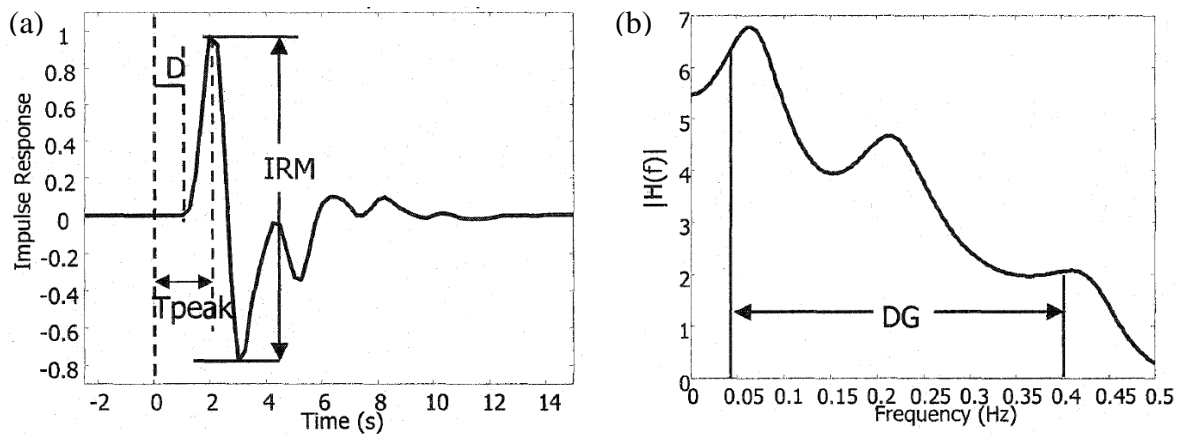


Figure 3.31 – Quantitative indicators extracted from the impulse response (a) and from the Fourier transform of the impulse response, or transfer function (b). From the impulse response (a), the impulse response magnitude (IRM), response latency (D) and time-to-peak duration (Tpeak) are calculated. From the transfer function (b), the dynamic gain (DG) is calculated (Jo, 2002 [14]).

4. METHODOLOGY

With CRSIDLab fully implemented, the second part of this study investigates data from a group of twenty-three obese boys, as described by Lesser *et al.* [113]. All subjects had a body mass index (BMI) greater than or equal to the 95th percentile for their age and gender. ECG, continuous BP and airflow were recorded for 10 min in two different conditions: supine and standing postures. These records were used to generate different autonomic quantitative indicators, both in time and frequency domains.

The data processing is mostly performed using CRSIDLab. The processing flow is represented by Figure 3.1. Besides the analyses performed through CRSIDLab, transfer function estimation in the frequency domain using the relation between the PSD of the output variable and the cross-power spectral density (CPSD) between the output and input variables is also performed, as described in section 4.4.

Once the quantitative indicators are obtained, statistical analyses, described in section 4.6, are used to verify whether the autonomic indicators can correctly measure the effect of different postures on the ANS. The results show that the influence of posture on the calculated autonomic indices is consistent with the underlying physiology and previous studies, supporting CRSIDLab as a toolbox capable of providing quantitative indicators of ANS activity.

4.1. EXPERIMENTAL PROTOCOL

The experimental protocol consisted of measuring ECG, continuous BP and airflow for 10 min, first in supine position, after each subject had been in this position for at least 5 min. Then, the measurements were taken in standing posture for another 10 min, also after the subjects had assumed such posture for at least 5 min. The 5 min period before recording allows hemodynamic balancing, so that the measurements reflect steady-state responses rather than transient responses [25]. Subjects maintained normal breathing patterns during the experiment.

ECG was recorded using the standard three-lead configuration and amplified using a BMA-200 amplifier (CWE Inc., Ardmore, USA). Airflow was recorded through a mask covering the nose and mouth of the subjects attached to pneumotachometer model 3700

(Hans Rudolph, Kansas City, USA). The continuous BP was recorded using Nexfin HD (BMEYE B.V., Amsterdam, The Netherlands), providing a non-invasive measure. All signals were acquired through the 12-bit analogue to digital converter (ADC) DAQPad-6020E (National Instruments, Austin, USA) and sampled at 512 Hz [25].

There are inter-patient factors that can influence HRV, such as genetics and family history, sex, age, medical condition and level of fitness [5]. Likewise, BPV is influenced by age, gender, BMI and mean BP [114]. The database used is considerably homogenous in relation to these inter-patient influences.

4.2. CARDIORESPIRATORY VARIABLES ANALYZED

As discussed in section 2.4, there are different variables that can be used to characterize the cardiorespiratory cycle duration and pressure information.

In this study RRI is used to characterize the cardiac cycle instead of HR because of the linear relation between RRI and the frequency of vagal activity, while both HR and RRI have a non-linear relation to the frequency of sympathetic activity [6].

Respiration is the main influence on HF BPV, but produces little effect when BPV is measured through DBP. Similarly, the 10-second-rhythm is the main influence of LF BPV, however this effect has little influence when BPV is measured through PP [67]. Furthermore, studies that employ a system modeling approach mostly use SBP to characterize the BP information [14, 21, 23, 24, 26, 46, 64, 115, 116] and, therefore, SBP is also employed in our study.

4.3. METHODS EMPLOYED FROM CRSIDLAB

CRSIDLab offers a variety of methods and range of parameters for the user to choose according to the requirements of the study and the data being analyzed. In this section the methods employed from CRSIDLab and related parameters are presented.

4.3.1. Pre-processing

Both raw ECG and continuous BP records were filtered using the low-pass filter with 35 Hz cut-off frequency, removing EMG noise from the ECG and high frequency noise from

the continuous BP. ECG did not present baseline wander. After low-pass filtering, both ECG and BP did not present powerline interference, requiring no further filtering stages.

RRI was extracted from ECG using the “Slow algorithm”, since processing time was not an issue and it performed better on our data set than the “Fast algorithm”. SBP was extracted from the continuous BP records using method 2, in which the BP data is segmented from previously extracted RRI data points. Method 2 was chosen to take advantage of processing both records simultaneously, presenting precise results. After automatic extraction, manual correction was performed through visual inspection when necessary. Any ectopic beats and corresponding SBP were also manually indicated.

Airflow was converted to ILV through integration and detrending was performed using a 0.02 Hz high-pass filter. We observed that lower cut-off frequencies were insufficient for some of the data and the other methods, linear and polynomial detrend, did not perform well for all records in our data set. Many of the presented trends were not linear and a single polynomial order did not produce consistent results across subjects as did the high-pass filter.

All data sets were aligned and resampled, as detailed in section 3.2.4, without truncating the data borders to ensure that all registers would have the same length. Ectopic beats in the ECG and the related SBP data points were interpolated using cubic splines. The borders were completed using constant padding. The adapted Berger algorithm was used to resample both RRI and SBP. Saini *et al.* [117] showed that linear interpolation and cubic splines introduce phase shifts to HRV estimates, shifting the power to lower frequencies, and that this effect is attenuated when using the algorithm described by Berger *et al.* [85]. ILV was resampled using cubic splines.

The highest HR among the data was considered for the choice of sampling frequency. The subject identified as AMD0038 presented RRI as low as 453 ms on a standing posture, which is equivalent to a HR of 132.45 bpm. Converting bpm to Hz yields a heart frequency of 2.2075 Hz, requiring a sampling frequency of at least 4.415 Hz to accurately represent the signal according to the Nyquist criterion. Clifford [5] suggests using a 7 Hz resampling frequency, considering the fact that the human heart beat can exceed 180 bpm, resulting in 2100 points for 5 min records. In this case, the first 2048 points could be used for PSD estimation. In this study, a 7 Hz resampling frequency was chosen.

4.3.2. PSD analysis

For PSD estimation only the first 5 min of each 10 min data sets was used, since this is the recommended duration for this type of analysis [4].

All three available methods, the Fourier transform, the Welch method, and the AR model, were used to estimate HRV and BPV, for a comprehensive demonstration of the toolbox use. HRV was calculated from the PSD of the RRI series, whereas BPV was obtained from the PSD of the SBP series. The Fourier transform was calculated over 2048 points for all three methods, considering the data had 2100 points after resampling. For both the Fourier transform and the Welch method, a Hanning window was applied to the data or data segments, since it one of the most used in this type of study, presenting the necessary sidelobe attenuation while providing a spectrum of good resolution [4, 83].

Due to the lack of standardization for segment duration in estimating HRV using the Welch method, Singh *et al.* [118] evaluated the effects of the segment duration and found that, for data resampled at 4 Hz, segment lengths of 256 samples (64 s) with 50% overlap provides an estimate that is both smooth and shows clearly outlined peaks when compared to segments of 128, 512 and 1024 samples. For data resampled at 7 Hz, 64 s is equivalent to 448 samples and so the next power of two was used, yielding segments of 512 samples with 50% overlap.

For AR model order selection, model orders ranging from 1 to 50 were tested for both RRI and SBP for all subjects from data in both postures, and the NRMSE between the measured and predicted outputs was calculated. The results are presented in Figure 4.1 as the mean NRMSE \pm standard deviation as a function of model order. Blue represents the NRMSE of the models estimated from supine data, while red is the NRMSE of the models estimated from standing data. For both variables in both postures the NRMSE seems to stabilize for orders greater than 20, which is within the range of recommended orders [4]. Therefore, we chose to use a model order of 20 for estimation of the PSDs using the AR model.

The quantitative indicators used for statistical analysis are the absolute areas in the LF and HF bands for both HRV and BPV measures, identified as HRV_{LF} , HRV_{HF} , BPV_{LF} , and BPV_{HF} , respectively. For HRV, the LF/HF ratio, $HRV_{LF/HF}$, is also analyzed.

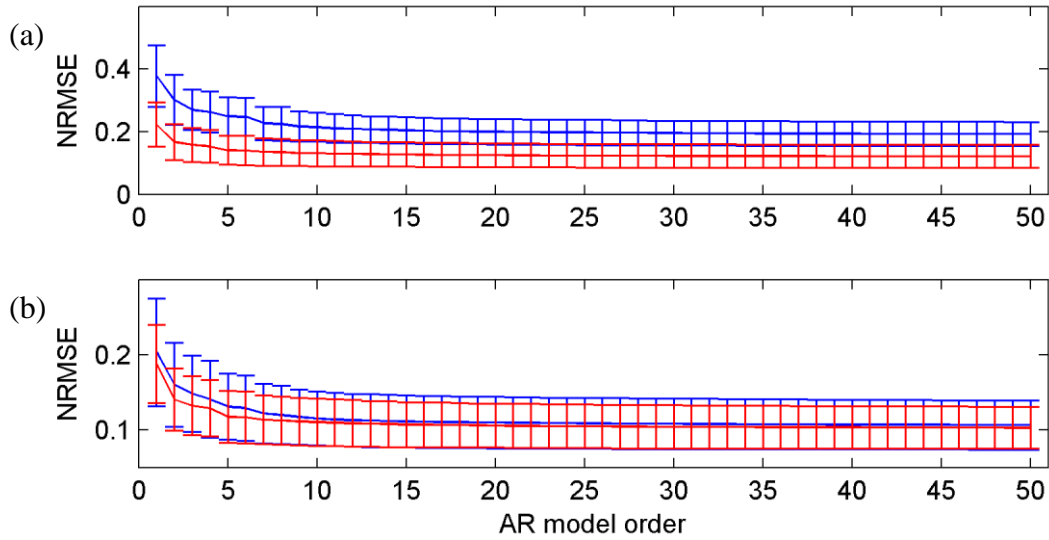


Figure 4.1 – AR model order effects on NRMSE between measured and predicted outputs for RRI (a) and SBP (b) records expressed as mean NRMSE \pm standard deviation for both supine (blue) and standing (red) postures.

4.3.3. System identification

System identification was performed using the three available models, the ARX, Laguerre and Meixner basis functions, and for this approach the full 10 min of data were used. For each subject at each posture, a system consisting of an RRI output with both ILV and SBP as inputs was built to estimate the RCC and ABR impulse responses. 50% of the data was used for model estimation, corresponding to the first 5 min of the records, and the other 50% was used for model validation. To determine the percentage of data used for model estimation and validation, tests were performed for ARX models using 50, 60, 70, and 80% of the data set for model estimation. The results are presented in Figure 4.2, which shows the NRMSE between measured outputs and the outputs estimated from the models \pm standard deviation as a function of the percentage of data used for model estimation. The NRMSE for the data recorded in supine posture is shown in blue, and for the data recorded in standing, red. The results show that the mean NRMSE and its standard deviation increase with increasing percentage of data used for estimation. The other parameters used for this test, such as orders and delays, were the same as those used to estimate the ARX models, as described next.

A 0.5 Hz low-pass Kaiser filter was applied to the data, followed by a polynomial detrend of order 5, as used in previous studies [14, 19, 64], in order to ensure stationarity. Previous

studies have considered the delay between SBP and RRI to be in the 0.5 to 1 s range, while the delay between ILV and RRI has been shown to be in the range of -2 to 1 s [14, 19]. For data sampled at sampling frequency of 7 Hz, this is equivalent to testing delays from 3 to 7 samples for the ABR impulse response and from -14 to 7 samples for the RCC impulse response. These ranges were used for the estimation of all impulse response models.

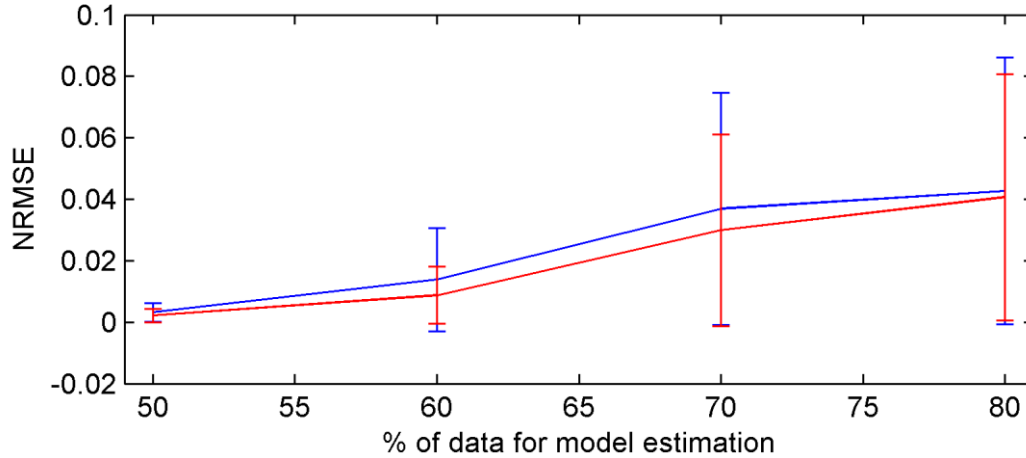


Figure 4.2 – Effects of the percentage of data used for model estimation in the NRMSE between measured and predicted outputs expressed as mean NRMSE \pm standard deviation for subjects in supine (blue) and standing (red) postures using an ARX model with the ILV and SBP as inputs and the RRI as output.

The aforementioned parameters were used to generate all models. Sections 4.3.3.1 and 4.3.3.2 discuss the parameters that are specific for each model structure used. Once all of the parameters to be tested are set, the models are selected using the MDL criterion, as used in many studies in this area for providing the shortest description of data, minimizing the number of parameters and residual variance [14, 19, 25, 64, 100].

Once the impulse responses h_{RCC} and h_{ABR} are generated, the quantitative indicators IRM and DG (total, LF, and HF), derived from the estimated impulse responses, are calculated. For h_{RCC} , the indicators are identified as RCC_{IRM} , RCC_{TOT} , RCC_{LF} and RCC_{HF} , respectively, while for the h_{ABR} they are identified as ABR_{IRM} , ABR_{TOT} , ABR_{LF} and ABR_{HF} , respectively.

4.3.3.1. ARX models

For ARX models the range of orders to be tested should also be set. Since the data is filtered and detrended before the identification procedure, an additional study to evaluate

the effect of ARX model order on NRMSE, similar to the one presented in section 4.3.2, was performed. Initially an AR model was estimated for the RRI data. Figure 4.3 (a) shows the resulting NRMSE as a function of this model order. Then, single input models were estimated for ILV and SBP as inputs and RRI as output, with the autoregressive order set to zero, as the autoregressive influence encompasses the effects of both inputs. These models would estimate the fraction of RRI data dependent on each input exclusively. Figure 4.3 (b) and (c) show the resulting NRMSE as a function of model order for ILV and SBP as inputs, respectively. In these figures, the blue line represents supine data, while the red line represents data in the standing posture. The remaining parameters, such as the delays associated with each input, the percentage of data used for model estimation and the criterion used to select the optimum model, were set as previously described and orders from 1 to 50 were tested. These results show an abrupt change in NRMSE up to around order 5, while NRMSE is practically stable for model order above 20. Therefore, the order selection range for both the autoregressive component and the exogenous inputs was set to be tested from 5 to 20 samples for the ARX model estimation.

Comparing Figure 4.3 (a) to Figure 4.1 (a), it is possible to see how the filtering and trend removal performed before system estimation result in more accurate models, as both the NRMSE mean values and the standard deviation decrease when these pre-processing steps are applied.

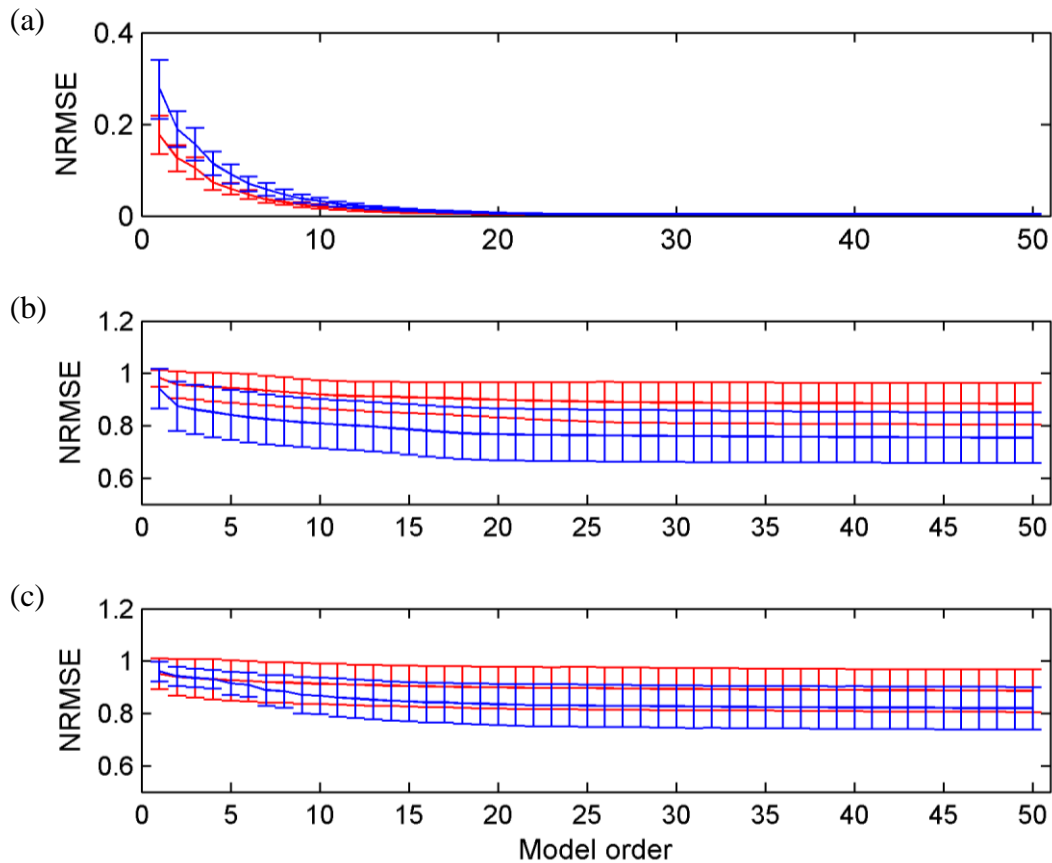


Figure 4.3 – (a) Model order effects on NRMSE between measured and predicted outputs for an AR model for RRI; (b) a model with ILV input and RRI output without an AR component; and (c) a model with SBP input and RRI output without an AR component, obtained in both supine (blue) and standing (red) postures. The mean NRMSE for each group at each order is presented with the error bars indicating the standard deviation.

4.3.3.2. LBF and MBF models

For LBF and MBF models, the system memory length and pole can be selected and a range of number of basis functions can be set. The pole should be selected so that the highest order basis function approaches zero close to the memory length [119]. Based on previous work that evaluated linear LBF models for cardiorespiratory system identification, 5 to 12 basis functions are used for both LBF and MBF models [14]. To find the best memory length, tests were performed for memories of 50 to 200 samples (7.14 to 28.6 s) in steps of 25 samples using LBF models. The poles were adjusted for each memory length. The results, shown in Figure 4.4, are inconclusive in terms of providing insight into the selection of an appropriate memory length, since there seems to be no relation between system memory length and decreased NRMSE.

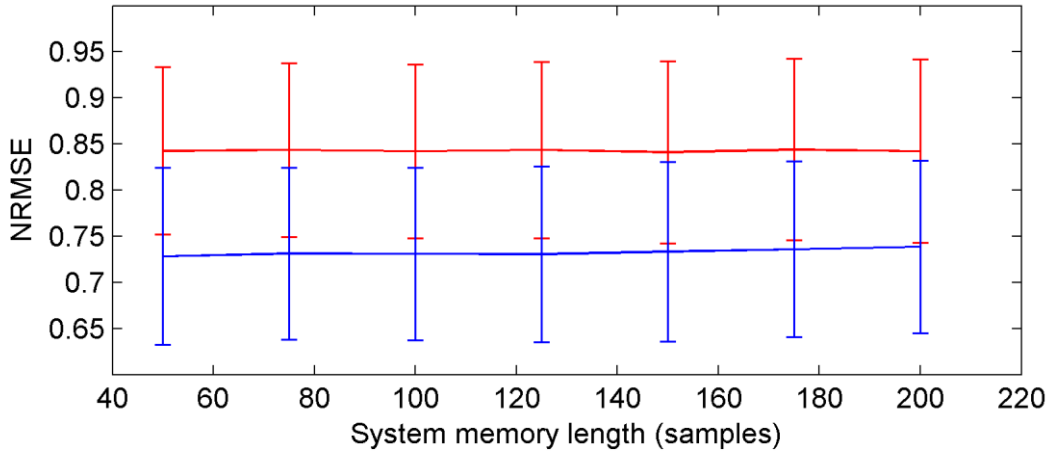


Figure 4.4 – Effects of the system memory length in the NRMSE between measured and predicted outputs expressed as mean NRMSE \pm standard deviation for subjects in supine (blue) and standing (red) postures using a LBF model with ILV and SBP as inputs and the RRI as output.

Another way to gain insight into the appropriate memory length is to analyze the impulse responses generated through the ARX models. For this purpose, all ARX model impulse responses were averaged and are shown in blue along with the corresponding standard deviations, in red, for supine and standing postures in Figure 4.5 (a) and (b), respectively, in which h_{RCC} is presented on top and h_{ABR} on the bottom for each condition. Previous studies have used a memory length of 50 samples for data resampled at 2 Hz [14, 19, 26], corresponding to 25 s, which would be equivalent to 175 samples for data resampled at 7 Hz. However, increasing memory length increases the model computation time. As there seems to be no significant impulse response content above 20 s for both h_{RCC} and h_{ABR} in supine and standing conditions, a memory length of 140 is selected.

The pole of 0.82 was selected through visual inspection for LBF functions, allowing all 12 basis functions to die out approximately at the chosen memory length of 140 samples, as shown in Figure 4.6.

Finally, the MBF generalization orders are tested from 0 to 5, based on previous studies [25, 26, 116]. The pole in this case is set to ensure the highest order basis function approaches zero close to the system memory length for the highest generalization order and the pole 0.76 was chosen, as shown in Figure 4.7.

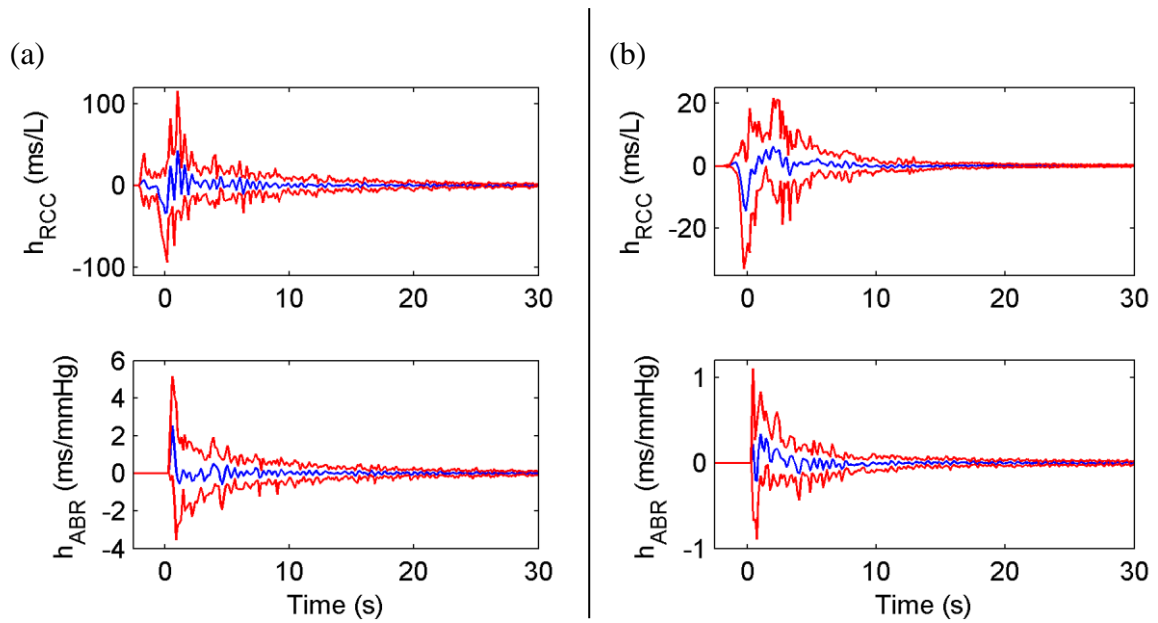


Figure 4.5 – ARX model impulse responses h_{RCC} and h_{ABR} for subjects in supine (a) and standing (b) postures presented as mean value (blue) \pm standard deviation (red).

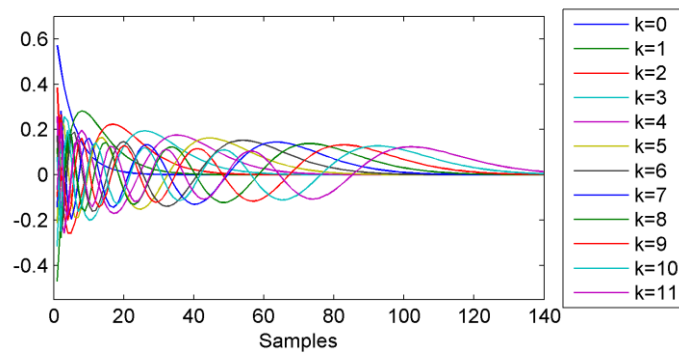


Figure 4.6 – Pole selection of $p = 0.82$ for the first 12 Laguerre basis functions, ranging from orders 0 to 11, with a system memory of 140, so that the last basis function approaches zero close to the memory length.

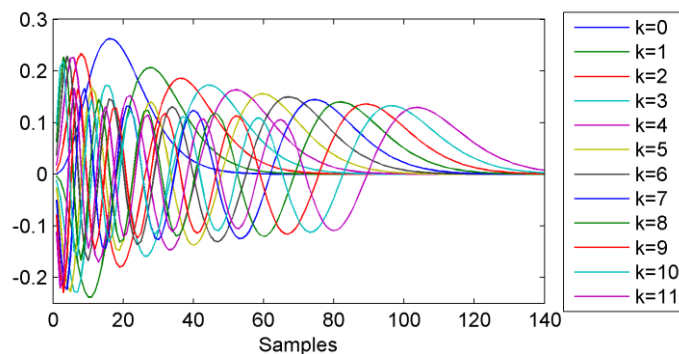


Figure 4.7 – Pole selection of $p = 0.76$ for the first 12 Meixner basis functions, ranging from orders 0 to 11, with a system memory of 140 and a generalization order of 5, so that the last basis function approaches zero close to the memory length.

4.4. TRANSFER FUNCTION ESTIMATION

Though transfer function estimation in the frequency domain is not implemented on CRSIDLab, it is the classical approach to estimating RSA and BRS, having been employed in many studies [22, 36, 37]. Therefore, this approach is implemented to further validate the results found by performing impulse response analyses through CRSIDLab.

The transfer function provides a characterization of a system in the frequency domain. To calculate the transfer function, first the definition of cross-correlation and the relationship between cross-correlation and autocorrelation must be addressed.

The cross-correlation is similar to the autocorrelation, but instead of representing how a signal correlates with the lagged versions of itself, it represents how two signals correlate to each other with different lags, providing information on the similarity between them [88]. The cross-correlation between two signals x and y of length N , r_{xy} , is given by:

$$r_{xy}(k) = \frac{1}{N} \sum_{n=1}^N x(n)y(n+k). \quad (4.1)$$

The point of maximum cross-correlation is an indicator of the time delay between two variables and the cross-correlation between a signal and sinusoids of varying frequencies can be used to decompose the signal similarly to performing a Fourier transform [88]. The Fourier transform of the CPSD, S_{uy} , is given as a function of the discrete frequency f by:

$$S_{uy}(f) = \sum_{k=1}^N r_{xy}(k) e^{\frac{-j2\pi f k}{N}}, \quad k = 0, \dots, N/2. \quad (4.2)$$

In a similar process as the one described from the autocorrelation function, the final expression for the Fourier transform of the cross-correlation can be found through mathematical manipulation:

$$S_{uy}(f) = \frac{1}{N} \sum_{k=1}^N \sum_{n=1}^N y(n)x(n+k) e^{\frac{-j2\pi f k}{N}}$$

$$S_{uy}(f) = \frac{1}{N} \sum_{k=1}^N x(n+k) e^{\frac{j2\pi f(n-k)}{N}} \sum_{n=1}^N y(n) e^{\frac{-j2\pi f n}{N}}$$

$$S_{uy}(f) = \frac{1}{N} X^*(k) Y(k). \quad (4.3)$$

S_{uy} in equation (4.3) represents the CPSD or cross-spectrum [106]. In this equation X^* is the complex conjugate of the Fourier transform of the signal x and Y is the Fourier transform of y . Describing an output signal y as the convolution sum in Equation (3.34) and substituting this expression on the cross-correlation considering the lagged version of y , $y(n+k)$, Equation (4.1) becomes

$$\begin{aligned} r_{xy}(k) &= \frac{1}{N} \sum_{n=1}^N x(n) \sum_{m=0}^{M-1} h(m)x(n+k-m) \\ &= \sum_{m=0}^{M-1} h(m) \frac{1}{N} \sum_{n=1}^N x(n)x(n+k-m) \\ &= \sum_{m=0}^{M-1} h(m)r_{xx}(k-m), \end{aligned} \quad (4.4)$$

where N is the length of x and M is the length of the impulse response h . Equation (4.4) is called the Wiener-Hopf equation [112] and substituting it into the CPSD, Equation (4.3) becomes

$$\begin{aligned} S_{uy}(f) &= \sum_{k=1}^N \sum_{m=0}^{M-1} h(m)r_{xx}(k-m) e^{\frac{-j2\pi fk}{N}} \\ S_{uy}(f) &= \sum_{m=0}^{M-1} h(m)e^{\frac{-j2\pi fk}{N}} \sum_{k=1}^N r_{xx}(k-m)e^{\frac{-j2\pi f(k-m)}{N}} \\ S_{uy}(f) &= H(f)S_{uu}(f), \end{aligned} \quad (4.5)$$

where r_{xx} is the autocorrelation function of signal x , S_{uu} is the Fourier transform of r_{xx} (PSD) and H is the Fourier transform of the impulse response h , or the transfer function. The transfer function

$$\hat{H}(f) = \frac{\hat{S}_{uy}(f)}{\hat{S}_{uu}(f)} \quad (4.6)$$

can be estimated from the estimated cross and autocorrelation estimates, \hat{S}_{uy} and \hat{S}_{uu} , respectively.

We perform transfer function estimation using the Fourier transform and the Welch methods. In this study the transfer function is estimated for the two subsystems of interest: the ABR, in which SBP is the input to RRI, and RSA, in which ILV is the input to RRI. Both Fourier transform and Welch methods are used. The quantitative indicators used for statistical analysis of the RSA are the areas of the magnitude response of the transfer functions for the LF and HF frequency bands, RSA_{LF} and RSA_{HF} . BRS is calculated from the areas from the ABR transfer functions, as described in the following section.

4.5. BAROREFLEX SENSITIVITY INDEXES

There are a few BRS indicators that can be calculated based on PSD, transfer function and impulse response analyses. Pagani *et al.* [120] first proposed the α_{LF} and α_{HF} indexes:

$$\alpha_{FB} = \sqrt{\frac{\int_{f_1}^{f_2} \hat{P}_{RRI}(k) dk}{\int_{f_1}^{f_2} \hat{P}_{SBP}(k) dk}}, \quad (4.7)$$

where the frequency band FB can be defined in the LF or HF frequency bands, by appropriate choice of the minimum and maximum frequencies f_1 and f_2 , respectively. The α_{LF} and α_{HF} indexes are descriptors of baroreflex gain, calculated from the PSD estimates of RRI and SBP for each frequency band, \hat{P}_{RRI} and \hat{P}_{SBP} , respectively. These indexes assume that changes in LF(HF) RRI are caused by changes in LF(HF) SBP. Lucini *et al.* [121] proposed the overall α -index:

$$\alpha = \frac{\alpha_{LF} + \alpha_{HF}}{2}, \quad (4.8)$$

as a measure of overall BRS gain, calculated as the mean value of the LF and HF bands.

The BRS can also be calculated from the spectral transfer function between SBP and RRI as:

$$BRS_{FB} = \frac{ABR_{FB}}{f_2 - f_1}, \quad (4.9)$$

where ABR_{FB} is the power (area) of a frequency band defined by the minimum frequency f_1 and the maximum frequency f_2 . This is a measure of how the RRI varies in response to changes in SBP for a given frequency band and presents indexes with the same units as

those produced by Equation (4.7), ms/mmHg [17]. The overall α -index is determined for the transfer function from the average between BRS_{LF} and BRS_{HF} , the BRS_{α} indicator.

The BRS as defined in Equation (4.9) is the same as the impulse response DG indicator, shown in Equation (3.37), which is already given as an output through CRSIDLab, and so the final BRS indicators are the ABR_{LF} , ABR_{HF} and ABR_{TOT} , described in section 4.3.3.

4.6. STATISTICAL ANALYSIS

In this study the same groups of subjects are evaluated under different conditions. To verify whether the mean values of the indicators differ on a significant level for the subjects in supine and standing postures, a repeated measures analysis of variance (ANOVA) test was applied to compare the quantitative indicators.

The repeated measures ANOVA assumes that the data sets have normal distribution and equal variance. Therefore, before performing the ANOVA test, the data sets are tested for normality using the Shapiro-Wilk test [122], which was shown to be more powerful than other similar tests even with a small number of samples [123]. Data that did not pass the normality test were log or square-root transformed [124]. All transformed data were found to be normal and to have equal variance (Brown-Forsythe test) [125].

Finally, the Pearson correlation [126]

$$r = \frac{\sum_{i=1}^n (X_i - \bar{X})(Y_i - \bar{Y})}{\sqrt{\sum_{i=1}^n (X_i - \bar{X})^2 \sum_{i=1}^n (Y_i - \bar{Y})^2}} \quad (4.10)$$

between two data series X_i and Y_i , $i = 1, \dots, n$, of mean values \bar{X} and \bar{Y} is used to assess the correlation between indicators that are reported to be associated. It is widely acknowledged that HF HRV is a measure of vagal activity related to RSA [3, 4, 6, 7], and some have claimed LF HRV reflects baroreflex activity [3, 67]. Recent studies have suggested that the reliability of traditional BRS estimates is highly dependent on the dominant causality between BP and HR and that the dominant causality shifts according to posture [47, 44]. Thus, the correlation analyses were performed between RSA/RCC and HRV indicators and between BRS/ABR and HRV indicators on both LF and HF for supine and standing postures. The correlation between LF spectral BRS and impulse response ABR indicators was also calculated in supine and standing postures to address the causality issue.

5. RESULTS

The results from the statistical analysis of the indicators presented are shown in this chapter. The variables analyzed include spectral HRV and BPV measures, as well as measures based on the impulse response and its corresponding spectrum (the system's transfer function). Correlation analyses between corresponding indicators using different techniques, as well as between LF and HF components of different indices, are performed to evaluate the differences and/or commonalities between related metrics.

All of the methods available in CRSIDLab for PSD analysis and model estimation were employed for a full demonstration of the toolbox. It is not the purpose of this study to compare the results from the different methods available for each analysis approach (univariate PSD, spectral transfer function and impulse response analyses), but to compare the results from each of these techniques.

5.1. HRV AND BPV

HRV was quantified from frequency analysis of the RRI, as discussed in section 3.3.1, using the Fourier transform, the Welch method, and the AR model. In all cases, there is a significant decrease in HRV_{HF} in standing posture compared to supine, which is a measure of vagal activity [3, 4, 6, 7], as shown in Figure 5.1.

Figure 5.2 illustrates the increase found in $HRV_{LF/HF}$ upon standing. $HRV_{LF/HF}$ is a measure of sympathovagal balance, where an increase indicates a shift towards dominant sympathetic activity and a decrease indicates a shift towards dominant vagal activity [4, 7].

BPV was quantified from the frequency analysis of SBP, also through the Fourier transform, Welch method and AR model. While BPV_{LF} is believed to be a measure of sympathetic vascular tone [67, 68, 69], the interpretation of BPV_{HF} is more controversial [70], as further discussed in chapter 6. Both indicators showed a statistically significant increase in standing posture compared to supine from all three spectra, as shown in Figure 5.3 and 5.4.

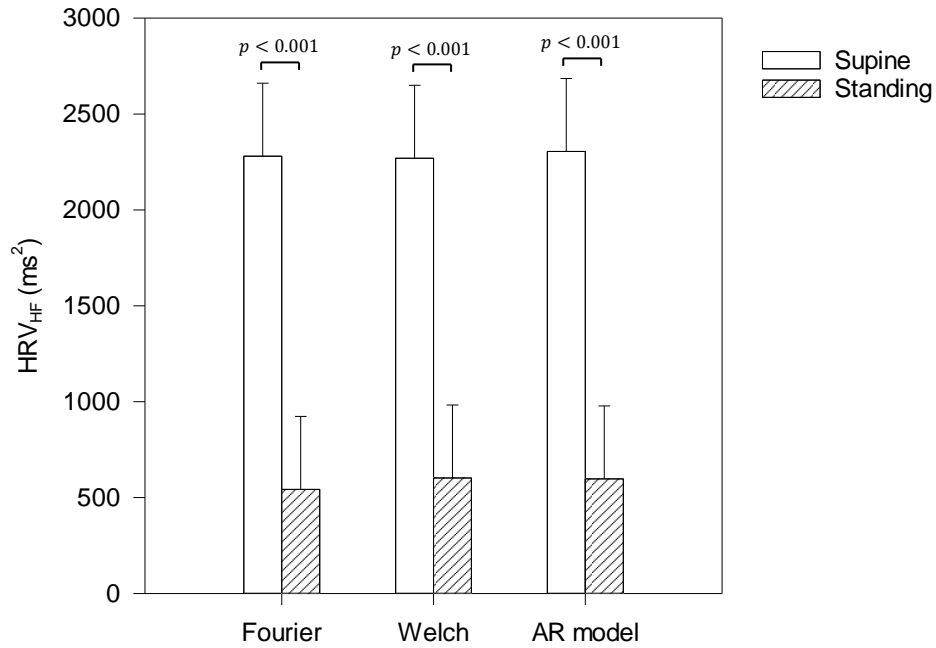


Figure 5.1 – High frequency heart rate variability, HRV_{HF} (0.15-0.4 Hz), for supine and standing postures calculated as the power spectral density (PSD) of the R-R interval (RRI) using the Fourier transform, the Welch method, and the AR model. The decrease in HRV_{HF} in standing is an indicator of tonal vagal withdrawal.

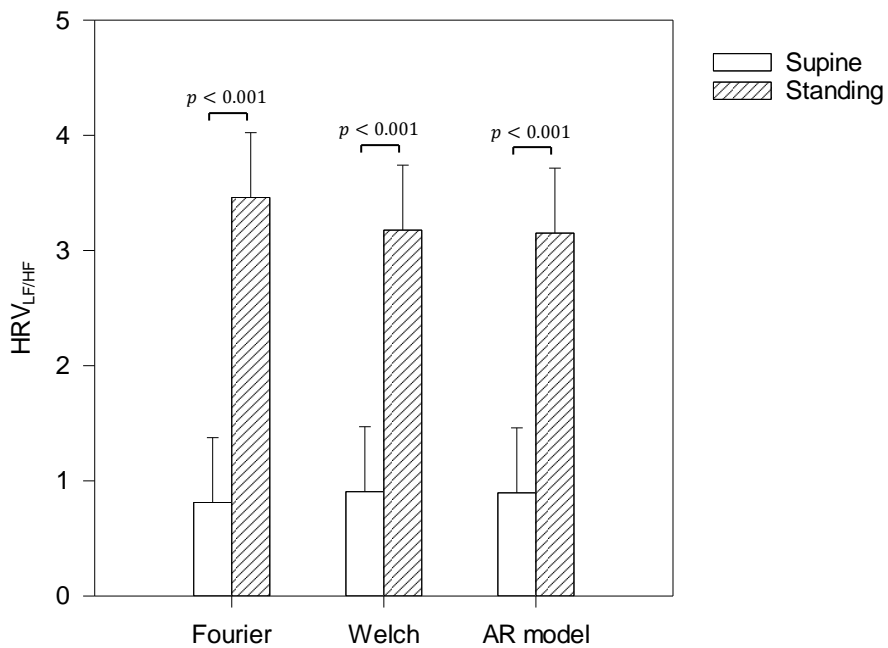


Figure 5.2 – Heart rate variability LF/HF ratio, $HRV_{LF/HF}$, for supine and standing postures calculated as the power spectral density (PSD) of the R-R interval (RRI) using the Fourier transform, the Welch method, and the AR model. The increase in $HRV_{LF/HF}$ in standing indicates a shift towards dominant sympathetic activity in sympathovagal balance.

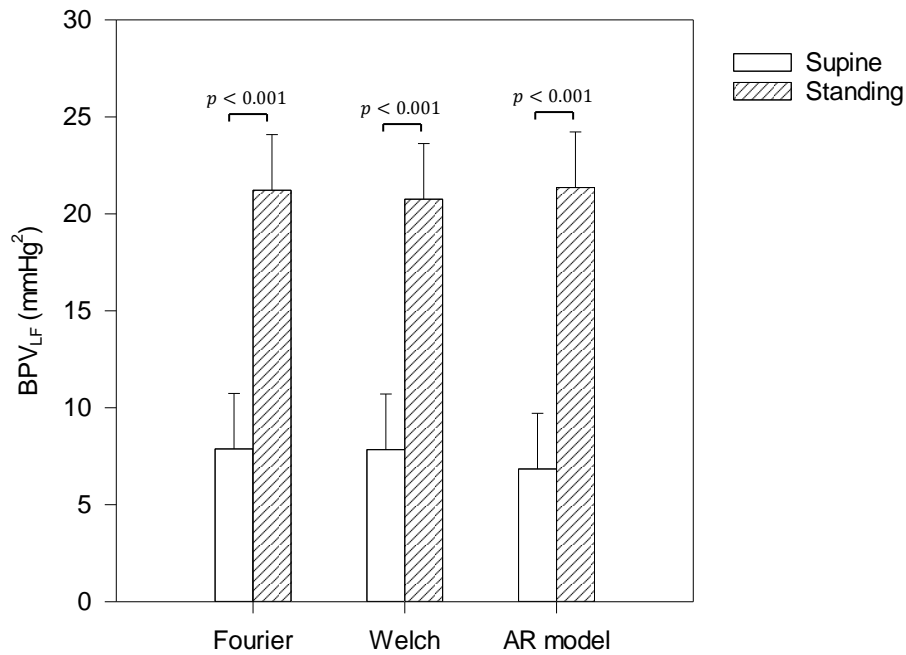


Figure 5.3 – Low frequency blood pressure variability, BPV_{LF} (0.04-0.15 Hz), for supine and standing postures calculated as the power spectral density (PSD) of systolic blood pressure (SBP) using the Fourier transform, the Welch method, and the AR model. The increase in BPV_{LF} upon standing indicates increased sympathetic vasomotor tone.

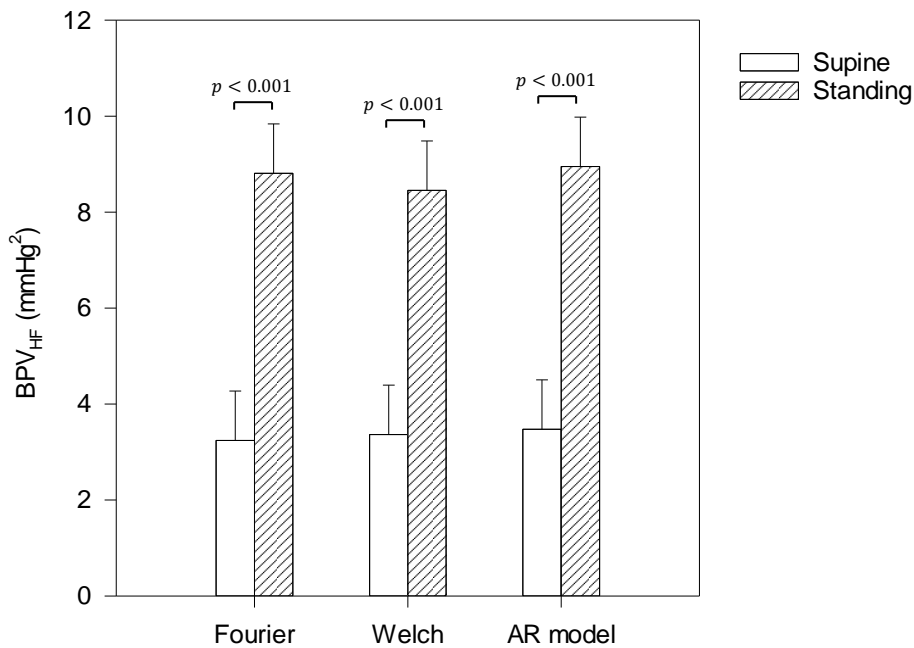


Figure 5.4 – High frequency blood pressure variability, BPV_{HF} (0.15-0.4 Hz), for supine and standing postures calculated as the power spectral density (PSD) of systolic blood pressure (SBP) using the Fourier transform, the Welch method, and the AR model. The meaning of the increase in BPV_{HF} upon standing is not a consensus among researchers.

5.2. RCC AND RSA

Quantitative indicators for RSA, presented in section 4.4, were obtained from the spectral transfer functions, estimated through both the Fourier transform and the Welch methods. The respiratory cardiac coupling, RCC, was quantified from the impulse responses generated from the ARX, LBF, and MBF models, as described in section 3.3.2.

Impulse response analysis is able to isolate the direct effects of respiration from the indirect effects, which are mostly mechanical and mediated through ABR (section 2.3), by having both ILV and SBP as model inputs [14]. Therefore, while RSA is a measure of both direct and indirect effects of respiration on HR, RCC quantifies the direct effects only.

5.2.1. Frequency domain transfer function

RSA transfer function analysis was performed through the Fourier transform and Welch methods. RSA_{LF} showed a significant decrease from supine to standing using both methods, as shown in Figure 5.5. Saul *et al.* [37] showed that RSA_{LF} is responsive under vagal blockade, suggesting both sympathetic and vagal branches act in LF.

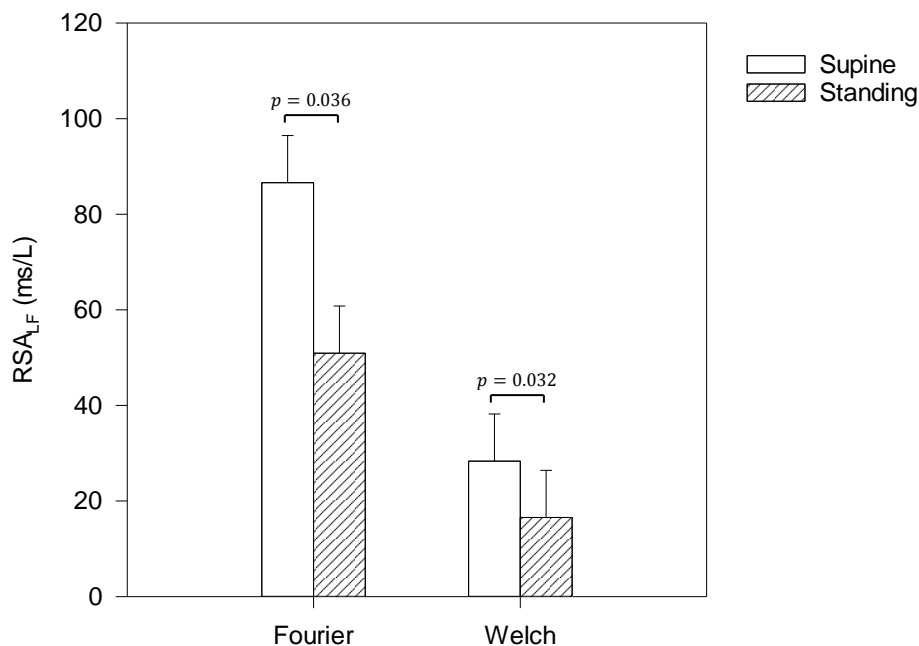


Figure 5.5 – Low frequency respiratory sinus arrhythmia, RSA_{LF} (0.04-0.15 Hz), quantifying the direct and indirect effects of respiration on heart rate, for supine and standing postures calculated from the transfer function estimated the Fourier transform, and Welch method. The interpretation of the decrease verified in RSA_{LF} in standing posture reflex combined vagal and sympathetic activity changes.

Figure 5.6 shows that there was also a significant decrease in RSA_{HF} upon standing. RSA is generally accepted as a measure of vagal activity [12, 13] and RSA_{HF} was shown to be absent during vagal blockade [37].

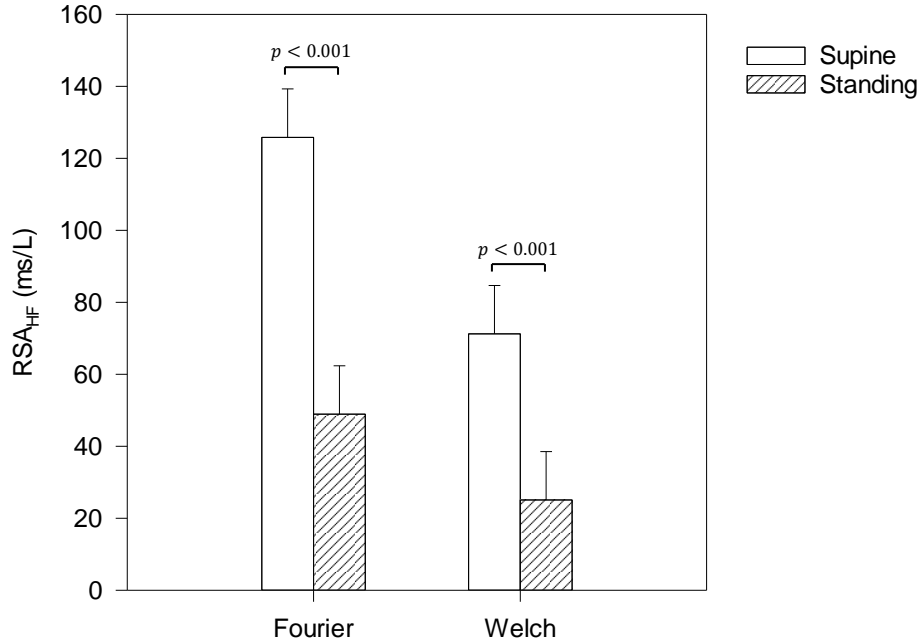


Figure 5.6 – High frequency respiratory sinus arrhythmia, RSA_{HF} (0.15-0.4 Hz), quantifying the direct and indirect effects of respiration on heart rate, for supine and standing postures obtained from the transfer function estimated using the Fourier transform, and Welch method. The decrease in RSA_{HF} in standing indicates tonal vagal withdrawal.

5.2.2. Impulse response

Since the impulse response is a reflection of the dynamic properties of the system, as addressed in section 3.3.2.6, impulse response analysis allows the verification of the dynamic response, besides gain. Table 5.1 presents the impulse response latency (mean \pm standard deviation) for the RCC impulse response in both supine and standing postures. No significant difference was observed. Nevertheless, in all models a negative latency between ILV and RRI is observed. This result is in accordance to the apparent non-causal relationship between ILV and RRI , reported by a number of previous studies [14, 24, 53].

The, RCC_{IRM} index, related to gain of the impulse response, showed a significant decrease from supine to standing, as presented in Figure 5.7, using either model. Being an overall indicator of the direct effects of respiration on HR, it is mainly an indicator of vagal activity [12, 13].

Table 5.1 – Respiratory-cardiac coupling (RCC) impulse response latency for subjects in supine and standing positions obtained from ARX, LBF and MBF models presented as mean value \pm standard deviation. There is no significant difference between postures, but the selection of negative delays implies a non-causal relationship.

Posture	ARX model	LBF model	MBF model
Supine	-0.801 ± 0.546	-1.975 ± 0.412	-2.044 ± 0.281
Standing	-0.770 ± 0.603	-1.913 ± 0.641	-2.012 ± 0.626

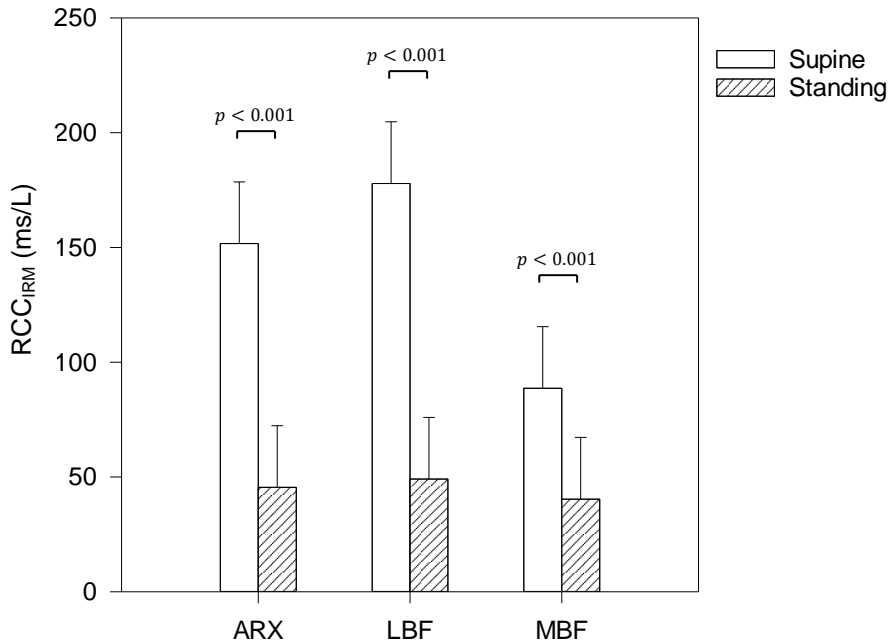


Figure 5.7 – Respiratory-cardiac coupling impulse response magnitude, RCC_{IRM} , as an overall measure of gain quantifying the direct effects of respiration on heart rate, for supine and standing postures, obtained from the impulse response estimated using the ARX, LBF, and MBF models. The decreased RCC_{IRM} found in standing posture indicates vagal withdrawal.

The RCC_{TOT} , a measure of the area under the curve (the transfer function gain) of both LF and HF bands combined, obtained from the spectral analysis of the impulse response as described in section 3.3.2.6, also showed a significant decrease from supine to standing, as shown in Figure 5.8. As the RCC_{IRM} , it is mainly an indicator of vagal activity [12, 13].

Both the LF and HF components of RCC, RCC_{LF} and RCC_{HF} , respectively, similarly show a significant decrease upon standing, as shown in Figure 5.9 and Figure 5.10. The interpretation of those indicators mainly correspond to the RSA_{LF} and RSA_{HF} , respectively, however in RCC analysis only the direct effects of respiration are reflected, while in RSA analysis an increase or decrease may be due to the indirect effects, which are mostly mechanical and not mediated by the ANS [14].

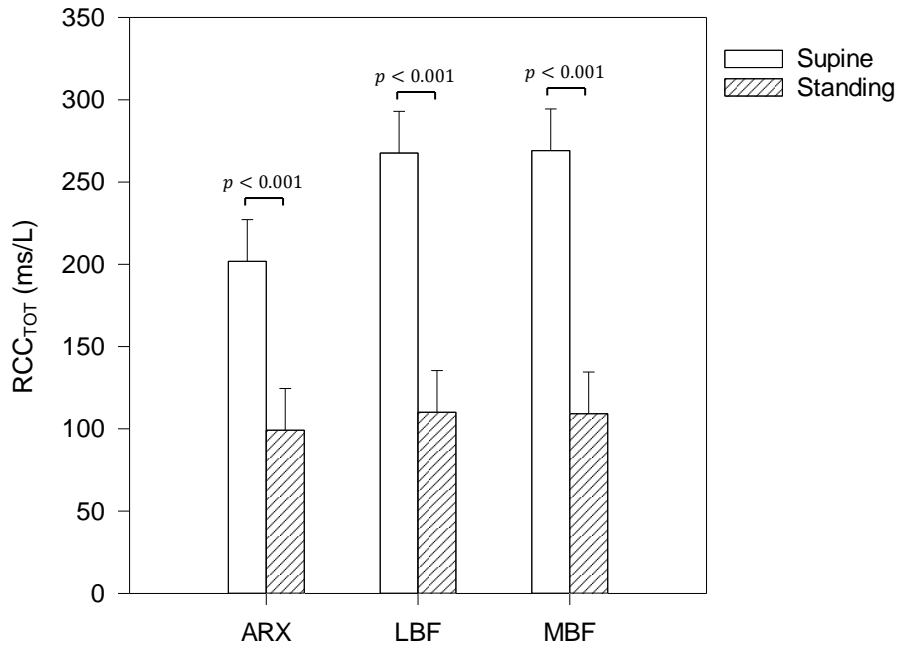


Figure 5.8 – Respiratory-cardiac coupling total dynamic gain, RCC_{TOT} (0.04-0.4 Hz), as an overall measure quantifying the direct effects of respiration on heart rate, for supine and standing postures, obtained from the impulse response estimated using the ARX, LBF and, MBF models. The decrease in RCC_{TOT} upon standing indicates vagal withdrawal.

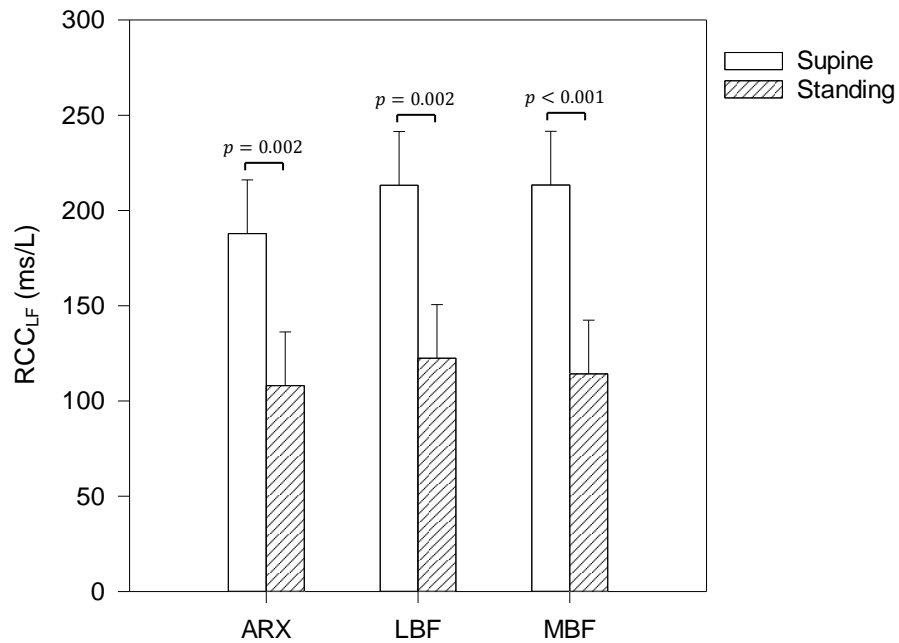


Figure 5.9 – Respiratory-cardiac coupling low frequency dynamic gain, RCC_{LF} (0.04-0.15 Hz), quantifying the direct effects of respiration on heart rate, for supine and standing postures obtained from the impulse response estimated using the ARX, LBF, and MBF models. The meaning of the decrease in RCC_{LF} upon standing results from the interaction of sympathetic and vagal activity shifts.

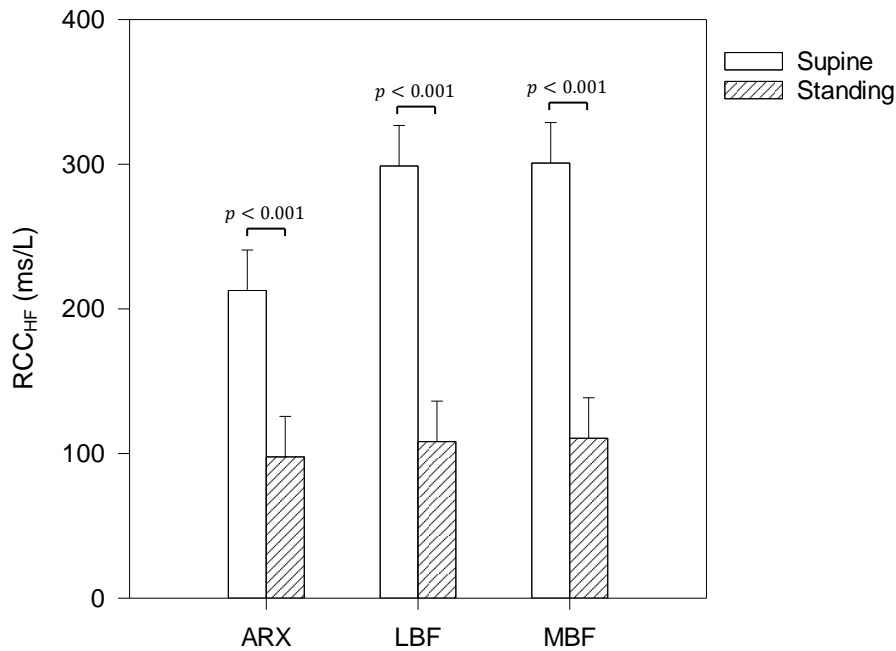


Figure 5.10 – Respiratory-cardiac coupling high frequency dynamic gain, RCC_{HF} (0.15-0.4 Hz), quantifying the direct effects of respiration on hear rate, for supine and standing postures obtained from the impulse response estimated using the ARX, LBF, and MBF models. The decrease in RCC_{HF} upon standing is an indicator of vagal withdrawal.

5.3. ABR AND BRS

The quantitative indicators for BRS were obtained in the frequency domain as the square root of the HRV/BPV ratio, obtained from PSD analysis using the Fourier transform, the Welch method, and the AR model (section 3.3.1), and also obtained from transfer functions, estimated through the Fourier transform and Welch methods. Both methods are described in section 4.5. The impulse response indicators of ABR were estimated from the ARX, LBF, and MBF models (section 3.3.2.6).

The relationship between BP and HR is essentially closed-loop, as illustrated in Figure 2.10. Indices of BRS obtained from spectral analyses are, by definition, unable to disentangle the feedforward and feedback paths involved in the baroreflex dynamics, since the temporal relationship between BP and HR is not preserved by this technique [115]. Impulse response based modeling, on the other hand, by considering the current output to be dependent upon only past and present, but not future measures of the outputs in the model definition, essentially “open the loop” mathematically [44, 47]. Thus, the ABR indices more correctly quantify the open-loop effects of SBP on RRI, and not the other way around.

5.3.1. Power spectral density

BRS indicators were calculated from the square root of the HRV/BPV ratio, obtained from PSD analyses using the Fourier transform, the Welch method, and the AR model. The α_{LF} index, considered a measure of both sympathetic and vagal activities [24, 37], presented significant decrease upon standing, as shown in Figure 5.11.

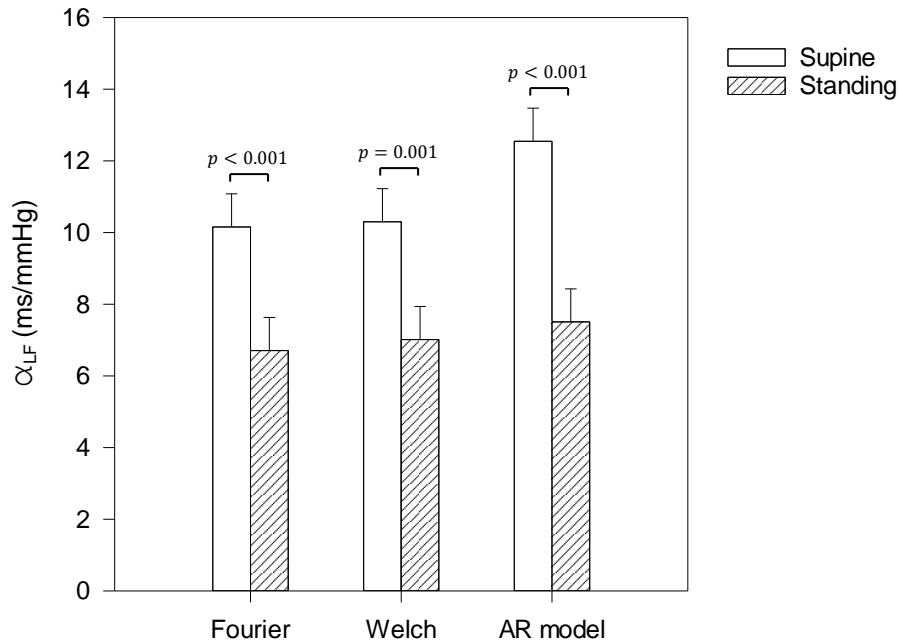


Figure 5.11 – Low frequency baroreflex sensitivity, α_{LF} (0.04-0.15 Hz), calculated as the square root of the HRV/BPV ratio, obtained from power spectral density (PSD) analysis using the Fourier transform, the Welch method, and the AR model, for subjects in supine and standing postures. The decrease in α_{LF} in standing reflects both vagal and sympathetic activities.

The α_{HF} index also showed significant decrease in standing, as illustrated in Figure 5.12. This is considered to be a purely vagal indicator [24, 37].

Finally, Figure 5.13 shows that the overall α index was also reduced in standing when compared to supine. Though the overall α indicator takes both frequency ranges into account, presenting information on both ANS branches, it is generally considered a measure of reflex vagal activity [41, 42].

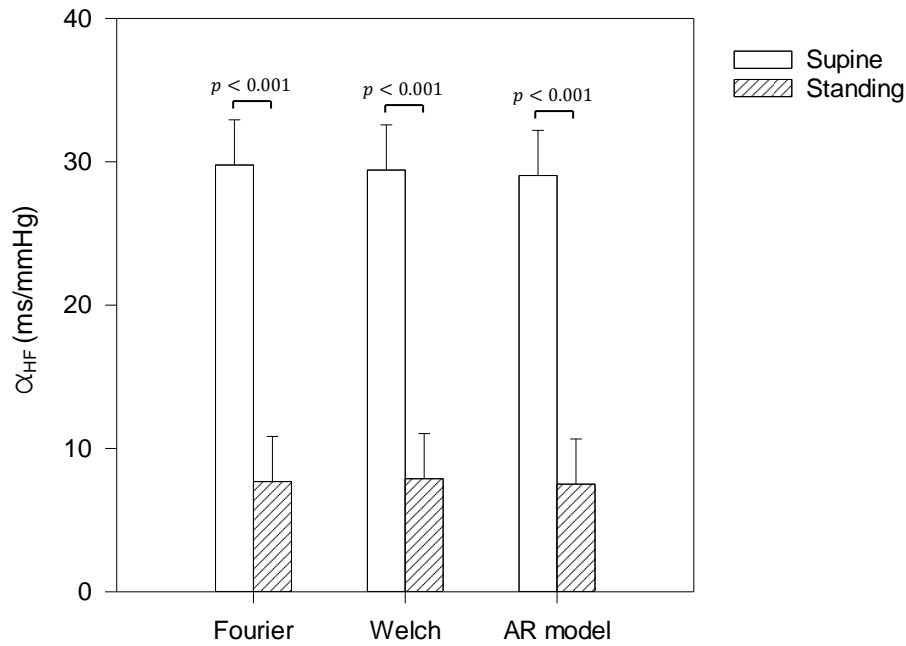


Figure 5.12 – High frequency baroreflex sensitivity, α_{HF} (0.15-0.4 Hz), calculated as the square root of the HRV/BPV ratio, obtained from power spectral density (PSD) analysis using the Fourier transform, the Welch method, and the AR model, for subjects in supine and standing postures. The decrease in α_{HF} in standing is related to decreased vagal activity.

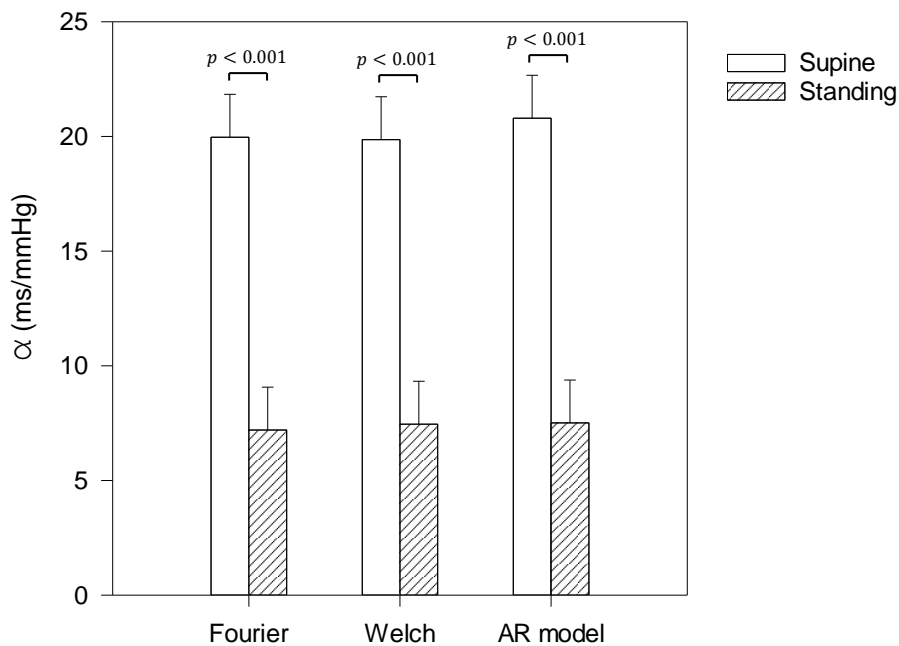


Figure 5.13 – Overall baroreflex sensitivity, α , calculated as the mean value between low frequency (0.04-0.15 Hz) and high frequency (0.15-0.4 Hz) sensitivities, α_{LF} and α_{HF} for subjects in supine and standing postures. α_{LF} and α_{HF} were calculated as the square root of the HRV/BPV ratio in each frequency band, obtained from power spectral density (PSD) analysis using the Fourier transform, the Welch method, and the AR model. The diminished reflex vagal activity in standing is indicated by the decrease in α .

5.3.2. Frequency domain transfer function

BRS transfer function was estimated from the Fourier transform and Welch methods. These indicators directly relate to those obtained through the relation between HRV and BPV. BRS_{LF} , as illustrated in Figure 5.14, significantly decreased upon standing, reflecting the effects of both sympathetic and vagal activities.

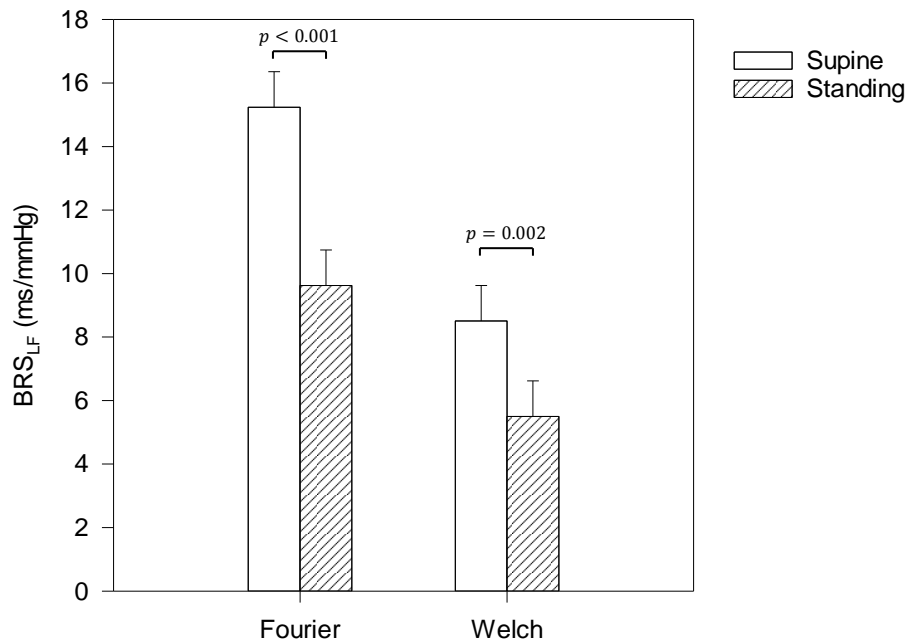


Figure 5.14 – Low frequency baroreflex sensitivity, BRS_{LF} (0.04-0.15 Hz), calculated from the transfer functions estimated using the Fourier transform, and the Welch method, for subjects in supine and standing postures. The reduction in BRS_{LF} in standing results from shifts in both vagal and sympathetic activities.

BRS_{HF} significantly decreased in standing posture compared to supine, as shown in Figure 5.15, suggesting vagal withdrawal.

Figure 5.16 illustrate the results found for BRS_{α} , showing a significant decrease upon standing and is mostly an indicator of reflex vagal activity.

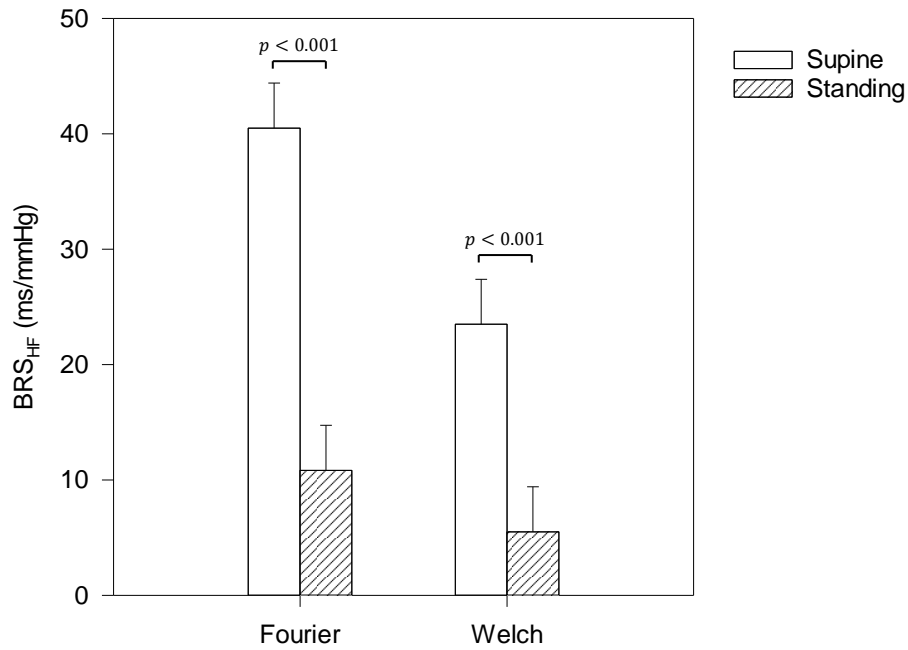


Figure 5.15 – High frequency baroreflex sensitivity, BRS_{HF} (0.15-0.4 Hz), calculated from the transfer functions estimated using the Fourier transform, and the Welch method, for subjects in supine and standing postures. The decrease in BRS_{HF} in standing relates to vagal activity withdrawal.

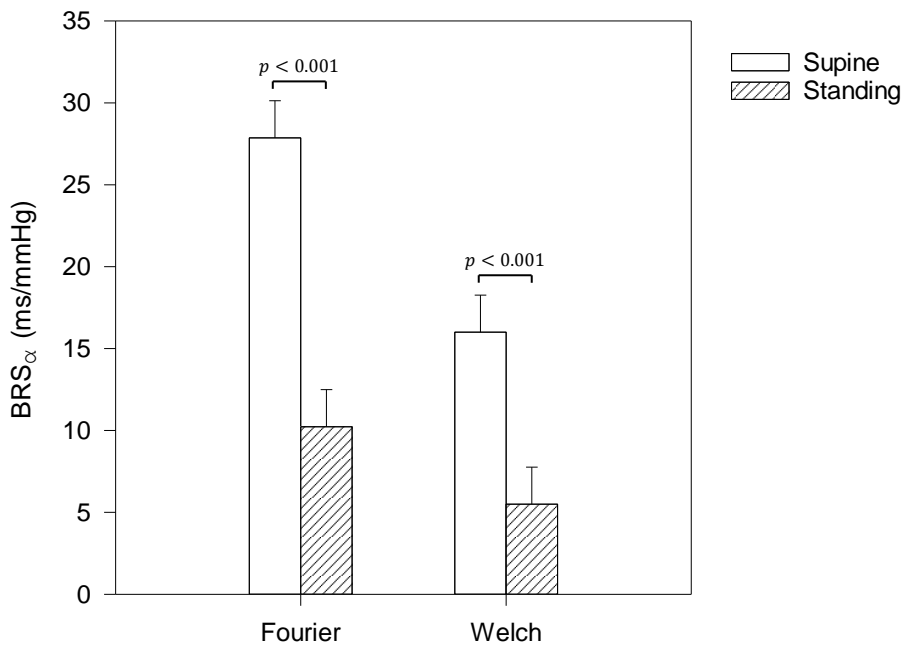


Figure 5.16 – Overall baroreflex sensitivity, BRS_{α} , calculated as the mean value between low frequency (0.04-0.15 Hz) and high frequency (0.15-0.4 Hz) sensitivities, BRS_{LF} and BRS_{HF} , for subjects in supine and standing postures. BRS_{LF} and BRS_{HF} were calculated in each frequency band from the transfer functions estimated using the Fourier transform, and the Welch method. BRS_{α} is proportional to reflex vagal activity.

5.3.3. Impulse response

The ABR impulse response was estimated from the ARX, LBF and MBF models. All ABR indicators related to the impulse response showed a significant decrease in standing. The ABR_{IRM} gain, an indicator of overall BRS gain, shown in Figure 5.17, presented significant decrease for all models.

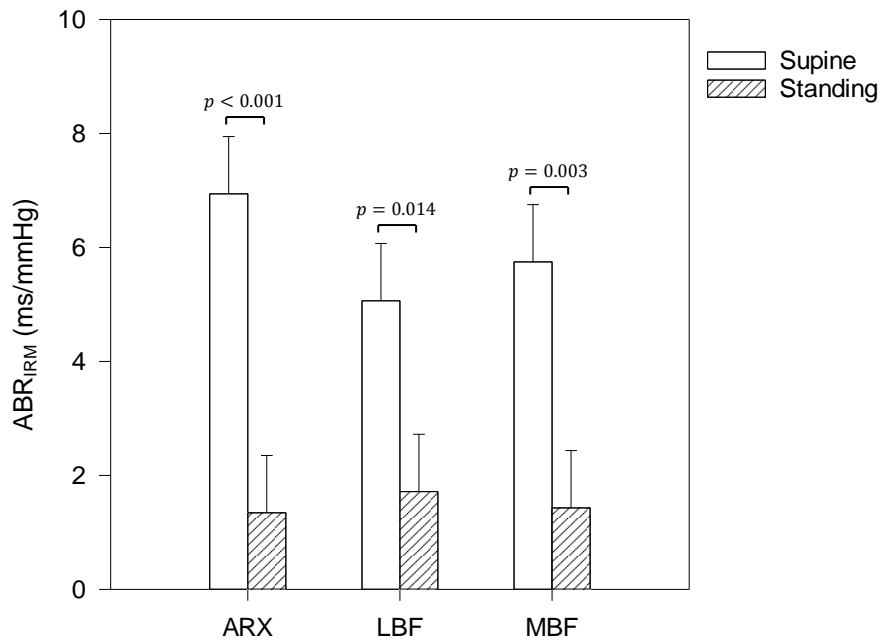


Figure 5.17 – Arterial baroreflex impulse response magnitude, ABR_{IRM} , as a measure of overall gain calculated from the impulse responses estimated through the ARX, LBF, and MBF models, for subjects in supine and standing postures.

The overall ABR_{TOT} gain, determined from the transfer function calculated from the impulse response in both the LF and HF regions, also significantly diminished in standing compared to supine, as illustrated in Figure 5.18.

Figure 5.19 shows the results for the ABR_{LF} gain. A significant decrease was only verified for the ABR_{LF} calculated from the ARX impulse response, but not from LBF and MBF.

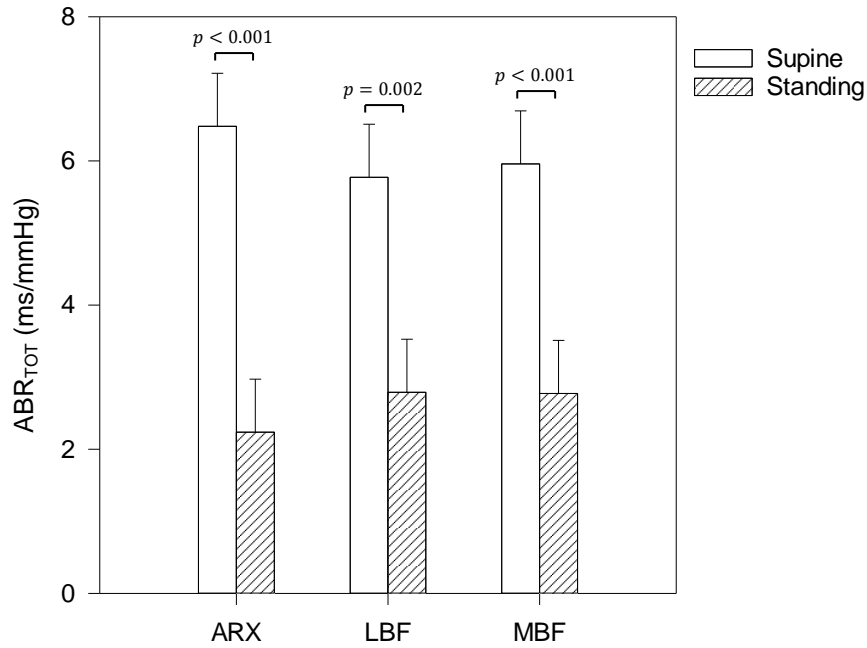


Figure 5.18 – Arterial baroreflex total dynamic gain, ABR_{TOT} (0.04-0.4 Hz), as an overall measure of gain calculated from the impulse responses estimated through the ARX, LBF, and MBF models, for subjects in supine and standing postures.

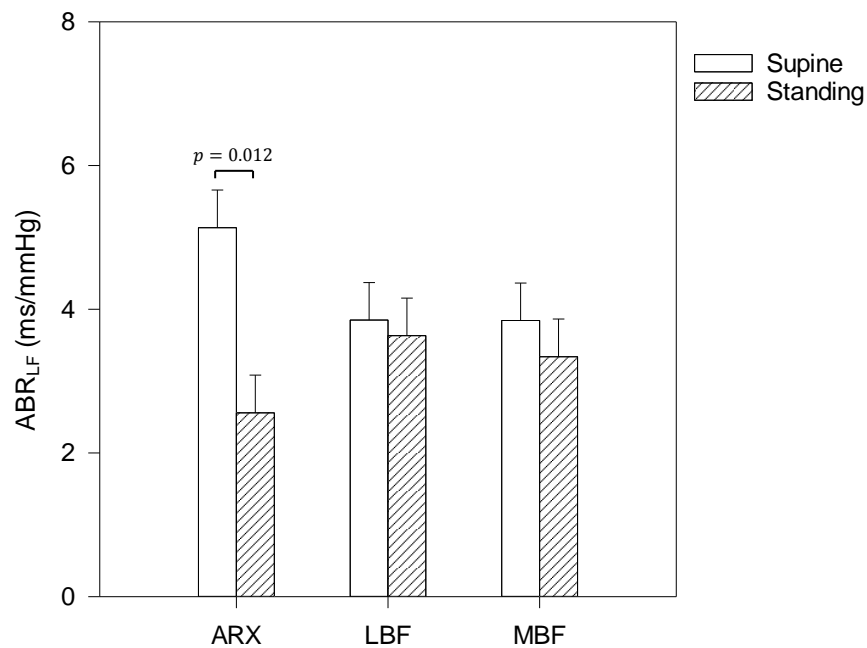


Figure 5.19 – Arterial baroreflex low frequency dynamic gain, ABR_{LF} (0.04-0.15 Hz), calculated from the impulse responses estimated through the ARX, LBF, and MBF models, for subjects in supine and standing postures.

As for the ABR_{HF} component, there was a significant decrease from supine to standing for all models, as shown in Figure 5.20.

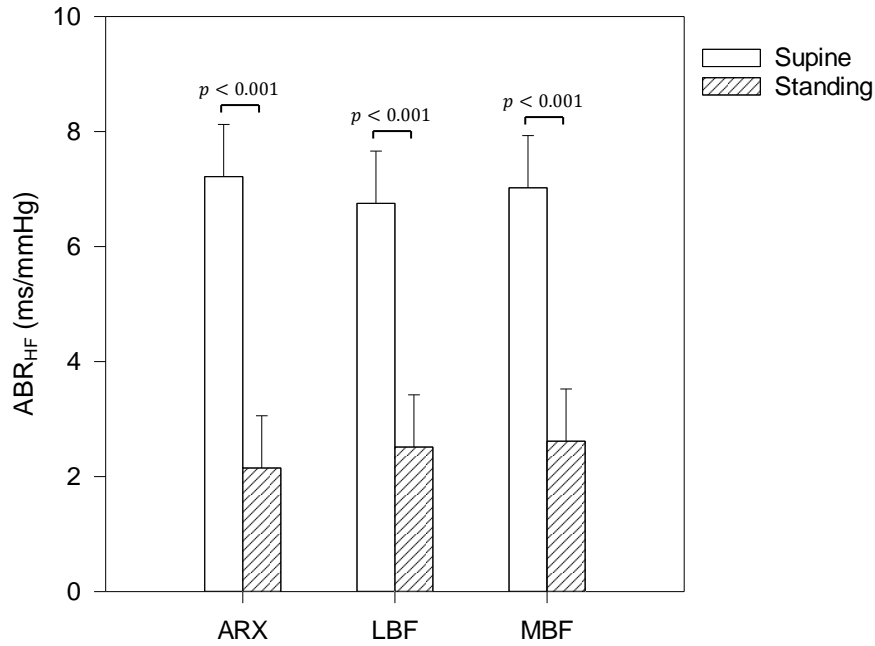


Figure 5.20 – Arterial baroreflex high frequency dynamic gain, ABR_{HF} (0.15-0.4 Hz), calculated from the impulse responses estimated through the ARX, LBF, and MBF models, for subjects in supine and standing postures.

5.4. CORRELATION ANALYSES

This section presents the results from the correlation analyses that were performed between pairs of indicators, as described in section 4.6.

5.4.1. HRV and RSA/RCC

HRV indicators were correlated to both RSA and RCC indicators, in both HF and LF in supine and standing postures, as detailed in the next subsections. The correlations were performed between the indicators obtained from all available methods for each case.

5.4.1.1. HF supine

In supine posture, both the RSA_{HF} index, calculated from the spectral transfer functions, and RCC_{HF} , calculated from the Fourier transform of the impulse responses, showed a strong positive correlation to the HRV_{HF} ($0.809 \leq r \leq 0.863, p < 0.001$), as shown in Table 5.2.

Table 5.2 – Pearson’s correlation coefficients and level of significance between HRV_{HF} , and both HF indicators of respiratory sinus arrhythmia (RSA) obtained from subjects in supine posture: RSA_{HF} , which quantifies direct and indirect effects of respiration on HRV and is derived from transfer function analysis, and RCC_{HF} , the respiratory-cardiac coupling (RCC), which accounts only for the direct influence of respiration on HRV and is derived from impulse response analysis.

HRV_{HF} (supine)	RSA_{HF} (supine)		RCC_{HF} (supine)		
	Fourier	Welch	ARX	LBF	MBF
Fourier	0.809***	0.860***	0.845***	0.814***	0.810***
Welch	0.812***	0.861***	0.850***	0.814***	0.810***
AR	0.815***	0.863***	0.851***	0.812***	0.814***

*** $p < 0.001$.

HRV_{HF} also showed strong correlation to the overall RCC gain indicator RCC_{IRM} , calculated from the impulse responses ($0.756 \leq r \leq 0.805, p < 0.001$). These correlations are presented in Table 5.3.

Table 5.3 – Pearson’s correlation coefficients and level of significance between HRV_{HF} and the impulse response magnitude (IRM), as a measure of overall gain of the respiratory-cardiac coupling (RCC), quantifying the direct effects of respiration on HRV through impulse response analysis, from subjects in supine posture.

HRV_{HF} (supine)	RCC_{IRM} (supine)		
	ARX	LBF	MBF
Fourier	0.762***	0.756***	0.805***
Welch	0.785***	0.761***	0.799***
AR	0.788***	0.758***	0.797***

*** $p < 0.001$.

5.4.1.2. HF standing

Both RSA_{HF} , calculated from the transfer functions, and RCC_{HF} , calculated from the impulse responses, also correlated strongly and positively to HRV_{HF} in standing posture ($0.772 \leq r \leq 0.905, p < 0.001$), as shown in Table 5.4.

There was a strong correlation between HRV_{HF} and the overall RCC gain indicator RCC_{IRM} ($0.700 \leq r \leq 0.903, p < 0.001$), presented in Table 5.5.

Table 5.4 – Pearson’s correlation coefficients and level of significance between HRV_{HF} and both HF indicators of respiratory sinus arrhythmia (RSA) obtained from subjects in standing posture: RSA_{HF} , which quantifies direct and indirect effects of respiration on HRV and is derived from transfer function analysis, and RCC_{HF} , the respiratory-cardiac coupling (RCC), which accounts only for the direct influence of respiration on HRV and is derived from impulse response analysis.

HRV_{HF} (stand)	RSA_{HF} (stand)		RCC_{HF} (stand)		
	Fourier	Welch	ARX	LBF	MBF
Fourier	0.885***	0.900***	0.823***	0.808***	0.772***
Welch	0.891***	0.905***	0.838***	0.831***	0.798***
AR	0.889***	0.904***	0.837***	0.837***	0.808***

*** $p < 0.001$.

Table 5.5 – Pearson’s correlation coefficients and level of significance between HRV_{HF} and the impulse response magnitude (IRM), as a measure of overall gain, of the respiratory-cardiac coupling (RCC), quantifying the direct effects of respiration on HRV through impulse response analysis, from subjects in standing posture.

HRV_{HF} (stand)	RCC_{IRM} (stand)		
	ARX	LBF	MBF
Fourier	0.893***	0.747***	0.700***
Welch	0.903***	0.781***	0.732***
AR	0.902***	0.789***	0.727***

*** $p < 0.001$.

While the correlations between HRV_{HF} and RSA_{HF} are stronger in standing, the correlations between HRV_{HF} and RCC_{HF} are stronger in the supine posture. Although the differences between the corresponding coefficients for each posture are small, they are consistent across all methods. An example of these findings is illustrated in Figure 5.21, comparing the correlations between HRV_{HF} (Fourier transform) and both RSA_{HF} (Fourier transform) (Figure 5.21 (a,c)), and RCC_{HF} (MBF model) (Figure 5.21 (b,d)), in supine (Figure 5.21 (a,b)), and standing (Figure 5.21 (c,d)) postures. While some of correlations between HRV_{HF} and RCC_{IRM} are stronger in standing, others are stronger in supine posture.

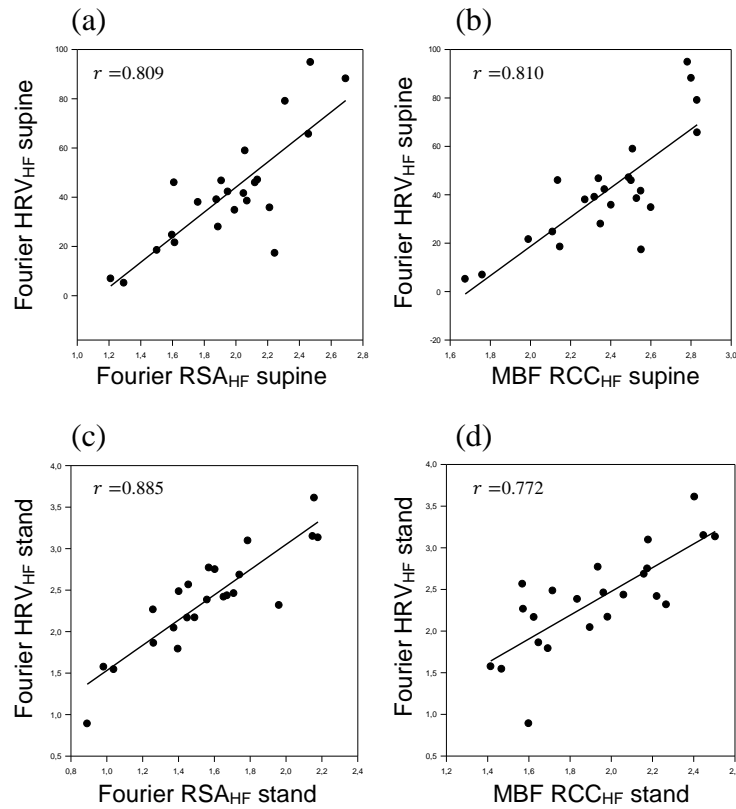


Figure 5.21 – Correlations between HRV_{HF} obtained from the Fourier transform method and RSA_{HF} , which quantifies direct and indirect effects of respiration on HRV and is derived from the Fourier transform transfer function (a,c); and between HRV_{HF} obtained from the Fourier transform method and RCC_{HF} , which accounts only for the direct influence of respiration on HRV, referred to as respiratory-cardiac coupling (RCC), derived from the Meixner basis function (MBF) impulse response (b,d). Comparing the correlations in supine (a,b) and standing (c,d) postures, it is shown that while the correlation between HRV_{HF} and RSA_{HF} is stronger in standing posture, the opposite is true between HRV_{HF} and RCC_{HF} .

5.4.1.3. LF supine

In supine posture there were no significant correlations between HRV_{LF} , and RSA_{LF} calculated from the spectral transfer functions. Comparing HRV_{LF} and RCC_{LF} , estimated from the impulse response, significant correlations were only found for RCC_{LF} estimated from LFB and MBF models, but not between the spectral HRV_{LF} index estimated from the Fourier transform PSD and RCC_{LF} estimated from the MBF model. The significant correlations were weak to moderate ($0.416 \leq r \leq 0.562, p < 0.05$), as shown in Table 5.6.

Table 5.6 – Pearson’s correlation coefficients and level of significance between HRV_{LF} , and both LF indicators of respiratory sinus arrhythmia (RSA) obtained from subjects in supine posture: RSA_{LF} , which quantifies direct and indirect effects of respiration on HRV and is derived from transfer function analysis, and RCC_{LF} , the respiratory-cardiac coupling (RCC), which accounts only for the direct influence of respiration on HRV and is derived from impulse response analysis.

HRV_{LF} (supine)	RSA_{LF} (supine)		RCC_{LF} (supine)		
	Fourier	Welch	ARX	LBF	MBF
Fourier	0.164	0.294	0.296	0.428*	0.381
Welch	0.284	0.453	0.392	0.562**	0.536**
AR	0.172	0.309	0.269	0.447*	0.416*

* $p < 0.05$; ** $p < 0.01$.

HRV_{LF} is moderately correlated to the overall indicator RCC_{IRM} ($0.450 \leq r \leq 0.608, p < 0.05$), as shown in Table 5.7.

Table 5.7 – Pearson’s correlation coefficients and level of significance between HRV_{LF} and the impulse response magnitude (IRM), as a measure of overall gain, of the respiratory-cardiac coupling (RCC), quantifying the direct effects of respiration on HRV through impulse response analysis, from subjects in supine posture.

HRV_{LF} (supine)	RCC_{IRM} (supine)		
	ARX	LBF	MBF
Fourier	0.485*	0.558**	0.548**
Welch	0.500*	0.572**	0.608**
AR	0.450*	0.514*	0.502*

* $p < 0.05$; ** $p < 0.01$.

5.4.1.4. LF standing

Table 5.8 presents the correlation results in the standing posture between HRV_{LF} and both RSA_{LF} and RCC_{LF} . The only non-significant correlations were those between HRV_{LF} and RCC_{LF} estimated from either the ARX or the MBF models, and the correlation between HRV_{LF} estimated from the Welch method and RCC_{LF} estimated from the ARX model. The significant correlations were weak to moderate ($0.417 \leq r \leq 0.607, p < 0.05$).

Table 5.8 – Pearson’s correlation coefficients and level of significance between HRV_{LF} , and both LF indicators of respiratory sinus arrhythmia (RSA) obtained from subjects in standing posture: RSA_{LF} , which quantifies direct and indirect effects of respiration on HRV and is derived from transfer function analysis, and RCC_{LF} , the respiratory-cardiac coupling (RCC), which accounts only for the direct influence of respiration on HRV and is derived from impulse response analysis.

HRV_{LF}	RSA_{LF}		RCC_{LF}		
	Fourier	Welch	ARX	LBF	MBF
Fourier	0.489*	0.578**	0.305	0.446*	0.377
Welch	0.460*	0.607**	0.358	0.493*	0.417*
AR	0.451**	0.584**	0.426*	0.513*	0.440*

* $p < 0.05$; ** $p < 0.01$.

HRV_{LF} is also moderately correlated to the overall indicator RCC_{IRM} ($0.448 \leq r \leq 0.663, p < 0.05$), using any method, as shown in Table 5.9.

Table 5.9 – Pearson’s correlation coefficients and level of significance between HRV_{LF} and the impulse response magnitude (IRM), as a measure of overall gain, of the respiratory-cardiac coupling (RCC), quantifying the direct effects of respiration on HRV through impulse response analysis, from subjects in standing posture.

HRV_{LF}	RCC_{IRM}		
	ARX	LBF	MBF
Fourier	0.547**	0.511*	0.448*
Welch	0.607**	0.560**	0.544**
AR	0.663***	0.546**	0.595**

* $p < 0.05$; ** $p < 0.01$; *** $p < 0.001$.

Comparing the supine and standing correlations shown in tables Table 5.6 and Table 5.8, it is clear from the correlation coefficients that the correlations are stronger in standing than supine for RSA_{LF} . There is no clear trend when comparing correlations between HRV and both RCC_{LF} and the overall RCC_{IRM} in terms of whether the stand or supine postures present stronger correlation coefficients.

5.4.1.5. LF and HF correlations

For all supine indices, the correlations between the corresponding HF indices were stronger than between the associated LF indices. For example, Figure 5.22 shows the correlation plots in for the HF (Figure 5.22 (a,b,c)) and LF (Figure 5.22 (d,e,f))

components. In particular, Figure 5.22 (a) and (d) show the correlation between the HF and LF components of HRV (AR model) and RSA (Fourier transform), respectively. Figure 5.22 (b) and (e) illustrate the correlation between the HF and LF components of HRV (Welch method) and RCC (MBF model). Finally, Figure 5.22 (c) and (f) show the correlation between the HF and LF components of HRV (Welch method) vs. RCC_{IRM} (ARX model). For all supine indices, the results show that the RSA and RCC indicators correlate more strongly to HRV in the HF than in the LF band. Likewise, the correlation between HRV and the overall indicator RCC_{IRM} is also stronger for the HF components.

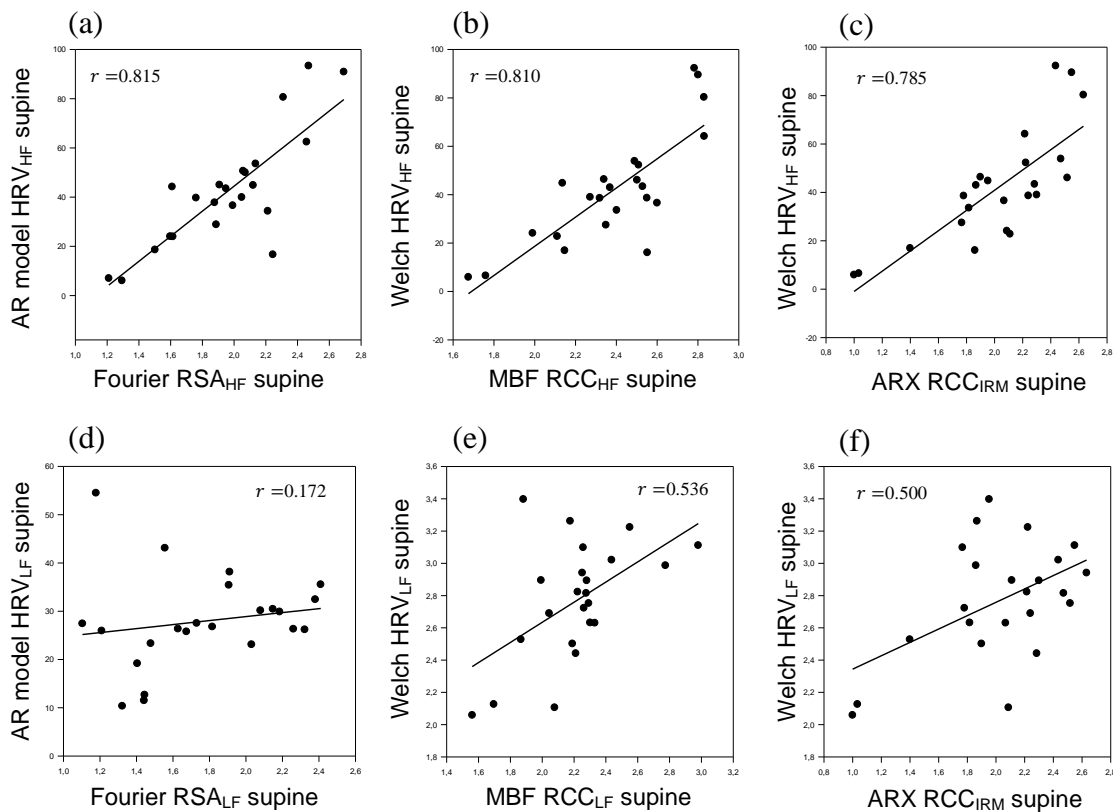


Figure 5.22 – Correlations for supine posture between HRV obtained from the AR model and respiratory sinus arrhythmia (RSA), which quantifies direct and indirect effects of respiration on HRV, derived from the Fourier transform transfer function (a,d); between HRV obtained from the Welch method and respiratory-cardiac coupling (RCC), which accounts only for the direct influence of respiration on HRV, from the MBF impulse response (b,e); and between HRV obtained from the Welch method and the impulse response magnitude (IRM), as a measure of overall gain, from the ARX impulse response (c,f). The correlations are stronger in HF (a,b,c) compared to LF (d,e,f) for all combinations.

Figure 5.23 illustrates the correlations between the same variables presented in Figure 5.22, but for the standing posture data. In standing posture the same tendencies as those

found for the supine posture are observed, with all correlations presenting stronger coefficients in HF rather than on the LF band.

These findings are consistent with the hypothesis that HF HRV reflects respiratory activity [3, 4, 6, 7], as the correlations between those mechanisms and HRV are strong in this frequency band. It is also consistent with the fact that respiratory mechanisms are considered mainly vagally mediated dynamics, as discussed in section 2.3.

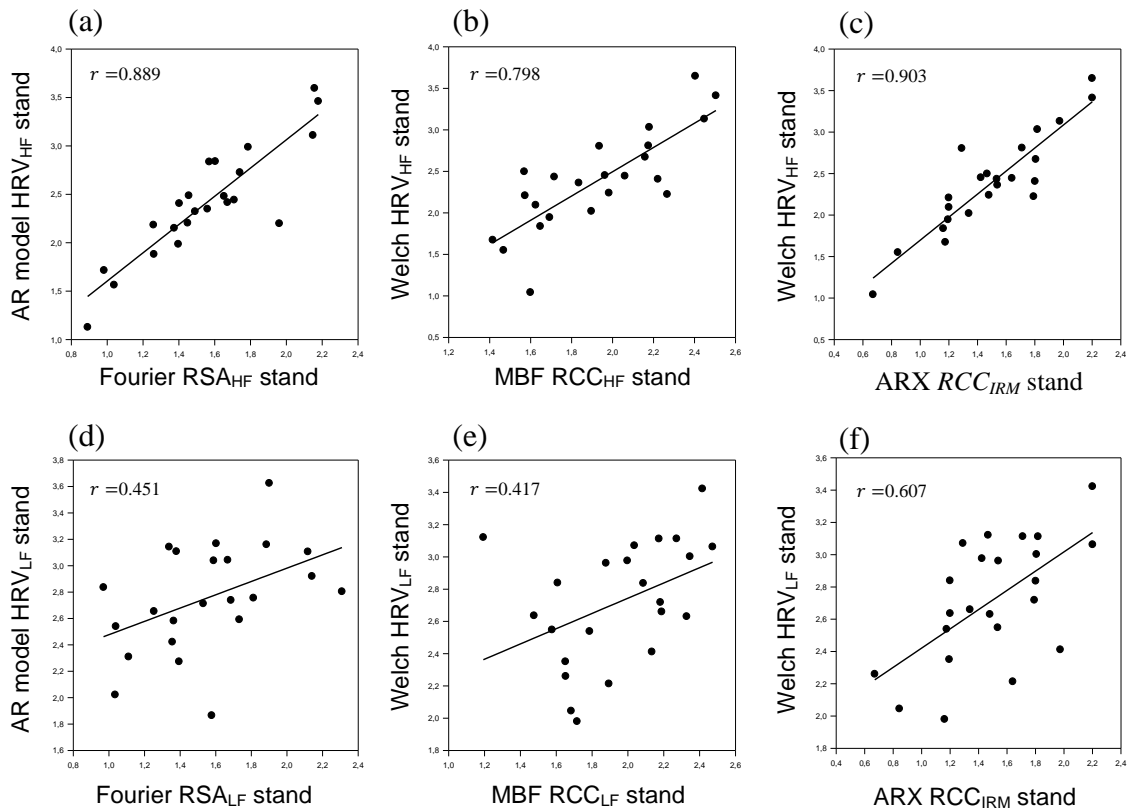


Figure 5.23 – Correlations for standing posture between HRV obtained from the AR model and respiratory sinus arrhythmia (RSA), which quantifies direct and indirect effects of respiration on HRV, derived from the Fourier transform transfer function (a,d); between HRV obtained from the Welch method and respiratory-cardiac coupling (RCC), which accounts only for the direct influence of respiration on HRV, from the MBF impulse response (b,e); and between HRV obtained from the Welch method and the impulse response magnitude (IRM), as a measure of overall gain, from the ARX impulse response (c,f). The correlations are stronger in HF (a,b,c) compared to LF (d,e,f) for all combinations.

5.4.2. HRV and BRS/ABR

HRV indicators were correlated to both BRS and ABR indices, in both HF and LF, in the supine and standing postures. In terms of the LF components, the correlations between spectral BRS indicators and impulse response ABR indicators were significant in standing,

but in supine correlation depended on the methods used. These results will be presented in the following subsections.

5.4.2.1. HF supine

The correlations between HRV_{HF} and the spectral BRS estimate, α_{HF} , as well as those between HRV_{HF} and BRS_{HF} obtained from spectral transfer functions, in supine, are moderate to strong ($0.695 \leq r \leq 0.787, p < 0.001$). These results are presented in Table 5.10.

Table 5.10 – Pearson’s correlation coefficients and level of significance between indicators of HRV_{HF} , and both baroreflex sensitivity (BRS) indicators, in supine posture: α_{HF} , calculated as the square root of the ratio between HRV and BPV powers, derived from PSD analyses; and BRS_{HF} , derived from the transfer function analysis.

HRV_{HF} (supine)	α_{HF} (supine)			BRS_{HF} (supine)	
	Fourier	Welch	AR	Fourier	Welch
Fourier	0.760***	0.787***	0.783***	0.704***	0.777***
Welch	0.742***	0.783***	0.778***	0.698***	0.767***
AR	0.731***	0.782***	0.780***	0.695***	0.758***

*** $p < 0.001$.

The correlations between HRV_{HF} and ABR_{HF} (obtained from the impulse responses), were weaker than those observed between HRV_{HF} and the spectral BRS estimates ($0.605 \leq r \leq 0.711, p < 0.01$). HRV_{HF} also showed a stronger correlation to the overall ABR gain indicator and ABR_{IRM} ($0.518 \leq r \leq 0.770, p < 0.05$). These correlations are shown in Table 5.11.

Table 5.11 – Pearson’s correlation coefficients and level of significance between HRV_{HF} and both indicators derived from the arterial baroreflex (ABR) impulse response, obtained in supine posture: ABR_{HF} , and ABR_{IRM} , the impulse response magnitude (IRM) as a measure of overall gain.

HRV_{HF} (supine)	ABR_{HF} (supine)			ABR_{IRM} (supine)		
	ARX	LBF	MBF	ARX	LBF	MBF
Fourier	0.711***	0.626**	0.631**	0.757***	0.613**	0.569**
Welch	0.691**	0.610**	0.610**	0.758***	0.585**	0.518*
AR	0.698***	0.605**	0.604**	0.770***	0.590**	0.520*

* $p < 0.5$; ** $p < 0.01$; *** $p < 0.001$.

5.4.2.2. HF standing

Table 5.12 shows the correlations between HRV_{HF} and both α_{HF} and BRS_{HF} . All results show a strong positive correlation ($0.826 \leq r \leq 0.888, p < 0.001$).

Table 5.12 – Pearson’s correlation coefficients and level of significance between indicators of HRV_{HF} , and both baroreflex sensitivity (BRS) indicators, in standing posture: α_{HF} , calculated as the square root of the ratio between HRV and BPV powers, derived from PSD analyses; and BRS_{HF} , derived from the transfer function analysis.

HRV_{HF} (stand)	α_{HF} (stand)			BRS_{HF} (stand)	
	Fourier	Welch	AR	Fourier	Welch
Fourier	0.875***	0.888***	0.886***	0.855***	0.851***
Welch	0.843***	0.875***	0.877***	0.829***	0.835***
AR	0.837***	0.873***	0.881***	0.826***	0.839***

*** $p < 0.001$.

Table 5.13 shows the correlations between HRV_{HF} and both ABR_{HF} and ABR_{IRM} ($0.465 \leq r \leq 0.569, p < 0.05$). These correlations are weaker than those obtained between HRV_{HF} and the spectral BRS estimates shown in table 5.12. In particular, while the correlations between HRV_{HF} and all ABR_{HF} indices were significant, the HRV_{HF} indices were only significantly correlated to the overall ABR gain indicator estimated from the ARX impulse response ($0.539 \leq r \leq 0.555, p < 0.01$).

Table 5.13 – Pearson’s correlation coefficients and level of significance between HRV_{HF} and both indicators derived from the arterial baroreflex (ABR) impulse response, obtained in standing posture: ABR_{HF} , and ABR_{IRM} , the impulse response magnitude (IRM) as a measure of overall gain.

HRV_{HF} (stand)	ABR_{HF} (stand)			ABR_{IRM} (stand)		
	ARX	LBF	MBF	ARX	LBF	MBF
Fourier	0.465*	0.510*	0.548**	0.539**	0.290	0.173
Welch	0.466*	0.551**	0.562**	0.537**	0.341	0.233
AR	0.476*	0.564**	0.569**	0.555**	0.354	0.240

* $p < 0.5$; ** $p < 0.01$.

Figure 5.24 shows the correlations between HRV_{HF} (Fourier transform) and the spectral BRS indicators, α_{HF} (Fourier transform) and BRS_{HF} (Fourier transform), in both postures. The correlations between HRV_{HF} and α_{HF} (Figure 5.24 (a,c)), and between HRV_{HF} and

BRS_{HF} (Figure 5.24 (b,d)) are illustrated for supine (Figure 5.24 (a,b)) and standing (Figure 5.24 (c,d)) postures. These results show that the correlations between the indices are stronger in standing posture.

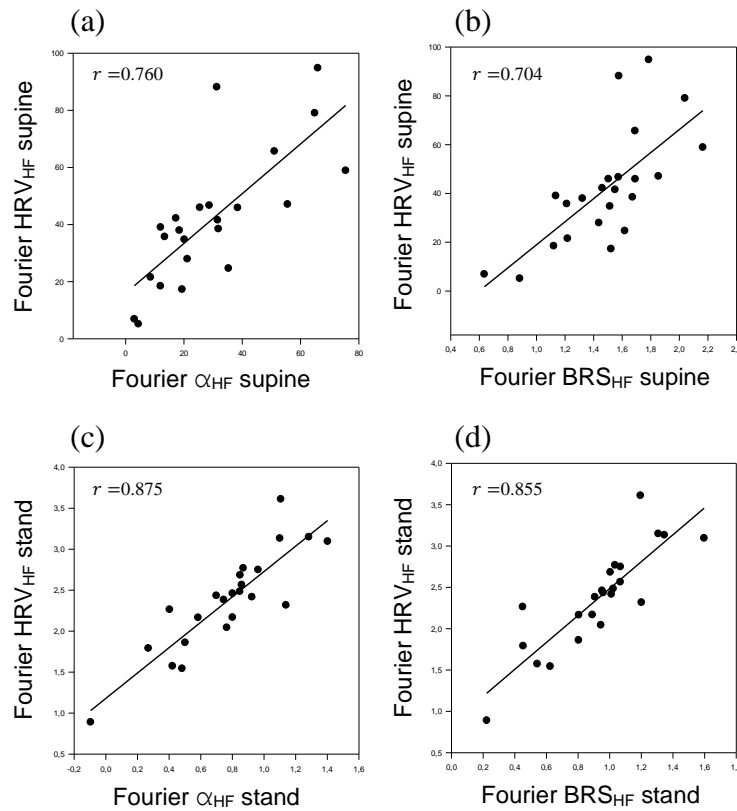


Figure 5.24 – Correlations between HRV_{HF} and spectral baroreflex sensitivity (BRS) indicators, all obtained from the Fourier transform: α_{HF} , which quantifies BRS from the square root of the ratio between HRV and BPV powers, obtained from PSD analysis (a,c); and BRS_{HF} , calculated from the transfer function analysis (b,d). The correlations are stronger in standing posture for spectral indicators (c,d) than supine (a,b).

Figure 5.25 shows the correlations between HRV_{HF} (Fourier transform) and the ABR (ARX model) indicators. In this case, the supine indices showed stronger correlations. Figure 5.25 (a,e) illustrates the correlations between HRV_{HF} and ABR_{HF} and Figure 5.25 (b,d) shows the correlations between HRV_{HF} and ABR_{IRM} , in supine (Figure 5.25 (a,b)) and standing (Figure 5.25 (e,f)) postures.

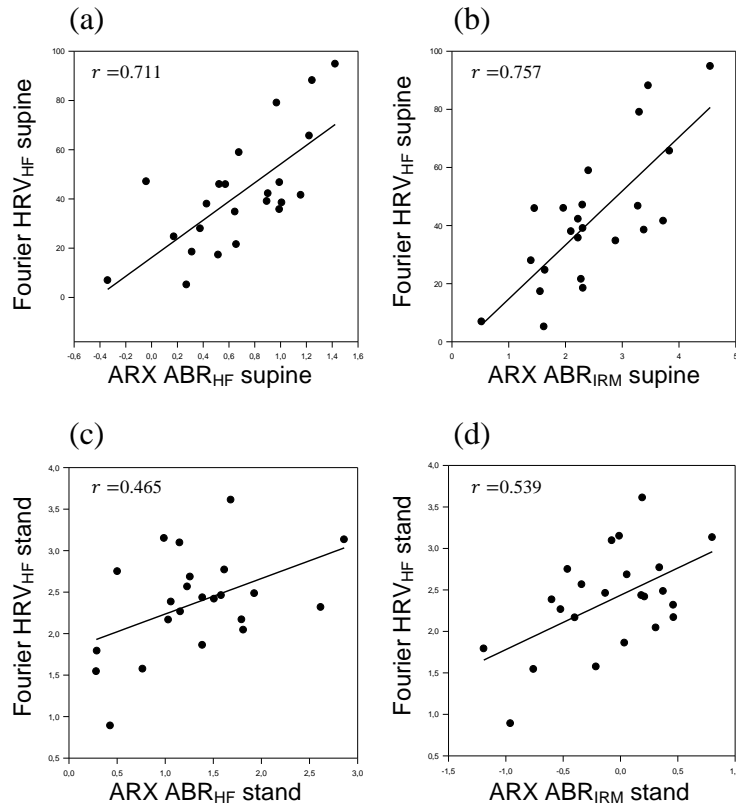


Figure 5.25 – Correlations between HRV_{HF} obtained from the Fourier transform and arterial baroreflex (ABR) ARX impulse response indicators: ABR_{HF} (c,g); and ABR_{IRM} , which is a measure of overall gain (d,h). The correlations are stronger in supine posture (a,b), rather than standing (e,f).

5.4.2.3. LF supine

In supine posture, HRV_{LF} correlates positively to the spectral BRS indicators α_{LF} and also to BRS_{LF} , obtained from spectral transfer functions, for all methods available ($0.418 \leq r \leq 0.662, p < 0.05$), as shown in Table 5.14.

Table 5.14 – Pearson’s correlation coefficients and level of significance between indicators of HRV_{LF} , and both baroreflex sensitivity (BRS) indicators, in supine posture: α_{LF} , calculated as the square root of the ratio between HRV and BPV powers, derived from PSD analyses; and BRS_{LF} , derived from the transfer function analysis.

HRV_{LF} (supine)	α_{LF} (supine)			BRS_{LF} (supine)	
	Fourier	Welch	AR	Fourier	Welch
Fourier	0.607**	0.662**	0.431*	0.559**	0.640**
Welch	0.573**	0.626**	0.418*	0.557**	0.631**
AR	0.644***	0.643***	0.485*	0.526**	0.595**

* $p < 0.05$; ** $p < 0.01$; *** $p < 0.001$.

Table 5.15 shows the positive correlations found between HRV_{LF} and ABR_{LF} , estimated from the impulse response ($0.390 \leq r \leq 0.560, p < 0.05$). The overall ABR_{IRM} indicator obtained from the ARX model showed no significant correlation to the HRV_{LF} indicators. The HRV_{LF} estimated from the Fourier transform and Welch methods and ABR_{IRM} calculated from LBF and MBF impulse responses present moderate correlations ($0.414 \leq r \leq 0.503, p < 0.05$).

Table 5.15 – Pearson’s correlation coefficients and level of significance between HRV_{LF} and both indicators derived from the arterial baroreflex (ABR) impulse response, obtained in supine posture: ABR_{LF} and ABR_{IRM} , the impulse response magnitude (IRM) as a measure of overall gain.

HRV_{LF} (supine)	ABR_{LF} (supine)			ABR_{IRM} (supine)		
	ARX	LBF	MBF	ARX	LBF	MBF
Fourier	0.494*	0.498*	0.453*	0.251	0.470*	0.414*
Welch	0.452*	0.556**	0.560**	0.172	0.503*	0.471*
AR	0.390*	0.490*	0.491*	0.162	0.341	0.253

* $p < 0.05$; ** $p < 0.01$.

Correlation between the impulse response ABR_{LF} indicator and the spectral BRS indicators α_{LF} and was significant for two of the nine combinations of methods, and between ABR_{LF} and BRS_{LF} , estimated from the spectral transfer function, for three of the six combinations. The significant correlations were moderate ($0.416 \leq r \leq 0.679, p < 0.05$), as shown in Table 5.16,

Table 5.16 – Pearson’s correlation coefficients and level of significance between the impulse response indicator of arterial baroreflex (ABR) ABR_{LF} , and the baroreflex sensitivity (BRS) indicators obtained from spectral methods in supine posture: α_{LF} , calculated as the square root of the ratio between HRV and BPV, and BRS_{LF} , obtained from the transfer function analysis.

ABR_{LF} (supine)	α_{LF} (supine)			BRS_{LF} (supine)	
	Fourier	Welch	AR	Fourier	Welch
ARX	0.416*	0.384	0.351	0.355	0.305
LBF	0.402	0.435*	0.344	0.464*	0.679***
MBF	0.281	0.303	0.165	0.350	0.523*

* $p < 0.05$; *** $p < 0.001$.

5.4.2.4. LF standing

Table 5.17 presents the correlation results between HRV_{LF} and both α_{LF} and BRS_{LF} in standing posture. For all methods correlations were strong ($0.650 \leq r \leq 0.792, p < 0.001$).

Table 5.17 – Pearson’s correlation coefficients and level of significance between indicators of HRV_{LF} , and both baroreflex sensitivity (BRS) indicators, in standing posture: α_{LF} , calculated as the square root of the ratio between HRV and BPV powers, derived from PSD analyses; and BRS_{LF} , derived from the transfer function analysis.

HRV_{LF} (stand)	α_{LF} (stand)			BRS_{LF} (stand)	
	Fourier	Welch	AR	Fourier	Welch
Fourier	0.792***	0.773***	0.735***	0.650***	0.778***
Welch	0.763***	0.772***	0.748***	0.657***	0.777***
AR	0.758***	0.760***	0.753***	0.688***	0.762***

*** $p < 0.001$.

The correlation between HRV_{LF} and ABR_{LF} , obtained from the impulse responses, presented in Table 5.18, was significant for all methods ($0.433 \leq r \leq 0.705, p < 0.05$). Correlation between HRV_{LF} and the overall ABR gain indicator ABR_{IRM} were only significant for the ABR_{IRM} estimated from the LBF model ($0.529 \leq r \leq 0.550, p < 0.01$).

Table 5.18 – Pearson’s correlation coefficients and level of significance between HRV_{LF} and both indicators derived from the arterial baroreflex (ABR) impulse response, obtained in standing posture: ABR_{LF} , and ABR_{IRM} , the impulse response magnitude (IRM) as a measure of overall gain.

HRV_{LF} (stand)	ABR_{LF} (stand)			ABR_{IRM} (stand)		
	ARX	LBF	MBF	ARX	LBF	MBF
Fourier	0.433*	0.700***	0.696***	0.309	0.529**	0.219
Welch	0.437*	0.685***	0.666***	0.288	0.550**	0.193
AR	0.450*	0.705***	0.672***	0.319	0.549**	0.216

* $p < 0.05$; ** $p < 0.01$; *** $p < 0.001$.

Table 5.19 shows the correlation between spectral BRS indicators, α_{LF} and BRS_{LF} , and the impulse response indicators ABR_{LF} . The correlations were strong for all indicators and methods ($0.549 \leq r \leq 0.860, p < 0.05$).

Table 5.19 – Pearson’s correlation coefficients and level of significance between the impulse response indicator of arterial baroreflex (ABR) ABR_{LF} , and the baroreflex sensitivity (BRS) indicators obtained from spectral methods in standing posture: α_{LF} , calculated as the square root of the ratio between HRV and BPV, and BRS_{LF} , obtained from the transfer function analysis.

ABR_{LF} (stand)	α_{LF} (stand)			BRS_{LF} (stand)	
	Fourier	Welch	AR	Fourier	Welch
ARX	0.594**	0.596**	0.617**	0.549**	0.613**
LBF	0.850***	0.835***	0.843***	0.811***	0.860***
MBF	0.817***	0.799***	0.813***	0.767***	0.832***

** $p < 0.01$; *** $p < 0.001$.

In LF, correlations between HRV_{LF} and the spectral BRS indicators, α_{LF} and BRS_{LF} , were stronger in standing posture, as was the case in HF. As an example, Figure 5.26 shows the correlation plots for supine (Figure 5.26 (a,b)) and standing (Figure 5.26 (c,d)) postures for the LF band. Figure 5.26 (a) and (c) illustrate the correlation between HRV_{LF} (Welch method) and α_{LF} (AR model) for supine and standing postures, respectively. Figure 5.26 (b) and (d) show the correlation between HRV_{LF} (AR model) and BRS_{LF} (Welch method), for supine and standing postures.

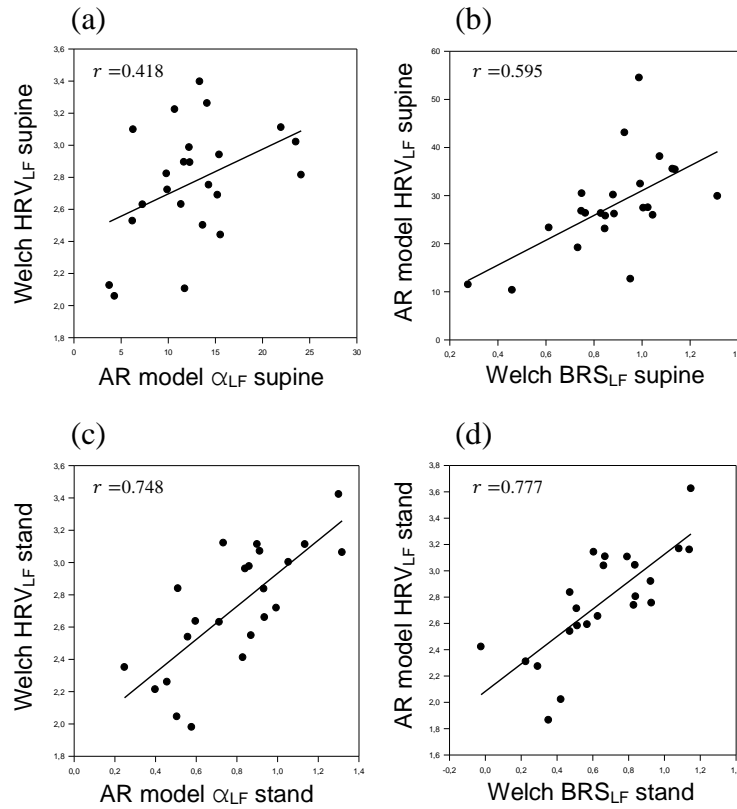


Figure 5.26 – Correlations between HRV_{LF} estimated through the Welch method and α_{LF} , which quantifies baroreflex sensitivity (BRS) from the square root of the ratio between HRV and BPV powers, obtained from PSD analysis using the AR model (a,c); and between HRV_{LF} estimated using the AR model and BRS_{LF} , calculated from the Welch method transfer function analysis (b,c). The correlations are stronger in standing (c,d) rather than supine (a,b) posture.

Stronger correlations were found in standing posture between HRV_{LF} and both ABR_{LF} and the overall ABR_{IRM} . Figure 5.27 shows correlation plots representing those relations in supine (Figure 5.25 (a,b)) and standing (Figure 5.27 (c,d)) postures. Figure 5.27 (a) and (c) illustrate the correlations between HRV_{LF} (Fourier transform) and ABR_{LF} (MBF model), while Figure 5.27 (b) and (d) show the correlation between HRV_{LF} (Fourier transform) and ABR_{IRM} (LBF model).

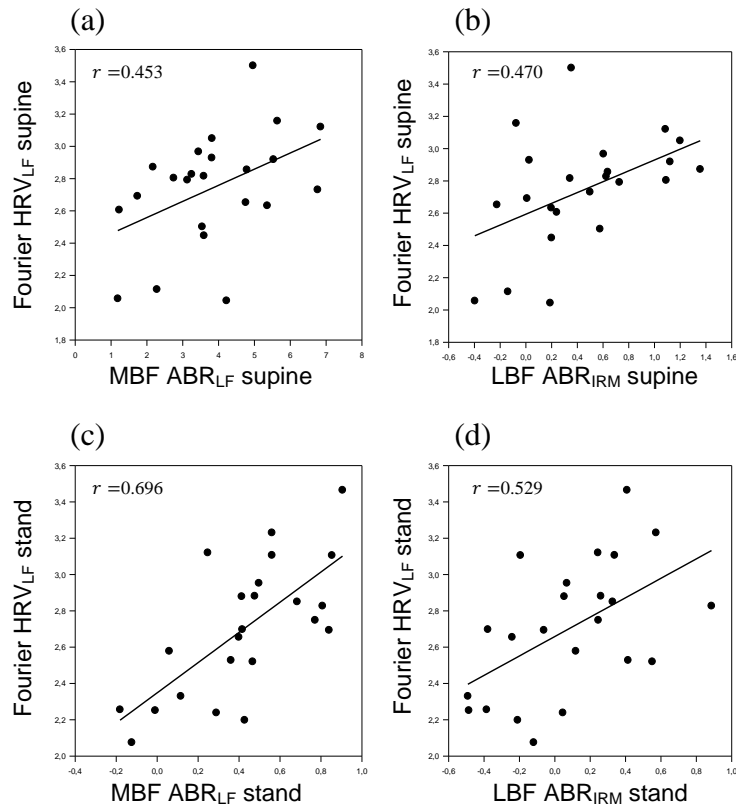


Figure 5.27 – Correlations between HRV_{LF} obtained from the Fourier transform and arterial baroreflex (ABR) impulse response indicators: ABR_{LF} , obtained from the Meixner basis function (MBF) impulse response (a,c); and ABR_{IRM} , which is a measure of overall gain, obtained from the Laguerre basis function (LBF) impulse response (b,d). The correlations are stronger in standing (c,d) rather than supine (a,b) posture.

Finally, the correlations between the impulse response indicator ABR_{LF} and spectral indexes α_{LF} and BRS_{LF} were much stronger in standing posture than supine, as illustrated in Figure 5.28 for supine (Figure 5.28 (a,b)) and standing (Figure 5.28 (c,d)) postures. Figure 5.28 (a) and (c) show the correlation between ABR_{LF} (MBF model) and α_{LF} (Welch method), while Figure 5.28 (a) and (c) show the correlation between ABR_{LF} (MBF model) and BRS_{LF} (Fourier transform).

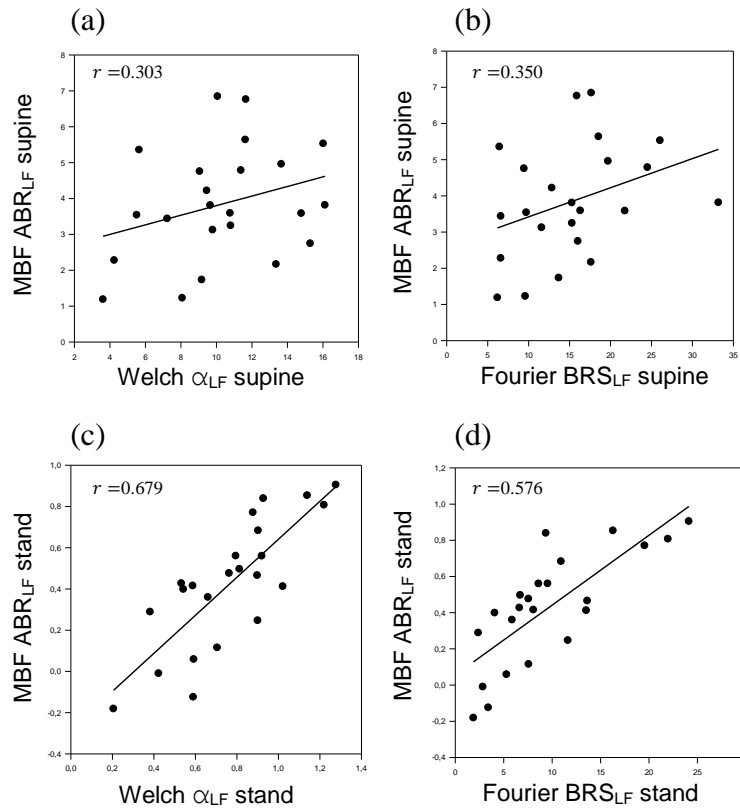


Figure 5.28 – Correlations between the arterial baroreflex (ABR) Meixner basis function (MBF) impulse response ABR_{LF} and spectral baroreflex sensitivity (BRS) indicators: α_{LF} , which quantifies BRS from the square root of the ratio between HRV and BPV powers, obtained from PSD analysis using the Welch method (a,c); and BRS_{LF} , calculated from the Fourier transfer function analysis (b,d). The correlations are stronger in standing (c,d) rather than supine (a,b) posture.

5.4.2.5. LF and HF correlations

The correlations between HRV and spectral BRS estimates are stronger in the HF than in the LF band for both supine and standing postures. Figure 5.29 shows examples of results found in supine posture. Figure 5.29 (a) and (c) show the correlation plot between α_{HF} and α_{LF} (AR model) and the corresponding HRV (Welch method) power. Figure 5.29 (b) and (d) show the correlation plot between HRV (Fourier transform) and BRS (Fourier transform) for the HF and LF components, respectively. Figure 5.30 brings the same correlations presented in Figure 5.29, but for the standing posture.

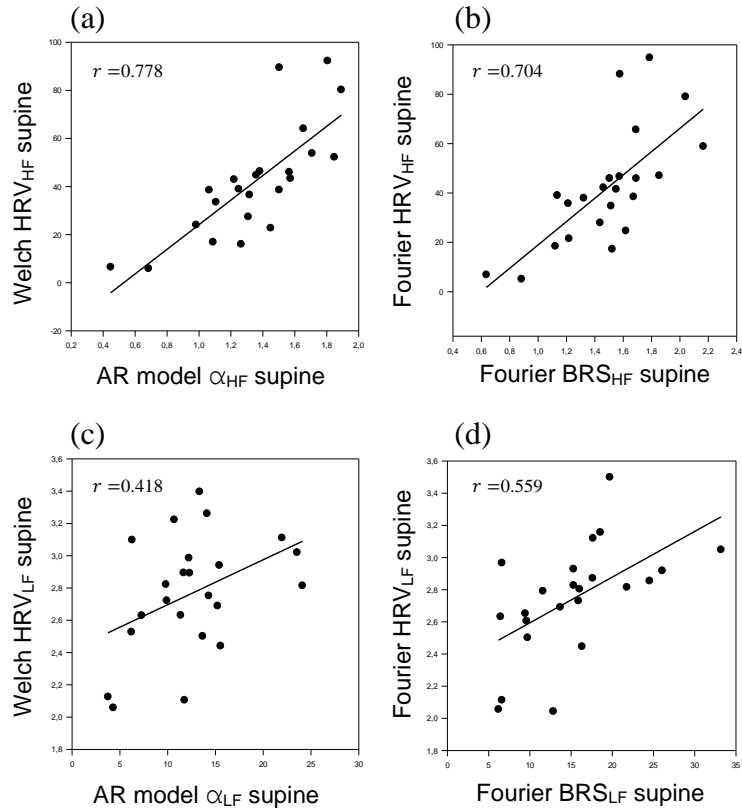


Figure 5.29 – Correlations for supine posture between HRV obtained from the Welch method (a,c) and Fourier transform (b,d), and spectral baroreflex sensitivity (BRS) indicators: α_{HF}/α_{LF} , which quantifies BRS from the square root of the ratio between HRV and BPV powers, obtained from PSD analysis using the AR model (a,c); and BRS_{HF}/BRS_{LF} , calculated from the Fourier transfer function analysis (b,d). The correlations are stronger in HF (a,b) rather than LF (c,d).

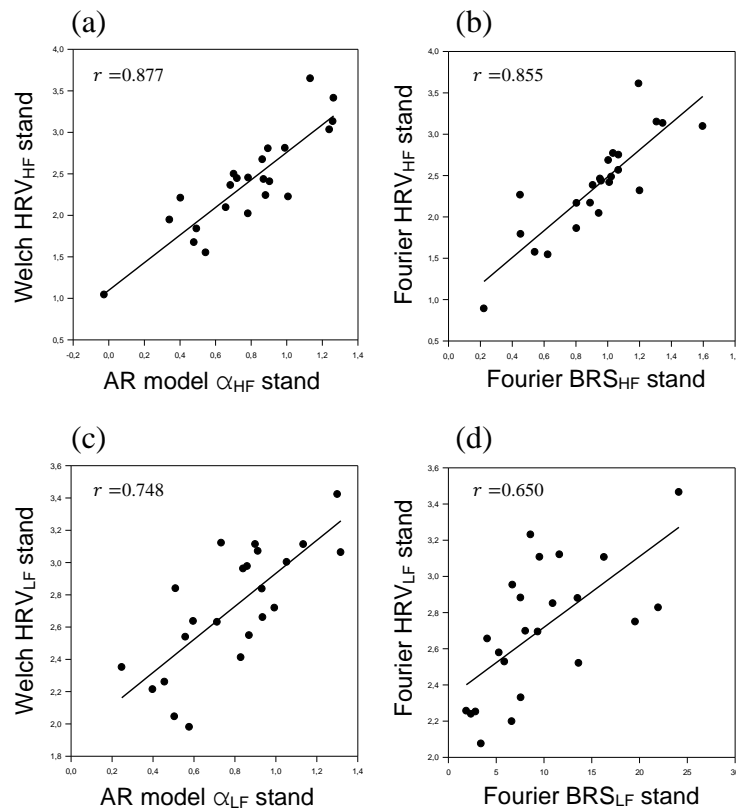


Figure 5.30 – Correlations for standing posture between HRV obtained from the Welch method (a,c) and the Fourier transform (b,d), and spectral baroreflex sensitivity (BRS) gain indicators: α_{HF}/α_{LF} , which quantifies BRS from the square root of the ratio between HRV and BPV powers, obtained from PSD analysis using the AR model (a,c); and BRS_{HF}/BRS_{LF} , calculated from the Fourier transfer function analysis (b,d). The correlations are stronger in HF (a,b) rather than LF (c,d), but the difference is small.

In supine posture, the correlations between HRV and impulse response ABR indicators were stronger in HF, as the examples in Figure 5.31 show. Figure 5.31 (a) and (c) illustrate the correlation plot between HRV (AR model) and ABR DG (ARX model) for corresponding HF and LF bands, respectively. Figure 5.31 (b) and (d) show the plot for the correlation between HF and LF components of HRV (Fourier transform) and ABR_{IRM} (MBF model).

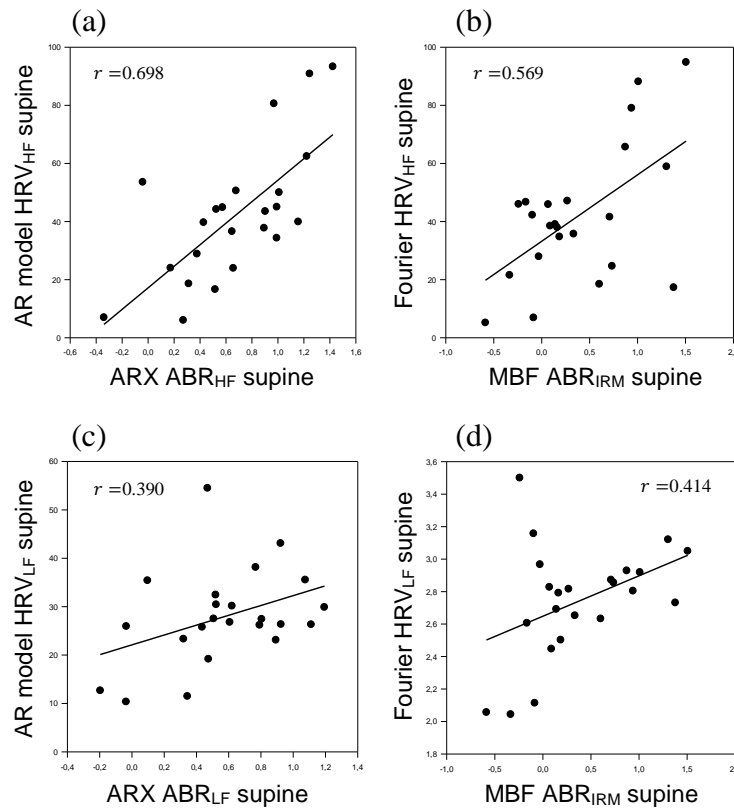


Figure 5.31 – Correlations for supine posture between HRV obtained from the AR model (a,c) and Fourier transform (b,d), and arterial baroreflex (ABR) impulse response gain indicators obtained from the ARX impulse response (a,b), and ABR_{IRM} , as a measure of overall gain, from the Meixner basis function (MBF) impulse response (c,d). The correlations are stronger in HF (a,b) rather than LF (c,d).

In standing posture, significant coefficients were only found for the ABR estimated from the ARX model in HF and in the LF, only for the ABR estimated from the LBF model. The correlations between HRV and ABR DG were stronger in supine posture for the ARX model estimates, and in standing postures for LBF and MBF models. As an example of each behavior, Figure 5.32 shows the correlation between HRV (AR model) and ABR DG (ARX model) (Figure 5.32 (a,c)) and between HRV (Fourier transform) and ABR DG (LBF model) (Figure 5.32 (b,d)), in the HF (Figure 5.32 (a,b)) and LF (Figure 5.32 (c,d)) bands.

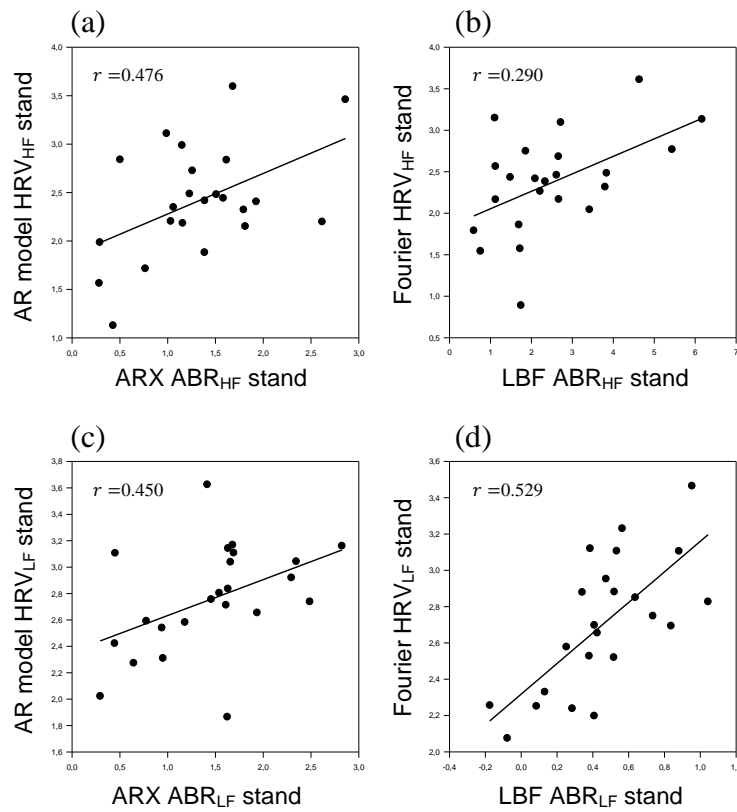


Figure 5.32 – Correlations for standing posture between HRV obtained from the AR model (a,c) and Fourier transform (b,d), and arterial baroreflex (ABR) impulse response gain indicators obtained from the ARX impulse response (a,b), and from the Laguerre basis function (LBF) impulse response (c,d). The correlations are slightly stronger in HF for the ARX impulse response indicators (a), but are much stronger in LF for LBF impulse response indicators (d).

6. DISCUSSION

The results point towards vagal withdrawal accompanied by a shift towards dominating sympathetic activity in standing, which is a sympathetic stimulus, compared to supine posture, in which the vagal tone is dominant. The database used for this study consists of subjects that are obese, but otherwise healthy. While level of fitness and BMI are factors that affect the ANS [5, 114], with evidence of reduced vagal and sympathetic activities in children [127, 128], our results regarding the effects of posture change were similar to those found by studies focusing on healthy non-obese subjects [24, 35, 36, 37, 38, 39, 129].

A number of studies have assessed the effects of postural changes associated with autonomic blockade to investigate vagal and sympathetic activity. In many studies of ANS response, drugs that selectively block one of the branches of the ANS are used to help differentiate the effect of a stimulus on each branch. In such studies, atropine is usually administered as a vagal blocker, while propranolol is used as a sympathetic blocker. For instance, Pomeranz *et al.* [35] combined the administration of those pharmacological agents with posture changes to determine how ANS responds using spectral measures of HRV. The study showed that there are both sympathetic and vagal activities in the LF region. Sympathetic activity appears to be a strong influence in LF in standing posture, but not in supine, while vagal activity is a strong influence in both postures. On the HF region of the RRI spectrum, vagal blockade resulted in a reduction of more than 90% of the area for both postures, while sympathetic blockade had no significant effects. Similar results were found by other studies [37, 129].

In our study, the HRV analysis showed a significant decrease in HRV_{HF} ($p < 0.001$ for all methods) as well as a significant increase in $HRV_{LF/HF}$ ($p < 0.001$ for all methods) in standing posture when compared to supine. While the $HRV_{LF/HF}$ increase indicates a shift in sympathovagal balance towards dominant sympathetic activity, the decrease in HRV_{HF} indicates an associated vagal withdrawal [4, 7, 35, 40]. These results are in accordance with the aforementioned study by Pomeranz *et al.* However, the shift towards dominant sympathetic activity could be a consequence exclusively from the vagal withdrawal or there could be a combined increase in sympathetic drive.

BPV analysis showed significant increase in both BPV_{LF} ($p < 0.001$ for all methods) and BPV_{HF} ($p < 0.001$ for all methods) from supine to standing. While several studies have shown that LF BPV is a measure of sympathetic vascular tone [67, 68, 69], HF interpretation is more controversial. Studies with animals have suggested that HF is mediated through the vagal system [7], while studies with patients who had heart transplant and therefore suffered cardiac denervation showed little alteration to HF BPV, suggesting that the mechanical effects of respiration may have a primary role [70, 130]. It has also been suggested that LF reflects myogenic vascular function, as well as sympathetic vascular tone and that the endothelial stress-induced release of nitric oxide is reflected in HF [131, 132].

The increase observed in BPV_{LF} in standing indicates an increase in sympathetic vasomotor tone, while the increase in HF could be an indication of elevated sympathetic drive. Moreover, the increase in BPV_{LF} was greater than that observed in BPV_{HF} , as also observed in other studies [40, 130]. Increased BPV has also been shown to be a predictor of reduced sensitivity of arterial and cardiopulmonary reflexes [70, 73], as confirmed by the verified decrease in RCC/RSA and ABR/BRS indicators in standing compared to supine posture.

RSA and BRS have also been assessed by associating the use of atropine and propranolol with different postures. Combining the supine position with propranolol provides a state of pure vagal activity, and combining the standing position with atropine results in a pure sympathetic condition. While drugs are chosen to block the opposing SNA branch, the posture is intended to increase activity of the unblocked branch. Applying this methodology and using the transfer function analysis for the determination of RSA and BRS, Mullen *et al.* [39] showed that both RSA and BRS are reduced in standing-atropine (sympathetic) condition compared to supine-propranolol (vagal) and also that in standing-atropine the activity is restricted to LF for both transfer functions. They also showed that under double blockade, both RSA and BRS were practically inexistent. These results have been verified by several other studies [24, 37, 36, 38].

The RSA and RCC indices estimated in the current study presented consistent results, even though the first encompasses both direct and indirect effects of respiration on HR, while the latter models exclusively the direct effects. A significant decrease in standing posture when compared to supine was found for all RSA and RCC indicators, in all methods used.

The reduction in HF indicators was also greater than in LF indicators. This has also been observed in previous studies under autonomic blockade [24, 36, 37, 38, 39]. RSA is generally a measure of vagal tone, even if there is a sympathetic component to the LF, and thus these results indicate a significant decrease in tonal vagal activity, as would be expected from the underlying physiology. Though the LF indicators may represent combined sympathetic and vagal activities, due to their lack of specificity, a decrease or increase in this index cannot be directly related to sympathetic tone.

For most of the estimated models, the cardiorespiratory modeling approach resulted in a negative delay between ILV and RRI. This result has also been reported in previous studies, suggesting a control level coupling between those variables, where RRI responds to the intent of respiration rather than respiration itself [14, 24, 53].

In order to verify how spectral HRV indices relate to the respiratory and baroreflex mechanisms, as those are the main mechanisms that influence HRV, correlation analyses were applied. Respiratory activity, whether quantified through RSA or RCC, correlated more strongly to HRV on the HF band than on the LF band. HRV_{HF} correlated more strongly to the overall RCC_{IRM} than HRV_{LF} did. These results may be a reflection of the fact that RSA and RCC are mechanisms mainly modulated by the vagal system and that respiration is a major contributor to HF HRV [3, 4, 6, 7].

Using a closed-loop multivariate dynamical adjustment model (CLMDA), Porta *et al.* [48] showed that the direct link between respiration and HR gradually decreases proportionally to head-up tilt table angles, while the indirect link mediated by ABR increased. A greater tilt angle is related to a stronger sympathetic postural stimulus and a more pronounced vagal withdrawal. The correlations between HRV and the impulse response based RCC were mostly weaker in standing posture than supine. As RCC measures only the direct effects of respiration, a weaker correlation in standing is in agreement with a decrease in this direct link, as observed from the tilt table experiment.

The correlations between HRV and the transfer function based RSA, however, was stronger in standing than supine posture in both HF and LF. This was consistent across all methods, though the differences found were small. The fact that correlations were stronger standing is probably due to the incorporation of indirect effects of respiration on RSA, since the indirect link between respiration and HR increases while the direct link decreases in this condition. These findings support the validity of RCC as a measure of the direct

effects of respiration on HR and show that even though RSA and RCC showed similar statistical trends between postures, they do bring different information.

Finally, the correlations between HRV and the overall RCC_{IRM} remained similar between supine and standing conditions, whether on HF or LF, with some relations showing a slight increase and others a slight decrease in either posture.

Baroreflex was assessed from the square-root of the HRV/BPV power ratio, in addition to transfer function and impulse response analyses. A significant decrease was found for all of the HF and overall BRS and ABR indicators from supine to standing. As observed in the RSA, RCC, and spectral HRV measures, the reduction on the HF indicators (α_{HF} , BRS_{HF} and ABR_{HF}) is larger than that observed on the LF (α_{LF} , BRS_{LF} and ABR_{LF}). Overall, baroreflex indices are a measure of reflex vagal activity, while RSA and HRV are measures of tonic vagal activity, which is suppressed by sympathetic activity [41, 42]. BRS is also known to inversely correlate to sympathetic activity [133], indicating increased sympathetic activity in standing as compared to supine, which is consistent with all of the data that points towards a sympathetic dominance in this posture.

The interpretation of the LF BRS indicators, however, is more complex than that of HF indices, since the results were not consistent among the methods available. While a significant decrease was found for all spectral LF indicators, α_{LF} and BRS_{LF} , the model based ABR_{LF} only showed significant decrease from supine to standing when estimating the impulse response from the ARX model, but not from LBF and MBF models. Some considerations must be made to interpret these results.

There is a closed-loop relationship between BP and RRI, that presents both feedback and feedforward components. Porta *et al.* [18] reported that estimating BRS through spectral methods leads to biased measures. This is reflected in an overestimation that was attributed to the incorporation of respiratory effects and the inability to differentiate between the feedforward and feedback effects, incorporating CID into the BRS estimate, when compared to the indices obtained through a modeling approach that impose delays and consider the respiration as an exogenous input. Therefore, spontaneous spectral BRS estimates are only reliable when causality is dominant on the baroreflex path. Our results reflect these findings, as the values found through both spectral methods (PSD and transfer function) presented higher absolute values than those found through any of the models. Recent studies have shown not only that the baroreflex causality (BP→RRI) is dominant in

standing posture, while in supine the dominance shifts to the CID (RRI→BP) path [45, 43], but also that this shift is proportional to graded head-up tilt [44, 46]. Our correlation analyses can help further understand the results considering the causality issue.

Correlations between HRV and spectral BRS estimates were stronger in the HF than in the LF band. The correlations between HRV and impulse response ABR indicators, however, differed according to the posture. In supine, correlations were stronger in HF than in LF, while in standing this was only the case for the ARX model, but not for the LBF and MBF models. Correlations between HRV and the overall ABR_{IRM} were mostly not significant for standing data, but in supine were stronger in HF than in LF. A high correlation to HRV HF is expected, as baroreflex is generally a measure of reflex vagal activity, as discussed. The fact that the correlations were stronger in LF in standing posture for the impulse response estimates could be due to the causality shift. The ARX model estimates were the only ones among the impulse response estimates that did not present this behavior and at the same time were the only indicators to show significant decrease in LF. The ARX model is the only one for which the uncoupling procedure is not performed during model estimation, thus these effects could be due to the indirect effects of respiration mediated through baroreflex, which are included in the ARX model, but not the LBF or MBF models, as the indirect link between respiration and HR is known to increase in standing [47, 48].

In the HF, the correlations between HRV and spectral BRS estimates were weaker in supine posture than standing, but the opposite was true between HRV and impulse response ABR estimates.

Correlations in the LF components between HRV and BRS estimates were stronger in standing posture compared to supine. This was also verified between standing vs. supine HRV and ABR estimates. The only exceptions were for ABR_{LF} calculated from the ARX model and the ABR_{IRM} calculated from the MBF model, for which no significant correlation was found in standing. Spectral and impulse response indicators correlate strongly in standing, but in supine there are only a few significant correlations and much weaker. This suggests that spectral and impulse response baroreflex estimates bring more similar information in the standing posture, when the baroreflex path is the dominating causality on the closed-loop dynamics between SBP and RRI, but decorrelate when CID becomes the dominating path, in supine posture.

Therefore, we cannot conclude that LF baroreflex gain, which reflects both sympathetic and vagal activities, is in fact decreased in standing, as the spectral estimates cannot accurately represent the reflex mechanism in supine posture. The decrease verified through the ARX model could be due to the indirect effects of respiration, while there was no decrease in the indicators obtained from the LBF and MBF models, which do not quantify those effects.

These results show that posture changes not only affect the gains of control and reflex mechanisms, but also the dominant causality on closed-loop relationships of the cardiorespiratory system. This reinforces the importance of studying the cardiorespiratory system as a whole and how the modelling approach can be used to clarify the relationship between those interacting variables.

7. CONCLUSION AND RECOMMENDATIONS

This study is composed of two parts, the development of CRSIDLab and its application on investigating the effects of posture changes on the ANS indicators.

Traditional HRV and BPV analyses consider only the fluctuation of these output variables and do not account for any interactions and reflex mechanisms, but are able to provide information on vagal and sympathetic tone. Classical HRV analysis showed an increase in HF with a decrease in the LF/HF ratio, leading to the conclusion that there is a shift towards sympathetic dominance associated with a reduction in vagal activity in standing compared to supine posture [4, 7, 35, 40]. A higher sympathetic vasomotor tone in standing is implied from the increase in LF BPV [67, 68, 69]. But while from the classical HRV analysis it can be concluded that there is a reduction in vagal activity in standing compared to supine posture, RCC/RSA and ABR/BRS analyses allows the discrimination between tonal and reflex activities [41, 42].

Transfer function analysis provides insights into the RSA and BRS regulatory mechanisms, but since this is an open-loop approach, there are limitations to the conclusions that can be drawn. This was made apparent through the correlation analyses, which showed, for instance, that the correlation between RSA and HR is stronger in standing, when the direct link between respiration and HR is weaker, but the indirect link is stronger [48], indicating the incorporation of these effects on the RSA estimate.

The system model identification approach, on the other hand, brings the possibility of modeling both respiratory and BP influences on HRV simultaneously, allowing the discrimination between direct effects of respiration, characterized by the RCC impulse response, and the indirect effects mediated through ABR. This is demonstrated by the fact that the correlations between HRV and RCC were stronger in supine, as is the direct link between respiration and HR, which was not the case for the RSA estimates. The imposition of time delays allows the restraining of causal and non-causal relations, separating the feedforward and feedback components, providing a way to computationally opening the loop. This was demonstrated by the fact that the correlations between BRS and ABR indicators were not significant in supine, when CID (RRI→BP) is the dominating causality in the closed-loop relationship between BP and HR, but were significant in standing, when the baroreflex path (BP→RRI) is the dominating causality [18, 43, 44, 45, 46], showing

that the ABR estimates seem to represent the baroreflex dynamics exclusively. Being able to differentiate between those regulating mechanisms provides sensible tools to further assess ANS response under different circumstances. These results are compatible with the physiology, demonstrating that CRSIDLab is effective in providing quantitative indicators of ANS activity.

There are limitations to the analyses proposed by this study and implemented on this toolbox. Previous studies have shown that second order nonlinearities provide considerable contribution, especially to the analysis of frequencies below 0.1 Hz, improving model accuracy and allowing for the observation of other dynamics involved [14, 134]. There has been some interest in studying the nonlinear relationships between the cardiorespiratory variables, employing Laguerre and Meixner basis functions to perform the expansion of Volterra-Wiener kernels [16, 19, 24, 25, 65, 116]. Since Laguerre and Meixner basis functions are already implemented, this would be a reasonable addition, complementing the current functionalities of the toolbox in future work.

Another limitation is that the methods employed rely on the assumption of stationarity, which not only delimits the duration of data records and requires processing such as the removal of slow trends, but also are unable to evaluate transient responses. Implementing time-varying models and alternatives for HRV analysis [19, 135] in future work can help to overcome those limitations.

There are many other possibilities for future work based on this research. Regarding CRSIDLab, it is always possible to include more methods and also variables that could be relevant, such as PP and MAP from BP. Currently system identification is performed based on cross-validation and with the use of some criterion to select the best model out of a given set. This process can be further improved by adding other constraints to the model selection process, such as residuals analysis and stability bounds.

Of all the indicators presented, the only one that is widely considered as a measure of sympathetic activity is LF BPV. All of the other indicators that do relate do the sympathetic branch, such as LF HRV, LF RCC and LF BRS, are either considered measures of both sympathetic and vagal branches, or present some controversy as to its interpretation. Therefore, without an invasive approach or use of pharmacological agents, few deductions can be made as to how sympathetic activity changes in response to any intervention. Chalacheva [134] has proposed an expansion of the cardiorespiratory model

presented in Figure 2.10 to explicitly incorporate the part of baroreflex that modulates total peripheral resistance as a measure of sympathetic activity. Therefore, another possible expansion of toolbox could include a measure of peripheral resistance, such as those obtained from peripheral arterial tonometry and laser Doppler flowmetry, as suggested by Chalacheva, as well as the necessary conditioning steps, to allow the identification of this dynamic.

Finally, we conclude that the presented modeling approach does provide means to disentangle the complex relationships of the cardiorespiratory system and is effective in differentiating feedback and feedforward effects, as well as isolating confounding mechanisms that exist in the cardiorespiratory dynamics. We also conclude that the presented CRSIDLab can effectively provide quantitative indicators of the ANS that are compatible with the knowledge available today.

REFERENCES

- [1] A. C. Guyton and J. E. Hall, "The Autonomic Nervous System and the Adrenal Medulla," in *Textbook of Medical Physiology*, Pennsylvania, Elsevier Inc., 2006, pp. 748-760.
- [2] E. N. Marieb and K. Hoehn, "The Autonomic Nervous System," in *Human Anatomy & Physiology*, Pearson Education, Inc., 2013, pp. 524-543.
- [3] F. Shaffer, R. McCraty and C. L. Zerr, "A healthy heart is not a metronome: an integrative review of the heart's anatomy and heart rate variability," *Frontiers in psychology*, vol. 5, p. 1040, 2014.
- [4] Task Force of the European Society of Cardiology and The North American Society of Pacing and Electrophysiology, "Heart rate variability: Standards of measurement, physiological interpretation and clinical use," *European Heart Journal*, vol. 17, no. 3, pp. 354-381, 1996.
- [5] G. D. Clifford, "Signal Processing Methods for Heart Rate Variability," Oxford, 2002.
- [6] G. G. Berntson, J. Thomas Bigger, D. L. Eckberg, P. Grossman, P. G. Kaufmann, M. Malik, H. N. Nagaraja, S. W. Porges, J. P. Saul, P. H. Stone and M. W. van der Molen, "Heart rate variability: Origins, methods, and interpretive caveats," *Psychophysiology*, vol. 34, no. 6, pp. 623-648, 1997.
- [7] M. Pagani, F. Lombardi, S. Guzzetti, O. Rimoldi, R. Furlan, P. Pizzinelli, G. Sandrone, G. Malfatto, S. Dell'Orto, E. Piccaluga, M. Turiel, G. Baselli, S. Cerutti and A. Malliani, "Power Spectral Analysis of Heart Rate and Arterial Pressure Variabilities as a Marker of Sympatho-Vagal Interaction in Man and Conscious Dog," *Circulation research*, vol. 59, no. 2, pp. 178-193, 1986.
- [8] R. W. DeBoer, J. M. Karemaker and J. Strackee, "Description of heart rate variability data in accordance with a physiological model for the genesis of heartbeats," *Psychophysiology*, vol. 22, no. 2, pp. 147-155, 1985.
- [9] F. Rahman, S. Pechnik, D. Gross, L. Sewell and D. S. Goldstein, "Low frequency power of heart rate variability reflects baroreflex function, not cardiac sympathetic innervation," *Clinical Autonomic Research*, vol. 21, no. 3, pp. 133-141, 2011.
- [10] A. C. Guyton and J. E. Hall, "Nervous Regulation of the Circulation, and Rapid Control of Arterial Pressure," in *Textbook of Medical Physiology*, Pennsylvania, Elsevier Inc., 2006, pp. 204-215.
- [11] E. N. Marieb and K. Hoehn, "The Cardiovascular System: Blood Vessels," in *Human Anatomy and Physiology*, Pearson Education, Inc., 2013, pp. 692-750.
- [12] A. Patwardhan, "Respiratory Sinus Arrhythmia," in *Wiley Encyclopedia of Biomedical Engineering*, New Jersey, John Wiley & Sons, Inc., 2006, pp. 3053-3060.
- [13] F. Yasuma and J.-i. Hayano, "Respiratory sinus arrhythmia: why does the heartbeat synchronize with respiratory rhythm?," *Chest Journal*, vol. 125, no. 2, pp. 683-690, 2004.
- [14] J. A. Jo, "Linear and Nonlinear Model-Based Assessment of Autonomic Control in

- Obstructive Sleep Apnea Syndrome (OSAS) During Wakefulness and Sleep," University of Southern California, Los Angeles, 2002.
- [15] E. N. Marieb and K. Hoehn, "The Cardiovascular System: The Heart," in *Human Anatomy & Physiology*, Pearson Education, Inc., 2013, pp. 658-691.
- [16] M. C. K. Khoo, "Modeling of autonomic control in sleep-disordered breathing," *Cardiovascular engineering*, vol. 8, no. 1, pp. 30-41, 2008.
- [17] T. Kuusela, "Methodological Aspects of Baroreflex Sensitivity Analysis," in *Heart Rate Variability (HRV) Signal Analysis: Clinical Applications*, Boca Raton, CRC Press, 2013, pp. 43-58.
- [18] A. Porta, G. Baselli, O. Rimoldi, A. Malliani and M. Pagani, "Assessing baroreflex gain from spontaneous variability in conscious dogs: role of causality and respiration," *American Journal of Physiology-Heart and Circulatory Physiology*, vol. 279, no. 5, pp. H2558-H2567, 2000.
- [19] S. Sangkatumvong, "Modeling of Cardiovascular Autonomic Control in Sickle Cell Disease," University of Southern California, Los Angeles, 2011.
- [20] M. C. K. Khoo, T.-S. Kim and R. B. Berry, "Spectral Indices of Cardiac Autonomic Function in Obstructive Sleep Apnea," *SLEEP*, vol. 22, no. 4, pp. 443-451, 1999.
- [21] G. Baselli, S. Cerutti, S. Civardi, A. Malliani and M. Pagani, "Cardiovascular Variability Signals: Towards the Identification of a Closed-Loop Model of the Neural Control Mechanisms," *IEEE Transactions on Biomedical Engineering*, vol. 35, no. 12, pp. 1033-1046, 1988.
- [22] G. Baselli, S. Cerutti, S. Civardi, D. Liberati, F. Lombardi, A. Malliani and M. Pagani, "Spectral and Cross-Spectral Analysis of Heart Rate and Arterial Blood Pressure Variability Signals," *Computers and Biomedical Research*, vol. 19, no. 6, pp. 520-534, 1986.
- [23] M. L. Appel, P. Saul, R. D. Berger and R. J. Cohen, "Closed-loop identification of cardiovascular regulation mechanisms," in *Computers in Cardiology*, Jerusalem, 1989.
- [24] K. H. Chon, R. Mukkamala, K. Toska, T. J. Mullen, A. A. Armoundas and R. J. Cohen, "Linear and Nonlinear System Identification of Autonomic Heart-Rate Modulation: A Noninvasive Method for the Evaluation of Cardiovascular Regulatory Mechanisms," *IEEE engineering in medicine and biology magazine*, vol. 16, no. 5, pp. 96-105, 1997.
- [25] F. M. G. S. A. Oliveira, "Autonomic and metabolic effects of obstructive sleep apnea in childhood obesity," University of Southern California, Los Angeles, 2011.
- [26] J. Chaicharn, Z. Lin, M. L. Chen, S. L. D. Ward, T. Keens and M. C. K. Khoo, "Model-Based Assessment of Cardiovascular Autonomic Control in Children with Obstructive Sleep Apnea," *Sleep*, vol. 32, no. 7, pp. 927-938, 2009.
- [27] J. L. A. Carvalho, A. F. Rocha, F. A. d. O. Nascimento, J. Souza Neto and L. F. Junqueira Jr., "Development of a Matlab Software for Analysis of Heart Rate Variability," in *6th International Conference on Signal Processing*, 2002.
- [28] P. Perakakis, M. Joffily, M. Taylor, P. Guerra and J. Vila, "KARDIA: A Matlab software for the analysis of cardiac interbeat intervals," *Computer Methods and Programs in Biomedicine*, vol. 98, no. 1, pp. 83-89, 2010.
- [29] K. Tobias, S. Sütterlin, S. M. Schulz and C. Vögele, "ARTiiFACT: a tool for heart

- rate artifact processing and heart rate variability analysis," *Behavior research methods*, vol. 43, no. 4, pp. 1161-1170, 2011.
- [30] M. P. Tarvainen, J.-P. Niskanen, J. A. Lipponen, P. O. Ranta-aho and P. A. Karjalainen, "Kubios HRV - Heart Rate Variability Analysis Software," *Computer Methods and Programs in Biomedicine*, vol. 113, no. 1, pp. 210-220, 2014.
- [31] L. Rodríguez-Liñares, A. J. Méndez, M. J. Lado, D. N. Olivieri, X. A. Vila and I. Gómez-Conde, "An open source tool for heart rate variability spectral analysis," *Computer Methods and Programs in Biomedicine*, vol. 103, no. 1, pp. 39-50, 2011.
- [32] L. Rodríguez-Liñares, M. J. Lado, X. A. Vila, A. J. Méndez and P. Cuesta, "gHRV: Heart rate variability analysis made easy," *Computer Methods and Programs in Biomedicine*, vol. 116, no. 1, pp. 26-38, 2014.
- [33] R. Maestri and G. D. Pinna, "POLYAN: A computer program for polyparametric analysis of cardio-respiratory variability signals," *Computer Methods and Programs in Biomedicine*, vol. 56, no. 1, pp. 37-48, 1998.
- [34] F. Badilini, M. Pagani and A. Porta, "HeartScope: a software tool addressing autonomic nervous system regulation," in *Computers in Cardiology*, Lyon, 2005.
- [35] B. Pomeranz, R. J. Macaulay, M. A. Caudill, I. Kutz, D. Adam, D. Gordon, K. M. Kilborn, A. C. Barger, D. C. Shannon, R. J. Cohen and H. Benson, "Assessment of autonomic function in humans by heart rate spectral analysis," *American Journal of Physiology-Heart and Circulatory Physiology*, vol. 248, no. 1, pp. H151-H153, 1985.
- [36] R. D. Berger, "Analysis of the cardiovascular control system using broad-band stimulation," Massachusetts Institute of Technology, Cambridge, 1987.
- [37] J. P. Saul, R. D. Berger, P. Albrecht, S. P. Stein, M. H. Chen and R. J. Cohen, "Transfer function analysis of the circulation: unique insights into cardiovascular regulation," *American Journal of Physiology - Heart and Circulatory Physiology*, vol. 261, no. 4, pp. H1231-H1245, 1991.
- [38] K. Yana, J. P. Saul, R. D. Berger, M. H. Perrott and R. J. Cohen, "A time domain approach for the fluctuation analysis of heart rate related to instantaneous lung volume," *IEEE transactions on biomedical engineering*, vol. 40, no. 1, pp. 74-81, 1993.
- [39] T. J. Mullen, M. L. Appel, R. Mukkamala, J. M. Mathias and R. J. Cohen, "System identification of closed-loop cardiovascular control: effects of posture and autonomic blockade," *American Journal of Physiology - Heart and Circulatory Physiology*, vol. 272, no. 1, pp. H448-H461, 1997.
- [40] M. Javorka, Z. Turianikova, I. Tonhajzerova, K. Javorka and M. Baumert, "The effect of orthostasis on recurrence quantification analysis of heart rate and blood pressure dynamics," *Physiological measurement*, vol. 30, no. 1, p. 29, 2008.
- [41] E. Vanoli, "Technology and physiology of baroreflex sensitivity," *Cardiac Electrophysiology Review*, vol. 1, no. 3, pp. 352-353, 1997.
- [42] G. M. De Ferrari, M. Landolina, M. Mantica, R. Manfredini, P. J. Schwartz and A. Lotto, "Baroreflex sensitivity, but not heart rate variability, is reduced in patients with life-threatening ventricular arrhythmias long after myocardial infarction," *American heart journal*, vol. 130, no. 3, pp. 473-480, 1995.
- [43] A. Porta, R. Furlan, O. Rimoldi, M. Pagani, A. Malliani and P. van de Borne, "Quantifying the strength of the linear causal coupling in closed loop interacting

- cardiovascular variability signals," *Biological cybernetics*, vol. 86, no. 3, pp. 241-251, 2002.
- [44] A. Porta, A. M. Catai, A. C. Takahashi, V. Magagnin, T. Bassani, E. Tobaldini, P. van de Borne and N. Montano, "Causal relationships between heart period and systolic arterial pressure during graded head-up tilt," *American Journal of Physiology-Regulatory, Integrative and Comparative Physiology*, vol. 300, no. 2, pp. R378-R386, 2011.
- [45] V. Turjanmaa, S. Kalli, M. Sydänmaa and A. Uusitalo, "Short-term variability of systolic blood pressure and heart rate in normotensive subjects," *Clinical Physiology and Functional Imaging*, vol. 10, no. 4, pp. 389-401, 1990.
- [46] L. Faes, G. Nollo and A. Porta, "Mechanisms of causal interaction between short-term RR interval and systolic arterial pressure oscillations during orthostatic challenge," *Journal of Applied Physiology*, vol. 114, no. 12, pp. 1657-1667, 2013.
- [47] S. Schulz, A. Felix-Constantin, I.-R. Edu, R. Schroeder, H. Costin, K.-J. Bär and A. Voss, "Cardiovascular and cardiorespiratory coupling analyses: a review," *Philosophical Transactions of the Royal Society A*, vol. 371, no. 1997, p. 20120191, 2013.
- [48] A. Porta, T. Bassani, V. Bari, E. Tobaldini, A. C. Takahashi, A. M. Catai and N. Montano, "Model-based assessment of baroreflex and cardiopulmonary couplings during graded head-up tilt," *Computers in biology and medicine*, vol. 42, no. 3, pp. 298-305, 2012.
- [49] A. C. Guyton and J. E. Hall, "Heart Muscle: The Heart as a Pump and Function of the Heart Valves," in *Textbook of Medical Physiology*, Philadelphia, Elsevier Inc., 2006, pp. 103-115.
- [50] S. Freeman, K. Quillin and L. Allison, *Biological Science*, Upper Saddle River: Prentice Hall, 2002.
- [51] B. Lown and R. L. Verrier, "Neural activity and ventricular fibrillation," *New England Journal of Medicine*, vol. 294, no. 21, pp. 1165-1170, 1976.
- [52] M. M. Wolf, G. A. Varigos, D. Hunt and J. G. Sloman, "Sinus arrhythmia in acute myocardial infarction," *Medical Journal of Australia*, vol. 2, no. 2, pp. 52-53, 1978.
- [53] R. D. Berger, J. P. Saul, P. Albrecht, S. P. Stein and R. J. Cohen, "Respiratory Effects on Arterial Pressure: A Novel Signal Analysis Approach," in *Engineering in Medicine and Biology Society*, New Orleans, 1988.
- [54] A. Ben-Tal, S. S. Shamailov and J. F. R. Paton, "Evaluating the physiological significance of respiration sinus arrhythmia: looking beyond ventilation-perfusion efficiency," *The Journal of Physiology*, vol. 590, no. 8, pp. 1989-2008, 2012.
- [55] A. C. Guyton and J. E. Hall, "Rhythmical Excitation of the Heart," in *Textbook of Medical Physiology*, Pennsylvania, Elsevier Inc., 2006, pp. 116-121.
- [56] A. C. Guyton and J. E. Hall, "The Normal Electrocardiogram," in *Textbook of Medical Physiology*, Pennsylvania, Elsevier Inc., 2006, pp. 123-130.
- [57] OpenStax College, "The Cardiovascular System: The Heart," in *Anatomy & Physiology*, OpenStax College, 2013, pp. 787-831.
- [58] A. C. Guyton and J. E. Hall, "Overview of the Circulation; Medical Physics of Pressure, Flow and Resistance," in *Textbook of Medical Physiology*, Pennsylvania, Elsevier Inc., 2006, pp. 161-170.

- [59] A. C. Guyton and J. E. Hall, "Vascular Distensibility and Functions of the Arterial and Venous Systems," in *Textbook of Medical Physiology*, Pennsylvania, Elsevier Inc., 2006, pp. 171-180.
- [60] J. Wagner, J. L. Clausen, A. Coates, O. F. Pedersen, V. Brusasco, F. Burgos, R. Casaburi, R. Crapo, P. Enright, C. P. M. van der Grinten, P. Gustafsson, J. Hankinson, R. Jensen, D. Johnson, N. MacIntyre, R. McKay, M. R. Miller, D. Navajas, R. Pellegrino and G. Viegi, "Standardisation of the measurement of lung volumes. ATS/ERS task force: Standardisation of lung function testing," *European Respiratory Journal*, vol. 26, no. 3, pp. 511-522, 2005.
- [61] J. H. T. Bates, G. Schmalisch, D. Filbrun and J. Stocks, "Tidal breath analysis for infant pulmonary function testing. ERS/ATS task force on standards for infant respiratory function testing.," *European Respiratory Journal*, vol. 16, no. 6, pp. 1180-1192, 2000.
- [62] E. N. Marieb and K. Hoehn, "The Respiratory System," in *Human Anatomy and Physiology*, Pearson Education, Inc., 2013, pp. 801-848.
- [63] A. C. Guyton and J. E. Hall, "Pulmonary Ventilation," in *Textbook of Medical Physiology*, Pennsylvania, Elsevier Inc., 2006, pp. 471-482.
- [64] V. Belozeroff, R. B. Berry, C. S. H. Sassoan and M. C. K. Khoo, "Effects of CPAP therapy on cardiovascular variability in obstructive sleep apnea: a closed-loop analysis," *American Journal of Physiology (Heart and Circulatory Physiology)*, vol. 282, no. 1, pp. H110-H121, 2002.
- [65] J. A. Jo, A. Blasi, E. Valladares, R. Juarez, A. Baydur and M. C. K. Khoo, "Model-based Assessment of Autonomic Control in Obstructive Sleep Apnea Syndrome during Sleep," *American Journal of Respiratory and Critical Care Medicine*, vol. 167, no. 2, pp. 128-136, 2003.
- [66] M. C. K. Khoo, "Mathematical Modeling," in *Physiological Control Systems: Analysis, Simulation, and Estimation*, Hoboken, John Wiley & Sons, Inc., 2000, pp. 13-38.
- [67] R. W. DeBoer, "Beat-to-beat blood-pressure fluctuations and heart rate variability in man: physiological relationships, analysis techniques and a simple model," Amsterdam, 1985.
- [68] S. Akselrod, D. Gordon, J. B. Madwed, N. C. Snidman, D. C. Shannon and R. J. Cohen, "Hemodynamic regulation: investigation by spectral analysis," *American Journal of Physiology - Heart and circulatory physiology*, vol. 249, no. 4, pp. H867-H875, 1985.
- [69] H. M. Strauss, E. A. Anderson, W. G. Haynes and K. C. Kregel, "Frequency response characteristics of sympathetically mediated vasomotor waves in humans," *American Journal of Physiology - Heart and Circulatory Physiology*, vol. 274, no. 4, pp. H1277-H1283, 1998.
- [70] G. Parati, J. P. Saul and M. Di Rienzo, "Spectral analysis of blood pressure and heart rate variability in evaluating cardiovascular regulation," *Hypertension*, vol. 25, no. 6, pp. 1276-1286, 1995.
- [71] A. M. Langager, B. E. Hammemberg, D. L. Rotella and H. M. Strauss, "Very low-frequency blood pressure variability depends on voltage-gated L-type Ca²⁺ channels in conscious rats," *American Journal of Physiology - Heart and Circulatory Physiology*, vol. 292, no. 3, pp. H1321-H1327, 2007.

- [72] H.-J. Choi, "Blood Pressure Variability and Its Management in Hypertensive Patients," *Korean Journal of Family Medicine*, vol. 33, no. 6, pp. 330-335, 2012.
- [73] G. Parati, J. E. Ochoa, P. Salvi, C. Lombardi and G. Bilo, "Prognostic Value of Blood Pressure Variability and Average Blood Pressure Levels in Patients with Hypertension and Diabetes," *Diabetes Care*, vol. 36, no. 2, pp. S312-S324, 2013.
- [74] D. I. Fotiadis, A. Likas, L. Michalis and C. Papaloukas, "Electrocardiogram (ECG): Automated Diagnosis," in *Wiley Encyclopedia of Biomedical Engineering*, Hoboken, John Wiley & Sons, Inc., 2006, pp. 1259-1275.
- [75] W. J. Tompkins, *Biomedical Digital Signal Processing: C-Language Examples and Laboratory Experiments for the IBM PC*, Madison: Willis J. Tompkins, 2000.
- [76] A. R. Moller, "Practical aspects of electrophysiological recording in the operating room," in *Intraoperative Neurophysiological Monitoring*, Totowa, Human Press, Inc., 2006, pp. 279-342.
- [77] M. B. Wilkinson and M. Outram, "Principles of pressure transducers, resonance, damping and frequency response," *Anaesthesia & Intensive Care Medicine*, vol. 10, no. 2, pp. 102-105, 2009.
- [78] L. A. Geddes, "The Direct Measurement of Blood Pressures," in *Handbook of blood pressure measurement*, Los Angeles, Springer Science & Business Media, 2013, pp. 3-50.
- [79] O. Rompelman and B. J. Ten Voorde, "Spectral Analysis of Fluctuations in Heart Rate and Blood Pressure," in *Computer Analysis of Cardiovascular Signals*, Amsterdam, IOS Press, 1995, pp. 3-15.
- [80] B. N. Li, M. C. Dong and M. I. Vai, "On an automatic delineator for arterial blood pressure waveforms," *Biomedical Signal Processing and Control*, vol. 5, no. 1, pp. 76-81, 2010.
- [81] M. Di Rienzo, P. Castiglioni and G. Parati, "Arterial Blood Pressure Processing," in *Wiley Encyclopedia of Biomedical Engineering*, Hoboken, John Wiley & Sons, Inc., 2006, pp. 98-109.
- [82] G. D. Clifford and L. Tarassenko, "Quantifying Errors in Spectral Estimates of HRV Due to Beat Replacement and Resampling," *IEEE Transactions on Biomedical Engineering*, vol. 52, no. 4, pp. 630-638, 2005.
- [83] T. Kuusela, "Methodological Aspects of Heart Rate Variability Analysis," in *Heart Rate Variability Analysis (HRV): Clinical Applications*, CRC Press, 2012, pp. 9-42.
- [84] J. L. Semmlow and B. Griffel, "Introduction," in *Biosignal and Medical Image Processing*, Boca Raton, CRC Press, 2014, pp. 1-28.
- [85] R. D. Berger, S. Askelrod, D. Gordon and R. J. Cohen, "An Efficient Algorithm for Spectral Analysis of Heart Rate Variability," *IEEE Transactions on Biomedical Engineering*, Vols. BME-33, no. 9, pp. 900-904, September 1986.
- [86] R. I. Kitney, T. Fulton, A. H. McDonald and D. A. Linkenst, "Transient interactions between blood pressure, respiration and heart rate in man," *Journal of biomedical engineering*, vol. 7, no. 3, pp. 217-224, 1985.
- [87] J. L. Semmlow and B. Griffel, "Spectral Analysis: Classical Methods," in *Biosignal and Medical Image Processing*, Boca Raton, CRC Press, 2014, pp. 77-118.
- [88] J. L. Semmlow and B. Griffel, "Biosignal Measurements, Noise, and Analysis," in *Biosignal and Medical Image Processing*, Boca Raton, CRC Press, 2014, pp. 29-76.

- [89] M. H. Hayes, "Spectrum Estimation," in *Statistical Digital Signal Processing and Modeling*, Hoboken, John Wiley & Sons, Inc., 1996, pp. 391-492.
- [90] P. D. Welch, "The Use of Fast Fourier Transform for the Estimation of Power Spectra: A Method Based on Time Averaging Over Short, Modified Periodograms," *IEEE Transactions on Audio and Electroacoustics*, vol. 15, no. 2, pp. 70-73, 1967.
- [91] J. L. Semmlow and B. Griffel, "Modern Spectral Analysis: The Search for Narrowband Signals," in *Biosignal and Medical Image Processing*, Boca Raton, CRC Press, 2014, pp. 163-192.
- [92] G. Baselli, A. Porta and G. Ferrari, "Models for the Analysis of Cardiovascular Variability Signals," in *Heart Rate Variability*, Armonk, Futura Publishing Company, Inc., 1995, pp. 135-145.
- [93] S. Akselrod, I. Pinhas, L. R. Davrath, Z. Shinar and E. Toledo, "Heart Rate Variability (HRV)," in *Wiley Encyclopedia of Biomedical Engineering*, Hoboken, John Wiley & Sons, Inc., 2006, pp. 1794-1805.
- [94] D. T. Westwick and R. E. Kearney, "Identification of Linear Systems," in *Identification of Nonlinear Physiological Systems*, IEEE Press, 2003, pp. 103-124.
- [95] K. J. Keesman, "Dynamic Systems Identification," in *System identification: an introduction*, London, Springer Science & Business Media, 2011, pp. 113-166.
- [96] S. R. Seydnejad and R. I. Kitney, "Analysis of HRV and BPV by a Nonlinear Closed Loop Model," in *Methodology and Clinical Applications of Blood Pressure and Heart Rate Analysis*, Amsterdam, IOS Press, 1999, pp. 49-71.
- [97] L. Ljung, "Preprocessing Data," in *System Identification: Theory for the User*, Upper Saddle River, Prentice Hall PTR, 1999, pp. 458-476.
- [98] D. T. Westwick and R. E. Kearney, "Models of Linear Systems," in *Identification of Nonlinear Physiological Systems*, IEEE Press, 2003, pp. 39-56.
- [99] T.-S. Kim and M. C. K. Khoo, "Estimation of cardiorespiratory transfer under spontaneous breathing conditions: a theoretical study," *American Journal of Physiology*, vol. 273, no. 2, pp. H1012-H1023, 1997.
- [100] C.-C. Chen, "Automated Cardiovascular System Identification," Department of Electrical Engineering and Computer Science, Massachusetts Institute of Technology, Cambridge, 1999.
- [101] P. Van den Hof and N. Brett, "System identification with generalized orthonormal basis functions," in *Modelling and identification with rational orthogonal basis functions*, Berlin, Springer-Verlag, 2005, pp. 61-102.
- [102] M. H. Asyali and M. Juusola, "Use of Meixner Functions in Estimation of Volterra Kernels of Nonlinear Systems With Delay," *IEEE Transactions on Biomedical Engineering*, vol. 52, no. 2, pp. 229-237, Fevereiro 2005.
- [103] B. Wahlberg, B. Ninness and P. Van den Hof, "Introduction," in *Modelling and Identification with Rational Orthogonal Basis Functions*, Delft and Stockholm, Springer, 2005, pp. 1-13.
- [104] B. Ninness and H. Hjalmarsson, "Numerical conditioning," in *Modelling and identification with rational orthogonal basis functions*, Berlin, Springer-Verlag, 2005, pp. 161-188.
- [105] A. C. Den Brinker, "Meixner-like Functions Having a Rational z-transform," *International Journal of Circuit Theory and Applications*, vol. 23, no. 3, pp. 237-

246, 1995.

- [106] D. T. Westwick and R. E. Kearney, "Background," in *Identification of Nonlinear Physiological Systems*, IEEE Press, 2003, pp. 13-38.
- [107] L. Ljung, "Parameter Estimation Methods," in *System Identification: Theory for the User*, Upper Saddle River, Prentice-Hall, Inc., 1999, pp. 197-246.
- [108] L. Ljung, "Model Structure Selection and Model Validation," in *System Identification: Theory for the User*, Upper Saddle River, Prentice-Hall, Inc., 1999, pp. 491-519.
- [109] L. Ljung, "Some classical and some new ideas for identification of linear systems," *Journal of Control, Automation and Electrical Systems*, vol. 24, no. 1-2, pp. 3-10, 2013.
- [110] D. T. Westwick and R. E. Kearney, *Identification of Nonlinear Physiological Systems*, Hoboken: John Wiley & Sons, Inc., 2003.
- [111] L. Ljung, "Time-Invariant Linear Systems," in *System Identification: Theory for the User*, Upper Saddle River, Prentice-Hall, Inc., 1999, pp. 18-62.
- [112] K. J. Keesman, "Correlation Methods," in *System Identification: An Introduction*, Berlin, Springer Science and Business Media, 2011, pp. 43-60.
- [113] D. J. Lesser, R. Bhatia, W. H. Tran, F. Oliveira, R. Ortega, T. G. Keens, S. D. Mittelman, M. C. K. Khoo and S. L. D. Ward, "Sleep fragmentation and intermittent hypoxemia are associated with decreased insulin sensitivity in obese adolescent Latino males," *Pediatric research*, vol. 72, no. 3, pp. 293-298, 2012.
- [114] T. Laitinen, J. Hartikainen, L. Niskanen, G. Geelen and E. Länsimies, "Sympathovagal balance is major determinant of short-term blood pressure variability in healthy subjects," *American Journal of Physiology (Heart and Circulatory Physiology)*, vol. 276, no. 4, pp. H1245-H1252, 1999.
- [115] J. Batzel, G. Baselli, R. Mukkamala and K. H. Chon, "Modelling and disentangling physiological mechanisms: linear and nonlinear identification techniques for analysis of cardiovascular regulation," *Philosophical Transactions of the Royal Society of London A: Mathematical, Physical and Engineering Sciences*, vol. 367, no. 1892, pp. 1377-1391, 2009.
- [116] P. Chalacheva and M. C. K. Khoo, "An extended model of blood pressure variability: incorporating the respiratory modulation of vascular resistance," in *Engineering in Medicine and Biology Society (EMBC), 35th Annual International Conference of the IEEE*, Osaka, 2013.
- [117] B. S. Saini, D. Singh and V. Kumar, "Comparison of re-sampling methods in the spectral analysis of RR-interval series data," *Signal Processing*, vol. 7, pp. 16-31, 2013.
- [118] D. Singh, K. Vinod, S. C. Saxena and K. K. Deepak, "Effects of RR segment duration on HRV spectrum estimation," *Physiological measurement*, vol. 25, no. 3, p. 721, 2004.
- [119] V. Z. Marmarelis, "Identification of Nonlinear Biological Systems Using Laguerre Expansions of Kernels," *Annals of Biomedical Engineering*, vol. 21, pp. 573-589, Novembro-Dezembro 1993.
- [120] M. Pagani, V. Somers, R. Furlan, S. Dell'Orto, J. Conway, G. Baselli, S. Cerutti, P. Sleight and A. Malliani, "Changes in autonomic regulation induced by physical

- training in mild hypertension," *Hypertension*, vol. 12, no. 6, pp. 600-610, 1988.
- [121] D. Lucini, M. Pagani, G. S. Mela and A. Malliani, "Sympathetic restraint of baroreflex control of heart period in normotensive and hypertensive subjects," *Clinical Science*, vol. 86, no. 5, pp. 547-556, 1994.
- [122] S. S. Shapiro and M. B. Wilk, "An analysis of variance test for normality (complete samples)," *Biometrika*, vol. 52, no. 3/4, pp. 591-11, 1965.
- [123] N. M. Razali and Y. B. Wah, "Power comparisons of Shapiro-Wilk, Kolmogorov-Smirnov, Lilliefors and Anderson-Darling tests," *Journal of statistical modeling and analytics*, vol. 2, no. 1, pp. 21-33, 2011.
- [124] J. H. McDonald, *Handbook of Biological Statistics*, Baltimore: Sparky House Publishing, 2014.
- [125] M. B. Brown and A. B. Forsythe, "Robust tests for the equality of variances," *Journal of the american statistical association*, vol. 69, no. 346, pp. 364-37, 1974.
- [126] K. H. Zou, K. Tuncali and S. G. Silverman, "Correlation and simple linear regression," *Radiology*, vol. 227, no. 3, pp. 617-628, 2003.
- [127] N. Nagai and T. Moritani, "Effect of physical activity on autonomic nervous system function in lean and obese children," *International journal of obesity*, vol. 28, no. 1, pp. 27-33, 2004.
- [128] P. Baum, D. Petroff, J. Classen, W. Kiess and S. Blüher, "Dysfunction of autonomic nervous system in childhood obesity: a cross-sectional study," *PloS one*, vol. 8, no. 1, p. e54546, 2013.
- [129] S. Akselrod, D. Gordon, F. A. Ubel, D. C. Shannon, A. C. Berger and R. J. Cohen, "Power spectrum analysis of heart rate fluctuation: a quantitative probe of beat-to-beat cardiovascular control," *Science*, pp. 220-222, 1981.
- [130] P. van de Borne, M. Schintgen, G. Niset, P. Schoenfeld, H. Nguyen, S. Degré and J.-P. Degaute, "Does cardiac denervation affect the short-term blood pressure variability in humans?," *Journal of hypertension*, vol. 12, no. 12, pp. 1395-1404, 1994.
- [131] H. M. Strauss, "Identification of blood pressure control mechanisms by power spectral analysis," *Clinical and experimental pharmacology and physiology*, vol. 34, no. 4, pp. 362-368, 2007.
- [132] Z. Kouchaki, M. Butlin, A. Qasem and A. P. Avolio, "Quantification of peripheral and central blood pressure variability using a time-frequency method," in *IEEE 38th Annual International Conference of the Engineering in Medicine and Biology Society (EMBC)*, Orlando, 2016.
- [133] D. P. Francis, A. J. Coats and P. Ponikowski, "Chemoreflex-baroreflex interactions in cardiovascular disease," in *Sleep Apnea: Implications in cardiovascular and cerebrovascular disease*, Boca Raton, CRC Press, 2000, pp. 33-60.
- [134] P. Chalacheva, "Modeling autonomic peripheral vascular control," University of Southern California, Los Angeles, 2014.
- [135] M. P. Tarvainen, S. Georgiadis, J. A. Lipponen, M. Hakkarainen and P. A. Karjalainen, "Time-varying spectrum estimation of heart rate variability signals with Kalman smoother algorithm," in *Annual international conference of the IEEE Engineering in Medicine and Biology Society*, Minneapolis, 2009.

APPENDICES

A – Patient data object description

A. PATIENT DATA OBJECT DESCRIPTION

The patient data object is composed of several different objects, created so that the information can be better organized. Table A.1 describes most of the objects that compose the *patientData* object, but the *dataUnit*, *varUnit* and *ilvUnit* objects are described on Table A.2, Table A.3 and Table A.4, since these are the objects that contain the actual data. The *patientSys* object is also described separately along with the *sysModel* object and the *imResp* object in Table A.5, Table A.6 and Table A.7.

Table A.1 – *patientData* object description

Object property	Description																																				
<i>info</i>	<i>patientInfo</i> object containing the information on the patient record. As the property names are self-explanatory, they are listed below: <i>ID</i> , <i>name</i> , <i>age</i> , <i>gender</i> , <i>origin</i> , <i>address</i> , <i>phone</i> , <i>email</i> , <i>date</i> , <i>protocol</i> , <i>physExam</i> (physical exam), <i>clinHis</i> (clinical history), <i>famHis</i> (family history).																																				
<i>sig</i>	<i>patientSig</i> object. <table border="1"> <thead> <tr> <th>Property</th> <th>Description</th> </tr> </thead> <tbody> <tr> <td><i>ecg</i></td> <td><i>ecgData</i> object. <table border="1"> <thead> <tr> <th>Property</th> <th>Description</th> </tr> </thead> <tbody> <tr> <td><i>raw</i></td> <td>Raw ECG stored in a <i>dataUnit</i> object.</td> </tr> <tr> <td><i>filt</i></td> <td>Filtered ECG stored in a <i>dataUnit</i> object.</td> </tr> <tr> <td><i>rri</i></td> <td>RRI stored in a <i>varUnit</i> object.</td> </tr> </tbody> </table> </td> </tr> <tr> <td><i>bp</i></td> <td><i>bpData</i> object. <table border="1"> <thead> <tr> <th>Property</th> <th>Description</th> </tr> </thead> <tbody> <tr> <td><i>raw</i></td> <td>Raw BP stored in a <i>dataUnit</i> object.</td> </tr> <tr> <td><i>filt</i></td> <td>Filtered BP stored in a <i>dataUnit</i> object.</td> </tr> <tr> <td><i>sbp</i></td> <td>SBP stored in a <i>varUnit</i> object.</td> </tr> <tr> <td><i>dbp</i></td> <td>DBP stored in a <i>varUnit</i> object.</td> </tr> </tbody> </table> </td> </tr> <tr> <td><i>rsp</i></td> <td><i>rspData</i> object. <table border="1"> <thead> <tr> <th>Property</th> <th>Description</th> </tr> </thead> <tbody> <tr> <td><i>raw</i></td> <td>Raw airflow stored in a <i>dataUnit</i> object.</td> </tr> <tr> <td><i>int</i></td> <td>Integrated airflow stored in a <i>dataUnit</i> object.</td> </tr> <tr> <td><i>ilv</i></td> <td>ILV stored in an <i>ilvUnit</i> object.</td> </tr> <tr> <td><i>filt</i></td> <td>Filtered ILV stored in an <i>ilvUnit</i> object.</td> </tr> </tbody> </table> </td> </tr> </tbody> </table>	Property	Description	<i>ecg</i>	<i>ecgData</i> object. <table border="1"> <thead> <tr> <th>Property</th> <th>Description</th> </tr> </thead> <tbody> <tr> <td><i>raw</i></td> <td>Raw ECG stored in a <i>dataUnit</i> object.</td> </tr> <tr> <td><i>filt</i></td> <td>Filtered ECG stored in a <i>dataUnit</i> object.</td> </tr> <tr> <td><i>rri</i></td> <td>RRI stored in a <i>varUnit</i> object.</td> </tr> </tbody> </table>	Property	Description	<i>raw</i>	Raw ECG stored in a <i>dataUnit</i> object.	<i>filt</i>	Filtered ECG stored in a <i>dataUnit</i> object.	<i>rri</i>	RRI stored in a <i>varUnit</i> object.	<i>bp</i>	<i>bpData</i> object. <table border="1"> <thead> <tr> <th>Property</th> <th>Description</th> </tr> </thead> <tbody> <tr> <td><i>raw</i></td> <td>Raw BP stored in a <i>dataUnit</i> object.</td> </tr> <tr> <td><i>filt</i></td> <td>Filtered BP stored in a <i>dataUnit</i> object.</td> </tr> <tr> <td><i>sbp</i></td> <td>SBP stored in a <i>varUnit</i> object.</td> </tr> <tr> <td><i>dbp</i></td> <td>DBP stored in a <i>varUnit</i> object.</td> </tr> </tbody> </table>	Property	Description	<i>raw</i>	Raw BP stored in a <i>dataUnit</i> object.	<i>filt</i>	Filtered BP stored in a <i>dataUnit</i> object.	<i>sbp</i>	SBP stored in a <i>varUnit</i> object.	<i>dbp</i>	DBP stored in a <i>varUnit</i> object.	<i>rsp</i>	<i>rspData</i> object. <table border="1"> <thead> <tr> <th>Property</th> <th>Description</th> </tr> </thead> <tbody> <tr> <td><i>raw</i></td> <td>Raw airflow stored in a <i>dataUnit</i> object.</td> </tr> <tr> <td><i>int</i></td> <td>Integrated airflow stored in a <i>dataUnit</i> object.</td> </tr> <tr> <td><i>ilv</i></td> <td>ILV stored in an <i>ilvUnit</i> object.</td> </tr> <tr> <td><i>filt</i></td> <td>Filtered ILV stored in an <i>ilvUnit</i> object.</td> </tr> </tbody> </table>	Property	Description	<i>raw</i>	Raw airflow stored in a <i>dataUnit</i> object.	<i>int</i>	Integrated airflow stored in a <i>dataUnit</i> object.	<i>ilv</i>	ILV stored in an <i>ilvUnit</i> object.	<i>filt</i>	Filtered ILV stored in an <i>ilvUnit</i> object.
Property	Description																																				
<i>ecg</i>	<i>ecgData</i> object. <table border="1"> <thead> <tr> <th>Property</th> <th>Description</th> </tr> </thead> <tbody> <tr> <td><i>raw</i></td> <td>Raw ECG stored in a <i>dataUnit</i> object.</td> </tr> <tr> <td><i>filt</i></td> <td>Filtered ECG stored in a <i>dataUnit</i> object.</td> </tr> <tr> <td><i>rri</i></td> <td>RRI stored in a <i>varUnit</i> object.</td> </tr> </tbody> </table>	Property	Description	<i>raw</i>	Raw ECG stored in a <i>dataUnit</i> object.	<i>filt</i>	Filtered ECG stored in a <i>dataUnit</i> object.	<i>rri</i>	RRI stored in a <i>varUnit</i> object.																												
Property	Description																																				
<i>raw</i>	Raw ECG stored in a <i>dataUnit</i> object.																																				
<i>filt</i>	Filtered ECG stored in a <i>dataUnit</i> object.																																				
<i>rri</i>	RRI stored in a <i>varUnit</i> object.																																				
<i>bp</i>	<i>bpData</i> object. <table border="1"> <thead> <tr> <th>Property</th> <th>Description</th> </tr> </thead> <tbody> <tr> <td><i>raw</i></td> <td>Raw BP stored in a <i>dataUnit</i> object.</td> </tr> <tr> <td><i>filt</i></td> <td>Filtered BP stored in a <i>dataUnit</i> object.</td> </tr> <tr> <td><i>sbp</i></td> <td>SBP stored in a <i>varUnit</i> object.</td> </tr> <tr> <td><i>dbp</i></td> <td>DBP stored in a <i>varUnit</i> object.</td> </tr> </tbody> </table>	Property	Description	<i>raw</i>	Raw BP stored in a <i>dataUnit</i> object.	<i>filt</i>	Filtered BP stored in a <i>dataUnit</i> object.	<i>sbp</i>	SBP stored in a <i>varUnit</i> object.	<i>dbp</i>	DBP stored in a <i>varUnit</i> object.																										
Property	Description																																				
<i>raw</i>	Raw BP stored in a <i>dataUnit</i> object.																																				
<i>filt</i>	Filtered BP stored in a <i>dataUnit</i> object.																																				
<i>sbp</i>	SBP stored in a <i>varUnit</i> object.																																				
<i>dbp</i>	DBP stored in a <i>varUnit</i> object.																																				
<i>rsp</i>	<i>rspData</i> object. <table border="1"> <thead> <tr> <th>Property</th> <th>Description</th> </tr> </thead> <tbody> <tr> <td><i>raw</i></td> <td>Raw airflow stored in a <i>dataUnit</i> object.</td> </tr> <tr> <td><i>int</i></td> <td>Integrated airflow stored in a <i>dataUnit</i> object.</td> </tr> <tr> <td><i>ilv</i></td> <td>ILV stored in an <i>ilvUnit</i> object.</td> </tr> <tr> <td><i>filt</i></td> <td>Filtered ILV stored in an <i>ilvUnit</i> object.</td> </tr> </tbody> </table>	Property	Description	<i>raw</i>	Raw airflow stored in a <i>dataUnit</i> object.	<i>int</i>	Integrated airflow stored in a <i>dataUnit</i> object.	<i>ilv</i>	ILV stored in an <i>ilvUnit</i> object.	<i>filt</i>	Filtered ILV stored in an <i>ilvUnit</i> object.																										
Property	Description																																				
<i>raw</i>	Raw airflow stored in a <i>dataUnit</i> object.																																				
<i>int</i>	Integrated airflow stored in a <i>dataUnit</i> object.																																				
<i>ilv</i>	ILV stored in an <i>ilvUnit</i> object.																																				
<i>filt</i>	Filtered ILV stored in an <i>ilvUnit</i> object.																																				
<i>sys</i>	Structure that contains fields that are <i>patientSys</i> objects.																																				

dataUnit object

The *dataUnit* object, described in Table A.2, is the object in which raw and filtered ECG and BP data as well as raw and integrated airflow data is stored.

Table A.2 – *dataUnit* object description

Object property	Description
<i>data</i>	Double array with the actual data.
<i>time</i>	Double array with the time stamp corresponding to <i>data</i> .
<i>fs</i>	Double indicating the sampling frequency of the <i>data</i> .
<i>specs</i>	Structure with any further information to describe <i>data</i> . For raw data, <i>specs</i> is an empty struct. For other type of data, <i>specs</i> vary according to the nature of the data.

ilvUnit object

The *ilvUnit* object is the object in which ILV and filtered ILV is stored. It has the same properties of a *dataUnit* object with added properties, as described below.

Table A.3 – *ilvUnit* object description

Object property	Description																						
<i>aligned</i>	<table border="1"> <thead> <tr> <th colspan="2"><i>alignedUnit</i> data</th> </tr> <tr> <th>Property</th> <th>Description</th> </tr> </thead> <tbody> <tr> <td><i>psd</i></td> <td> <table border="1"> <thead> <tr> <th colspan="2"><i>psdUnit</i> object.</th> </tr> <tr> <th>Property</th> <th>Description</th> </tr> </thead> <tbody> <tr> <td><i>psdFFT</i></td> <td>Double array with the Fourier transform PSD of the ILV or filtered aligned data.</td> </tr> <tr> <td><i>psdAR</i></td> <td>Double array with the AR model PSD of the ILV or filtered aligned data.</td> </tr> <tr> <td><i>psdWelch</i></td> <td>Double array with the Welch method PSD of the ILV or filtered aligned data.</td> </tr> <tr> <td><i>freq</i></td> <td>Double array with the time stamp of the PSDs.</td> </tr> <tr> <td><i>specs</i></td> <td>Structure with information on the parameters of the PSDs.</td> </tr> </tbody> </table> </td> </tr> <tr> <td><i>dataUnit</i></td> <td><i>dataUnit</i> object storing aligned variable data.</td> </tr> </tbody> </table>	<i>alignedUnit</i> data		Property	Description	<i>psd</i>	<table border="1"> <thead> <tr> <th colspan="2"><i>psdUnit</i> object.</th> </tr> <tr> <th>Property</th> <th>Description</th> </tr> </thead> <tbody> <tr> <td><i>psdFFT</i></td> <td>Double array with the Fourier transform PSD of the ILV or filtered aligned data.</td> </tr> <tr> <td><i>psdAR</i></td> <td>Double array with the AR model PSD of the ILV or filtered aligned data.</td> </tr> <tr> <td><i>psdWelch</i></td> <td>Double array with the Welch method PSD of the ILV or filtered aligned data.</td> </tr> <tr> <td><i>freq</i></td> <td>Double array with the time stamp of the PSDs.</td> </tr> <tr> <td><i>specs</i></td> <td>Structure with information on the parameters of the PSDs.</td> </tr> </tbody> </table>	<i>psdUnit</i> object.		Property	Description	<i>psdFFT</i>	Double array with the Fourier transform PSD of the ILV or filtered aligned data.	<i>psdAR</i>	Double array with the AR model PSD of the ILV or filtered aligned data.	<i>psdWelch</i>	Double array with the Welch method PSD of the ILV or filtered aligned data.	<i>freq</i>	Double array with the time stamp of the PSDs.	<i>specs</i>	Structure with information on the parameters of the PSDs.	<i>dataUnit</i>	<i>dataUnit</i> object storing aligned variable data.
<i>alignedUnit</i> data																							
Property	Description																						
<i>psd</i>	<table border="1"> <thead> <tr> <th colspan="2"><i>psdUnit</i> object.</th> </tr> <tr> <th>Property</th> <th>Description</th> </tr> </thead> <tbody> <tr> <td><i>psdFFT</i></td> <td>Double array with the Fourier transform PSD of the ILV or filtered aligned data.</td> </tr> <tr> <td><i>psdAR</i></td> <td>Double array with the AR model PSD of the ILV or filtered aligned data.</td> </tr> <tr> <td><i>psdWelch</i></td> <td>Double array with the Welch method PSD of the ILV or filtered aligned data.</td> </tr> <tr> <td><i>freq</i></td> <td>Double array with the time stamp of the PSDs.</td> </tr> <tr> <td><i>specs</i></td> <td>Structure with information on the parameters of the PSDs.</td> </tr> </tbody> </table>	<i>psdUnit</i> object.		Property	Description	<i>psdFFT</i>	Double array with the Fourier transform PSD of the ILV or filtered aligned data.	<i>psdAR</i>	Double array with the AR model PSD of the ILV or filtered aligned data.	<i>psdWelch</i>	Double array with the Welch method PSD of the ILV or filtered aligned data.	<i>freq</i>	Double array with the time stamp of the PSDs.	<i>specs</i>	Structure with information on the parameters of the PSDs.								
<i>psdUnit</i> object.																							
Property	Description																						
<i>psdFFT</i>	Double array with the Fourier transform PSD of the ILV or filtered aligned data.																						
<i>psdAR</i>	Double array with the AR model PSD of the ILV or filtered aligned data.																						
<i>psdWelch</i>	Double array with the Welch method PSD of the ILV or filtered aligned data.																						
<i>freq</i>	Double array with the time stamp of the PSDs.																						
<i>specs</i>	Structure with information on the parameters of the PSDs.																						
<i>dataUnit</i>	<i>dataUnit</i> object storing aligned variable data.																						
<i>dataUnit</i>	<i>dataUnit</i> object storing variable data.																						

varUnit object

The *varUnit* object is the object in which RRI, SBP and DBP is stored. It has the same properties of an *ilvUnit* object with added properties, as described in Table A.4.

Table A.4 – *varUnit* object description

Object property	Description
<i>ectopic</i>	Double array with the indexes of ectopic beat related variables on the <i>data</i> property of this object's <i>ilvUnit</i> properties.
<i>index</i>	Double array with the indexes of the variables on the <i>data</i> property of this object's <i>ilvUnit</i> properties in relation to the record it was extracted from.
<i>ilvUnit</i>	<i>ilvUnit</i> storing the variable data and the variable PSD data.

patientSys object

The *patientSys* object, described in Table A.5, is the object in which a system is stored, composing the *sys* property of the *patientData* object's structure fields.

Table A.5 – *patientSys* object description

Object property	Description
<i>data</i>	<i>iddata</i> object containing the system itself with the experiments <i>Estimation data</i> and <i>Validation data</i> , if less than 100% of the data was set for estimation.
<i>trends</i>	<i>iddata</i> object containing the trends extracted from the system with the experiments <i>Estimation data</i> and <i>Validation data</i> , if less than 100% of the data was set for estimation.
<i>models</i>	Structure that contains fields that are <i>sysModel</i> objects.

sysModel object

The *sysModel* object, described in Table A.6, is the object in which a model is stored, composing the *models* property of the *patientSys* object's structure fields. The *sysImResp* object which composes the *imresp* property is described in Table A.7.

Table A.6 – *sysModel* object description

Structure field	Description
<i>name</i>	String identifying model tag in the format <i>modelX</i> , where X is a sequential number.

<i>type</i>	String identifying model type (AR, ARX, LBF or MBF).
<i>outputData</i>	Cell array containing the system output for estimation and validation (if any).
<i>outputName</i>	Cell string identifying output variable (RRI, HR, SBP, DBP or ILV).
<i>outputUnit</i>	Cell string identifying output unit (ms, bpm, mmHg, L).
<i>inputName</i>	Cell string identifying input variable(s) (RRI, HR, SBP, DBP and/or ILV).
<i>inputUnit</i>	Cell string identifying input unit(s) (ms, bpm, mmHg and/or L).
<i>ts</i>	Double indicating the sampling interval.
<i>order</i>	Double array indicating the order of each term or the number of basis functions used for each term in the format [na nb1 nb2]. For LBF or MBF models na = 0.
<i>delay</i>	Double array indicating the delays of each input in samples in the format [nk1 nk2].
<i>theta</i>	Double array with the estimated model coefficients.
<i>sysMem</i>	Double indicating system memory length. Empty for AR/ARX models.
<i>pole</i>	Double indicating pole used to generate basis functions. Empty for AR/ARX models.
<i>genOrd</i>	Double indicating generalization order used to generate basis functions. Empty for AR/ARX or Laguerre basis function models.
<i>fit</i>	Double array indicating the fit between measured and predicted output for estimation and validation data.
<i>simOutEst</i>	Predicted output for estimation data set (<i>iddata</i> object).
<i>simOutVal</i>	Predicted output for validation data set (<i>iddata</i> object).
<i>imResp</i>	<i>imResp</i> data object containing the system impulse response(s).
<i>notes</i>	String describing the system and model.

imResp object

The *imResp* object, described in Table A.7, stores the model's impulse response data.

Table A.7 – *imResp* object description

Object property	Description
<i>impulse</i>	Cell array with the impulse response. If there are two inputs, the impulse response for the first input can be accessed in <i>impulse</i> {1} and the response for the second input in <i>impulse</i> {2}.
<i>time</i>	Double array with the impulse response's time stamp.
<i>indicators</i>	Structure (described below) with the indicators extracted from the impulse response(s).

dataUnit.specs

The *dataUnit* object, described in Table A.2 presents a *specs* property that is a struct with different fields, depending on the data type. Table A.8 presents the fields for each data type along with a brief description. Data types that are not addressed present an empty struct as the *specs* property.

Table A.8 – *specs* property fields according to the type of data in a *dataUnit* object

Data type	Field in <i>specs</i>	Description										
Filtered ECG / BP	<i>notch</i>	Notch filter tolerance.										
	<i>lowPass</i>	Low-pass filter cut-off frequency.										
	<i>highPass</i>	High-pass filter cut-off frequency (ECG only).										
RRI / SBP / DBP	<i>type</i>	String identifying the record from which the variable was extracted. This field must correspond to one of the two options: <i>raw</i> , <i>filt</i> . If it is non-existent, CRSIDLab will consider <i>raw</i> .										
	<i>algorithm</i>	String indicating the algorithm used to extract the variables. Can be set by the user as preferred.										
ILV/Filtered ILV	<i>method</i>	<i>Struct</i> with at least one field, <i>id</i> , and a possible second complimentary field, <i>fc</i> or <i>order</i> .										
		<table border="1"> <thead> <tr> <th>Field</th> <th>Description</th> </tr> </thead> <tbody> <tr> <td><i>id</i></td> <td>String indicating the detrending method applied.</td> </tr> <tr> <td><i>fc</i> or <i>order</i></td> <td>If <i>method.id</i> is <i>High-pass filter</i>, additional field <i>fc</i> must exist, indicating the filter's cut-off frequency. If <i>method.id</i> is <i>Polynomial</i>, additional field <i>order</i> must exist, indicating the polynomial order.</td> </tr> </tbody> </table>	Field	Description	<i>id</i>	String indicating the detrending method applied.	<i>fc</i> or <i>order</i>	If <i>method.id</i> is <i>High-pass filter</i> , additional field <i>fc</i> must exist, indicating the filter's cut-off frequency. If <i>method.id</i> is <i>Polynomial</i> , additional field <i>order</i> must exist, indicating the polynomial order.				
Field	Description											
<i>id</i>	String indicating the detrending method applied.											
<i>fc</i> or <i>order</i>	If <i>method.id</i> is <i>High-pass filter</i> , additional field <i>fc</i> must exist, indicating the filter's cut-off frequency. If <i>method.id</i> is <i>Polynomial</i> , additional field <i>order</i> must exist, indicating the polynomial order.											
Aligned variables	<i>method</i>	String indicating the method used to resample the variable.										
	<i>ectopic</i>	String indicating how ectopic beats and related variables were handled.										
	<i>type</i>	Exclusive for aligned and resampled variable originating from RRI: indicates whether aligned RRI output is RRI or HR.										
	<i>border</i>	<i>Struct</i> with two fields, <i>start</i> and <i>end</i> .										
		<table border="1"> <thead> <tr> <th>Field</th> <th>Description</th> </tr> </thead> <tbody> <tr> <td><i>start</i></td> <td><i>Struct</i> with two fields, <i>ref</i> and <i>value</i>.</td> </tr> <tr> <td></td> <td> <table border="1"> <thead> <tr> <th>Field</th> <th>Description</th> </tr> </thead> <tbody> <tr> <td><i>ref</i></td> <td>String indicating the variable used as reference for the end of the aligned data set, or indicating the number of samples was set.</td> </tr> </tbody> </table> </td> </tr> </tbody> </table>	Field	Description	<i>start</i>	<i>Struct</i> with two fields, <i>ref</i> and <i>value</i> .		<table border="1"> <thead> <tr> <th>Field</th> <th>Description</th> </tr> </thead> <tbody> <tr> <td><i>ref</i></td> <td>String indicating the variable used as reference for the end of the aligned data set, or indicating the number of samples was set.</td> </tr> </tbody> </table>	Field	Description	<i>ref</i>	String indicating the variable used as reference for the end of the aligned data set, or indicating the number of samples was set.
Field	Description											
<i>start</i>	<i>Struct</i> with two fields, <i>ref</i> and <i>value</i> .											
	<table border="1"> <thead> <tr> <th>Field</th> <th>Description</th> </tr> </thead> <tbody> <tr> <td><i>ref</i></td> <td>String indicating the variable used as reference for the end of the aligned data set, or indicating the number of samples was set.</td> </tr> </tbody> </table>	Field	Description	<i>ref</i>	String indicating the variable used as reference for the end of the aligned data set, or indicating the number of samples was set.							
Field	Description											
<i>ref</i>	String indicating the variable used as reference for the end of the aligned data set, or indicating the number of samples was set.											

	<i>value</i>	End of the aligned data set, given in seconds.
<i>end</i>	<i>Struct with two fields, ref and value.</i>	
	Field	Description
	<i>ref</i>	String indicating the variable used as reference for the start of the aligned data set.
	<i>value</i>	Start of the aligned data set, given in seconds.

method

String indicating the method used to complete border samples.

tag

Aligned variable identification as will be shown on CRSIDLab for user selection. Standard form reads:
A&R VAR data (X Hz – Y samples)
 VAR: RRI, HR, SBP, DBP, ILV, Filtered ILV.
 X: Frequency used to resample the variable.
 Y: Number of samples after resampling.
